UNIVERSITY OF OKLAHOMA

GRADUATE COLLEGE

HISTORY MATCHING OF 3D RESERVOIR MODELS WITH COMPLEX NON-GAUSSIAN DISTRIBUTIONS OF THE MODEL PARAMETERS

A DISSERTATION

SUBMITTED TO THE GRADUATE FACULTY

in partial fulfillment of the requirements for the

Degree of

DOCTOR OF PHILOSOPHY

By

CHINEDU C. AGBALAKA
Norman, Oklahoma
2010

HISTORY MATCHING OF 3D RESERVOIR MODELS WITH COMPLEX NON-GAUSSIAN DISTRIBUTIONS OF THE MODEL PARAMETERS

A DISSERTATION APPROVED FOR THE
MEWBOURNE SCHOOL OF PETROLEUM AND GEOLOGICAL ENGINEERING

BY

Dean S. Oliver, Committee Chair

Carl H. Sondergeld

Deepak Devegowda

Chandra S. Rai

Randy G. Keller

DEDICATION

To the memories of Sochiebuka C. Agbalaka and Sochima Agbalaka.

To all great scholars, past and present, on whose shoulders we stand . . .

"As far as the laws of mathematics refer to reality, they are not certain, and as far as they are certain, they do not refer to reality."—Albert Einstein

ACKNOWLEDGEMENTS

My special thanks goes primarily to my adviser Dr. Dean S. Oliver who inarguably is one of the best advisers any graduate student can ask for. My deep thanks to the members of my doctoral committee, Drs. Sondergeld; Rai; Devegowda; and Keller, for the many useful comments that helped shape this dissertation.

Special thanks to the MPGE staff for their ever ready help whenever needed. Specific thanks to Shalli, Sonya and Michael whose help I had repeatedly sought and who willingly extended their help whenever needed. The help of the ISS staff is deeply appreciated particularly the DSO, Danika Hines.

To my friends and colleagues in the *OU Consortium on Ensemble Methods*, the many nights we have spent in Sarkeys Energy Center has been worthwhile and the spirit of cooperation we shared is next to none. To all my other friends, too numerous to mention, thank you for all your help, support, and encouragement.

Very special thanks to Mary Oliver for the many thanksgiving meals, for her kindness and hospitality.

Many thanks to my parents and siblings, for all their prayers and words of encouragement. To my wife Ngozi without whose support, encouragement and sacrifice it would have been impossible to complete my PhD study, thank you my love for always being there and for being an instrument of blessing to me. To my son, Chinedu V. Agbalaka, thank you for understanding the need for daddy to be away even when you needed some father–son time. I will make it up to you somehow.

Finally, to God Almighty, in Whom we live and move and have our being... *Non nobis, Domine, non nobis, sed nomini tuo da gloriam: super misericordia tua et veritate tua; (Psalm 115:1).*

TABLE OF CONTENTS

LIST OF TABLES

LIST OF FIGURES

ABSTRACT

Although the first application of the ensemble Kalman filter (EnKF) as a technique for sequential assimilation of noisy measurements was to a numerical weather prediction problem, remarkable research progress has been made in adapting this technique for application to data assimilation problems in reservoir engineering. Since its first application to a fairly simple parameter estimation problem in petroleum engineering less than a decade ago, the ensemble Kalman filter has been applied to fairly complex sequential model calibration problems in reservoir engineering with remarkable success. The reason for the rapid increase in the application of EnKF to data assimilation problems in reservoir engineering is partly due to the ease of implementing this technique; it is unnecessary to determine sensitivities from adjoint equations and the correlations between the model parameters and predicted data are estimated from the ensemble. Also the information from previously assimilated data are stored within the ensemble of conditional models such that it is unnecessary to repeat the history matching on previously assimilated data whenever new data are available for assimilation.

Despite the encouraging performance of EnKF applied to sequential model calibration problems in reservoir engineering, the formulation of the ensemble Kalman filter is based on some critical assumptions (linear forward model and Gaussian model priors) that are generally not valid for reservoir engineering problems. The EnKF performance is optimal if at each data assimilation timestep, the prior state vector is linearly related to the predicted data and the distribution of the prior state vector is multivariate Gaussian. The state vector in reservoir engineering applications consists of the static model variables and the dynamic model variables, i.e., gridblock

pressures and saturations for a black oil model. Some potential issues with EnKF applied to data assimilation problems in reservoir engineering include the following: non-Gaussian dynamic and/or static model parameters in the state vector, nonlinear model–data relationship, etc. Usually, the presence of severe nonlinearities is resolved by iteration, which also resolves the problem of non-Gaussian dynamic variables. However, for history matching problems with complex non-Gaussian model parameters, such as facies variables, vertical flow barriers, multimodal model variables, etc, the nonlinear effects are exacerbated and the performance of the EnKF in adjusting the models to obtain predictions that match production data is significantly degraded.

In this dissertation, I focus on history matching problems with non-Gaussian model parameters for which the standard EnKF will perform very poorly without modifications. I identify some of the difficulties in the application of the EnKF to the problem of updating facies models to match both production measurements and facies observations at the well locations and propose some modifications at the update step that improve the overall performance of the ensemble Kalman filter. I also introduce the concept of using pseudo-model variables for jointly updating the discrete facies variables and the multimodal rock properties in a way that is consistent with the EnKF updating scheme. The problem of updating reservoir models with vertical flow barriers using EnKF is also addressed in this dissertation. Estimation of vertical flow barriers is of practical importance in reservoir simulation studies as these flow barriers influence recovery mechanisms, gravity drainage processes and the selection of optimal well performance parameters. I outline three very efficient and fairly general methods for parameterizing the vertical transmissibility barriers between reservoir zones so that zonal communication can be shut off if production data indicate that there should be no communication. The EnKF will generally perform very poorly in generating conditional samples of the reservoir models if the posterior PDF is multimodal. I

introduce a two-stage ensemble Kalman filter technique for application to history matching problems with multiple modes. I demonstrate the advantage of two-stage EnKF technique on a fairly complex low-order reservoir model with non-Gaussian model parameters and show that it converges to a better history match solution than the standard EnKF.

CHAPTER I

INTRODUCTION

History matching is an inverse estimation problem where parameters of a reservoir model are adjusted so that predictions from the history matched model honor the field measurements. The history matched model(s) are then used for future prediction of the reservoir performance, which is necessary for reservoir development planning and optimization. To assess the prediction risks and/or evaluate prediction uncertainty, it is common to calibrate multiple reservoir models to field measurements and compute various statistics from the ensemble of predicted data. Accurate quantification of prediction uncertainty requires that the conditional PDF of the model be sampled correctly. In general, the number of unknown model parameters in the reservoir simulation model is large and the shape or form of the conditional PDF of the model is usually not known.

The Bayesian approach provides a convenient framework for integrating dynamic and static data with a prior PDF of the model to obtain a formal expression for generating realizations of the model from a posterior PDF. Usually the process of generating a conditional model from the posterior is recast as a nonlinear optimization problem that seeks to minimize a misfit functional defined by the weighted sum of squared errors between, (1) the noisy production measurements and the data predicted by the model, and (2) a conditional realization of the model parameters and an unconditional realization of the model parameters. The prior (unconditional) model parameters are the geologically consistent model variables estimated from the initial best-guess knowledge of the reservoir using information from cores, well logs, outcrops, etc.

Two broad approaches have been used traditionally to obtain conditional realizations of the reservoir model by minimizing a misfit functional: (1) a gradient-based approach, which uses formulations such as the Gauss-Newton method, quasi-Newton method, steepest descent method, etc and (2) a non-gradient-based or derivative-free approach such as simulated annealing, genetic algorithm, Markov chain Monte Carlo (McMC), etc. Both approaches have their respective strengths and weaknesses. The derivative-free approach does not require gradient computation but evaluates the objective function by making multiple simulation runs for different realizations of the model parameters. This approach becomes prohibitively expensive for large-scale history matching applications. The gradient-based approach, on the other hand, requires much fewer simulation runs but involves the computation of gradients, which can be quite expensive. Methods for obtaining the gradients include numerical perturbation and adjoint methods. The numerical perturbation method is fairly easy to implement but becomes prohibitively expensive if the number of model parameters is large. The adjoint method (Wu et al., 1999; Zhang and Reynolds, 2002) is a fairly efficient way for computing gradients but is also rather inflexible (adjoint codes are simulator specific and are thus not portable) and in some instances requires an inordinate amount of time to implement. Traditional implementation of both the gradient-based and gradient-free approaches are nonrecursive, i.e., the optimization problem has to be re-solved whenever new data are available, thereby making the methods unsuitable for online data assimilation problems where data are continuously/intermittently available for updating the reservoir models.

Sequential data assimilation refers to a process where the parameters of a reservoir model are adjusted to match production data as they become available while preserving the history of previously matched data. If an ensemble of reservoir models are calibrated to production measurements at each data assimilation timestep, then a discrete approximation of the posterior PDF conditional on all previously assimilated

data is available at any data assimilation timestep. Various statistical inferences may be obtained from the conditional models, which may be used for reservoir management planning. The ensemble Kalman filter (EnKF) has recently been introduced (Evensen, 1994; Houtekamer and Mitchell, 1998) as a data assimilation tool for continuous assimilation of atmospheric data in numerical weather prediction problems (Anderson and Anderson, 1999; Hamill et al., 2000; Houtekamer and Mitchell, 2001). The problem of data assimilation in petroleum engineering is in many respects similar to the numerical weather prediction problem, i.e., both problems deal with large-scale, nonlinear dynamical systems, but fundamental differences between both problems also exist; these relate to initialization of the dynamic states, estimation of the static and dynamic model parameters, accounting for model error, need for constraints on some state variables, etc. Despite these difference, the ensemble Kalman filter has been applied successfully, with modifications, to data assimilation problems in petroleum engineering (Nævdal et al., 2002; Lorentzen et al., 2005; Gu and Oliver, 2005; Evensen et al., 2007; Devegowda et al., 2007; Agbalaka and Oliver, 2008; Zhang and Oliver, 2009; Chen and Oliver, 2010).

The ensemble Kalman filter is a Monte-Carlo based approach to history matching in which multiple geologically-based realizations of the reservoir are sequentially calibrated to production measurements in lieu of a single model. Because multiple realizations of the reservoir model are updated at each data assimilation timestep, a suite of reservoir models that honor data is available at all times and it is thus possible to quantify uncertainty in the prediction of future reservoir performance from the ensemble. If the number of measurements assimilated at each timestep is fairly moderate (as is the case in this dissertation), the bulk of the cost in implementing the EnKF technique is the simulation time required to run all the realizations of the reservoir model.

The optimal performance of the EnKF in generating conditional models that represent a correct sampling of the posterior PDF depends critically on two assumptions: (1) the prior PDF of the model variables should be approximately Gaussian; and (2) the relationship between the static models variables (e.g., porosity and permeability), the dynamic model variables (e.g., gridblock pressures and saturations) and the predicted data should be approximately linear. When these assumptions are not strongly violated, the EnKF approximately samples the posterior PDF correctly and provides reasonable quantification of uncertainty (Gao et al., 2006). However, for cases where these assumptions are violated, using the EnKF technique without modification will result in suboptimal performance of the EnKF in sampling the conditional PDF of the model (Gu and Oliver, 2007; Li and Reynolds, 2009) leading to poor history match to data and poor estimation of the reservoir model parameters (Agbalaka and Oliver, 2010). Several approaches have been presented for dealing with nonlinearity in the state variables for application to history matching. Since the gridblock pressures and saturations are also updated when data are assimilated, the magnitude of the correction to the gridblock saturations is commonly used as a measure of the severity of the nonlinear effects. At any data assimilation timestep with severe nonlinearity, very large changes are made to the saturation field resulting in physically implausible saturation values (Gu and Oliver, 2006; Agbalaka and Oliver, 2008). Similar observation of inconsistent updates to the compositions in a compositional reservoir model has been reported by Phale and Oliver (2009). Gu and Oliver (2006) used a normal-score transform of water saturation to avoid non-physical saturation but unrealistic oscillations in water saturation values were still observed. Phale and Oliver (2009) and Wang et al. (2009) independently used a constrained EnKF approach to enforce physically plausible bounds on the state variables. Chen et al. (2009) updated an approximately-Gaussian saturation arrival time in lieu of directly updating the water saturation. The updated water saturation variables were obtained from the updated

saturation arrival time using a nonlinear interpolation. In some other cases, the iterative ensemble filters have been used to obtain consistent updates to both the static and dynamic model variables when the problem is very nonlinear (Zupanski, 2005; Gu and Oliver, 2007; Li and Reynolds, 2009).

In this dissertation, I focus on the problem where the second critical assumption of the EnKF (complex non-Gaussian distributions of the model parameters) is not honored and propose approaches for dealing with specific occurrences of this problem. Recall that under this condition, the performance of the ensemble Kalman filter is degraded leading to very poor match to data and very poor estimates of the model parameters. Specifically, I consider the problems of EnKF applied to history matching (1) reservoir facies models, (2) models with vertical flow barriers, and (3) model with non-Gaussian model priors and multimodal posterior PDF.

All the facies models presented in this dissertation were obtained by truncating one or more Gaussian random fields (GRFs) using the truncated pluriGaussian simulation. The initial application of EnKF to the problem of history matching an ensemble of 2D geological facies model, obtained by truncating two Gaussian random fields, was reported in Liu and Oliver (2005b,a). Since then the work has been extended to more complex and nonlinear 3D facies history matching problems by Agbalaka and Oliver (2008) and Zhao et al. (2008). Apart from the truncated pluriGaussian approach, the level sets method for generating facies models have been combined with EnKF for history matching (Moreno et al., 2008). Also, Sun et al. (2009a) and Sarma and Chen (2009) applied EnKF to the problem of history matching facies models generated from multipoint geostatistics. Sun et al. (2009a) utilized a Gaussian mixture model based approach for a single-phase flow problem in hydrology and Sarma and Chen (2009) used a kernel-PCA based approach for a two-phase reservoir engineering problem, although the history matching results of Sarma and Chen (2009) were very

poor. The problem of obtaining conditional realizations of facies models from assimilating production data using EnKF is very difficult. Some of these difficulties include: (1) how to mitigate excessive loss in ensemble variability, (2) how to re-constrain the predicted facies at the well locations if they do not match the facies observations after assimilating production data, (3) how to update the multimodal petrophysical properties of the facies, etc. To address these difficulties, I present and discuss approaches based respectively on (1) localizing the updates to the facies models when facies data are assimilated, (2) decoupling the assimilation of dynamic production measurements and static facies data at each assimilation timestep, and (3) using the concept of pseudo-model variables for modeling the intra-facies properties when these are uncertain, heterogenous and nonuniform. These approaches seem to work quite well for the data assimilation problems presented in this dissertation.

I also present a general approach for coupling the EnKF technique with the problem of estimating the location of vertical flow barriers from assimilating production data. By modeling the vertical transmissibility multipliers as flow barriers and parameterizing the transformed multipliers as Gaussian random variables, the distribution of the vertical transmissibility barriers between zones can be estimated in a consistent way using the EnKF. I discuss three alternative parameterizations of the vertical flow barrier based on different representations of the probability of observing a transmissive vs. impermeable barrier at each grid location.

Finally, I describe a novel two-stage EnKF technique that provides a practical framework for applying the EnKF to history matching problems with multiple modes. The proposed approach utilizes two sequential stages of EnKF to generate conditional samples of the reservoir models around a mode of the posterior multimodal PDF instead of the mean. The non-Gaussian model parameters in this case were transformed using a shifted-sigmoid function. Throughout this dissertation, significant violation of the EnKF linearity assumption is handled in one of two ways: (1) implementing

a formulation of the iterative EnKF, the ensemble randomized maximum likelihood filter (EnRMLF), proposed by Gu and Oliver (2007) or (2) rerunning the model from time zero after assimilating data.

There are seven chapters in this dissertation. The Bayesian updating framework is discussed briefly in Chapter 2 as well as formulations of the Kalman filter, the extended Kalman filter and the ensemble Kalman filter. Chapter 3 describes several techniques for extending the application of the standard EnKF to the problem of obtaining conditional realizations of the facies models from assimilating production data. The petrophysical properties in this case are assumed to be uniform, homogenous and known. Chapter 4 extends the application of EnKF to the problem of history matching geological facies to account for the uncertainty in the distribution of the petrophysical properties. Because the distribution of petrophysical properties is different in each facies, the probability density for petrophysical properties is multimodal and the EnKF assumption of Gaussianity is not valid. The chapter describes the idea behind using the pseudo-properties distribution in each facies class as a proxy to the multimodal distribution of the actual petrophysical properties such that consistent updates to both the petrophysical properties and the facies variables are obtained using EnKF. Chapter 5 illustrates the application of EnKF to the problem of estimating the spatial distribution of vertical transmissibility barriers from assimilating production data. Chapter 6 introduces the two-stage EnKF for generating conditional samples of the reservoir model for a low-order history matching problem with multiple modes. The main conclusions are discussed in Chapter 7.

CHAPTER II

BAYESIAN UPDATING, KALMAN FILTER AND ENSEMBLE KALMAN FILTER

2.1 The Bayesian Updating Problem

In this section I summarize the important aspects of the Bayesian updating problem. More detailed discussions may be found in Jazwinski (1970); Arulampalam et al. (2002); Lewis et al. (2006).

In the Bayesian approach to estimating the parameters and/or state of a dynamical system, the probability density function (PDF) of the system is estimated using the set of all available information, which may include direct or indirect measurements of the state. In an online estimation problem where measurements for updating the PDF are sequentially available at discrete time intervals, a recursive Bayesian updating approach is convenient. In this case, sequential sets of data are used to recursively update the PDF whenever they are available without reprocessing previous data sets. Recursive updating (filtering) consists fundamentally of two stages, namely: (1) a prediction stage where the PDF is evolved from one measurement time to the next, and (2) an update stage where newly available data are used to adjust the prediction PDF.

Suppose $y_k \in \mathbb{R}^{n_y}$, denotes a state vector containing all the relevant information needed to describe the dynamical system at time, t_k. Suppose also that the evolution of the state vector between two consecutive timesteps, t_{k-1} and t_k, is governed by,

$$y_k = \psi_k(y_{k-1}, \omega_k), \tag{2.1}$$

where $\omega_k \in \mathbb{R}^{n_\omega}$ is an independent and identically distributed (iid) system noise

that captures the errors in the model at time t_k and $\psi_k : \mathbb{R}^{n_y} \times \mathbb{R}^{n_\omega} \rightarrow \mathbb{R}^{n_y}$ is possibly a nonlinear function of the state vector defining its evolution. A sequence of measurements,

$$d_{obs,k} = h_k(y_{k-1}, \epsilon_k), \tag{2.2}$$

is available at distinct time intervals where $h_k : \mathbb{R}^{n_y \times n_\epsilon} \rightarrow \mathbb{R}^{n_d}$ is possibly a nonlinear function of the state vector that predicts data and $\epsilon_k \in \mathbb{R}^{n_\epsilon}$ is an i.i.d. measurement noise. The updating problem may then be stated as follows: Given a sequence of noisy measurements, $D_{obs,k} = \{d_{obs,1}, d_{obs,2} \ldots, d_{obs,k}\}$, estimate the PDF of the state vector, $p(y_k|D_{obs,k})$, conditional on the set of all available measurements at time t_k. Conceptually, this PDF is obtained recursively from two stages involving a prediction stage and a filtering stage.

Without loss of generality we suppose that the PDF, $p(y_{k-1}|D_{obs,k-1})$, is available at time, t_{k-1}. Note that $p(y_0|D_{obs,0}) = p(y_0)$ is the probability of the initial state vector. The prediction stage uses the state vector evolution equation to obtain the prior PDF of the state at time t_k via the Chapman-Kolmogorov equation,

$$p(y_k|D_{obs,k-1}) = \int p(y_k|y_{k-1}) p(y_{k-1}|D_{obs,k-1}) \mathrm{d}y_{k-1}, \tag{2.3}$$

where the fact that Eq. 2.1 defines a first-order Markov process has been used, i.e., current state vector only depends on the previous state vector. Eq. 2.3 is the one step predictor probability density and $p(y_k|y_{k-1})$ is the one-step transition probability that is uniquely determined by the properties of ω_k, given the dynamics in Eq. 2.1. When new measurements, $d_{obs,k}$, are available at time t_k, the prior PDF, $p(y_k|D_{obs,k-1})$, from Eq. 2.3 is updated using Bayes' rule as,

$$p(y_k|D_{obs,k}) = \frac{p(D_{obs,k})}{p(D_{obs,k-1})} p(d_{obs,k}|y_k) p(y_k|D_{obs,k-1}), \tag{2.4}$$

where $p(d_{obs,k}|y_k)$ is the likelihood function defined by the measurement model (Eq. 2.2) and Eq. 2.4 defines the filter probability density for generating conditional realizations of the state vector, y_k, at timestep, t_k. The filter probability density is then

evolved to the next timestep, t_{k+1}, when the next set of data, $d_{obs,k+1}$, are used to update the PDF and thus the cycle of prediction and filtering is repeated. Eqs. 2.3 and 2.4 form the basis for the optimal recursive Bayesian solution. Usually, there is no closed form analytical solution to the recursive propagation of the PDFs and the only recourse is to find approximate solutions (suboptimal filters such as the extended Kalman filters, particle filters, etc) or in some instances, to impose fairly restrictive assumptions to obtain exact analytical solutions (optimal filters such as the Kalman filter and grid-based filter).

2.2 The Kalman Filter

The Kalman filter (Kalman, 1960; Kalman and Bucy, 1961) was first derived for solving state estimation problems in linear dynamical systems. It provides an analytically tractable form of the optimal recursive Bayesian solution for updating multivariate Gaussian PDFs of the state vector subject to the following assumptions:

1. The model error, ω_k, is multivariate Gaussian with $E[\omega_k] = 0$ and $E[\omega_k \omega_k^T] = Q_k$. $E[\cdot]$ is the expectation operator.

2. The measurement noise, ϵ_k, is also multivariate Gaussian with $E[\epsilon_k] = 0$ and $E[\epsilon_k \epsilon_k^T] = C_{D,k}$.

3. ω_k and ϵ_k are temporally uncorrelated, i.e., $E[\omega_k \omega_{k-1}^T] = E[\omega_{k-1} \omega_k^T] = 0$ and $E[\epsilon_k \epsilon_{k-1}^T] = E[\epsilon_{k-1} \epsilon_k^T] = 0$. Also ω_k and ϵ_k are uncorrelated ($E[\omega_k \epsilon_k^T] = E[\epsilon_k \omega_k^T] = 0$) at any data assimilation timestep, t_k.

4. The dynamical model, $\psi_k(y_{k-1}, \omega_k)$ (Eq. 2.1), is linear in both the state vector, y_{k-1}, and the model error, ω_k, such that the state evolution between consecutive timesteps (t_{k-1} and t_k) is given by,

$$y_k = \Psi_k y_{k-1} + \sigma_k(y_{k-1}) \omega_k, \tag{2.5}$$

where $\sigma(y_{k-1}) \in \mathbb{R}^{n_y \times n_\omega}$ is a matrix that maps the model error, ω_k, from $\mathbb{R}^{n_\omega}$ to $\mathbb{R}^{n_y}$ and Ψ_k is a state vector transition matrix that evolves the state vector from time t_{k-1} to time t_k.

5. The measurement model, $h_k(y_{k-1}, \epsilon_k)$, is linear in both the state vector, y_{k-1}, and the measurement noise, ϵ_k, such that,

$$d_{obs,k} = H_k y_{k-1} + \epsilon_k, \tag{2.6}$$

where H_k is a measurement operator matrix that relates the state vector to theoretical data.

If these assumptions hold, then the prior and posterior PDFs are both Gaussian and it is sufficient to estimate the first two moments of the PDF to completely characterize the distribution function at any time. The Gaussian PDFs for generating realizations of the prior and posterior state vectors are given by,

$$\begin{aligned} p(y_k|D_{obs,k-1}) &= \mathcal{N}(\hat{y}_{k|k-1}, C_{y,k|k-1}) \\ p(y_k|D_{obs,k}) &= \mathcal{N}(\hat{y}_{k|k}, C_{y,k|k}), \end{aligned} \tag{2.7}$$

where the subscripts $k|k-1$ and $k|k$ denote the estimate at timestep t_k conditional on measurements at timesteps t_{k-1} and t_k respectively. $\hat{y} = E[y]$ denotes the expected value of the vector y. $\hat{y}_{k|k-1}$ and $C_{y,k|k-1}$ in Eq. 2.7 are the mean and covariance of the Gaussian PDF from the prediction stage estimated as,

$$\begin{aligned} \hat{y}_{k|k-1} &= \Psi_k \hat{y}_{k-1|k-1}, \\ C_{y,k|k-1} &= \sigma_k(y_{k-1}) Q_{k-1} \sigma_k^T(y_{k-1}) + \Psi_k C_{y,k-1|k-1} \Psi_k^T. \end{aligned} \tag{2.8}$$

Eq. 2.8 is an expression for the prediction stage of the Kalman filter. The conditional mean, $\hat{y}_{k|k}$, and covariance, $C_{y,k|k}$, of the Gaussian PDF estimated from the filtering stage is given explicitly by,

$$\begin{aligned} \hat{y}_{k|k} &= \hat{y}_{k|k-1} + K_k(d_{obs,k} - H_k \hat{y}_{k|k-1}) \\ C_{y,k|k} &= (I - K_k H_k) C_{y,k|k-1}, \end{aligned} \tag{2.9}$$

where

$$S_k = H_k C_{y,k|k-1} H_k^T + C_{D,k} \tag{2.10}$$

and

$$K_k = C_{y,k|k-1} H_k^T S_k^{-1} \tag{2.11}$$

are the covariance of the innovation term $(d_{obs,k} - H_k \hat{y}_{k|k-1})$ and the Kalman gain matrix respectively. The Kalman filter is an optimal estimator subject to a Gaussian prior and the condition that all the given assumptions are satisfied. However, applications of the method to problems in reservoir engineering have been limited because some of the assumptions usually do not hold. Also, because of the need to explicitly obtain, update and evolve the full covariance of the state vector at each update step, use of the technique for large-scale data assimilation problems typical in petroleum engineering is computationally very expensive. However, instances of the application of the Kalman filter to estimation problems in petroleum engineering with very small number of parameters have been reported in Mansure et al. (1999) and Corser et al. (2000).

2.3 The Extended Kalman Filter

The extended Kalman filter (EKF) was derived to extend the applications of the Kalman filter to nonlinear dynamical systems and nonlinear measurement models with Gaussian additive noise respectively represented by,

$$y_k = \psi_k(y_{k-1}) + \sigma_k(y_{k-1})\omega_k \tag{2.12}$$

and

$$d_{obs,k} = h_k(y_{k-1}) + \epsilon_k. \tag{2.13}$$

However, similar to the Kalman filter, EKF also assumes that the prior and posterior PDFs are approximately Gaussian such that only the mean and covariance of the PDF are updated and propagated at each timestep. Consequently, the expressions for the PDFs at the prediction and filtering steps are essentially similar to the Kalman filter expressions given in Eq. 2.7. However, because $\psi_k(\cdot)$ and $h_k(\cdot)$ are nonlinear functions of y_{k-1}, expressions for the expected values of the state vector and the observations as well as their respective covariances are generally not straightforward to obtain. In the extended Kalman filter technique, the means are obtained by retaining only the first two terms of the Taylor series expansions around the previous conditional estimate of the mean state vector. The mean state vectors for the prediction and filtering stages at any timestep, t_k, are given respectively by,

$$\hat{y}_{k|k-1} = E[\psi_k(y_{k-1|k-1}, \omega_k)] \approx \psi_k(\hat{y}_{k-1|k-1}) \tag{2.14}$$

and

$$\hat{y}_{k|k} = E[h_k(y_{k|k-1}, \epsilon_k)] \approx \hat{y}_{k|k-1} + \hat{K}_k(d_{obs,k} - h_k(\hat{y}_{k|k-1})). \tag{2.15}$$

$\hat{K}_k$ is the Kalman gain obtained by linearizing about the most current estimate of the conditional mean of the state vector, $\hat{y}_{k|k-1}$. Similarly, for propagating the covariance matrix, a matrix of partial derivatives (the Jacobian) evaluated around the current estimate of the mean state vector is first obtained from,

$$\begin{aligned} \hat{\Psi}_k &= \nabla_y \psi_k|_{\hat{y}_{k-1|k-1}} \\ \hat{H}_k &= \nabla_y h_k|_{\hat{y}_{k|k-1}}, \end{aligned} \tag{2.16}$$

where $|_{\hat{y}_{k-1|k-1}}$ and $|_{\hat{y}_{k|k-1}}$ indicate the estimates of the mean state vector for evaluating the Jacobian matrices, $\hat{\Psi}_k$ and $\hat{H}_k$ respectively. For the EKF, the linearized estimates of $\hat{H}_k$, $\hat{\Psi}_k$ and $\hat{K}_k$ are used in lieu of H_k, Ψ_k and K_k in Eqs. 2.8–2.11 and the prediction and filtering steps essentially proceeds the same way as in the Kalman filter. The extended Kalman filter suffers from several disadvantages including filter

divergence due to linearization, underestimation of the true covariance, etc. Also, if the true PDF is non-Gaussian, then the Gaussian approximation in the EKF will fail to describe the PDF well. Because the full covariance matrix is evaluated at each prediction and filtering steps, the EKF cannot be applied to large scale reservoir engineering and history matching problems. Although several modifications to the extended Kalman filter for highly nonlinear and non-Gaussian problems have been proposed such as the unscented Kalman filter (Julier and Uhlmann, 1997; Wan and Van Der Merwe, 2000) and higher-order filters, these are generally not applicable to petroleum engineering problems with large number of parameters. Examples of EKF application to petroleum engineering with small number of parameters has been reported in Eisenmann et al. (1994) and Liu et al. (2009).

2.4 The Ensemble Kalman Filter, EnKF

The ensemble Kalman filter (EnKF) is a Monte-Carlo approach to solving the Bayesian updating problem presented in Eqs. 2.3–2.4. It was originally developed by Evensen (1994) and Houtekamer and Mitchell (1998) for large scale data assimilation problems in numerical weather prediction. The EnKF uses an ensemble of state vectors, Y_k, to represent the PDF of the dynamical system at any timestep, t_k. Subject to the Kalman filter assumptions and given a Gaussian prior PDF, the ensemble Kalman filter converges asymptotically to the Kalman filter solution as the number of ensemble members increases. The major differences between the EnKF and its precursors (Kalman filter and EKF) are: (1) the full covariance matrix is not propagated explicitly between data assimilation timesteps. Rather a sample covariance matrix may be approximated from the ensemble members making it suitable for high dimensional problems; and (2) evaluation of the Jacobian matrix at each data assimilation is not required. Efficient evaluation of the Jacobian matrix for nonlinear problems requires

the derivation of adjoint equations that are fairly complex and also time consuming. Additionally, the adjoint equations are not portable and have to be re-derived once the dynamical model changes. Consequently, EnKF provides a computationally more efficient approach to assimilating data for large-scale problems and has also been shown to perform better than the extended Kalman filter for strongly nonlinear problems (Zang and Malanotte-Rizzoli, 2003).

The basic idea of the ensemble Kalman filter is that Monte Carlo samples, i.e., realizations from the prior PDF, $p(y_k|D_{obs,k-1})$, at time t_k are used to approximate the forecast/prediction distribution function. The evolution of the PDF (Eq. 2.3) is approximated by evolving each ensemble member using the nonlinear forward model (Eq. 2.12). The Monte-Carlo samples from the prediction/forecast step are then used in the linear Kalman filter update equation to obtain a Monte Carlo approximation of the posterior PDF, $p(y_k|D_{obs,k})$. Hence, the assumption of a linear measurement model and a Gaussian measurement distribution is also implicit in the EnKF formulation. The EnKF is initialized by randomly sampling the initial PDF, $p(y_0)$, which is assumed known and collecting the Monte Carlo samples in an ensemble of state vectors, denoted by $Y_0 = [y_1^T, y_2^T, \ldots, y_{n_e}^T]^T$, where n_e is the number of ensemble members and y_j denotes the jth ensemble member.

Since the ensemble Kalman filter was first introduced, it has been applied (with some modifications) to various problems in numerical weather prediction (Houtekamer and Mitchell, 2001; Hamill and Snyder, 2002; Evensen, 2003; Anderson et al., 2005; Thomas et al., 2009; Sakov et al., 2010), ground water hydrology (Reichle et al., 2002; Chen and Zhang, 2006; Franssen and Kinzelbach, 2009; Sun et al., 2009a,b; Wang et al., 2009) and petroleum engineering (Nævdal et al., 2002; Gu and Oliver, 2005; Liu and Oliver, 2005b; Wen and Chen, 2007; Agbalaka and Oliver, 2008; Seiler et al., 2009; Chen and Oliver, 2010).

2.4.1 EnKF applied to data assimilation problems in reservoir engineering

For applications to reservoir engineering, the EnKF solves a combined parameter and state estimation problem such that at the kth data assimilation timestep, the jth state vector, $y_{j,k}$, is expressed as,

$$y_{j,k} = \begin{bmatrix} m_{j,k}^T & f_k^T(m_{j,k}) & g_k^T(m_{j,k}) \end{bmatrix}^T, \tag{2.17}$$

where m is the vector of static model parameters (usually the gridblock permeability and porosity) that do not change between data assimilation timesteps but are updated whenever data are assimilated, $f(m)$ is the vector of state variables consisting of the dynamic model parameters (typically gridblock pressures and saturations in a black oil model) that evolve between data assimilation timesteps and define the state of the reservoir model. Usually, the uncertainty in the dynamic variables is a function of the uncertainty in the static model parameters and where applicable, uncertainty in the specification of the initialization conditions such as the location of the initial water-oil contact and/or gas-oil contact, etc. $g(m)$ is the data predicted by m, which may include the following measurements: bottomhole pressure data; water, oil or liquid rate data; watercut data; etc. $g(\cdot)$ is commonly included in the state vector as a diagnostic variable and terms such as $C_y H^T$ and $H C_y H^T$ that depend on the nonlinear relationship between the model parameters and predicted data are approximated efficiently from the ensemble.

Similar to the implementation of the Kalman filter and the extended Kalman filter, the application of EnKF to data assimilation problems in reservoir engineering also consists of two sequential steps: a prediction/forecast step and an update/analysis step. The prediction step is given by,

$$y_{j,k}^p = \psi_k(y_{j,k-1}^u), \tag{2.18}$$

where $y_{j,k}^p \equiv y_{j,k|k-1}$, i.e., the state vector at time t_k conditional on data up to time t_{k-1}

and $y^u_{j,k} \equiv y_{j,k|k}$, i.e., the state vector at time t_k conditional on data up to time t_k. The superscripts p and u stand respectively for predicted and updated. $\psi_k(\cdot)$ represents a function (the reservoir simulator in this case) that solves the reservoir flow and transport equations using the input state vector at t_{k-1} as the initial conditions and outputs the predicted values of the dynamic model variables at time t_k. Note that the static model variables do not change between data assimilation timesteps such that $m^u_{j,k-1} = m^p_{j,k} = \psi_k(m^u_{j,k-1})$. However, the dynamic model variables are re-solved during the forecast/prediction step and $f_k(m^p_{j,k}) = f_k(m^u_{j,k-1}) = \psi_k[f_{k-1}(m^u_{j,k-1})]$. Note that for reservoir engineering applications the model error, ω_k, at any timestep, t_k, is almost always neglected. Recently, Aanonsen (2009) discusses the possibility of accounting explicitly for model error in reservoir engineering applications.

Following the prediction step, the analysis/update step modifies the ensemble of state vectors to obtain filtered estimates of the state vectors that match the newly available set of production data. Subsequently, the prediction run is repeated again and this cycle of update and prediction is continued until all data are assimilated. The expression for the update step is similar to the Kalman filter update equation (Eq. 2.9) and the EnKF update to the jth state vector is given by,

$$\begin{aligned} y^u_{j,k} &= y^p_{j,k} - C^p_{Y,D,e,k}\left(C_{D,D,k} + C_{D,k}\right)^{-1}\left(d_{j,k} - d_{\mathrm{obs},j,k}\right) \\ &= y^p_{j,k} - C^p_{Y,e,k}H_k^T\left(H_k C^p_{Y,e,k}H_k^T + C_{D,k}\right)^{-1}\left(H_k y^p_{j,k} - d_{\mathrm{obs},j,k}\right) \\ &= y^p_{j,k} - K_{e,k}(d_{j,k} - d_{\mathrm{obs},j,k}), \end{aligned} \tag{2.19}$$

where $C^p_{Y,D,e,k} = C^p_{Y,e,k}H_k^T$ is the ensemble approximation of the cross-covariance between the state vector and the predicted data; $C^p_{Y,e,k}$ is the state vector covariance matrix approximated from the ensemble and $H_k \in \mathbb{R}^{n_{d,k}\times n_{y,k}}$ is a matrix made up of two submatrices that include an $n_{d,k} \times (n_{y,k} - n_{d,k})$ zero matrix and an $n_{d,k} \times n_{d,k}$ identity matrix. $n_{y,k}$ and $n_{d,k}$ are respectively the dimension of the state vector and the number of data assimilated at time t_k. The product $H_k y^p_{j,k}$ extracts the predicted data from the jth state vector, $y^p_{j,k}$, i.e., $H_k y^p_{j,k} = d_{j,k} = g_k(m^p_{j,k})$. $\mathbf{C}_{D,D,k} = H_k C^p_{Y,e,k}H_k^T$ is

the data covariance matrix estimated from the ensemble of predicted data and $C_{D,k}$ is the measurement error covariance. $K_{e,k}$ is the ensemble estimate of the Kalman gain matrix. $d_{\text{obs},j,k}$ is the perturbed noisy measurement expressed as,

$$d_{\text{obs},j,k} = d_{\text{obs},k} + \varepsilon_{j,k}. \tag{2.20}$$

$d_{\text{obs},k}$ is the noisy measurement at time t_k and $\varepsilon_{j,k}$ is the perturbation added to the noisy measurement to obtain the perturbed noisy measurement assimilated by the jth ensemble member. Burgers et al. (1998) showed that the addition of random noise to the noisy measurements is necessary to ensure that the analysis variance is correct. $\varepsilon_{j,k}$ is a zero-mean Gaussian variable with $E[\varepsilon_{j,k}, \varepsilon_{j,k}^T] = C_{D,k}$. Explicit evaluation of the the full covariance matrix, $C_{Y,e,k}^p$, in Eq. 2.19 is unnecessary as the dimension of the state vector is usually very large. Only the matrices $C_{Y,e,k}^p H_k^T$ and $H_k C_{Y,e,k}^p H_k^T$ are computed and the dimensions of these matrices are much lower than the full covariance matrix, $C_{Y,e,k}^p$.

An assumption of Gaussianity in the prior model distribution and the measurement distribution is implicit in the EnKF analysis step. Consequently, the EnKF performance is suboptimal for highly nonlinear problems and as such iteration may be necessary to obtain reasonable match to production measurements and update to the model variables. This EnKF formulation requiring iteration is referred to as the iterative EnKF (Gu and Oliver, 2007; Li and Reynolds, 2009). The iterative EnKF essentially solves an optimization problem, using a Gauss-Newton formulation with reduced step length, to obtain conditional realizations of the static model variables from the PDF, $p(m|d_{obs,k})$, at any required timestep, t_k. The explicit form of the PDF is given by,

$$p(m|d_{obs,k}) = \exp\left[\frac{1}{2}\left(\left\|m - m_{\text{pr}|k-1}\right\|_{C_M^{-1}}^2 + \left\|g(m) - d_{\text{obs},k}\right\|_{C_D^{-1}}^2\right)\right], \tag{2.21}$$

where $\|A\|_W^2 = A^T W A$ is the weighted norm of matrix A and $m_{\text{pr}|k-1}$ is the prior model conditional on production measurements up to time t_{k-1}. Eq. 2.21 also assumes

a prior Gaussian PDF and Gaussian measurement errors. Note that because the measurement model is nonlinear, the posterior PDF need not be Gaussian. The model that maximizes the conditional PDF of Eq. 2.21 is obtained by iteratively solving the following expression,

$$m^{l+1} = \beta_l m_{pr|k-1} + (1-\beta_l)m^l - \beta_l C_M G_l^T \left(C_D + G_l C_M G_l^T\right)^{-1} \\ [g(m^l) - d_{\mathrm{obs},k} - G_l(m^l - m_{\mathrm{pr}|k-1})]. \tag{2.22}$$

β_l and G_l are respectively the step size and sensitivity matrix at the lth iteration. We note from Eq. 2.22 that for the iterative EnKF only the static model variables are updated in each iteration. The dynamic model variables and the predicted data are obtained by rerunning the reservoir model from time zero using values of the updated model parameters. This adds to the computational cost of the iterative EnKF.

The main difference between the various forms of the iterative EnKF presented by Gu and Oliver (2007) and Li and Reynolds (2009) is in the computation of the sensitivity matrix. Gu and Oliver (2007) approximate the sensitivity matrix from the ensemble while Li and Reynolds (2009) compute the individual sensitivities of the ensemble members and thus rely on solving the adjoint equations. Consequently, the form of the iterative EnKF proposed by Gu and Oliver (2007), referred to as the ensemble randomized maximum likelihood filter (EnRML), is computationally less expensive. However, because the EnRML is based on a single average sensitivity matrix, all the realizations move in a single descent direction and the distribution of updated ensemble from this method will not approximate a multimodal PDF very well. However, the iterative EnKF of Li and Reynolds (2009) that uses individual sensitivity information from the ensemble members will generally perform better at sampling multiple peaks of a multimodal conditional PDF. For some types of problem having multiple local minima with one global minimum, the approach that uses a single global average sensitivity is less likely to get stuck in a local minimum compared to one that computes individual sensitivities.

The iterative EnKF is computationally more expensive than the standard EnKF and is thus not usually implemented at all data assimilation timesteps. It is only implemented if the nonlinearity at any data assimilation timestep is significant. This usually shows up as fairly large changes to the saturation variables during the EnKF update stage. Consequently, the saturation change is monitored at each data assimilation timestep and if the maximum saturation change in any grid cell exceeds a predetermined threshold, the iterative EnKF is implemented. In this dissertation the iterative EnKF of Gu and Oliver (2007) was utilized whenever necessary for the data assimilation problems presented in Chapters 4 and 5. The thresholds in both chapters ranged from 0.25 to 0.30. The average sensitivity matrix, $\tilde{G}$, from the EnRML is evaluated as,

$$\tilde{G} = \Delta D(\Delta M)^{+}, \tag{2.23}$$

where ΔD and ΔM are respectively the matrices of the mean deviations of the predicted data and model parameters; A^{+} denotes the pseudo-inverse of matrix A.

CHAPTER III

LOCALIZATION AND SEQUENTIAL CALIBRATION TO PRODUCTION AND FACIES DATA

3.1 Background

The first application of the ensemble Kalman filter to the problem of conditioning facies models, generated by truncating two Gaussian random fields, to production data was by Liu and Oliver (2005b) and they showed that the EnKF converges to a better history match solution compared to a gradient-based minimization method. Since then the EnKF technique has been applied by several authors to facies history matching problems of varying complexity (Agbalaka and Oliver, 2008; Moreno et al., 2008; Zhao et al., 2008; Sun et al., 2009a; Lorentzen et al., 2009).

3.1.1 Issues with EnKF applied to facies

The problem of EnKF applied to history matching facies models is in general very difficult. Most of the issues in EnKF implementation, related to history matching applied to facies, are encountered during the analysis step. In this section we briefly present and discuss four such issues and also identify three unsolved issues that are addressed subsequently in this chapter.

3.1.1.1 Issue #1: Assimilating non-numerical facies data

The first issue involves the problem of handling non-numerical facies data at the update step. This problem may be overcome by using a proxy, f_p, to represent the mismatch between the simulated facies and the facies observation (Liu and Oliver,

2005b). The facies mismatch proxy is given by,

$$f_{p,i} = \begin{cases} 0, & f_{sim,i} = f_{obs,i} \\ 1, & f_{sim,i} \neq f_{obs,i}. \end{cases} \qquad \forall i : 1 \leq i \leq n_{fobs}, \tag{3.1}$$

where $f_{p,i}$, $f_{sim,i}$ and $f_{obs,i}$ are respectively the facies mismatch proxy, the simulated facies and the facies observation at the ith well location and n_{fobs} is the number of facies observations. This formulation also ensures that the contribution of each facies mismatch term in updating the facies variables are weighted equally.

3.1.1.2 Issue #2: Enforcing the constraint on mismatched facies at the well locations during data assimilation

The second issue deals with the possibility of destroying previously matched facies at the well locations when production data are assimilated at any timestep. Liu and Oliver (2005b) proposed a solution to this problem by implementing a facies matching loop (for a 2D problem) where the production and facies data are simultaneously reassimilated until the constraint on the facies mismatch observations at all well locations are enforced. This approach seems to be effective if large changes are not made to the dynamic model variables, i.e., the gridblock saturations and pressures. However, the continuous iteration to enforce the facies mismatch constraint could potentially result in significant changes to the state vectors such that the estimates of the static model variables (the gridblock facies) will not be consistent with the updated dynamic model variables. To illustrate, Fig. 3.1 shows the saturation changes at each data assimilation timesteps for the problem of EnKF applied to history matching of geologic facies. The wells in the model are completed in a five-spot water injection pattern. The injector is controlled primarily by a constant surface injection rate target with a secondary constraint on the maximum bottomhole pressure. Production is at a constant reservoir volume rate with a secondary minimum bottomhole pressure constraint. At each data assimilation timestep, the constraint on the mismatch between the predicted facies and the observed facies is enforced, whenever necessary,

using the iterative scheme of Liu and Oliver (2005b). Clearly, from the 6th to the

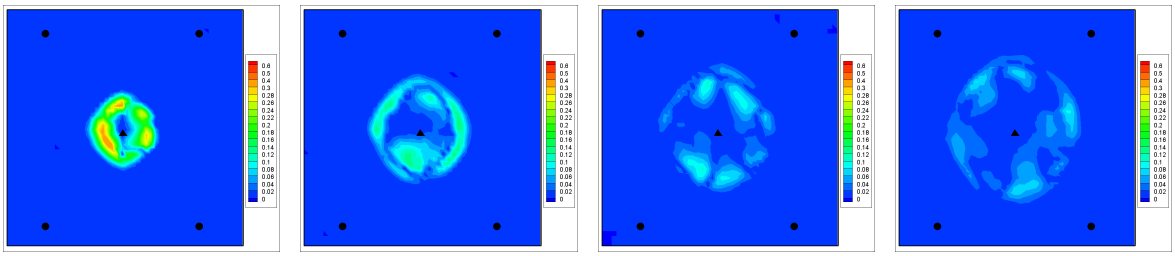

(a) Timestep 1. (b) Timestep 2. (c) Timestep 3. (d) Timestep 4.

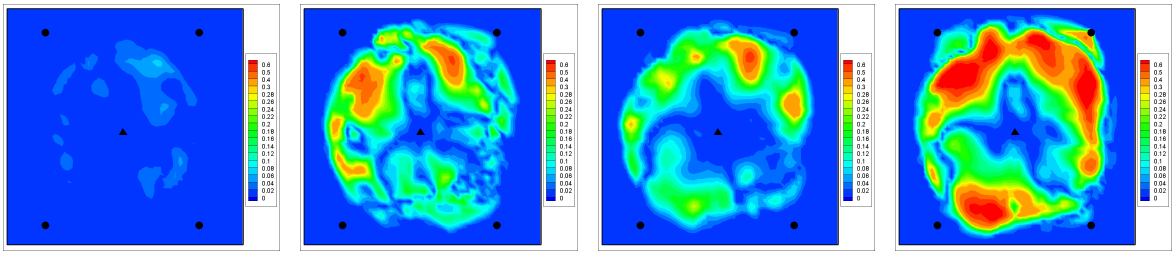

(e) Timestep 5. (f) Timestep 6. (g) Timestep 7. (h) Timestep 8.

Figure 3.1: Change in saturation at the first eight data assimilation timesteps for a randomly selected realization. The iterative enforcement scheme of Liu and Oliver (2005b) was used to enforce facies mismatch constraint. Figs. 3.1(f)–3.1(h) show huge and incorrect corrections to the saturation field.

8th data assimilation timesteps, very significant changes were made to the saturation fields and the assumption of linearity fails to hold in this case. Also at the 8th data assimilation timestep (Fig. 3.1(h)), it was difficult constrain the predicted well facies in some of the ensemble members to match the facies observation using the iterative scheme of Liu and Oliver (2005b). Furthermore, the continuous iteration to match the facies and production data may result in incorrect weighting of the production data relative to the prior model mismatch. To address the problem of large changes to the saturation variables from continuous iteration, Liu and Oliver (2005b) suggested limiting the number of iterations needed to enforce the constraint on facies mismatch observations to 2 or 3 iterations and discarding the ensemble members that do not match the facies observations thereafter. While this approach of eliminating the ensemble members with mismatched facies at the well locations ensures that updates to the state vectors are consistent, it exacerbates the problem of rank deficiency and

sampling errors. For the history matching problem from which the example in Fig. 3.1 was obtained, more than 10 ensemble members that do not honor the facies observations had to be discarded at the eight data assimilation timestep (Fig. 3.1(h)) after 2–3 iterations. Clearly, it would be advantageous to develop method for iteratively enforcing the facies constraints that does not reduce ensemble size.

3.1.1.3 Issue #3: Excessive loss in ensemble variability from assimilating production data and facies data

Excessive reduction of variance seems to be a bigger problem with EnKF applied to history matching geological facies than with EnKF applied to history matching Gaussian random permeability and porosity fields. Consequently, the third issue deals with the problem of severe loss in ensemble variability resulting in filter divergence. Filter divergence refers to the situation where the error covariance matrix approximated from the ensemble becomes very small leading to a filter gain that is also small. The result is that subsequent observations will have little effect on the model estimate, the final estimates of the model parameters will be different from the true parameters and predictions from the final model will diverge. Two potential sources of filter divergence are underestimation of forecast error covariance (due to sampling errors or complete collapse in variability of the ensemble members) and overestimation of the forecast error covariance due to long-range spurious correlation (Hamill et al., 2001). Spurious correlation results from using finite ensemble size to approximate the covariance matrix and as such the impact can be reduced by increasing the ensemble size. Some of the techniques that have been used to ameliorate the tendency towards variance deficiency (filter divergence) include the double EnKF (Houtekamer and Mitchell, 1998) or inflation of the background error covariance (Anderson and Anderson, 1999). A third approach, is the localization of the forecast error covariance through a Schur product with a correlation function having compact support (Houtekamer and Mitchell, 2001; Hamill et al., 2001). This product tends to reduce

the spurious long-scale correlation that results in an ensemble with insufficient variance. Consequently, in this chapter we also investigate the use of localization with facies to prevent collapse of the ensemble variance during data assimilation.

3.1.1.4 Issue #4: Choice of starting time for future prediction

The EnKF update of the state vector (comprising the static and dynamic model variables) at each data assimilation timestep assumes that the predicted data are linearly related to the state variables and the state variables are linearly related to the model parameters. If this assumption is not strongly violated, the updates to the static and dynamic model parameters are consistent. Consistency in this case implies that the estimate of the dynamic model variables at the update step is approximately the same as one would obtain by rerunning the simulation from time zero to the current assimilation step using the most current estimates of the static parameters. The goal of history matching is to obtain predictions from the ensemble of calibrated models for reservoir management, planning and development. For EnKF applied to history matching geological facies, the relationship between the facies variables and data is so highly nonlinear that the final facies field does not always honor early production data well. Consequently, the final estimates of the dynamic variables may not be consistent with the final estimates of the static model variables and future predictions may not always be correct without re-initializing the dynamic model variables. Bases on the foregoing, we also evaluate, in this chapter, whether a forecast from the final state is better than a forecast from time zero using the final parameter fields.

3.1.1.5 Choice of ensemble size

The final issue investigated in this chapter is not specific only to EnKF applied to facies but relates to the choice of suitable ensemble size for data assimilation. This usually involves a tradeoff between additional computational expense versus adequate

representation of the error statistics obtained from the ensemble. Consequently, the impact of using three different ensemble sizes of 40, 120, and 240, on the history matching results and the estimates of the model parameters is also presented.

3.2 Generating Facies Realizations Using Truncated PluriGaussian Simulation

The truncated pluriGaussian method simulates the randomness of the facies distribution by truncating two or more Gaussian random fields into separate regions representing the different facies types. This technique presents a practical tool for mapping from a continuous state space to a discrete state space (indicators) and honors the underlying covariances, cross-covariances and proportions of the facies. The truncation of multiple Gaussian random fields to obtain facies realizations was formalized by Galli et al. (1994). Le Loc'h et al. (1994) showed various results of truncating bi-Gaussian fields using rectangular partitions while varying the cross-correlation factor, anisotropy and variogram type. An example of choosing more complex truncations was also presented and discussed by the authors. Le Loc'h and Galli (1997) examined some practical issues associated with implementing the truncated pluriGaussian method, which include structural analysis (truncation choice with thresholds estimation and fitting of the indicator variogram) and conditional simulation of facies data. They presented governing equations as well as examples for computing the thresholds and variogram models and applied them to a conditional simulation problem. Xu et al. (2006) presented a generalization of the pluriGaussian simulation method that allows for the specification of complex facies contacts and transitions using a binary, dynamic contact matrix. The truncated pluriGaussian method has also been used for stochastic simulation of rock fractures (Dowd et al., 2007).

An attractive feature of the truncated pluriGaussian method is that the geostatistical parameters for generating realizations of the facies model is completely specified

by the covariance of the Gaussian functions and the truncation thresholds. The process of generating realizations of the facies variables using the truncated pluriGaussian simulation is initialized by generating, firstly, N different Gaussian random functions $(Y_j, 1 \leq j \leq N)$ that are then transformed to corresponding facies variable by truncation. Conceptually, the N Gaussian functions define a theoretical space with N dimensions and a realization of the Gaussian random function, $\mathbf{Y} \in \mathbb{R}^N$ define a point in an N-dimensional space. The facies variables may be regarded as labels that are assigned to different parts of this space. Suppose that for an arbitrary location, $\mathbf{x}$, D_i represents a partition of the N-dimensional Gaussian space labeled as F_i (facies i) and $\mathbf{Y}(\mathbf{x}) = [Y_1(\mathbf{x}) \ \ldots \ Y_N(\mathbf{x})]$ is a row vector of N Gaussian functions. Then,

$$1_{F_i}(\mathbf{x}) = 1 \Leftrightarrow \mathbf{Y}(\mathbf{x}) \in D_i, \tag{3.2}$$

where 1_{F_i} is an indicator function for facies i. The partition, D_i, of the Gaussian that corresponds to F_i is related to $\mathrm{p}_{F_i}(\mathbf{x})$, the proportion of F_i at point $\mathbf{x}$, which is usually assumed known. Note that $\mathrm{p}_{F_i}(\mathbf{x})$ also defines the probability of having F_i at a spatial location, $\mathbf{x}$, expressed as,

$$\begin{aligned} \mathrm{p}_{F_i}(\mathbf{x}) &= \mathrm{P}[\text{facies at location } \mathbf{x} = F_i] = \mathrm{E}[1_{F_i}(\mathbf{x})] \\ &= \mathrm{P}[\mathbf{Y}(\mathbf{x}) \in D_i] = \frac{1}{\sqrt{2\pi|\Sigma|}} \int_{D_i} \exp\left(-\frac{1}{2}\mathbf{y}^T\Sigma^{-1}\mathbf{y}\right) \mathrm{d}\mathbf{y}, \end{aligned} \tag{3.3}$$

where $\mathrm{P}[\cdot]$ defines the probability of the argument, $\mathrm{E}[\cdot]$ is an expectation operator, Σ is the covariance of the standard (zero-mean, unit-variance) N-variate Gaussian distribution function and $|\Sigma|$ is the determinant of Σ. Subject to some constraints, D_i and Σ may be determined from Eq. 3.3 for given values of p_{F_i} (Armstrong et al., 2003).

While any arbitrary number (≥ 2) of Gaussian random fields can be used with the pluriGaussian simulation, only two Gaussian fields are used in practice as this is usually sufficient for generating facies models with desired contacts between the different facies types in the model. For the case where only two Gaussian functions

are truncated to obtain a facies variable, the truncation map is defined in a two-dimensional space. The truncation map contains information on the proportions of the different facies types in the model and the permissible transitions between the different facies types. The truncation map is also known as the rock type rule, facies transition map, truncation threshold map and threshold map. The most common form of the truncation map is made up of thresholds that form rectangles, i.e., line parallel to the major coordinate axes, although other nonconventional truncation maps based on thresholds that form intersecting lines (Liu and Oliver, 2004, 2005b) and thresholds that form intersecting ellipses (Zhao et al., 2008) have been used.

Depending on the shape and form of the thresholds in the truncation map, the spatial configuration of the facies obtained by truncating the two Gaussian random fields will be different. To illustrate, the two Gaussian random fields in Fig. 3.2 will be truncated using three different truncation maps to obtain three facies maps with different spatial configuration of the facies.

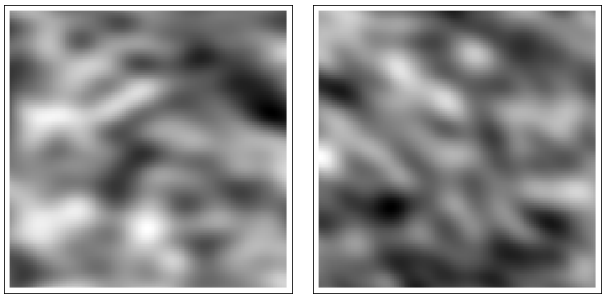

(a) Y1. (b) Y2.

Figure 3.2: Two Gaussian random fields, Y1 and Y2, truncated to obtain the facies maps in Figs. 3.3(d)–3.3(f) using different truncation maps (Figs. 3.3(a)–3.3(c)).

Figures 3.3(a)–3.3(c) shows three different truncation maps, which differ by threshold types. Figure 3.3(a) is an example of a conventional (rectangular) truncation map obtained by partitioning the 2D Gaussian space into rectangles. By contrast, Figs. 3.3(b)–3.3(c) are two examples of nonconventional truncation maps with thresholds that respectively form intersecting lines (Liu and Oliver, 2004) and intersecting

ellipse (Zhao et al., 2008). The intersecting lines thresholds consists of three intersecting lines that partition the 2D Gaussian space into a maximum of seven different facies types. The elliptical truncation map uses two intersecting ellipses to partition the 2D Gaussian space only into two facies. Three different Facies maps obtained by truncating the two Gaussian random fields (Fig. 3.2) using the three different truncation maps (Figs. 3.3(a)–3.3(c)) are shown in Figs. 3.3(d)–3.3(f). Note that each facies map was obtained by using the truncation map immediately above it to truncate the biGaussian fields. In this chapter, the facies maps were obtained by truncating two Gaussian random fields using truncation maps made up of intersecting lines thresholds. The method of moving averages (Oliver, 1995) was used to generate realizations of the Gaussian random fields that are truncated to obtain initial facies maps conditional on static facies observations at the well locations.

3.3 Simulation Model Description

The simulation model is a 3-layer facies model with five wells arranged in a 5-spot waterflooding pattern and completed in all three layers of the model. There are $50 \times 50 \times 3$ active grid blocks and the dimension of each gridblock is 30 ft $\times$ 30 ft $\times$ 20 ft. Only two phases, oil and water, are present in the simulation model. The grid locations of the five wells in the simulation model are shown in Table 3.1. The four producers in the reservoir model are identified throughout as Prod1–Prod4.

Table 3.1: Grid coordinates of the different well locations

Coordinate	**Injector**	**Prod1**	**Prod2**	**Prod3**	**Prod4**
x	25	9	9	41	41
y	25	5	45	45	5

Three different types of geologic facies identified as facies 1, facies 2 and facies 3 (alternatively F1, F2 and F3) are present in the facies model. The petrophysical properties (porosity and horizontal permeability) in each facies are assumed to be uniform

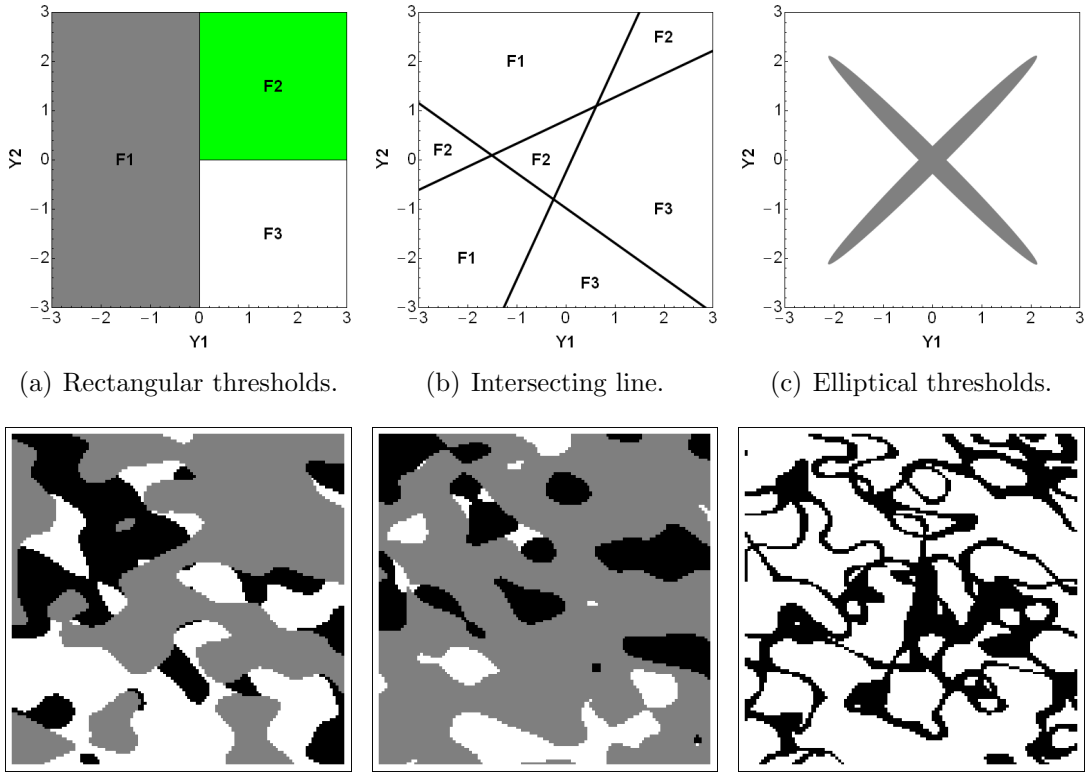

(a) Rectangular thresholds. (b) Intersecting line. (c) Elliptical thresholds.

(d) Facies map 1. (e) Facies map 2. (f) Facies map 3.

Figure 3.3: Realizations of the facies map showing the dependence of the spatial configuration of the facies variables on the truncation map. The facies maps were obtained by truncating the BiGaussian fields in Fig. 3.2 using the corresponding truncation maps in row 1.

and homogenous with no uncertainty. Only the location of the facies boundaries and thus the spatial distribution of the facies variables are assumed to be uncertain such that once the facies variables are determined, the porosity and permeability in the facies are also determined. The values of the facies porosity and permeability used in the model are presented in Table 3.2. Note that a k_v/k_h ratio of 0.2 was assumed for all the facies class.

Table 3.2: Values of porosity and permeability in each facies.

Properties	**Facies 1**	**Facies 2**	**Facies 3**
Permeability (mD)	274	55	632
Porosity	0.195	0.140	0.250

We note from Table 3.2 that facies 1–3 are respectively the medium, low and high permeability facies. As previously noted, all the facies models were generated by truncating two Gaussian random fields using a non-standard truncation map with thresholds that comprises three intersecting lines similar to Fig. 3.3(b). Different truncation maps corresponding to the three layers in the simulation model were used for truncating the corresponding biGaussian random fields for generating the facies maps. Furthermore, the expected values of the facies proportions are assumed to be stationary, i.e., the same truncation map was used at each grid location in any layer for truncating the Gaussian variables to obtain the corresponding facies variables. Fifteen static measurements of the facies at the well locations in the reference model are available for conditioning the prior models to facies observations. The facies observations from the reference model are presented in Table 3.3. All the initial realizations of the facies model were conditioned to these static measurements before data assimilation.

Waterflooding commenced from the first day of production and continued for a total period of 500 days. All the producers operated at a constant flowing bottomhole pressure (BHP) constraint of 2500 pounds per square inch (psi). The injection rate

Table 3.3: Facies observations at the different well locations

Layer	Injector	Prod1	Prod2	Prod3	Prod4
1	facies 3	facies 2	facies 2	facies 3	facies 1
2	facies 3	facies 1	facies 2	facies 2	facies 1
3	facies 3	facies 2	facies 1	facies 3	facies 1

was fixed at a fixed surface rate target of 7,500 stock tank barrels per day (STB/D) with a secondary maximum BHP constraint of 7,000 psi.

The first set of data was assimilated at day 10 and thereafter, subsequent sets of data were assimilated every ten days. The assimilated data were facies observations at the well locations, bottomhole pressure (p_{bh}) from the injector, water rate data (q_w) and liquid rate data (q_L), both from each of the four producers. After water breakthrough has been observed in all four producers, a total of 24 data (15 facies observation, 1 bottomhole pressure datum, 4 liquid rate data and 4 water rate data) were assimilated at each assimilation timestep. The last set of data was assimilated at day 190. Ten days after assimilating the last set of data, a new well was drilled at the gridblock with coordinates (46,25) to further evaluate the issue of the best starting time for future prediction. Note that the facies at the grid location with the new well is not conditioned to facies observation.

Variability in the ensemble of updated state and model variables is maintained by the addition of random noise to the noisy production measurements to obtain an ensemble of virtual/perturbed observations at each data assimilation timestep. The random noise was sampled from a zero mean Gaussian probability density function (PDF) with the following variances:(1) 9 psi^2 for p_{bh}, (2) 5 $(STB/D)^2$ for q_L and q_w, and (3) 10^{-6} for the facies data. Although facies data should have zero measurement error, we assume a finite but negligible error by using a value of 10^{-6} for the variance of the measurement error. This is necessary to ensure that the inverse of the data mismatch covariance can be computed. Also the value of the error variance used is small enough to have minimal effect on the inverse.

The production measurements in this chapter are synthetic data obtained from running a commercial black oil reservoir simulator forward in time using the reference / true facies model. The reference model is assumed known in this case even though it is typically unknown in real applications. This assumption that the reference model is known enables the evaluation of the performance of the EnKF technique in estimating the model parameters. The reference facies maps are shown in Fig. 3.4.

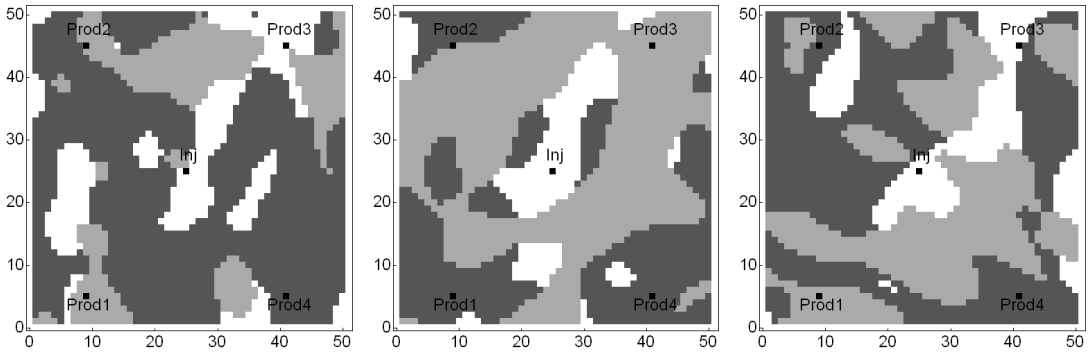

(a) Layer 1. (b) Layer 2. (c) Layer 3.

Figure 3.4: Reference facies maps. The white color is the high permeability facies (F3). The light and dark shades of gray are respectively the low (F2) and medium (F1) permeability facies. The black dots are the well locations.

The shape of the relative permeability (rel-perm) curves used for all simulation runs in this chapter is shown in Fig. 3.5. The same rel-perm curves were used in generating the synthetic data from the reference models and also the predicted data from the ensemble of facies models. Note that the rel-perm curves in Fig. 3.5 were also used for the simulation runs discussed in Chapters 4–5.

An initial ensemble of 240 reservoir models was generated using the same geostatistical parameters as the reference model. As noted earlier the initial realizations were conditioned to the facies observations at the well locations. Three different ensemble sizes of 40, 120, and 240 were used in this study and these were sampled from this initial set of 240 reservoir models. Finally, because the facies variables are highly non-Gaussian, they were not updated directly at the data assimilation timestep; the Gaussian variables for truncation were updated in lieu of the facies variables.

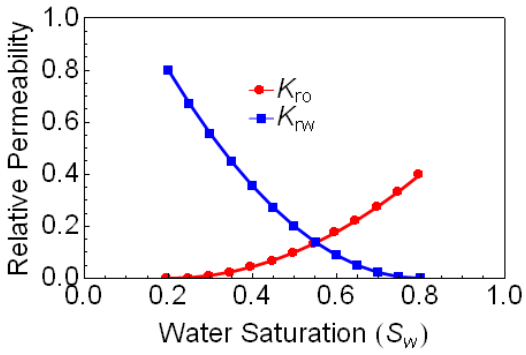

Figure 3.5: Relative permeability curves used in all the simulation models.

3.4 Case 1: Sequential Assimilation of Facies and Production Data Without Localization

In this section, we propose an approach to iteratively enforce the constraints on facies mismatch observations when updates to the model variables from assimilating production data have caused them to be violated. When data are conditionally independent, the order of data assimilation is irrelevant if the correct posterior probability distribution function (PDF) are computed from assimilation. For nonlinear and non-Gaussian problems, however, EnKF provides an approximation to the correct PDF so the order of data assimilation is important. What we propose is to decouple the assimilation of production and facies data such that at any data assimilation timestep, the production data are assimilated firstly and if the constraints on the facies mismatch observation are violated in the updated ensemble, we iterate only on the facies constraint. By only iterating on the facies observations, we avoid the problem of improperly weighting the production data relative to the prior model mismatch. The iterative enforcement of the facies constraint may, however, still result in very large changes to the dynamic state variables as shown in Fig. 3.1. This problem may be solved by reformulating the state vector whenever facies data are assimilated so that only the facies variables are updated at this stage. Formally, when production data are assimilated both static and dynamic model variables are updated and the

ensemble of state vectors is defined by,

$$Y = \begin{bmatrix} Y_1 \\ Y_2 \\ \Theta \end{bmatrix} = \begin{bmatrix} Y_{1,1} & Y_{1,2} & \dots & Y_{1,n_e} \\ Y_{2,1} & Y_{2,2} & \dots & Y_{2,n_e} \\ \Theta_1 & \Theta_2 & \dots & \Theta_{n_e} \end{bmatrix}, \tag{3.4}$$

where Y is the ensemble of state vectors, Y_1 and Y_2 are the ensembles of the two Gaussian random fields and Θ is the ensemble of dynamic model/state variables. Assuming the prior assimilated production data have violated the constraint on the facies, the ensemble of state vectors in Eq. 3.4 is reformulated by removing the updated vectors of dynamic model variables, Θ, and the ensembles of the two Gaussian random fields are iteratively updated from assimilating facies data until the constraint on facies mismatch observations are enforced. The update equation for the iterative enforcement step is given by,

$$\begin{aligned} Y_{f,i}^{l+1} &= Y_{f,i}^{l} - K_f^l f_{p,i}^l \\ &= Y_{f,i}^{l} - C_{YF}(C_f + C_{FF})^{-1} f_{p,i}^l, \end{aligned} \tag{3.5}$$

where $Y_{f,i}$ is the ith state vector consisting of only the two GRFs, K_f is the Kalman gain approximated from the ensemble, C_{YF} is the cross covariance between the facies mismatch proxy (Eq. 3.1) and the state vector, C_{FF} and C_f are respectively the covariance of the facies mismatch proxy and diagonal covariance of the noise in facies measurement. l denotes the iteration index.

Although it may not be obvious from Eq. 3.5, a sequence of smooth corrections $(-K_f^1 f_p^1, \dots, -K_f^l f_p^l, \dots)$ are added iteratively to the GRFs until a match between the predicted facies and the facies observations is obtained. A graphical illustration of how the iterative re-enforcement step works is shown in Fig. 3.6 for a simple 1D model with 100 gridblocks. There are 3 different facies types (F1, F2 and F3) obtained by truncating a single Gaussian random field. The iterative update to a single realization of the GRF, out of 80, is presented. Each pair of the dotted blue vertical lines corresponds to a grid location with facies observations and the length

of each pair is restricted to the Gaussian interval corresponding to the specific facies type. The initial GRF has 2 grid locations (corresponding to gridblocks 24 and 99) where the Gaussian random variables are in the wrong intervals (Fig. 3.6(a)). Figures 3.6(e)–3.6(g) show the sequence of smooth corrections applied to Gaussian random field (Figs. 3.6(a)–3.6(c)) at each iteration to obtain Gaussian variables that are in the correct intervals (Fig. 3.6(d)) that satisfy the constraint on the facies mismatch observations. Note that for Gaussian variables in the correct interval, the value of the correction term is nearly zero.

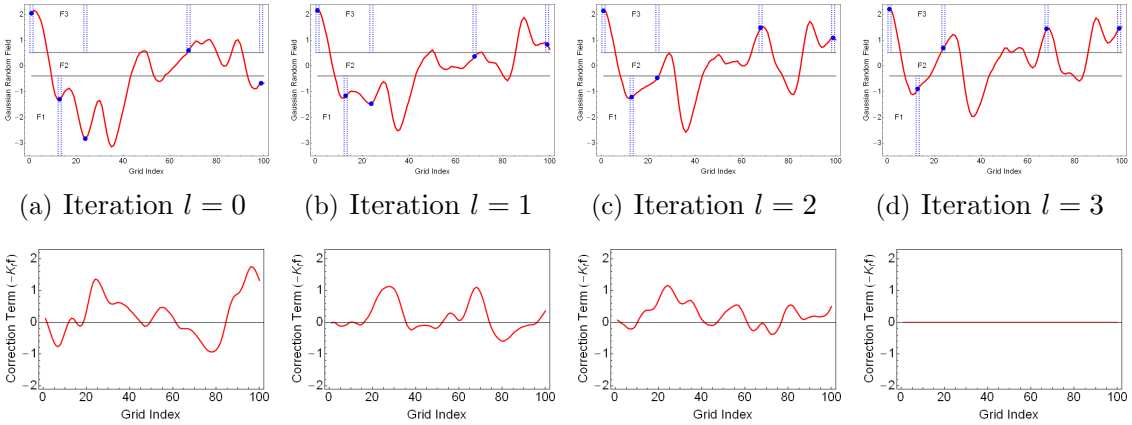

(a) Iteration $l = 0$ (b) Iteration $l = 1$ (c) Iteration $l = 2$ (d) Iteration $l = 3$

(e) Correction to $\mathbf{Y}^0$ (f) Correction to $\mathbf{Y}^1$ (g) Correction to $\mathbf{Y}^2$ (h) Correction to $\mathbf{Y}^3$

Figure 3.6: Simple 1D illustration of the iterative enforcement of the constraints on facies mismatch observation. Top row is the evolution of the GRF and bottom row is the sequence of smooth corrections added to the GRF to enforce constraints. Blue circles (top row) are estimates of Gaussian variables at the observation locations (pair of blue dotted vertical lines). The labels F1, F2, and F3 are facies types in different intervals.

From the foregoing, after a match between the ensemble of the predicted facies at the well locations and the facies observations is obtained, the updated estimates of the facies maps (obtained by truncating the updated GRFs) and dynamic parameters (gridblock pressures and saturations) are used for the next short-range forecast until the next set of production data is available for assimilation. Based on our proposed formulation, it is possible to iterate as many times as is necessary to enforce the constraints on facies mismatch observations without the problem of incorrect weighting

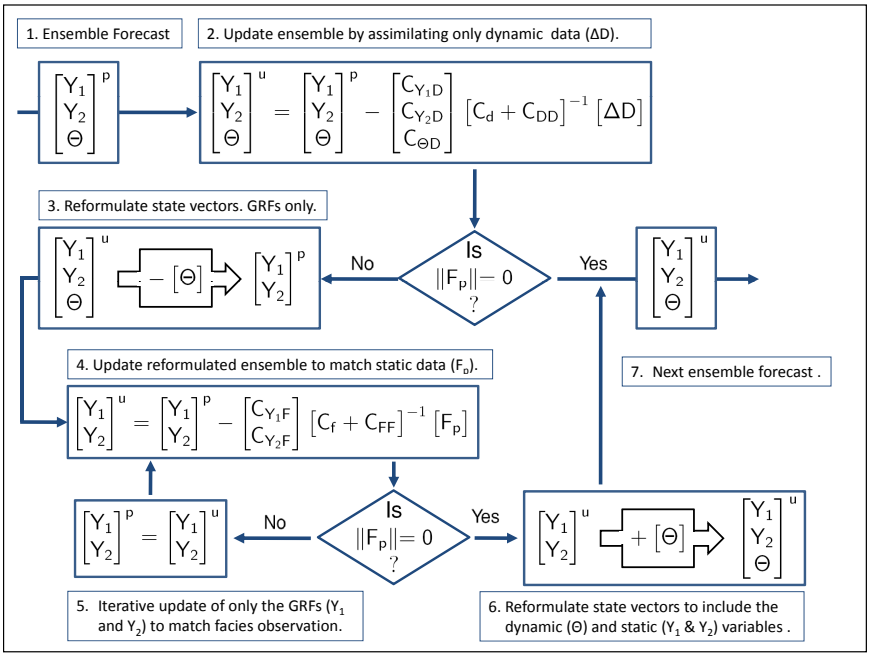

Figure 3.7: Flowchart for iteratively enforcing the constraints on facies mismatch observations. $C_{\xi D}$ is the cross-covariance between model parameter ξ and predicted data. $C_{\xi F}$ is the cross-covariance between model parameter ξ and the facies mismatch proxy. ΔD is the ensemble of predicted data mismatch and F_p is the ensemble of facies mismatch proxy. $\|A\|$ is the norm of matrix A.

of the assimilated production data relative to the prior model mismatch and without inducing very large (incorrect) changes to the saturation and pressure fields (Fig. 3.1). Figure 3.7 is a flowchart of the major implementation steps of the proposed iterative enforcement of the constraints on facies mismatch observations.

For the problem of EnKF applied to history matching geological facies, excessive loss in ensemble variability is generally a much bigger problem. The requirement to iterate whenever the constraints on facies mismatch observations are violated will also also exacerbate this problem. The EnKF implementation consists of short range forecasts of simulated data between data assimilation timesteps. The spread in short-range prediction of the ensemble is an indicator of model diversity and thus of the variability between the ensemble members. While some reduction in prediction spread is expected from conditioning the ensemble to data, excessive reduction is undesirable as this will result in filter divergence since the ensemble variability will be too low. Figure 3.8 shows the variability in ensemble prediction for three different types of data at each data assimilation timestep for ensemble sizes of 40 (Figs. 3.8(a)–3.8(c)), 120 (Figs. 3.8(d)–3.8(f)) and 240 (Figs. 3.8(g)–3.8(i)). The prediction spread at each data assimilation timestep is obtained by a forward simulation run (using a commercial reservoir simulator) from the previous data assimilation timestep to the next data assimilation timestep using the ensemble estimates of the static and dynamic model variables from the previous timestep.

Before the first water breakthrough time (day 120) the ensemble size of 40 performed fairly well in the short-range prediction match to measured data and the measured data are generally contained in the ensemble prediction spread. The ensemble of predicted BHP data for an ensemble size of 40 shows a consistent decrease in ensemble variability with data assimilation and after day 120, the ensemble variability is so small that the facies models could not be adjusted to obtain short-range prediction match to data for the remaining data assimilation timesteps (Fig. 3.8(a)).

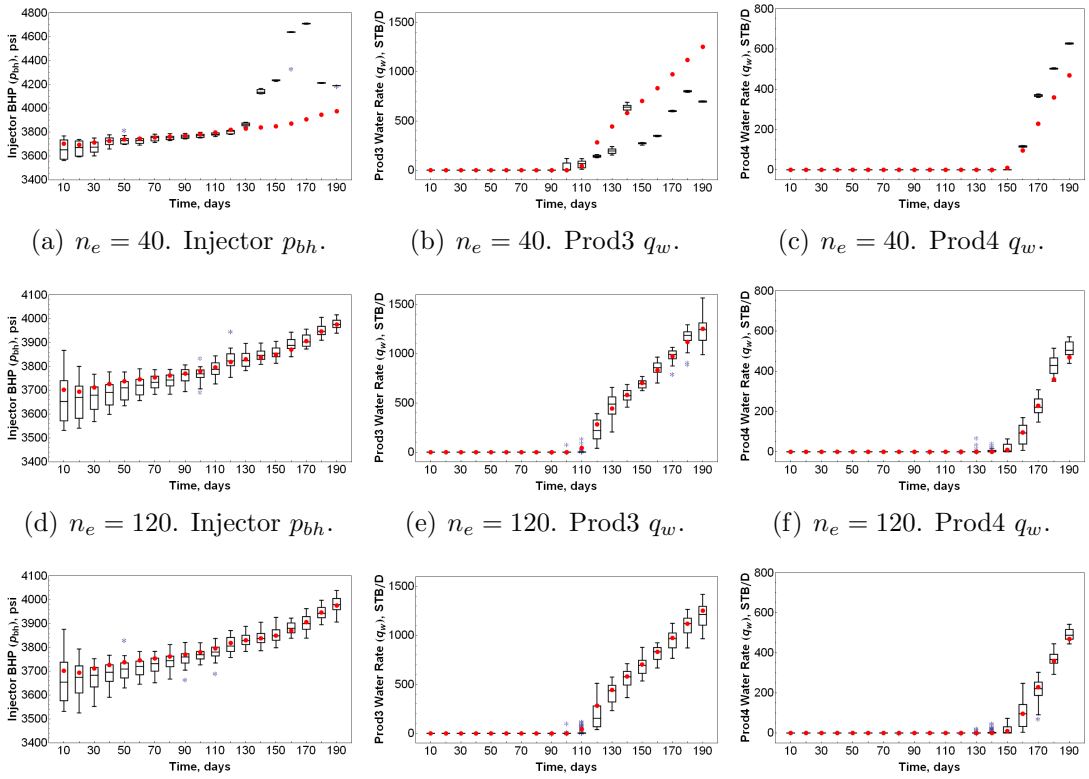

(a) $n_e = 40$. Injector p_{bh}. (b) $n_e = 40$. Prod3 q_w. (c) $n_e = 40$. Prod4 q_w.

(d) $n_e = 120$. Injector p_{bh}. (e) $n_e = 120$. Prod3 q_w. (f) $n_e = 120$. Prod4 q_w.

(g) $n_e = 240$. Injector p_{bh}. (h) $n_e = 240$. Prod3 q_w. (i) $n_e = 240$. Prod4 q_w.

Figure 3.8: Variability in short range predictions for the case without localization. The red dots are the production measurements and the box-whisker plots are the ensemble of short range forecasts from the previous data assimilation timestep. n_e is the ensemble size. Filter divergence occurred for the ensemble size of 40 (top row). Predictions from ensemble sizes of 120 and 240 (middle and bottom rows respectively) do not show evidence of filter divergence and match data better.

Similar observation of the effect of too low ensemble variability is evident in the very low spread in ensemble prediction and the lack of match to the q_w data from producers 3 and 4 for the same ensemble size (Figs. 3.8(b)–3.8(c)). By contrast, the ensemble sizes of 120 (Figs. 3.8(d)–3.8(f)) and 240 (Figs. 3.8(g)–3.8(i)) show evidence of sufficient ensemble variability for the entire data assimilation period and the filter appears not to diverge for both ensemble sizes. Additionally, at each data assimilation timestep the production data are contained in the short-range prediction spread for both ensemble sizes.

At each update step, the forecast error covariance and the Kalman gain are approximated using statistics obtained from the ensemble members. If the ensemble spread is overly underestimated, the ensemble approximations of these parameters will be incorrect. Estimates of the facies boundaries and spatial distribution of the facies variables at each data assimilation timestep are obtained by adjusting the values of the GRFs at the update step. The joint impact of assimilating both production and facies data on the ensemble spread may be analyzed by examining the between-ensemble variance of the model parameters at each data assimilation timestep. To this end, the average ensemble variance of the two GRFs at each data assimilation timestep (Eq. 3.6) is utilized and the value is obtained as,

$$\overline{\overline{Y}} = \frac{1}{2n_g} \sum_{i=1}^{2n_g} \left[\frac{1}{n_e - 1} \sum_{j=1}^{n_e} (Y_{i,j} - \overline{Y}_i)^2 \right]. \tag{3.6}$$

$\overline{\overline{Y}}$ is the average variance of the bi-Gaussian random fields from all three layers in the model; i and j are respectively the gridblock and ensemble member indices; n_e is the number of ensemble members and $n_g = n_x n_y n_z$ is the total number of gridblocks with n_x, n_y and n_z being the number of gridblocks in the $x-$, $y-$ and $z-$ directions respectively. $\overline{Y}_i$ is the mean value of the GRF at the ith grid location. The factor of 2 in Eq. 3.6 accounts for the fact that there are two Gaussian random fields. The plot of the time evolution of the average variance of the GRFs as a function of the three

ensemble sizes is presented in Fig. 3.9(a). Figure 3.9(b) also shows the number of iterations required to enforce the constraints on the mismatch to facies observations at the well locations at each data assimilation timestep.

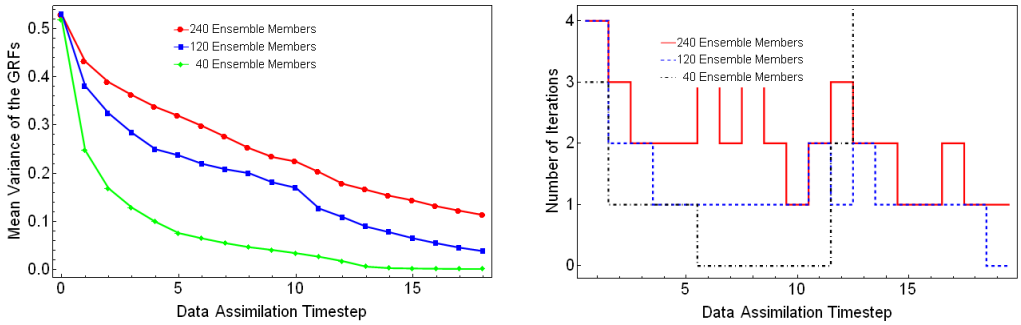

(a) Mean of GRF variances.

(b) Facies mismatch iteration.

Figure 3.9: Time evolution of the GRFs' mean variance and the number of iterations for facies mismatch constraints enforcement. Case without localization. Fig. 3.9(a) shows a reduction in ensemble variability for all ensemble sizes and a complete loss of variability for the ensemble size of 40. Also, facies mismatch constraints were enforced in less than 4 iterations if the filter does not diverge.

Figure 3.9(a) shows that the most significant reduction in ensemble variability occurred after the first data assimilation timestep for all ensemble sizes with a reduction of one-fifth, one-third and one-half of the ensemble variances for the ensemble sizes of 240, 120 and 40 respectively. This is indicative of the magnitude of the information content from assimilating data at the first data assimilation timestep relative to the high uncertainty in the initial models conditioned only to static facies data. Also, no more than four iterations were required to constrain the facies mismatch observations at the first data assimilation timestep (Fig. 3.9(b)) for all the ensemble sizes. The ensemble size of 40 shows evidence of more pronounced loss in ensemble variability; about 86% of the initial ensemble variability has been lost by the fifth data assimilation timestep. By the 13th data assimilation timestep the ensemble variability is virtually nonexistent such that irrespective of how may times one iterates, it is impossible to constrain the facies mismatch observations to honor the facies data at the well locations (Fig. 3.9(b)). The ensemble sizes of 120 and 240 exhibit a more gradual

reduction in variability with data assimilation. For the ensemble size of 120, there is a sharp reduction in ensemble variance between the 10th and 11th assimilation time. This illustrates the impact of sudden availability of new data on the ensemble variability; at the 10th assimilation time, the first water rate data became available for assimilation. This sudden reduction in variability is not as evident when the ensemble size is increased to 240, reflecting the robustness of the larger ensemble sizes to the assimilation of data with new information. At the end of the data assimilation period, the initial average variance of the GRF has been reduced by 99.8%, 92.8% and 78.6% respectively for ensemble sizes of 40, 120 and 240.

Figure 3.9(b) shows that for the ensemble sizes of 120 and 240, a maximum of 3 iterations was required to enforce the constraints on the facies mismatch observations at each timestep; a notable exception is at the first data assimilation timestep where 4 iterations were required to enforce the constraints for the ensemble size of 240. Also, the number of iterations needed to enforce the constraints on the facies mismatch observations appears to be a function of the ensemble size. It seems that for larger ensemble sizes, the number of iterations required for constraint enforcement is generally greater (Fig. 3.9(b)). This is related to the fact that as the ensemble size increases, the number of ensemble members with facies mismatch at the well locations also increases.

Figure 3.10 shows the evolution of the updates to a randomly selected realization of the facies map from the ensemble size of 240. Evidently, as data were assimilated and the facies boundaries adjusted, the realization of the facies maps in Fig. 3.10 appears geologically plausible. All the well facies are well constrained at each timestep and match the facies observations from the reference model (Fig. 3.4(b)). It is also evident from Fig. 3.10 that as more data were assimilated, facies 3 (white shade) appears to be eroded by facies 1 (dark gray shade) and both facies are subsequently eroded by facies 2 (light gray shade). Consequently, the facies maps appear to capture qualitatively

some of the global features evident in layer 2 of reference model (Fig. 3.4(b)).

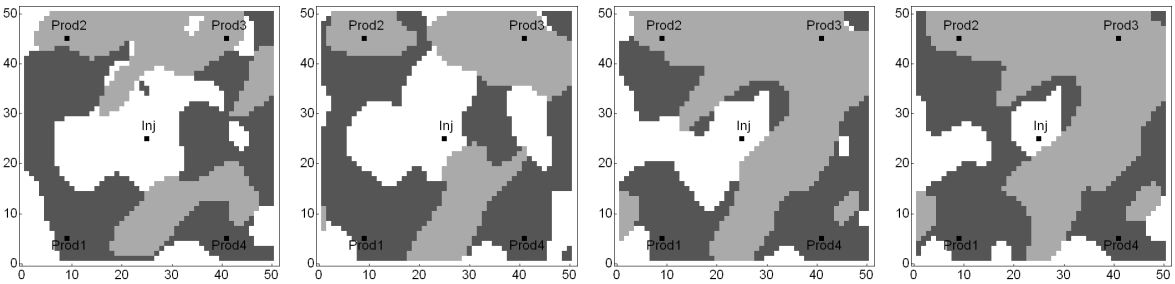

(a) Timestep 1. (b) Timestep 6. (c) Timestep 11. (d) Timestep 16.

Figure 3.10: Evolution of a randomly selected realization of a facies map from layer 2 for an ensemble size of 240. Results from case without localization. The facies distribution becomes increasingly similar to the reference case (Fig. 3.4(b)) as data are assimilated.

Three random realizations of the initial and final facies realizations from EnKF with decoupled assimilation of production and facies data for the three ensemble sizes are presented in Fig. 3.11. All the selected realizations from the ensemble size of 40 (column 2 of Fig. 3.11) are exactly alike due to the collapse in ensemble variability noted earlier for this ensemble size. Compared to the ensemble size of 40, some variability is still evident in the selected final realizations for the ensemble size of 120 and final realizations from the ensemble size of 240 exhibit the most variability. Realizations of the initial facies map (column 1 in Fig. 3.11) and the final ensemble from the ensemble size of 40 appear qualitatively very different from the reference model. In general, the facies at the well locations in the final facies map for the ensemble with 40 members do not match the facies observations. Qualitatively, the ensemble sizes of 120 and 240 seems to acceptably reproduce the features in the reference model and all the well facies in the ensemble final models match the facies observations.

Recall that the initial facies maps were generated by truncating two Gaussian random fields using a truncation map with three intersecting lines that form the thresholds. Consequently, the facies proportions estimated from the initial ensemble

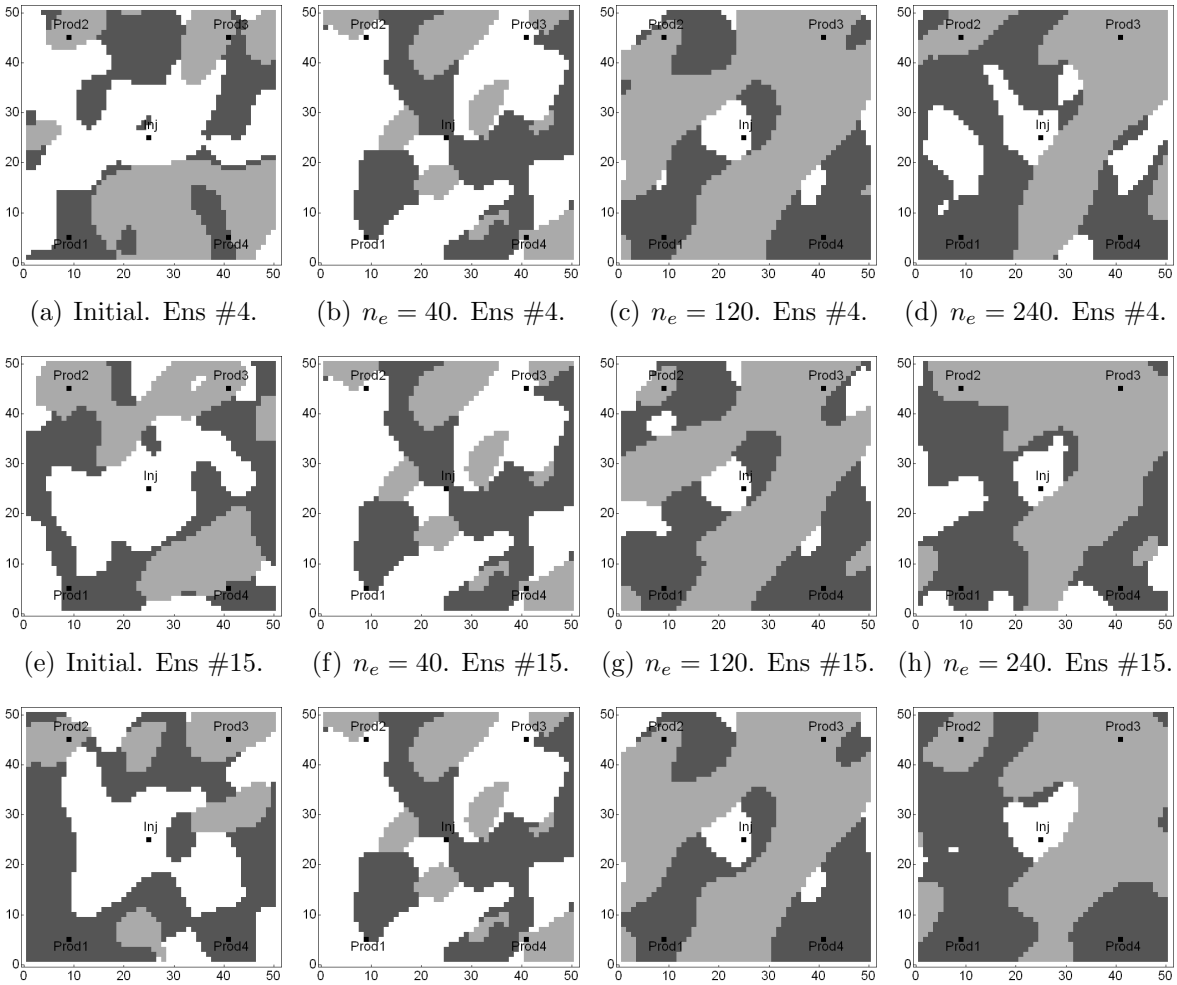

(a) Initial. Ens #4. (b) $n_e = 40$. Ens #4. (c) $n_e = 120$. Ens #4. (d) $n_e = 240$. Ens #4.

(e) Initial. Ens #15. (f) $n_e = 40$. Ens #15. (g) $n_e = 120$. Ens #15. (h) $n_e = 240$. Ens #15.

(i) Initial. Ens #26. (j) $n_e = 40$. Ens #26. (k) $n_e = 120$. Ens #26. (l) $n_e = 240$. Ens #26.

Figure 3.11: Three randomly selected realizations of the initial and final facies maps from layer 2 for case without localization. n_e is the ensemble size and Ens # is the ensemble member number. Realizations from the ensemble size of 40 (column 2) are exactly alike due to collapse in variability. By contrast, realizations from the ensemble with 120 (column 3) and 240 (column 4) members exhibit higher variability and the facies distribution are qualitatively very similar to the reference case (Fig. 3.4(b)).

should be centered around the expected value of the proportions computed from the truncation map. Usually, the expected proportions from the truncation maps are different from the reference proportions due to the initial uncertainty in the static data used in determining the thresholds. Consequently, as the the facies variables are adjusted during history matching so that predictions from the facies maps match measured data, the distribution of the facies proportions should approach the reference proportions. Figure 3.12 shows the initial (gray histograms) and final (green histograms) distributions of the facies proportions in layer 2 for the three different ensemble sizes. The red vertical line shows the value of the reference facies proportions and the blue vertical line is the expected value of the facies proportion obtained from the threshold map. In all instances in Fig. 3.12 the mean values of the initial facies proportions are generally centered about the expected facies proportions from the truncation maps and do not match the reference facies proportions. With the exception of facies 1 proportions, the distribution of the final facies proportions (green bars) from the ensemble size of 40 (Figs. 3.12(a)–3.12(c)) do not match the reference facies proportions. Histograms of the final proportions from the ensemble sizes of 120 (Figs. 3.12(d)–3.12(f)) and 240 (Figs. 3.12(g)–3.12(i)) are generally better at estimating the reference facies proportions.

A global measure of the performance of the EnKF with decoupled assimilation of production and facies data is from the facies probability map for each facies type. To obtain the facies probability maps, the probabilities of observing each facies at the each grid location are estimated from the ensemble. Figure 3.13 shows the final facies probability maps from layer 2 for facies 1 (top row), facies 2 (middle row) and facies 3 (bottom row) estimated from all three ensemble sizes. The reference facies indicator maps are also shown for comparison. Probabilities of 0 and 1 correspond respectively to the black and white regions of the maps and intermediate probabilities correspond to regions with different shades of gray. The probability map for the ensemble size of

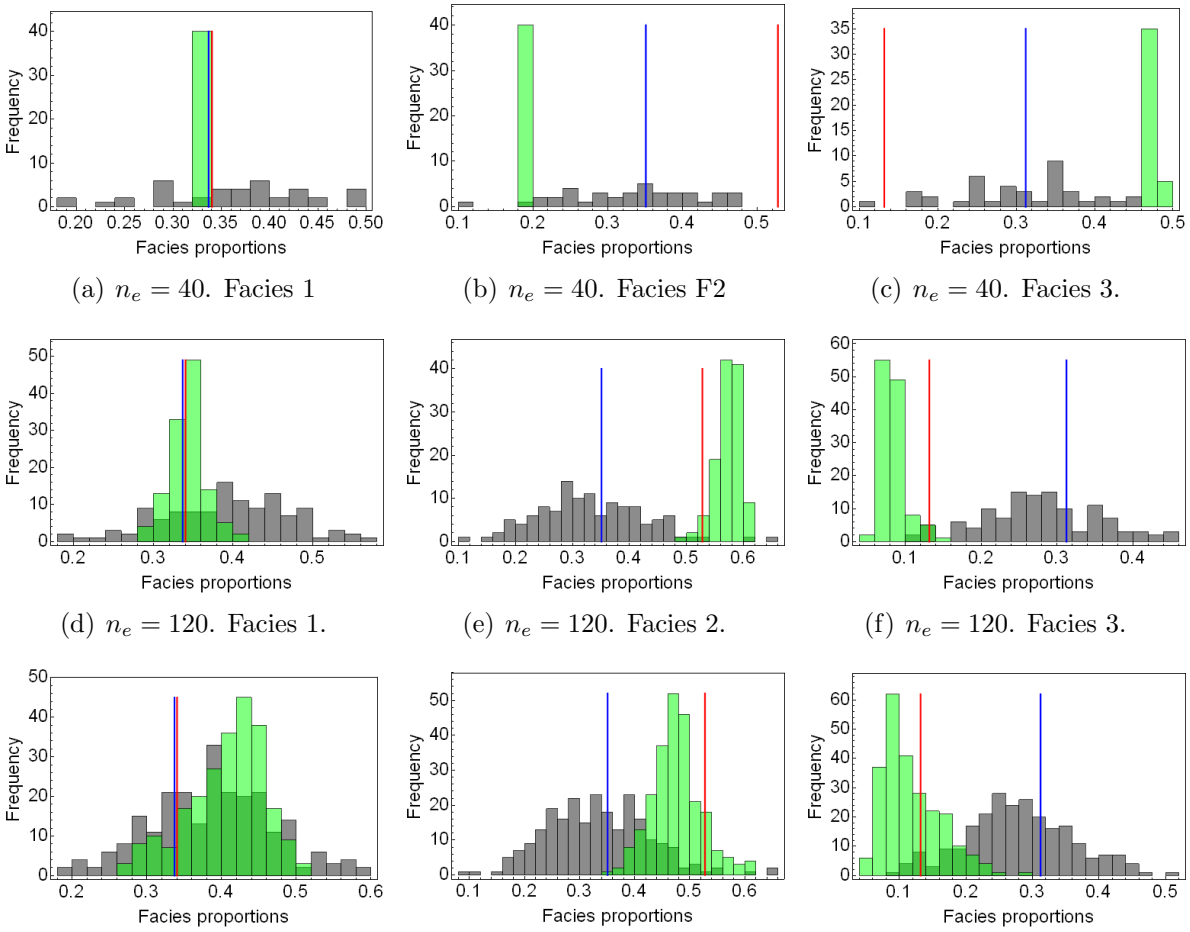

(a) $n_e = 40$. Facies 1 (b) $n_e = 40$. Facies F2 (c) $n_e = 40$. Facies 3.

(d) $n_e = 120$. Facies 1. (e) $n_e = 120$. Facies 2. (f) $n_e = 120$. Facies 3.

(g) $n_e = 240$. Facies 1. (h) $n_e = 240$. Facies 2. (i) $n_e = 240$. Facies 3.

Figure 3.12: Histograms of layer 2 facies proportions estimated from the initial and final ensembles with 40 (top row), 120 (middle row) and 240 (bottom row) members for the case without localization. The red and blue lines are respectively the reference proportions and the expected proportions from the truncation map. The gray and green histograms are respectively the initial and final proportions. The final estimates of the facies proportions are generally better for the ensemble with 120 and 240 members.

40 looks nothing like the reference indicator maps. Qualitatively, the maps from the ensemble sizes of 120 and 240 seem to reproduce some of the global features in the reference maps.

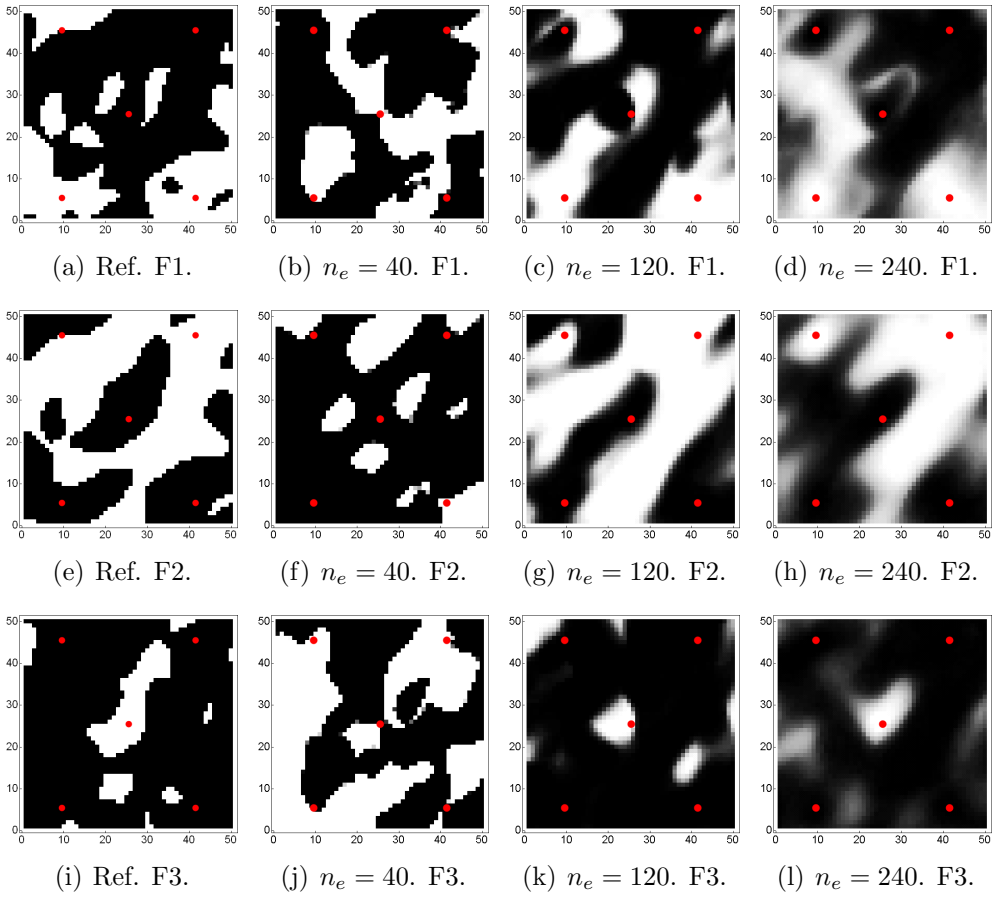

(a) Ref. F1. (b) $n_e = 40$. F1. (c) $n_e = 120$. F1. (d) $n_e = 240$. F1.

(e) Ref. F2. (f) $n_e = 40$. F2. (g) $n_e = 120$. F2. (h) $n_e = 240$. F2.

(i) Ref. F3. (j) $n_e = 40$. F3. (k) $n_e = 120$. F3. (l) $n_e = 240$. F3.

Figure 3.13: Layer 2 reference indicator map (column 1) and final probability maps for ensemble sizes of 40, 120 and 240 (columns 2–4 respectively). F1, F2 and F3 are facies 1–3 respectively. Black and white shades are probabilities of 0 and 1 respectively, and gray shades are probabilities between 0 and 1. Qualitatively, the probability maps from the ensemble with 120 and 240 members are generally better than the ensemble with 40 members in reproducing features in the reference indicator map. Results from case without localization.

3.5 Case 2: Localizing the Updates to the Gaussian Random Fields from Assimilating Facies Data

The EnKF technique uses a limited number of realizations to generate a reduced rank approximation to the model covariance matrix. Depending on the ensemble size and the amount of data assimilated, the ensemble may lose all variability leading to filter divergence; a situation where additional available observations for assimilation are no longer honored during successive cycles of data assimilation. This situation was observed in Case 1 for an ensemble size of 40 where a complete loss of ensemble variability, after the 12th data assimilation timestep, led to divergence of the filter performance. In general, the likelihood of having filter divergence decreases as the ensemble size increases. Recall from Case 1 that the loss in ensemble variability at the end of data assimilation was nearly 100% for an ensemble size of 40; 93% for an ensemble size of 120 and 77% for an ensemble size of 240. We note that while the ensemble sizes of 120 and 240 did not lose all variability, the reduction in ensemble variability at the end of data assimilation was quite significant. In this section, we investigate the possibility of ameliorating the problem of collapse in ensemble variability (observed in case 1) by localizing the adjustment to the bi-Gaussian random fields during data assimilation through a Schur product of the Kalman gain with a compactly supported fifth-order function. Recall that the bi-Gaussian random fields are truncated to determine the facies distribution. In some instances, the Schur product has been used to to filter the approximation of the forecast covariance at large distance, and to increase the effective rank of the ensemble (Houtekamer and Mitchell, 2001). The Schur product, also known as the Hadamard product, is an element-wise multiplication of two matrices A and B resulting in a third matrix C of the same dimensions as A and B. The product of the elements of the matrices is given by,

$$c_{i,j} = a_{i,j} b_{i,j}, \tag{3.7}$$

where $p_{i,j}$ denotes the element in the ith row and jth column of an arbitrary matrix P. If C_o defines the correlation matrix or filter, then the expression for the Kalman gain at the analysis step is modified thusly:

$$\begin{aligned} K_L &= C_o \circ K_e, \\ &= C_o \circ \left[C_{YD} \left(C_{DD} + C_D \right)^{-1} \right]. \end{aligned} \tag{3.8}$$

where K_L and K_e are respectively the Kalman gain matrices with and without localization. $A \circ B$ represents the element-wise multiplication of matrices A and B.

We note from Eq. (3.8) that the Schur product in our application is applied to the Kalman gain and not just the cross-correlation matrix, C_{YD}. The element-wise multiplication of the Kalman gain with an appropriately chosen correlation matrix, $\mathbf{C}_o$, ensures that only a localized area of influence is updated. Recall that the Kalman gain is an $N_s \times N_d$ matrix, where N_s is the dimension of the state vector and N_d is the number of data at each timestep. Each column of the Kalman gain matrix corresponds to a single observation and the element-wise multiplication of each column of the Kalman gain is centered at the corresponding observation location. The correlation matrix, C_o, takes a value of unity at the observation location and decreases monotonically to zero beyond the region of influence governed by a predefined correlation length. Mitchell et al. (2002) showed the importance of keeping the size of the nonzero region large enough to include the region of true correlation to data. The correlation function (Φ) used in constructing the correlation matrix is a fifth-order compact function of Gaspari and Cohn (1999) defined as,

$$\Phi(\delta, L) = \begin{cases} -\frac{1}{4}\left(\frac{\delta}{L}\right)^5 + \frac{1}{2}\left(\frac{\delta}{L}\right)^4 + \frac{5}{8}\left(\frac{\delta}{L}\right)^3 - \frac{5}{3}\left(\frac{\delta}{L}\right)^2 + 1, & 0 \le \delta \le L; \\ \frac{1}{12}\left(\frac{\delta}{L}\right)^5 - \frac{1}{2}\left(\frac{\delta}{L}\right)^4 + \frac{5}{8}\left(\frac{\delta}{L}\right)^3 + \frac{5}{3}\left(\frac{\delta}{L}\right)^2 & \\ \qquad -5\left(\frac{\delta}{L}\right) + 4 - \frac{2}{3}\left(\frac{\delta}{L}\right)^{-1}, & L < \delta \le 2L; \\ 0, & \delta > 2L, \end{cases} \tag{3.9}$$

where L is the length scale of the correlation function and $\delta = \|\delta_{ij}^k\|$ is the Euclidean distance between any grid point (i, j) and an observation location, k.

Following the formulation developed in the previous section for sequentially assimilating the decoupled production and facies data, the Kalman gain is not localized when production data are assimilated but a global update is made to the state vector (Eq. 3.4) at this stage. During the iterative enforcement of the constraints on the facies mismatch observations when only the facies data (or more precisely the facies mismatch proxies defined in Eq. 3.1) are assimilated, the updates to the Gaussian random fields are localized by the taking a Schur product of the Kalman gain and correlation function on a layer-by-layer basis. Recall that during the iterative enforcement of the constraints, the dynamic model variables are not included in the state vector and are thus not localized. The length scale, L, used for the correlation function, Φ, was chosen such that the range of the correlation function is about the same as the longest principal range of the covariance of the underlying Gaussian random field. Also the same initial realizations of the facies model from Case 1 were also used in the current case for history matching.

Plots of the variability in the short range ensemble predictions at each data assimilation timestep for the three different ensemble sizes with localized Kalman gain matrix are presented in Fig. 3.14. Figures 3.14(a)–3.14(c) show that for the case with localization, sufficient prediction spread was maintained for the ensemble size of 40 at each data assimilation timestep and the production data were generally within the spread of the ensemble prediction at each timestep. Although the spread appears to be quite small at the latter data assimilation timesteps, the divergence of the filter, which was observed in Case 1 for the same ensemble size (Figs. 3.8(a)–3.8(c)) is clearly mitigated in this case. The ensemble prediction spread for ensemble sizes of 120 and 240 seem to be generally sufficient for the cases with and without localization and the measured data are contained within the spread of the short-range prediction.

Figure 3.15(a) shows the evolution of the mean variance of the GRFs for the three different ensemble sizes in Case 2. Recall that in Case 1 the ensemble variance

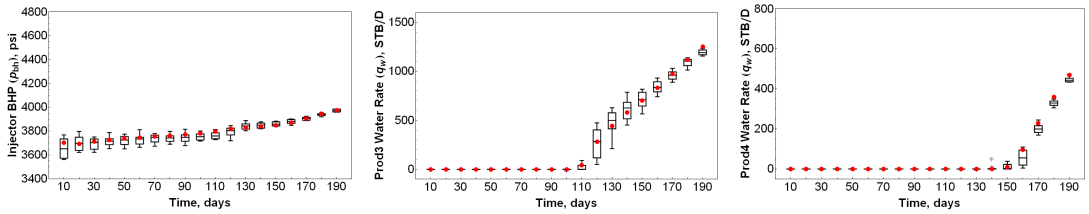

(a) $n_e = 40$. Injector p_{bh}. (b) $n_e = 40$. Prod3 q_w (c) $n_e = 40$. Prod4 q_w

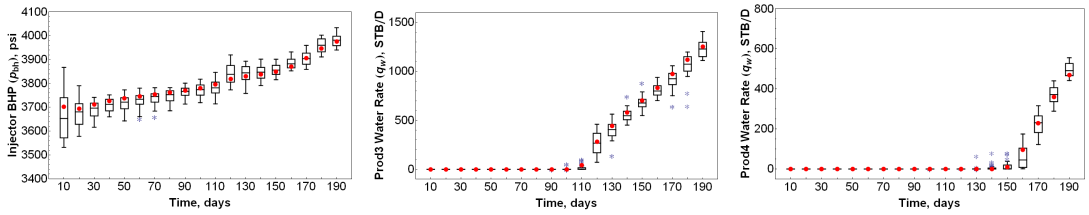

(d) $n_e = 120$. Injector p_{bh}. (e) $n_e = 120$. Prod3 q_w (f) $n_e = 120$. Prod4 q_w

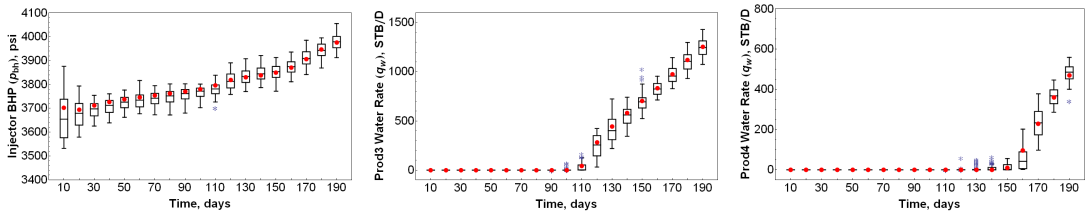

(g) $n_e = 240$. Injector p_{bh}. (h) $n_e = 240$. Prod3 q_w (i) $n_e = 240$. Prod4 q_w

Figure 3.14: Variability in short range predictions for the case with localization. The box-and-whisker plots are the ensemble predictions and the red dots are production measurements. n_e is the ensemble size. The filter did not diverge for all ensemble sizes and data are generally well matched.

reduced respectively by 52%, 28% and 18% for ensemble sizes of 40, 120 and 240, after assimilating the first set of data. For the current case, the corresponding reduction in ensemble variability after assimilating the same set of data was significantly lower with values of 15%, 6% and 4% respectively for ensemble sizes of 40, 120 and 240. Similarly, at the end of history matching, the mean reduction in variance of the GRFs for the three ensemble sizes (40, 120 and 240 in this order) were respectively 97.6%, 60% and 37.8% resulting in final ensemble variability that is significantly higher when localization is used than when it is not. Also while the ensemble size of 40 lost all variability after the 12th data assimilation timestep for the case without localization, it appears that with localization during facies constraint enforcement, the collapse in variability is significantly mitigated for the same ensemble size although the final average variance appears to be quite low. Also the variability in the final ensemble of with localization is about 7% greater than the variability in the final ensemble of 240 without localization.

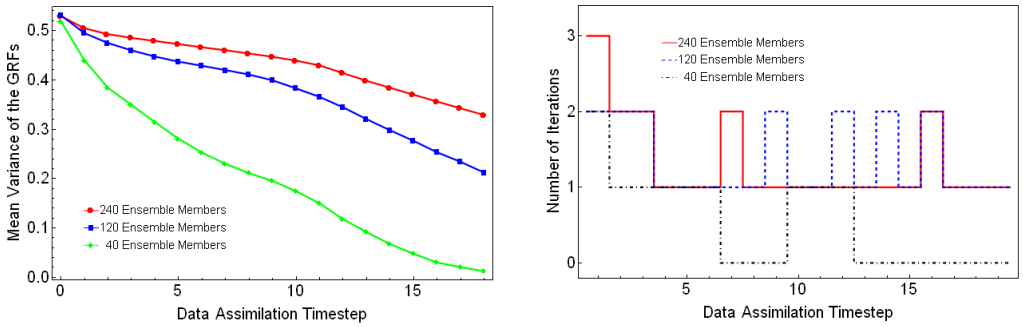

(a) Mean of GRF variances.

(b) Facies mismatch iteration.

Figure 3.15: Time evolution of the GRFs' mean variance and the number of iterations for facies constraint enforcement. Case with localization. With localization, pronounced decrease in ensemble variability is mitigated. Less than 3 iterations needed for facies mismatch enforcement at each timestep.

The maximum number of iterations needed to enforce the constraint on facies mismatch observations at each data assimilation timestep is presented in Fig. 3.15(b). Because localization was done on a layer-by-layer basis, the number of iterations

required to enforce the constraints varied per layer. For all the ensemble sizes, no more than three iterations were required for constraint enforcement any timestep where it was necessary to assimilate facies data.

Three realizations of the final facies maps from layer 2 for the ensemble with 40 members are presented in Fig. 3.16. The initial facies maps for these realizations have been presented in Fig. 3.11. The final facies maps shown in Fig. 3.16 are significantly different from the initial maps reflecting the impact of data conditioning. The global features in all the selected realizations are quite similar although each realization also exhibits distinctive features not present in the other realizations. Compared to the final realizations for the same ensemble size from Case 1 (Figs. 3.11(b), 3.11(f) and 3.11(j)) the final realizations in this case seem, at least qualitatively, to better reproduce the features in the reference facies model (Fig. 3.4(b)). Also, while it was impossible to enforce constraints on facies mismatch observations for the case without localization once the filter diverged, we note that with localization the simulated facies at the well locations all match the facies observations. Finally, although sample realization from the ensemble sizes of 120 and 240 are not shown in Fig. 3.16, the final facies maps exhibited significantly higher variability compared to the case without localization and the distributions of the facies variables in the final facies maps were similar to those in the reference facies maps.

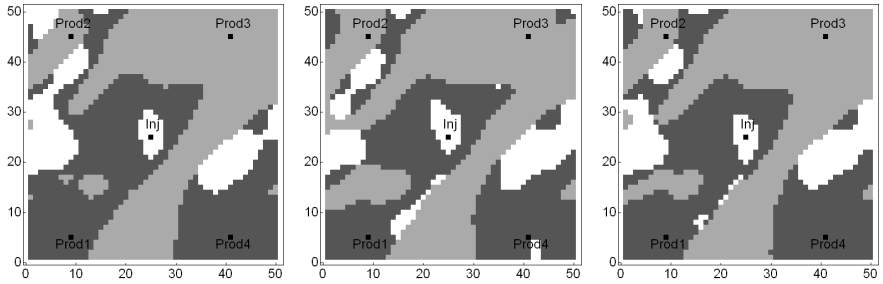

(a) Realization #4. (b) Realization #15. (c) Realization #26.

Figure 3.16: Final facies realizations from layer 2 for an ensemble size of 40 from the case with localization. The final facies distribution better reproduce the reference facies distribution and also match facies observations.

The distributions of the initial (gray bars) and final (green bars) estimates of the layer 2 facies proportions are presented in Fig. 3.17. The red and blue vertical lines respectively show the values of the reference facies proportions and the expectation of the facies proportions obtained from the threshold map. Of note is the significant improvement in the performance of the ensemble with 40 members in estimating the facies proportions (Figs. 3.17(a)–3.17(c)) compared to the performance of the case without localization for the same ensemble size (Figs. 3.12(a)–3.12(c)). For all the ensemble sizes in Case 2, the spread around the truth was reduced after data assimilation and the distributions of the facies proportions were adjusted correctly towards the reference values. Additionally, the facies proportions for the ensemble sizes of 120 and 240 seem to be better distributed around the reference values for Case 2 compared to Case 1.

3.6 Case 3: Starting Time for Future Predictions. From Time Zero or From End of History Matching Using Final Estimated State Variables

An important issue in history matching geological facies using EnKF is the choice of correct starting time for future predictions after all data are assimilated. Two possibilities are: (1) prediction from the end of data assimilation using the ensemble of final gridblock pressures and saturations estimated from EnKF and (2) re-initializing the gridblock pressures and saturations and predicting from time zero. To evaluate the best starting point for future predictions, we compute the root mean square error (RMSE) and the spread of the predicted data (injector BHP and water producing rates from the four producers) averaged over the future prediction period of 310 days. Additionally, we also examine the impact of the starting point for prediction on the predictive performance of a new well (Prod5) drilled at grid location (46,25), which began producing after the data assimilation period.

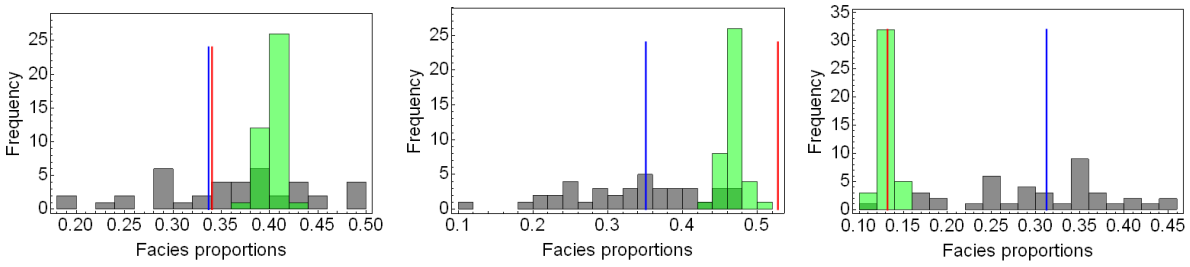

(a) $n_e = 40$. Facies 1. (b) $n_e = 40$. Facies 2. (c) $n_e = 40$. Facies 3.

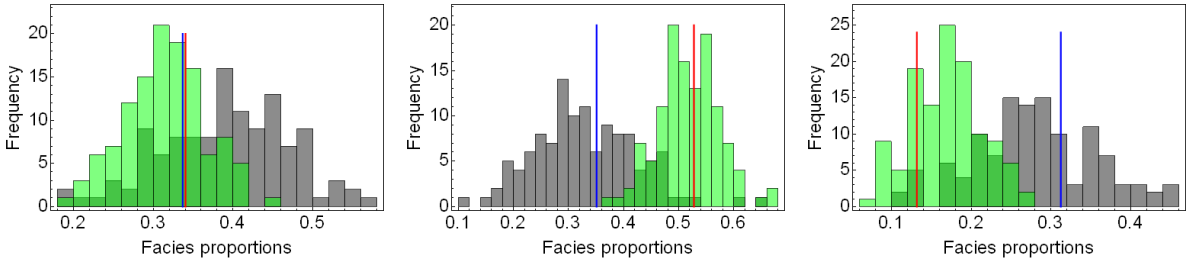

(d) $n_e = 120$. Facies 1. (e) $n_e = 120$. Facies 2. (f) $n_e = 120$. Facies 3.

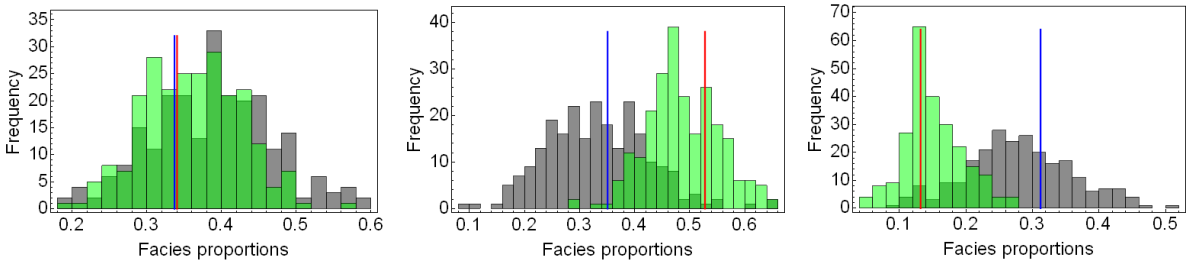

(g) $n_e = 240$. Facies 1. (h) $n_e = 240$. Facies 2. (i) $n_e = 240$. Facies 3.

Figure 3.17: Histograms of the initial (grey histograms) and final (green histograms) estimates of the facies proportion from layer 2 for ensemble sizes of 40 (top row), 120 (middle row) and 240 (bottom row) from the case with localization. The red line is the reference proportion and the blue line is the expected proportion from the truncation map. With localization, final proportions from the ensemble size of 40 match the reference proportions better.

The average RMSE and the average spread of the predicted data from the final ensembles for the case without localization are presented in Fig. 3.18. We observe from Fig. 3.18 that for the ensemble sizes of 120 (Figs. 3.18(b) and 3.18(e)) and 240 (Figs. 3.18(c) and 3.18(f)) respectively, the average prediction spread and RMSE from rerunning the model from time zero or running from the end of data assimilation are essentially equal. Also, for the same ensemble sizes, predicted data for the newly drilled well (Prod5) appear not to be sensitive to the starting time for future predictions. Under this condition, it is reasonable to predict using the final estimates of the dynamic state variables from history matching instead of rerunning the model from time zero. Because of filter divergence, which occurred when data were assimilated using the ensemble size of 40, the predictive performance is dependent on the choice of the starting time for future prediction (Figs. 3.18(a) and 3.18(d)).

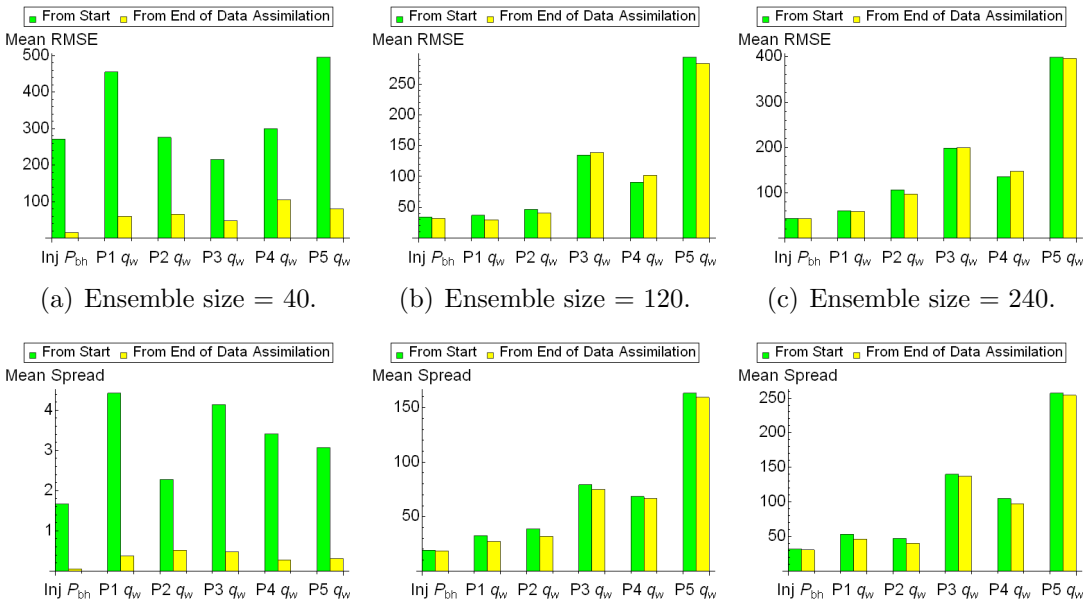

(a) Ensemble size = 40. (b) Ensemble size = 120. (c) Ensemble size = 240.

(d) Ensemble size = 40. (e) Ensemble size = 120. (f) Ensemble size = 240.

Figure 3.18: Average RMSE (top row) and spread (bottom row) for future predictions from time zero (green bars) and from end of data assimilation (yellow bars) for the case without localization. P1–P5 are respectively producers 1–5. With the exception of the ensemble size of 40, comparable prediction performances are obtained regardless of choice of starting time for future prediction.

By contrast, it is evident from Fig. 3.19 that when the updates to the facies variables are localized during data assimilation, the ensemble predictions from final realization for all the ensemble sizes seem to depend strongly on the choice of starting point for future prediction. Figures 3.18(a)–3.18(c) shows that the prediction spread is severely underestimated if the predictions are obtained from running the simulation from the end of data assimilation using the final estimated dynamic model variables. Clearly, when localization is used, the final estimates of the dynamic state variables from EnKF are not consistent with the final estimates of the static model parameters and it is necessary to re-initialize the state variables to re-establish consistency by rerunning from time zero.

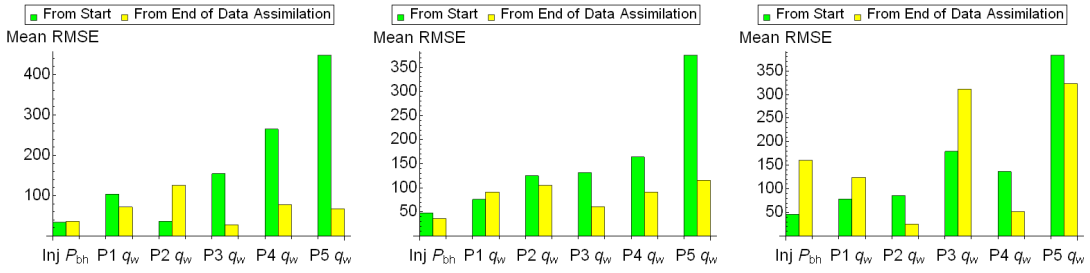

(a) Ensemble size = 40. (b) Ensemble size = 120. (c) Ensemble size = 240.

(d) Ensemble size = 40. (e) Ensemble size = 120. (f) Ensemble size = 240.

Figure 3.19: Average RMSE (top row) and spread (bottom row) in future predictions from time zero (green bars) and from end of data assimilation (yellow bars) for the case with localization. P1–P5 are respectively producers 1–5. Final estimated state variables are inconsistent with the final model parameter in this case resulting in the strong dependence of predictive performance on the starting time for future predictions.

Predictions of water rate data from Prod3 for the periods with history matched and future data obtained by running the simulator from time zero using the final

model parameters for the cases with (top row) and without (bottom row) localization are presented in Fig. 3.20. The vertical line demarcates the end of history matching and the red circles are predicted data from the reference model. The ensemble predictions at each time with data is represented by a box-and-whisker plot. Localization seems to have improved the predictive performance of the ensemble size of 40 (Figs. 3.20(d) and 3.20(a)) although the prediction spread appears to be too low and the future predictions are also somewhat biased in this case. The predictive performance of the ensemble sizes of 120 and 240 for the models with and without localization are generally good and match the reference predictions acceptably well. However, compared to the predictions from the models for the case with localization the future predictions from the models for the case without localization appear to be biased and the ensemble variability appears to be somewhat smaller.

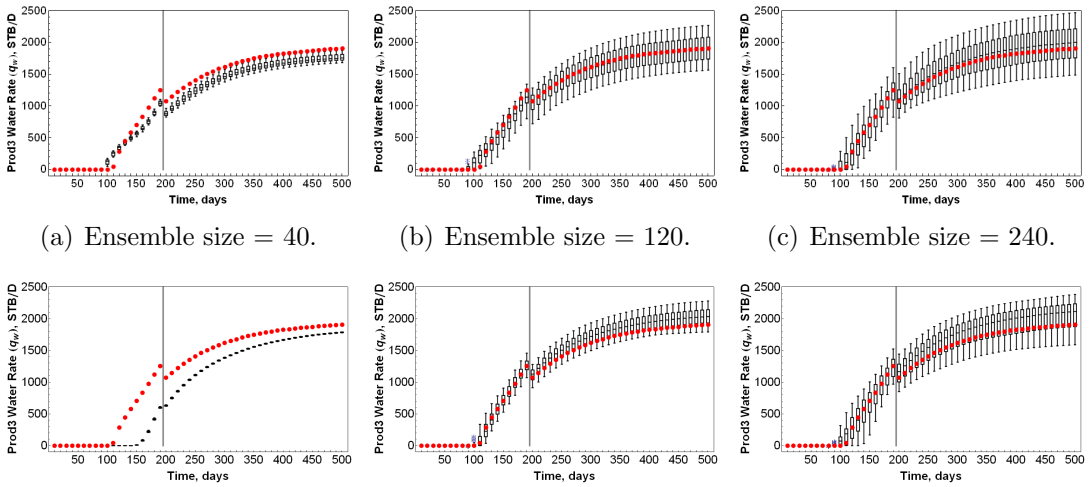

(a) Ensemble size = 40. (b) Ensemble size = 120. (c) Ensemble size = 240.

(d) Ensemble size = 40. (e) Ensemble size = 120. (f) Ensemble size = 240.

Figure 3.20: q_w data from Prod3 predicted from time zero for the cases with (top row) and without (bottom row) localization. The vertical line demarcates the period of pure prediction and the red dots are data. The box-and-whisker plots are the ensemble predictions. Data match is generally better (less bias) with localization (top row).

Figure 3.21 presents a comparison of the average root mean square prediction error and average prediction spread as a function of the different ensemble sizes. The

average was taken over the ensemble of predicted data for the period after history matching and all predictions were made from time zero. Predictions from the ensemble without localization (Figs. 3.21(c)–3.21(d)) seem to depend on the ensemble size. The estimates of the mean RMSE and mean spread in predicted data for the ensemble sizes of 120 and 240 respectively appear to differ somewhat significantly. However, for ensemble predictions from the case with localization, the values of the mean RMSE and mean spread for the ensemble sizes of 120 and 240 are quite similar. The prediction spread for the ensemble with 40 members (red bars) for both cases (with and without localization) are significantly underestimated.

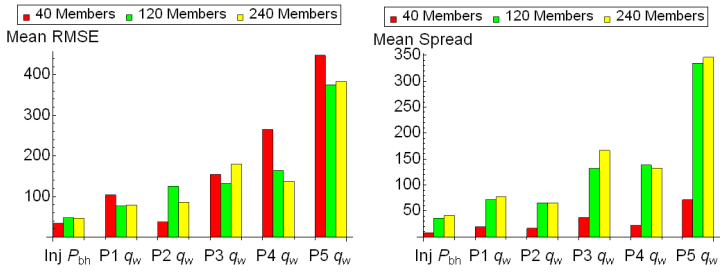

(a) Localization (b) Localization

(c) No Localization (d) No Localization

Figure 3.21: Comparative performance of different ensemble sizes in predicting "future" data for the cases with (top row) and without (bottom row) localization. Predictions are from time zero. Case without localization that shows a strong ensemble-size dependence for ensemble sizes of 120 and 240. In all cases, an ensemble size of 40 appears to be too small.

3.7 Chapter Summary

Three issues related to the difficulty in applying the ensemble Kalman filter technique to the problem of updating the distribution of facies variables to match production

data were identified and investigated in this chapter. Specifically, I addressed the problem of (1) how to iteratively constrain the simulated facies at the well locations to honor the facies observations when a mismatch occurs from assimilating production data, (2) how to mitigate the problem of rapid loss in ensemble variability for facies history matching, and (3) determining the best starting time for future prediction.

I solved the first issue by implementing a sequential global assimilation technique where the assimilation of production and facies data are decoupled and the production data are assimilated firstly followed, if necessary, by the assimilation of the facies data. Where it is necessary to assimilate the facies data, the state vector is reformulated to include only the static model parameters, i.e., the GRFs that are truncated to obtain the facies maps, avoiding large and incorrect updates to the state variables. Although the quality of the results are sensitive to the ensemble size, sequential global assimilation at each timestep seems to have solved the problems of improper weighting of the production data relative to the prior model mismatch and inconsistent updates to the state variables. On the other hand, repeated global updates to the model variables from assimilating both facies and production data resulted in very fast decrease in ensemble variability for all three ensemble sizes and a total loss in ensemble variability for the smallest ensemble size of 40.

The issue of collapse in ensemble variance was the focus of my second investigation in this chapter. Without localization, there is an increased tendency towards rank deficiency particularly for small ensemble sizes. Localizing the adjustments to the facies field when facies data are assimilated seems to mitigate the problem of variance deficiency resulting in an overall improvement in the history matching and prediction results that were obtained. When the ensemble size is small compared to the number of independent data, the localized adjustment of the state vector is a very important technique for mitigating loss of rank in the ensemble. Implementing a distance-based localization of the facies adjustment appears to mitigate the problem of variance

deficiency in the ensembles by ensuring that sufficient variability in the ensemble is maintained throughout the data assimilation period.

For the issue on the best starting point for future predictions, it was observed that when data are sequentially assimilated without localization, for a five-spot well pattern with water breakthrough in all the wells, the results of predicting the future reservoir performance using the final estimates of the dynamic variables as the initial states are similar to predictions from time zero where the dynamic variables are re-initialized. However, when the adjustments to the facies field are localized, predicting from the final states are incorrect due to layer-by-layer discontinuity in the distribution of the state variables, which results from using a layer-by-layer localization scheme. Under this condition, it is better to re-initialize the state variables and predict from time zero rather than use the final estimates of the state variables.

For the three ensemble sizes investigated, it appears that an ensemble size of 40 is too small and resulted in the poorest match to data. With localization, the ensemble size of 120 appears to be sufficiently large for the history matching problem discussed in this chapter and the predictive performance obtained was fairly close to that of the ensemble with 240 members.

CHAPTER IV

UPDATING MULTIMODAL FACIES PROPERTIES FROM ASSIMILATING PRODUCTION DATA USING ENKF

4.1 Background

Currently published works on history matching geological facies (Hu et al., 2001; Ravalec-Dupin et al., 2004; Liu and Oliver, 2005b; Hoffman and Caers, 2007; Agbalaka and Oliver, 2008; Moreno et al., 2008) typically assume that the petrophysical properties of each facies are uniform and homogeneous facies with no associated uncertainty such that the petrophysical properties were not estimated during history matching. While this assumption is appealing from an ease of implementation and methodology validation viewpoint, a more realistic approach will require a relaxation of these assumptions to account for situations where (1) the distribution of the petrophysical properties are nonuniform, heterogeneous and uncertain and also needs to be updated when production data are assimilated. Because the distribution of petrophysical properties is different in each facies, the probability density for petrophysical properties is multimodal and the EnKF assumption that the model parameter distribution is approximately multivariate Gaussian is not honored in this case.

Zhao et al. (2008) applied the EnKF to a facies history matching problem where the petrophysical properties in each facies were uncertain but also uniform and homogeneous, i.e., each facies is characterized by a singe value of the permeability and porosity. Because the facies properties were uniform, it was fairly straightforward to generate prior realizations of these properties by sampling a multivariate normal

distribution. The facies models they used were obtained by truncating two Gaussian random fields using two non-standard truncation maps. Sarma and Chen (2009) considered the problem of directly updating the homogenous but uncertain permeability in the facies. At each update step, the facies permeabilities were mapped to a kernel space where the Gaussian assumption is approximately honored and consistent linear updates can be made to the model parameters. They used channelized facies models generated from a multipoint geostatistical technique. Based on their approach, the discontinuity in permeability estimates were preserved in the final models but the match to production data was quite poor.

This chapter focuses on the application of the EnKF to a history matching problem where the petrophysical properties in the facies model are nonuniform, heterogeneous and uncertain such that the PDF of petrophysical properties is multimodal. We present a practical approach for updating both the facies boundaries and the multimodal properties to be consistent with the updated facies model. We then compare the performance of the proposed method with the results based on two other standard approaches. In the first approach, only the petrophysical properties are directly adjusted and in the second approach, the petrophysical are left at their initial values; only the spatial distribution of the different facies variables is adjusted. Additionally, we address a limitation of the approach to updating the facies model using proxies for the facies mismatch observations, which first appeared in Liu and Oliver (2004) and discuss modifications that make it somewhat more robust. We test our proposed approach on facies models with nonstationary proportions and evaluate the performance of the EnKF on variations in the nonstationarity of the facies proportions. All facies models presented in this paper were generated by truncating a single Gaussian field using a rectangular truncation map although our proposed approach extends straightforwardly to facies models obtained by truncating more than one Gaussian field or from using the level-sets method (Moreno et al., 2008).

4.1.1 Brief overview of the truncated Gaussian simulation

The truncated Gaussian method is a geostatistical technique for generating a conditional or unconditional realization of the reservoir facies model by truncating a single Gaussian realization whose dimension is the same as the facies model. The original application of this method was on a problem in mining engineering (Journel and Isaaks, 1984). It was first applied to a reservoir engineering problem of modelling fluvio-deltaic reservoirs by Matheron et al. (1987). As noted in Chapter 3, the values of the thresholds in the truncation map depend on the spatial proportions of each facies, P_{f_j}, which are usually assumed known. For the truncated Gaussian simulation, one only needs to evaluate,

$$s_i(\mathbf{u}) = \begin{cases} -\infty, & i = 0 \\ \Phi^{-1}\left[\sum_{j=1}^{i} P_{f_j}(\mathbf{u})\right], & 0 < i < n \\ +\infty, & i = n, \end{cases} \tag{4.1}$$

Eq. 4.1 to obtain the thresholds; where $\Phi(\cdot)$ is the standard normal cumulative distribution function, $s_i(\cdot)$ is the ith threshold and f_j is the jth facies. The proportion of f_j at any point $\mathbf{u}$ is the probability of finding f_j at that point. This is described mathematically by,

$$\begin{aligned} P_{f_j}(\mathbf{u}) &= E[1_{f_j}] = p(s_{j-1}(\mathbf{u}) \leq z(\mathbf{u}) < s_j(\mathbf{u})) \\ &= \Phi(s_j) - \Phi(s_{j-1}), \end{aligned} \tag{4.2}$$

where $p(\cdot)$ evaluates the probability of its argument. When the facies proportions are nonstationary, the values of the truncation thresholds are allowed to vary as a function of location (Eq. 4.2). In general, varying the distance between $s_{j-1}(\mathbf{u})$ and $s_j(\mathbf{u})$ also varies the probability of occurrence of facies j at location $\mathbf{u}$. As discussed in Chapter 3, the acceptance-rejection technique was used with the method of moving averages (Oliver, 1995) to generate Gaussian realizations that are truncated to obtain conditional facies models.

4.2 Joint Updating of the Facies Boundaries and Petrophysical Properties: Bayesian Formulation

At any timestep, t_k, the conditional PDF we are interested in sampling from is expressed as, $p(\mathbf{f}_k, \mathbf{m}_k|\mathbf{D}_k)$, where $\mathbf{f}_k$ and $\mathbf{m}_k$ are respectively the vectors of discrete facies variables and static model variables comprising the uncertain petrophysical properties. Define $\mathbf{D}_k = \{\mathbf{d}_{obs,k}, \ldots, \mathbf{d}_{obs,1}\}$ as a collection of measured data from time t_1 through to time t_k. From Bayes theorem, the conditional PDF at time t_k is given by,

$$p(\mathbf{f}_k, \mathbf{m}_k|\mathbf{D}_k) \propto L(\mathbf{f}_k, \mathbf{m}_k|\mathbf{d}_{obs,k})p(\mathbf{m}_k|\mathbf{f}_k, \mathbf{D}_{k-1})p(\mathbf{f}_k|\mathbf{D}_{k-1}), \tag{4.3}$$

where $p(\mathbf{m}_k|\mathbf{f}_k, \mathbf{D}_{k-1})$ and $p(\mathbf{f}_k|\mathbf{D}_{k-1})$ are respectively the prior conditional PDFs of the facies variables and petrophysical properties and $L(\mathbf{f}_k, \mathbf{m}_k|\mathbf{d}_{obs,k})$ is the joint likelihood of the facies variables and and petrophysical properties. For notational convenience, Eq. 4.3 may be rewritten as,

$$p(\mathbf{f}, \mathbf{m}|\mathbf{d}_{obs}) \propto L(\mathbf{f}, \mathbf{m}|\mathbf{d}_{obs})p(\mathbf{m}|\mathbf{f})p(\mathbf{f}), \tag{4.4}$$

where the time index in Eq. 4.4 has been suppressed for convenience. In general, the prior PDFs and the likelihood are non Gaussian leading to a non-Gaussian conditional PDF. Since manipulation of Gaussian PDFs is mathematically more tractable and the formulation of the EnKF is predicated on the assumption of prior and posterior PDFs that are approximately multivariate Gaussian, the goal is to substitute the non-Gaussian PDFs of the facies variables and petrophysical properties with alternative PDFs that are more nearly Gaussian. By using a suitably defined mapping function, the data model part of the likelihood function can be formulated such that proxies for the facies variables and petrophysical properties generated from the alternative PDFs are subsequently mapped back to domains of the discrete facies variables and multimodal facies properties for data prediction.

Recall that the truncated Gaussian/pluriGaussian technique provides a framework for obtaining a facies realization, $\mathbf{f}$, from truncating a GRF, $\mathbf{z}$, through the relationship $\mathbf{f} = \varphi(\mathbf{z})$, where $\varphi(\cdot)$ represents any suitably defined truncation scheme. One may then substitute the PDF of the facies model, $p(\mathbf{f})$, with an alternative multivariate Gaussian PDF, $p(\mathbf{z})$, of the Gaussian random vector, $\mathbf{z}$. To obtain a Gaussian proxy to the PDF $p(\mathbf{m}|\mathbf{f})$ of $\mathbf{m}$, we define a collection,

$$\mathbf{M} = \left[(\mathbf{m}^1)^T \quad \dots \quad (\mathbf{m}^j)^T \quad \dots \quad (\mathbf{m}^{n_f})^T \right]^T, \tag{4.5}$$

comprising vectors of pseudo-model variables ($\mathbf{m}^j$). Each pseudo-model vector, $\mathbf{m}^j$, in Eq. 4.5 consists of petrophysical properties belonging only to facies j and n_f defines the number of facies. The pseudo-model vector is always written with a superscript, which identifies the facies class to which it belongs. It is necessary to distinguish between the vector of pseudo-model variables ($\mathbf{m}^j \in \mathbb{R}^{n_M}$) and the vector of actual model variables ($\mathbf{m} \in \mathbb{R}^{n_M}$). $\mathbf{m}$ is the vector of multimodal petrophysical properties that correspond to the facies model $\mathbf{f}$, i.e., the petrophysical properties at any grid location $\mathbf{u}$ is determined by the facies type at the same grid location. $\mathbf{m}^j$ is a vector of petrophysical properties corresponding to facies j. Note that in this case, the petrophysical properties at all grid locations belongs to facies class j regardless of the actual distribution of the different facies classes in the model, $\mathbf{f}$. Based on the foregoing, we replace the non-Gaussian prior PDF of the petrophysical properties (alternatively, the model variables), $p(\mathbf{m}|\mathbf{f})$, with a Gaussian prior PDF of the pseudo-model variables, $p(\mathbf{M})$. Consequently, the proxy to the posterior PDF may be expressed be expressed as,

$$p(\mathbf{z}, \mathbf{M}|\mathbf{d}_{obs}) \propto p(\mathbf{d}_{obs}|\mathbf{z}, \mathbf{M}) p(\mathbf{M}|\mathbf{z}) p(\mathbf{z}), \tag{4.6}$$

For uncorrelated Gaussian measurement noise, Eq. 4.6 may be expressed explicitly

as,

$$p(\mathbf{z},\mathbf{M}|\mathbf{d}_{obs}) \propto \exp\left[-0.5\left(\|\mathbf{z}-\mathbf{z}_{pr}\|^2_{\mathbf{C}_z^{-1}} + \|\mathbf{M}-\mathbf{M}_{pr|z}\|^2_{\mathbf{C}^{-1}_{M|z}} + \|\tilde{g}(\mathbf{z},\mathbf{M})-\mathbf{d}_{obs}\|^2_{\mathbf{C}_D^{-1}}\right)\right], \tag{4.7}$$

where $\mathbf{C}_z$ and $\mathbf{C}_{M|z}$ are respectively the covariances of the GRFs and the pseudo-model variables, $\|\mathbf{A}\|^2_{\mathbf{W}}$ is a weighted norm equal to $\mathbf{A}^T\mathbf{W}\mathbf{A}$ and $\tilde{g}(\mathbf{z},\mathbf{M})$ is a nonlinear data model. Note that the subscript, $(\cdot|z)$, on the expressions for the mean and covariance of the pseudo-model variables in Eq. 4.7 illustrates the conditional dependence of the estimates of these parameters on z. For a posterior Gaussian PDF, the vector, $\mathbf{\Omega} = [\mathbf{z}^T\ \mathbf{M}^T]^T$, that maximizes the conditional PDF in Eq. 4.7 is given by,

$$\mathbf{\Omega} = \mathbf{\Omega}_{pr} - \mathbf{C}_\Omega\mathbf{G}^T\left(\mathbf{G}\mathbf{C}_\Omega\mathbf{G}^T + \mathbf{C}_D\right)^{-1}\left(\tilde{g}(\mathbf{z},\mathbf{M}) - \mathbf{d}_{obs}\right). \tag{4.8}$$

If the conditional PDF is strongly non Gaussian, then the optimal vector, $\mathbf{\Omega}$, may be obtained iteratively using Gauss-Newton with reduced step length as,

$$\mathbf{\Omega}^{l+1} = \beta_l\mathbf{\Omega}_{pr} + (1-\beta_l)\mathbf{\Omega}^l - \beta_l\mathbf{C}_\Omega\mathbf{G}_l^T\left(\mathbf{G}_l\mathbf{C}_\Omega\mathbf{G}_l^T + \mathbf{C}_D\right)^{-1}\left(\tilde{g}(\mathbf{z},\mathbf{M}) - \mathbf{d}_{obs} - \mathbf{G}_l(\mathbf{\Omega}^l - \mathbf{\Omega}_{pr})\right), \tag{4.9}$$

where $\mathbf{G}$ is the sensitivity matrix, l is the iteration index, β is the step length and $\mathbf{C}_\Omega$ is the covariance matrix for $\mathbf{\Omega}_{pr}$ with the subscript pr denoting prior. Observe that for a Gaussian PDF, using the Gauss-Newton with full step length, $\beta = 1$, gives an expression similar to Eq. 4.8.

At any data assimilation timestep, t_k, the data model, $\tilde{g}(\cdot)$ transforms the conditional estimates of $\mathbf{z}$ and $\mathbf{M}$ from the previous data assimilation timestep, t_{k-1}, to obtain realizations of the facies variables and model variables (petrophysical properties) for predicting data. The facies realization is obtained by truncating $\mathbf{z}$ and the conditional model variables ($\mathbf{m}$) are obtained straightforwardly by using a mapping given by,

$$\mathbf{m}(\mathbf{u}) = \sum_{j=1}^{n_f} 1_{f_j}(\mathbf{u})\,\mathbf{m}^j(\mathbf{u}), \tag{4.10}$$

where $\mathbf{m}(\mathbf{u})$ is the value of the actual-model variable, $\mathbf{m}$, at grid location $\mathbf{u}$; $1_{f_j}(\mathbf{u})$ is an indicator function that takes a value of 1 if facies j is present at location $\mathbf{u}$ and a value of zero otherwise; $\mathbf{m}^j(\mathbf{u})$ is the petrophysical property of the jth facies class at grid location $\mathbf{u}$. Because $\tilde{g}(\cdot)$ is nonlinear, the likelihood may be strongly non Gaussian in which case it may be necessary to iterate.

4.2.1 Assimilating facies observations

The Bayesian updating scheme of Eq. 4.6 is based on assimilating only production measurements at each timestep. When facies data are also available, the conditional PDF is given by,

$$\begin{aligned} p(\mathbf{z}, \mathbf{M}|\mathbf{f}_{obs}, \mathbf{d}_{obs}) &\propto p(\mathbf{f}_{obs}, \mathbf{d}_{obs}|\mathbf{z}, \mathbf{M})p(\mathbf{z}, \mathbf{M}) \\ &\propto p(\mathbf{f}_{obs}|\mathbf{z}, \mathbf{M})p(\mathbf{d}_{obs}|\mathbf{z}, \mathbf{M})p(\mathbf{M}, \mathbf{z}) \\ &\propto p(\mathbf{f}_{obs}|\mathbf{z})p(\mathbf{M}, \mathbf{z}|\mathbf{d}_{obs}), \end{aligned} \tag{4.11}$$

where the result follow mostly from using the property of conditional independence. Note that explicit expression for the PDF $p(\mathbf{M}, \mathbf{z}|\mathbf{d}_{obs})$ in Eq. 4.11 has been given in Eq. 4.7. $p(\mathbf{f}_{obs}|\mathbf{z})$ is equivalent to the likelihood of the GRF given the facies observations and the expression is potentially non-Gaussian. However, if we assume a Gaussian measurement error reflecting the possibility of error in modeling facies observations then the likelihood may be expressed as,

$$p(\mathbf{f}_{obs}|\mathbf{z}) \propto \exp\left[-\frac{1}{2}\|\tilde{\varphi}(\mathbf{z}) - \mathbf{f}_{obs}\|^2_{\mathbf{C}_f^{-1}}\right] = \exp\left[-\frac{1}{2}\|\tilde{\varphi}(\mathbf{z}) - \mathbf{f}_{true} - \boldsymbol{\varepsilon}_f\|^2_{\mathbf{C}_f^{-1}}\right], \tag{4.12}$$

where $\tilde{\varphi}(\mathbf{z}) = \mathbf{f}_{sim}$ is the vector of simulated facies obtained by truncating the GRF at the locations with facies observations, $\mathbf{f}_{obs}$ is the "noisy" facies observation and $\mathbf{f}_{true}$ is the true facies observation. $\boldsymbol{\varepsilon}_f \sim \mathbb{N}(0, \mathbf{C}_f)$ is the facies measurement error where $\sim \mathbb{N}(\boldsymbol{\mu}, \boldsymbol{\Sigma})$ denotes a normally distributed random variables with mean $\boldsymbol{\mu}$ and covariance $\boldsymbol{\Sigma}$. $\mathbf{C}_f$ is the diagonal covariance of facies measurement errors. In general, the possibility of error in modeling facies observations is negligibly small and the

diagonal elements of $\mathbf{C}_f$ are set to very small values. Note that this also ensures that the simulated facies at the well locations will exactly match the facies observations during optimization.

From the foregoing, the PDF for generating realizations of the GRFs conditional on the facies observations is given by,

$$p(\mathbf{z}|\mathbf{f}_{obs}) \propto \exp\left[-\frac{1}{2}\left(\|\tilde{\varphi}(\mathbf{z}) - \mathbf{f}_{obs}\|^2_{\mathbf{C}^{-1}_{D,f}} + \|\mathbf{z} - \mathbf{z}_{pr}\|^2_{\mathbf{C}^{-1}_{z}}\right)\right], \tag{4.13}$$

and the expression for the GRF that maximizes the PDF is given by,

$$\mathbf{z}_{(d_{obs},f_{obs})} = \mathbf{z}_{(d_{obs})} - \mathbf{C}_{z_{(d_{obs})}}\mathbf{G}^T\left[\mathbf{G}\mathbf{C}_{z_{(d_{obs})}}\mathbf{G}^T + \mathbf{C}_f\right]^{-1}\left(\tilde{\varphi}(\mathbf{z}) - \mathbf{f}_{obs}\right). \tag{4.14}$$

From the foregoing, the conditional facies model is obtained by truncating the conditional GRF, i.e., $\mathbf{f}_{(d_{obs},f_{obs})} = \varphi(\mathbf{z}_{(d_{obs},f_{obs})})$. The subscript (d_{obs}, f_{obs}) identifies the vector that has been conditioned to both production and facies data while the subscript (d_{obs}) identifies the vector conditioned only to production data. $\mathbf{G}$ and $\mathbf{C}_{z(d_{obs})}$ are respectively the sensitivity matrix and the covariance of the GRF.

Since facies observations and simulated facies data are nonnumeric, a meaningful representation of the facies mismatch term in Eq. 4.14 may be obtained by replacing the facies mismatch term $(\tilde{\varphi}(\mathbf{z}) - \mathbf{f}_{obs})$ by a facies mismatch proxy $(\mathbf{f}_p)$ defined previously in Eq. 3.1. Consequently, Eq. 4.14 reduces to,

$$\mathbf{z}_{(d_{obs},f_{obs})} = \mathbf{z}_{(d_{obs})} - \mathbf{C}_{z_{(d_{obs})}}\mathbf{G}^T\left[\mathbf{G}\mathbf{C}_{z_{(d_{obs})}}\mathbf{G}^T + \mathbf{C}_f\right]^{-1}\mathbf{f}_p. \tag{4.15}$$

Evaluating $\mathbf{G}$ in Eq. 4.15 is nontrivial as $\mathbf{f}_p$ is not differentiable. Consequently using a gradient-based optimization technique is mathematically intractable unless an approximation to the facies proxy can be derived that is at least C^1 continuous. By contrast, Eq. 4.15 can be evaluated fairly easily using EnKF as the analytically intractable terms, $\mathbf{C}_{z(d_{obs})}\mathbf{G}^T$ and $\mathbf{G}\mathbf{C}_{z(d_{obs})}\mathbf{G}^T$, are approximated from the ensemble without requiring explicit computation of the gradient.

4.3 Framework for EnKF Applied to Facies with Nonuniform and Heterogenous Petrophysical Properties

Following the formulation discussed in section 4.2, an arbitrary state vector, y_j, is given by,

$$y_j = \begin{bmatrix} \mathbf{z}^T & \mathbf{M}^T & \mathbf{S}^T & \mathbf{P}^T \end{bmatrix}_j^T, \tag{4.16}$$

where $\mathbf{P}$ and $\mathbf{S}$ are respectively the vectors of gridblock pressures and saturations. For our purpose in this chapter, the vectors of pseudo-model variables, $\mathbf{M}$, in Eq. 4.16 are defined explicitly as,

$$\mathbf{M} = \begin{bmatrix} \ln \mathbf{k}_1^T & \dots & \ln \mathbf{k}_{n_f}^T & \boldsymbol{\phi}_1^T & \dots & \boldsymbol{\phi}_{n_f}^T \end{bmatrix}^T, \tag{4.17}$$

where $\mathbf{k}_i$ and $\boldsymbol{\phi}_i$ are respectively the vectors of permeability and porosity belonging to facies i. From the state vector formulation of Eq. 4.16, the EnKF update step is essentially carried out the standard way. Figure 4.1 illustrates the basic idea behind the joint updating of the facies variables and multimodal petrophysical properties using EnKF.

In our current implementation, since the data model $\tilde{g}(\mathbf{z}, \mathbf{M})$ may be strongly nonlinear at some data assimilation timesteps, the maximum absolute change to the saturation field at each update step is monitored and if it exceeds a predefined threshold, an iterative form of the ensemble Kalman filter is implemented. The choice of a threshold value to use is generally subjective but if it is set too low or too high then one either has to iterate at every step (which is computationally very expensive depending on the size of the problem) or not iterate at all even in the presence of significant nonlinearity. For our purpose, a threshold of 0.25 was used at the first four data assimilation timesteps and then 0.3 for the remaining data assimilation timesteps. The iterative EnKF of Gu and Oliver (2007), the ensemble randomized maximum likelihood (EnRML) filter, is implemented whenever iteration is required.

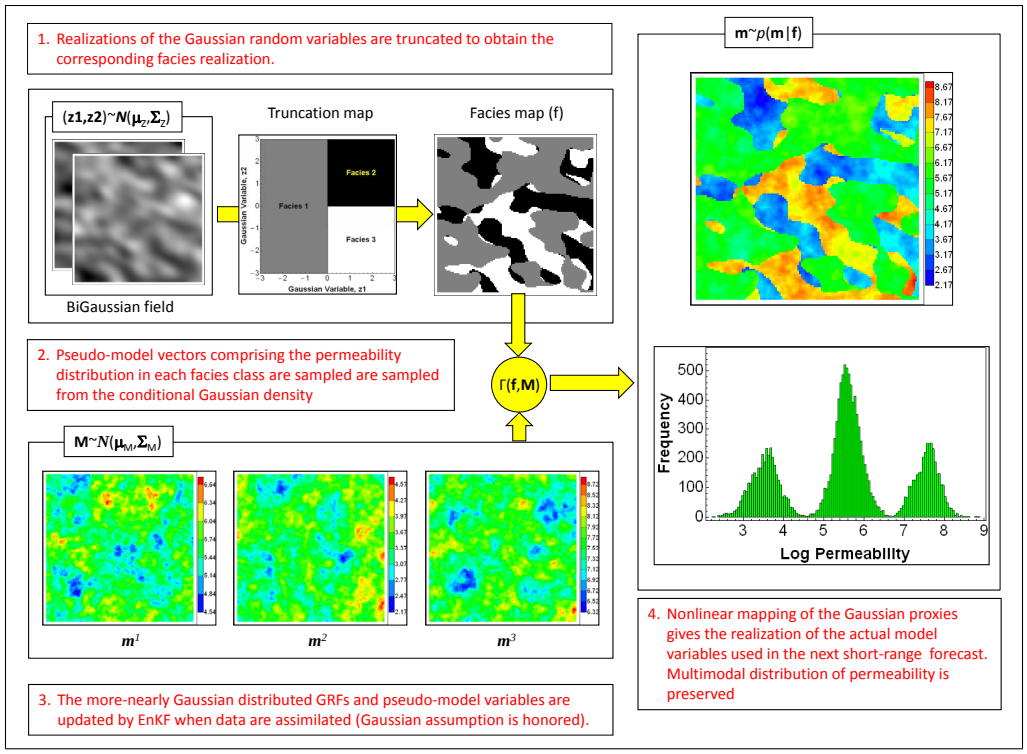

Figure 4.1: Joint updating of facies and petrophysical properties using EnKF.

Unlike a gradient-based optimization approach requiring explicit computation of the local sensitivity to obtain the conditional model (Eqs. 4.8 and 4.9) the EnKF technique updates the state vectors using a single global average estimate of the model–data correlation; alternatively the EnRML uses a global average sensitivity. The advantage of updating the pseudo-model variables using a global average sensitivity stems from the observation that the update to each pseudo-model variable is based potentially on two sources of information namely:

1. Local sensitivity and the spatial correlation between the model variables in each pseudo-model vector such that members of the pseudo-model vector that are not present in the simulation model (i.e., in the null space of the local sensitivity, $\mathbf{G}$) are also updated based on correlation with model variables whose sensitivities are nonzero (Fig. 4.2).

2. Global averaging feature of the EnKF "sensitivity matrix". Due to the uncertainty in the spatial distribution of the facies, it is reasonable to expect that at any grid location, **u**, not conditioned to facies observation, all the facies classes present in the model may be found in the ensemble of facies classes at **u**. Consequently, the state vectors will provide information on local sensitivities of the pseudo-model variables at location **u** corresponding to the different facies classes. Each local sensitivity information is averaged over the sub-ensemble with similar facies class to obtain a suite of average sensitivities to the different pseudo-model variables corresponding to the different facies classes. As a result all the pseudo-model variables are potentially updated at each data assimilation timestep using the global average sensitivities from the sub-ensembles.

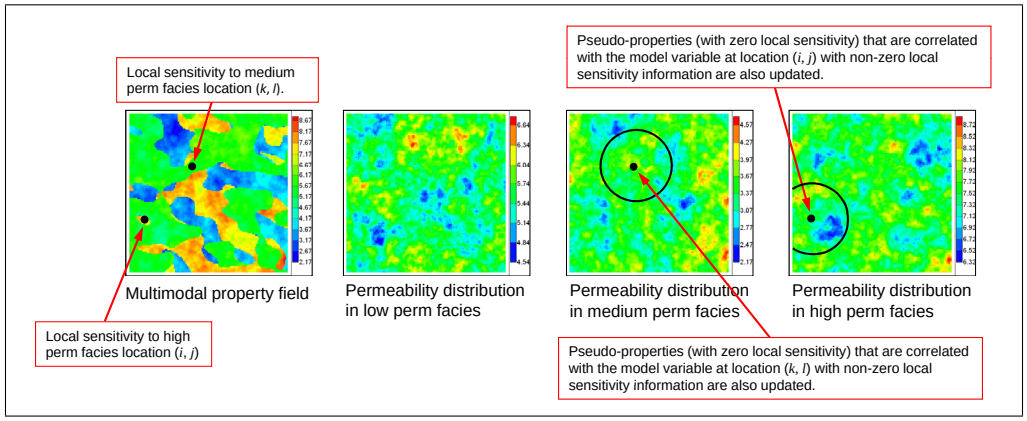

Figure 4.2: Updating of pseudo-properties with zero sensitivity using model correlation. The black circles are regions correlated with model variables having nonzero sensitivities.

As discussed in section 3.4 after assimilating production data, it may be necessary to also assimilate well facies data to obtain Gaussian variables that are in the correct intervals of the corresponding well facies. In what follows, we extend the iterative re-enforcement scheme reported in Liu and Oliver (2005b) and Agbalaka and Oliver (2008) by proposing a solution to the problem where the solution can potentially get stuck in a local minimum during the iterative enforcement of the constraints on facies

mismatch observations. To this end, recall (Eq. 3.5) that the expression for iteratively enforcing these constraints is given by,

$$\begin{aligned} \mathbf{z}^{l+1} &= \mathbf{z}^{l} - \mathbf{K}_f^l \mathbf{f}_p^l \\ &= \mathbf{z}^{l} - \mathbf{C}_{zF}^l (\mathbf{C}_{FF}^l + \mathbf{C}_f)^{-1} \mathbf{f}_p^l, \end{aligned} \tag{4.18}$$

where $\mathbf{K}_f$ is the Kalman gain, $\mathbf{C}_{zF}$ and $\mathbf{C}_{FF}$ are respectively the cross-covariance between the GRFs and the facies mismatch proxy and covariance of the facies mismatch proxy. As noted earlier (Eq. 4.12), $\mathbf{C}_f$ is a diagonal covariance matrix of measurement noise in facies data. A value of 10^{-4} is used throughout for the diagonal elements of $\mathbf{C}_f$. Our choice of $\sigma_f^2 = 10^{-4}$ is ad hoc and was chosen simply because it satisfies the requirement that the value of the noise variance be small enough to ensure an exact match of the facies data. Additionally, because the diagonal elements of $\mathbf{C}_f$ are nonzero, adding $\mathbf{C}_f$ to the potentially singular matrix $\mathbf{C}_{FF}$ in Eq. 4.18 ensures that the inverse can be evaluated. Note that we do not add stochastic errors to the facies observations so this is different from a seemingly similar procedure discussed in Jazwinski (1970, pp. 301–307) where the noise covariance of a dynamical system is inflated and then added to the error covariance matrix of the dynamical system to prevent filter divergence.

The expression for the Kalman gain, $\mathbf{K}_f$, in Eq. 4.18 is an ensemble approximation of the term,

$$\mathbf{C}_{z_{(d_{obs})}} \mathbf{G}^T \left[\mathbf{G} \mathbf{C}_{z_{(d_{obs})}} \mathbf{G}^T + \mathbf{C}_f \right]^{-1}, \tag{4.19}$$

in Eq. 4.14. Because the EnKF approximately linearizes the problem over a broad range of model variables, it is less likely to get stuck in local minima unlike a gradient-based approach. However, since the facies mismatch proxies are assimilated at this stage, the solution may sometimes get stuck in a local "minimum" particularly if all the ensemble members have simulated facies that do not match the facies observation at a specific well location. To illustrate, suppose that the ensemble of simulated facies at the kth observation location do not match the corresponding facies observation,

i.e., the facies mismatch proxy, $f_{p,j}(k) = 1$, $\forall j : 1 \leq j \leq n_e$, where $f_{p,j}(k)$ denotes the facies mismatch proxy of the jth ensemble at the kth well location. The mean of all the facies mismatch proxy at the kth, well location will be $\overline{f}_p(k) = 1$ and the residual term $f_{p,j}(k) - \overline{f}_p(k) = 0$ will be zero for all the ensemble members. It then follows that irrespective of how many times one iterates using Eq. 4.18, it is impossible to update the ensemble of Gaussian random fields to obtain values of the Gaussian variables in the correct intervals corresponding to the observed facies at the kth location. To overcome this restriction, we propose the addition of small perturbations to the ensemble of facies mismatch proxies. These perturbations are unconditional realizations of the pseudo-noise in the facies data, i.e., random samples from the Gaussian distribution, $\mathcal{N}(0, \sigma_f^2)$. Define $\xi_j \sim \mathcal{N}(0, \sigma_f^2)$ as the jth random perturbation added to $f_{p,j}(k)$ and let $\overline{\xi}$ be the mean perturbation obtained by averaging over the n_e realizations of ξ_j. Then $(f_{p,j}(k) + \xi_j) - (\overline{f}_p(k) + \overline{\xi}) = \xi_j - \overline{\xi}$ represents the perturbed residual term that reintroduces variability to the ensemble. Using this technique, constraints to facies mismatch observation were re-constrained in less than 3 iterations whenever all ensemble members have mismatched facies at a specific well location.

When the GRF that parameterizes the facies are updated using Eq. 4.18, care must be taken to ensure that only parameters in localized regions with valid correlation to the facies observations are adjusted. Agbalaka and Oliver (2008) defined a localized region of influence through a Hadamard product of the Gaspari-Cohn correlation function with the Kalman gain. In this work we utilized the distance dependent localization function of Furrer and Bengtsson (2007) given by,

$$\rho(h) = \frac{C(h)^2 n_e}{C(h)^2 n_e + C(h)^2 + C(0)^2} \tag{4.20}$$

where $C(\cdot)$ is any valid covariance function and h is the separation distance. The spherical covariance function was used in this work and the localization range was set at a value slightly larger than the maximum range of the Gaussian random field. This ensured that regions with valid correlation to the Gaussian variables at the well

locations are also updated when facies data are assimilated.

An ensemble size of 100 was used in all the examples discussed in this chapter.

4.3.1 Algorithm for updating multimodal facies properties using EnKF

The basic steps for implementing our proposed approach is as follows:

1. Generate the initial ensemble of state vectors comprising

   - realizations of Gaussian random fields ($\mathbf{z}$) and
   - realizations of pseudo-model variables ($\ln k$ and ϕ).

2. Truncate the ensemble of Gaussian random fields to obtain the corresponding ensemble of facies maps. Conditional on the facies maps, generate n_e realizations of the actual (multimodal) model variables, $\mathbf{m}$, from the ensemble of pseudo-models using Eq. 4.10.

3. Run the reservoir simulator to the next data assimilation timestep for the n_e realizations of $\mathbf{m}$.

4. Update the ensemble of state vectors using the EnKF standard update equation .

5. Check whether the assumption of linearity has been violated. If the linear assumption is still valid, go to step 6 else

   (a) Include only $\mathbf{M}$ and $\mathbf{z}$ in the state vector and iteratively update the state vector using the EnRML filter.

   (b) At the end of each EnRML iteration ensure that the facies observations are honored at the well locations as described in step 6.

6. Check the simulated facies at the well locations in all the ensemble members. If some or all the realizations have well facies that do not match the facies

observations, iteratively update the Gaussian random fields using Eq. 4.18 until all facies observations are matched by the ensemble of simulated facies data.

7. If there are still data available for assimilation, go back to 2 else stop.

4.4 Reservoir Model Description

The reservoir model is a 1500 ft × 1500 ft × 60 ft, 3-layer model with only two phases (oil and water) present. Each gridblock has a dimension of 30 ft × 30 ft × 20 ft and all the grid blocks are active. There are 4 producers and 1 injector arranged in a 5-spot waterflooding pattern with perforations in all three layers. The injector is controlled primarily by a maximum surface injection rate with a secondary constraint on the maximum bottomhole pressure. All the producers flow at the same constant flowing bottomhole pressure. The gridblock locations of the wells in the model are presented in Table 4.1.

Table 4.1: Grid coordinates of the well locations in the simulation model.

Coordinate	Injector	Producer 1	Producer 2	Producer 3	Producer 4
x	25	9	9	41	41
y	25	5	45	45	5

Three different types of geologic facies identified as high permeability sand (Facies 1 or F1), medium permeability sand (Facies 2 or F2) and low permeability sand (Facies 3 or F3) are present in all the layers. In all the facies maps, Facies 1 corresponds to the dark gray shade, Facies 2 to the light gray shade and Facies 3 to the white shade. There are 15 facies observations with 3 observations from each well. The well positions are indicated by black dots on facies maps. The distribution of the petrophysical properties in each facies differ markedly for different facies. The permeability is log-normally distributed and the porosity is normally distributed. The vertical permeability is taken to be 20% of the horizontal permeability.

Production was for 400 days and data were assimilated every 20 days for 220 days.

The remaining days in which production data were assimilated were used to assess the predictive performance of the history matched models. Water injection started from the first day of production and lasted through the period of production. The wells with water breakthrough information during the data assimilation period were producers 3 and 4 for Examples 1 and 2 and producers 1, 2 and 4 for Example 3. At each data assimilation timestep, 9 production data were assimilated and included the bottomhole pressure (p_{bh}) from the injector, water production rates (q_w) from the four producers, and total liquid production rates (q_L) also from the four producers. The facies data were assimilated whenever it is necessary to enforce the constraint on facies mismatch observation after assimilating production data. Note that the oil-water relative permeability curves shown in Fig. 3.5 were also used in all the reservoir simulation models presented in this chapter.

4.5 Description of Experiments

Unconditional realizations of pseudo-properties ($\ln k$ and ϕ) in each facies class were generated using the sequential Gaussian simulation technique (Deutsch and Journel, 1998). An exponential variogram model was used and the variogram parameters were assumed known. Values of the first two statistical moments characterizing the distributions of the porosity and $\ln k$ for different facies are given in Table 4.2. The performance of the proposed approach for joint updating of the pseudo-properties and facies variables was tested on three synthetic problems designed with different features of nonstationarity.

Table 4.2: Mean and standard deviation of $\ln k$ and ϕ for generating the pseudo-properties in each facies class.

	Permeability ($\ln k$)		Porosity (ϕ)	
	μ_k	σ_k	μ_ϕ	σ_ϕ
Facies1	7.60	0.30	0.330	0.01
Facies2	5.86	0.30	0.230	0.01
Facies3	4.32	0.35	0.110	0.01

4.5.1 Example 1 description: Facies model with horizontal nonstationarity

Nonstationarity is generally characterized by significant lateral change in facies proportions in the reservoir within the area of interest. In truncated Gaussian simulation, this is handled by using different proportions curves for different areas of the reservoir model. Since the thresholds (Eq. 4.1) depend on the facies proportions, these too will vary as a function of location. In Example 1, the nonstationarity in the facies proportions is principally in the horizontal direction and the same proportions map was used to compute the thresholds (Eq. 4.1) in all 3 layers. For generating realizations of the facies models in Example 1, the trend in the facies proportions is assumed to be primarily in the x-direction and a cross-section of the trend is shown in Fig. 4.3. The directions of maximum and minimum continuity of the facies are respectively in the NS- and EW-directions and the Gaussian field for truncation was generated with a fairly long correlation length (about 20 gridblock sizes) in the NS-direction with an anisotropic ratio of 2. The Gaussian random variables in the three layers of the model are assumed to be vertically uncorrelated. The facies observations at the well locations are the same in all layers and are presented in Table 4.3.

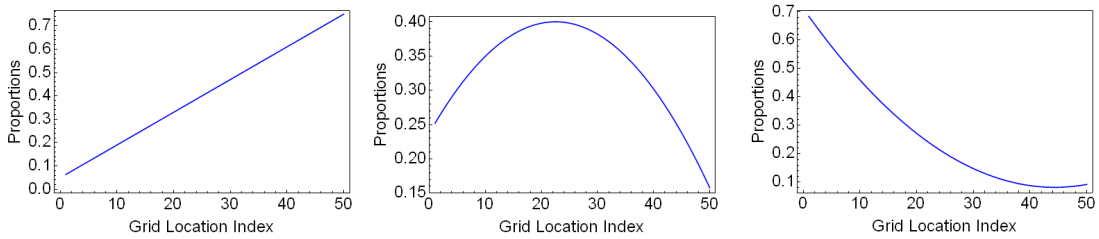

(a) Facies 1 Proportions (b) Facies 2 Proportions (c) Facies 3 Proportions

Figure 4.3: Cross section of the trends in facies proportions for Example 1.

Table 4.3: Facies observations at the well locations for all three layers in the reservoir model for Examples 1 and 2.

Injector	Producer 1	Producer 2	Producer 3	Producer 4
facies 2	facies 3	facies 3	facies 1	facies 1

The reference facies permeability maps for this example are given in Fig. 4.4. Note that the distribution of $\ln k$ in these maps are discontinuous at the boundaries of the different facies types. In general, the warmer colors in each $\ln k$ correspond to high values of permeability. The histograms of the $\ln k$ maps from Fig. 4.4 are presented in Fig. 4.4.

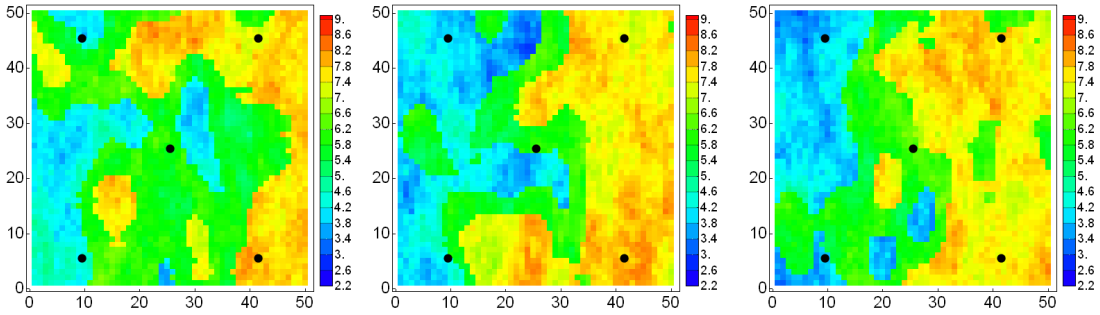

(a) Layer 1 (b) Layer 2 (c) Layer 3

Figure 4.4: Reference $\ln k$ maps examples 1 and 2 showing the well locations as black circles.

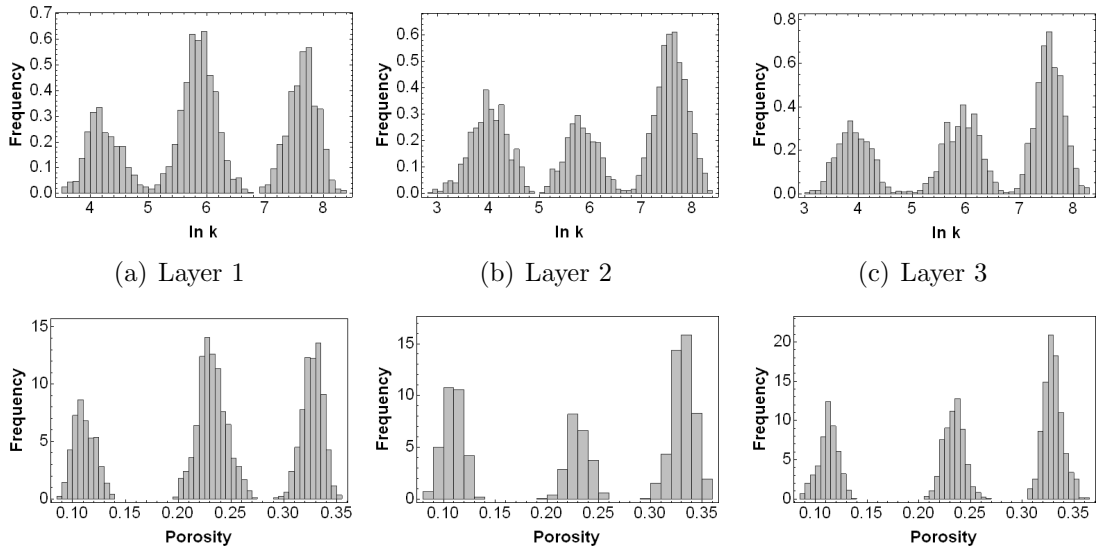

(a) Layer 1 (b) Layer 2 (c) Layer 3

(d) Layer 1 (e) Layer 2 (f) Layer 3

Figure 4.5: Reference $\ln k$ and ϕ histogram for examples 1 and 2. The distribution of the petrophysical properties in each layer is clearly multimodal.

4.5.2 Example 2 description: Impact of incorrect stationarity assumption

The second example examines the history match performance of the EnKF where the realizations are generated with the wrong assumption of horizontal stationarity when the reservoir unit (reference model) is laterally nonstationary. ssentially we attempt to answer the following question: "Given that the reservoir unit of interest is a realization from a nonstationary facies transition model, what is the effect on history matching results if a stationary facies transition model is used for truncating the GRFs to obtain the facies maps during history matching? This is a problem of practical importance because, geological phenomena always have some degree of nonstationarity and depending on the scale of investigation, the choice between stationary vs. nonstationary models becomes subjective (Armstrong et al., 2003). The reference model for this example is the same as Example 1 (Figs. 4.4 and 4.5). Realizations of the facies model for Example 2 were generated by truncating a Gaussian field using thresholds computed by assuming that the facies proportions are equal (≈ 0.33) and the same at all grid locations. The initial facies realizations were conditioned on well facies observations and the geostatistical parameters are the same as the reference model. Figure 4.6 shows a randomly selected realization of the facies model generated based on the stationarity assumption. The permeability and porosity in this example were also nonuniform and heterogeneous.

4.5.3 Example 3 description: Facies model with horizontal and vertical nonstationarity

The third and final example investigates the history matching performance of the proposed joint-updating approach for the case where the facies proportions are laterally and vertically nonstationary. The initial facies realizations were generated conditional on the well facies observations in Table 4.4 and the reference facies maps are shown in Fig. 4.7.

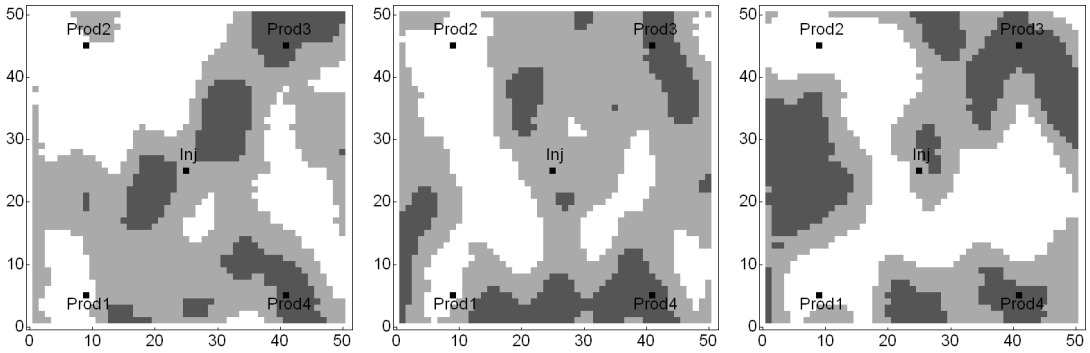

(a) Layer 1 (b) Layer 2 (c) Layer 3

Figure 4.6: Initial facies field for a randomly selected realization from Example 2. Facies proportions are assumed stationary.

Table 4.4: Well facies for Example 3

Layer	Injector	Producer 1	Producer 2	Producer 3	Producer 4
1	facies 2	facies 3	facies 3	facies 1	facies 1
2	facies 2	facies 1	facies 2	facies 3	facies 2
3	facies 2	facies 2	facies 1	facies 2	facies 3

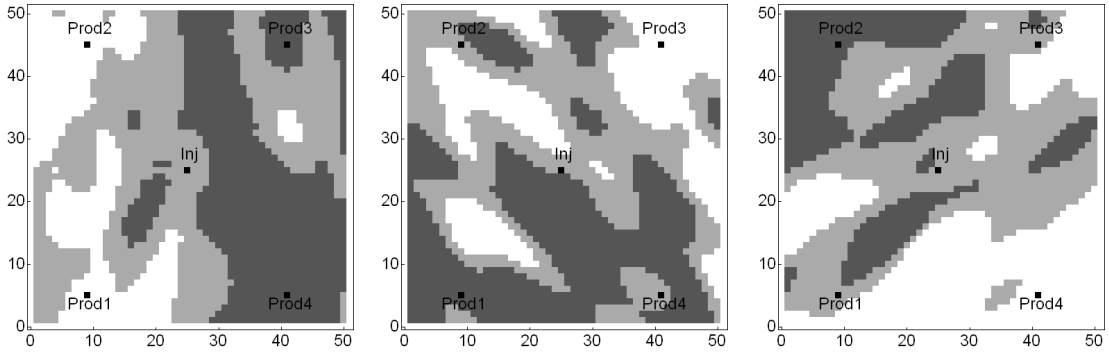

(a) Layer 1 (b) Layer 2 (c) Layer 3

Figure 4.7: Facies distribution in the reference model for Example 3.

4.6 Results and Discussions

In this section we evaluate the performance of the proposed approach for joint estimation of the facies variables and the petrophysical properties of the facies on the three history matching problems discussed in the preceding section. We also compare the performance of our proposed approach with those from two alternative implementations of the ensemble Kalman filter for which (1) only the multimodal petrophysical properties ($\ln k$ and ϕ) are adjusted directly; and (2) only the facies variables (more specifically, the GRFs that parameterize the transformed facies variables) are adjusted. Although both alternative approaches were tested on the two examples discussed earlier, we only present and analyze results of their performance for Example 1 as similar conclusions hold for Example 2. For convenience, the approach based on adjusting only the petrophysical properties directly will be referred to as the properties-only approach and the approach based on adjusting only the GRFs that parameterize the transformed facies as the facies-only approach. Our proposed implementation for joint updating of the facies variables and petrophysical properties will be referred to as the pseudo-properties approach.

4.6.1 Results for Example 1

The predicted injector p_{bh} data and producers' q_L data from the initial and final ensembles are presented in Fig. 4.8. At each each timestep with production measurement, a box-and-whisker plot of the ensemble prediction is shown. The base and top of each box in the box-and-whisker plot correspond respectively the P10 and P90 values of the predicted data. The horizontal line through the middle of each box in the box-and-whisker plot is the P50 value. Outliers are indicated by asterisks and represent data values that are ≥ 1.5 times the interquantile range from the edge of the box. The vertical line in the each plot in Fig. 4.8 demarcates the end of the history matching period. The initial uncertainty in the estimate of the model

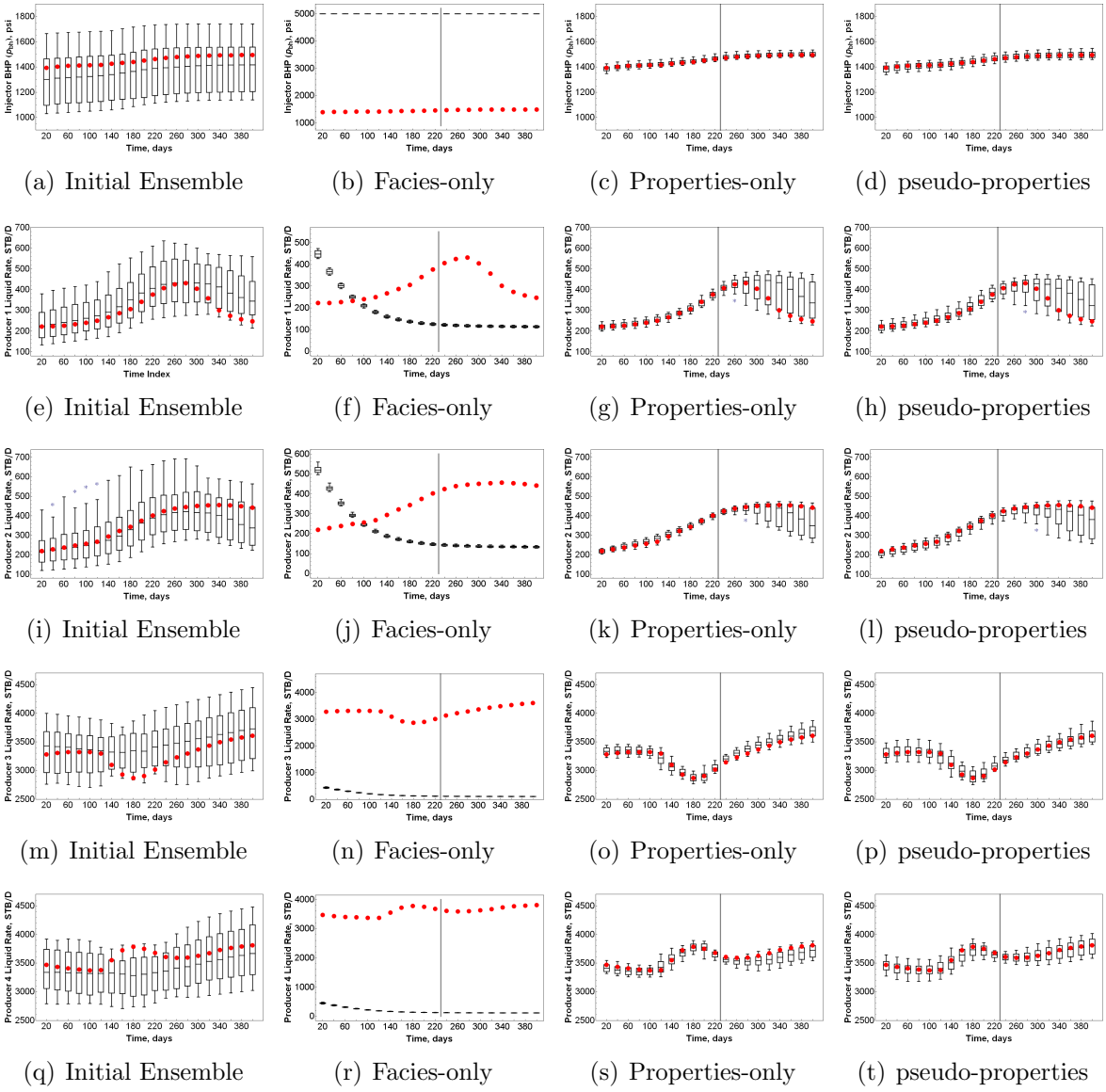

(a) Initial Ensemble (b) Facies-only (c) Properties-only (d) pseudo-properties

(e) Initial Ensemble (f) Facies-only (g) Properties-only (h) pseudo-properties

(i) Initial Ensemble (j) Facies-only (k) Properties-only (l) pseudo-properties

(m) Initial Ensemble (n) Facies-only (o) Properties-only (p) pseudo-properties

(q) Initial Ensemble (r) Facies-only (s) Properties-only (t) pseudo-properties

Figure 4.8: Prediction of Injector BHP (top row) and liquid rate data from the four producers (last four rows) from initial and final models for Example 1. Vertical line demarcates the end of history matching period. Filled circles are production measurements. The box-and-whisker plots are ensemble predictions. The filter diverged for the facies-only approach (column 2) and the best matches to data were from the properties-only approach (column 3) and the pseudo-properties approach (column 4).

parameters shows as a substantial spread in predicted data (column 1 of Fig. 4.8). The prediction result from the facies-only approach (column 2 of Fig. 4.8) shows that merely adjusting the facies boundaries in this case results in complete loss of ensemble variability leading to filter divergence, resulting in negligible prediction spread and very poor match to production measurement. Filter divergence refers to the situation where data are ignored during data assimilation due to loss of ensemble variability leading to unrealistically high confidence in the model estimates each time data are assimilated and too low weight on the assimilated data. Because only the facies boundaries were adjusted at each timestep in this case, very large compensatory updates were made to the Gaussian variables that parameterize the transformed facies variables leading to rapid collapse of the ensemble variance. From the foregoing, accounting for the uncertainty in the estimates of the gridblock permeabilities and porosities may be necessary for improving the predictability from the final models. This is supported by the improvement in history matching results for the approaches based on either adjusting only the petrophysical properties (column 3 of Fig. 4.8) or explicitly updating both the petrophysical properties and facies boundaries (column 4 of Fig. 4.8). Both methods resulted in appreciable reduction in initial prediction uncertainty. Additionally their capability in predicting "future" performance (right of the vertical line) appears reasonable as the production measurements are contained within the spread of the predicted and the ensemble prediction seems to match the reference prediction quite well.

Quantitatively, the performance of the different approaches may be compared by evaluating the root mean square deviation (equivalently, root mean square error, RMSE) of the ensemble of predicted data from the measured data. We expect that for mild departure from the assumptions of linearity and Gaussianity in the EnKF, the magnitude of the RMSE should be about the same as the standard error of measurement. The standard errors of measurements used in the examples were 10

psi for injector p_{bh} and 10 STB/D for both water and liquid rates. Before water breakthrough, a standard error of measurement of 0.001 STB/D was used for the water rate data. Table 4.5 shows the average RMSE taken over the history matching period of 220 days. For comparison, the standard errors of measurement for the different production data are presented in Row 1 of Table 4.5.

Table 4.5: Average RMSE of predicted data for the history matching period in Example 1. Actual refers to the standard error of measurement.

	Injector (psi)	Prod1 (STB/D)		Prod2 (STB/D)		Prod3 (STB/D)		Prod4 (STB/D)	
	p_{bh}	q_L	q_w	q_L	q_w	q_L	q_w	q_L	q_w
1. Actual	10	10	0.001	10	0.001	10	10	10	10
2. Initial model	155	68	0.03	66	0.50	343	217	353	238
3. Facies-only	3576	131	0.020	150	0.020	2927	361	3311	60
4. Pseudo-properties	17	16	0.002	14	0.002	78	65	76	64
5. Properties-only	12	10	0.002	11	0.002	62	37	63	24

Row 2 in Table 4.5 shows that the average RMSE values from the initial ensemble are much higher than corresponding values from the pseudo-properties (Row 4) and the properties-only (Row 5) approaches respectively. For the properties-only and pseudo-properties approaches, the average RMSE of the p_{bh} data from the injector and the rates data from producers 1 and 2 are about the same as the standard error of measurement. However, the average RMSE for the predicted liquid and water rate data from producers 3 and 4 are somewhat higher than the indicated by measurement error. The facies-only approach had the worst match to data and in general the RMSE values from the final ensemble in this case (Row 3) are significantly higher than those from the initial ensemble and the final ensembles from the properties-only and pseudo-properties approaches respectively.

It is apparent from Table 4.5 that the average RMS prediction errors from the properties-only approach are lower than those from the pseudo-properties approach. To test if the predictive performance of the properties-only is significantly different from that of the pseudo-properties approach we utilized the modified Levene's

test (Levene, 1960) popularly referred to as the Brown–Forsythe test on equality of variances (Brown and Forsythe, 1974). This test is known to be fairly robust to non-Gaussian distributions. The null hypothesis (H_0) is that the observed variability in prediction errors from the properties-only and pseudo-properties approaches are due to random variations, i.e., the data mismatch are not significantly different. The Brown–Forsythe test statistic, W, is defined as,

$$W = \frac{N-k}{k-1} \frac{\sum_{i=1}^{k} N_i (\overline{Z}_i - \overline{Z})^2}{\sum_{i=1}^{k} \sum_{j=1}^{N_i} (Z_{ij} - \overline{Z}_i)^2}, \tag{4.21}$$

where k is the number of methods being compared and is equal to 2 in this case, N is the total number of (data mismatch) samples, N_i is the number of samples from the ith method. $Z_{ij} = \Delta D_{ij} - \widetilde{\Delta D}_i$ with ΔD_{ij} as the jth data mismatch in the ith group and $\widetilde{\Delta D}_i$ as the median data mismatch in the ith group. $\overline{Z}$ is the mean of all Z_{ij} and $\overline{Z}_i$ is the mean of Z_{ij} from the ith group. The Brown-Forsythe test rejects the hypothesis that the variances of the data mismatch from both methods are equal if $W > F_{\alpha,k-1,N-k}$; where $F_{\alpha,k-1,N-k}$ is the upper critical value of the F distribution with $k-1$ and $N-k$ degrees of freedom given a significance level of α.The test result showed that (in the absence of additional information) at 5% level of significance there is enough evidence to conclude that the variability in the data mismatch from both approaches are significantly different. Consequently, the alternative hypothesis is accepted and the properties–only approach is general better in matching production data than the pseudo-properties approach.

Table 4.6 shows the within-ensemble spread of the predicted data from the initial and final models for the history matched period. The spread in production data is generally a measure of the diversity in flow behavior. The prediction spread of the initial ensemble (Row 1 in Table 4.6) is very high reflecting the presence of significant diversity in the ensemble of initial model variables due uncertainty in the prior estimates of the model parameters. Compared to the initial models, the prediction spread of the pseudo-properties and properties-only approaches are significantly

smaller. Also, the prediction spread from the pseudo-properties approach is generally higher than the prediction spread from the properties-only approach. Relative to the magnitude of the average RMSE of predicted data for the facies-only (Row 3, Table 4.5), the prediction spread in this case is too low. Note that the very low spread for the predicted q_W data for producers 1 and 2 from the properties-only and pseudo-properties approaches reflects the absence of water breakthrough data in these wells.

Table 4.6: Spread in predicted data from the history matched period for Example 1.

	Injector (psi)	Prod1 (STB/D)		Prod2 (STB/D)		Prod3 (STB/D)		Prod4 (STB/D)	
	p_{bh}	q_L	q_w	q_L	q_w	q_L	q_w	q_L	q_w
1. Initial model	128	61	0.02	66	0.50	240	168	243	144
2. Facies-only	0	5	0.0007	5	0.0008	6	0	5	0
3. Pseudo-properties	16	13	0.002	12	0.002	68	52	68	41
4. Properties-only	11	9	0.001	8	0.001	50	32	50	23

The within-ensemble spread of the predicted data for the "future period" (period after history matching) is presented in Table 4.7. It is evident that while the spread in the history matched models from the pseudo-properties (Row 3) and properties-only (Row 4) approaches are much lower than the prediction spread in the initial models, they are in general higher than similar prediction spread from the history matched period (Table 4.6). The spread of injector p_{bh} data from both approaches and Producer 3 q_L data from the properties-only approach appears to be similar for the periods before and after history matching. The future prediction results from the pseudo-properties and properties-only approaches show that there is still a great deal of diversity in the ensemble of final models. The future prediction spread for the facies-only approach (Row 2) is very low as a result of the collapse in ensemble variability during data assimilation and there is very little diversity in the final ensemble.

Table 4.7: Spread in the predicted "future" data for Example 1.

	Injector (psi)	Prod1 (STB/D)		Prod2 (STB/D)		Prod3 (STB/D)		Prod4 (STB/D)	
	p_{bh}	q_L	q_w	q_L	q_w	q_L	q_w	q_L	q_w
Initial model	127	71	14	77	22	298	408	288	357
Pseudo-properties	15	46	12	34	6	60	97	72	163
Properties-only	11	47	13	31	7	50	73	60	143

4.6.2 Assessing the geologic plausibility of the history matched models

Figure 4.9 shows two randomly selected realizations of the initial and final $\ln k$ maps. We observe that some features from the initial model are clearly present in some of the final models (see bottom row of Fig. 4.9 where a patch of high permeability facies centered at grid location (12,20) is evident in the final models from the properties-only and pseudo-properties approaches). Similarly, new features from assimilating production data are also present in the final maps (an obvious example is the high permeability sand body in Fig. 4.9(d), running vertically from the top to the middle of the map). The two history matched realizations from the facies-only approach (second column) are very different from the initial maps and appear to have petrophysical property distribution from predominantly two facies types: the high permeability facies and the low permeability facies. The petrophysical property distribution from the medium permeability facies is clearly not present. Also the predicted facies at the well locations are generally incorrect and do not match the facies observations. Clearly, both realizations from the facies-only approach are not geologically plausible realizations. The final $\ln k$ maps obtained by adjusting only the petrophysical properties of the different facies (third column in Fig. 4.9) appear to be much smoother than the initial maps and perhaps too smooth for realizations from a facies model. The final $\ln k$ maps from the properties-only approach are not nearly as discontinuous as one would have expected for properties maps from a facies model. The $\ln k$ maps from the pseudo-properties approach are clearly discontinuous (column 4 in Fig. 4.9) and are consistent with properties from an underlying facies map.

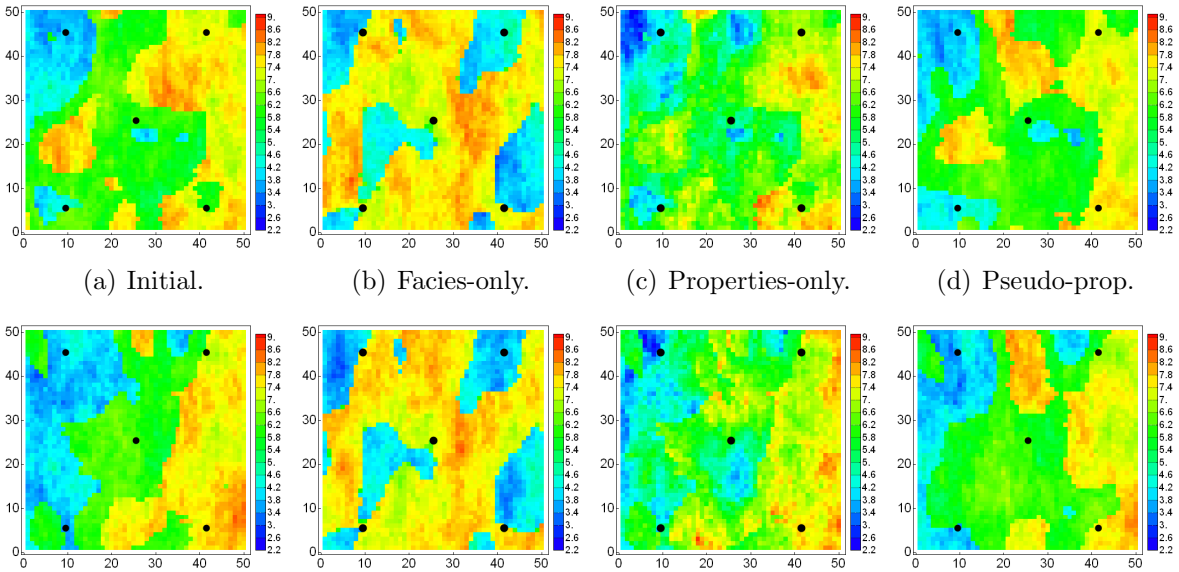

(a) Initial. (b) Facies-only. (c) Properties-only. (d) Pseudo-prop.

(e) Initial. (f) Facies-only. (g) Properties-only. (h) Pseudo-prop.

Figure 4.9: Random realizations of Layer 2 $\ln k$ maps from initial and final ensembles for Example 1. Back circles are well locations. The final $\ln k$ maps from the facies-only approach (column 2) are from only two facies classes (in contrast with three classes in the initial model (column 1)) and are thus geologically implausible. $\ln k$ maps from the properties-only approach (column 3) are too smooth for properties from a facies model. The $\ln k$ maps from the pseudo-properties approach are consistent with properties from a facies model.

Figure 4.10 shows the global histograms of the initial and final distributions of the petrophysical properties in Layer 2 of the facies model obtained from all n_e realizations. Judging by the trimodality of the initial histograms (Figs. 4.10(a) and 4.10(e)) and the final histograms from the pseudo-properties approach (Figs. 4.10(d) and 4.10(h)) it appears, at least qualitatively, that the respective realizations from each group (initial and pseudo-properties) might have come from the same parent distribution as the reference model (Figs. 4.5(b) and 4.5(e)). Conversely, the histograms of final $\ln k$ and ϕ realizations from the facies-only (Figs. 4.10(b) and 4.10(f)) and properties-only (Figs. 4.10(c) and 4.10(g)) approaches seem to be samples from parent population distributions that are respectively bimodal and unimodal. Both histograms are qualitatively very different from the initial and reference histograms.

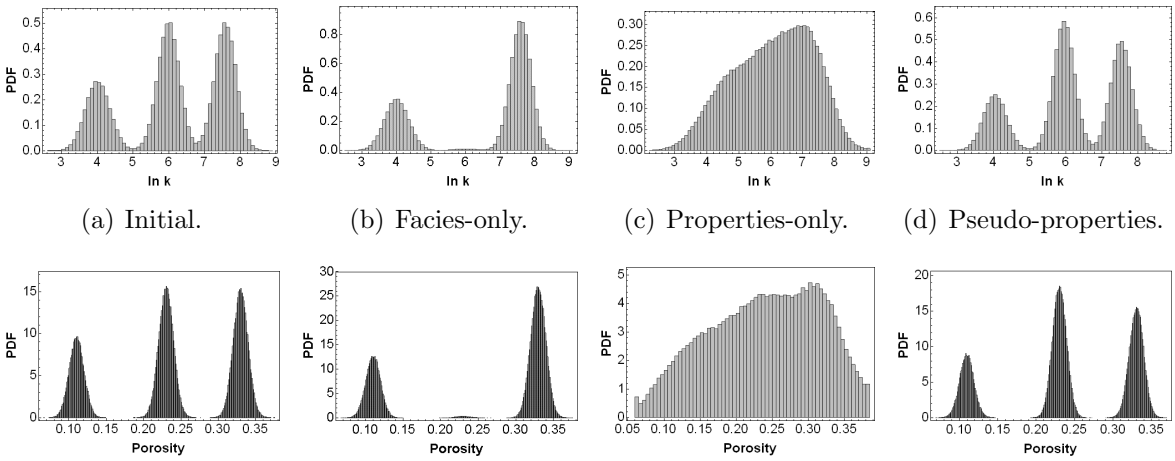

(a) Initial. (b) Facies-only. (c) Properties-only. (d) Pseudo-properties.

(e) Initial. (f) Facies-only. (g) Properties-only. (h) Pseudo-properties.

Figure 4.10: $\ln k$ (top row) and porosity (bottom row) histograms from layer 2 of Example 1. The facies-only and properties-only approaches respectively have bimodal and unimodal histograms that differ significantly from the initial and reference histograms. Histograms from the pseudo-properties approach are consistent (multimodality) with the initial and reference histograms.

Geologic plausibility of the final $\ln k$ and ϕ was assessed by testing the hypothesis that the $\ln k$ and ϕ histograms from the reference model and from the different approaches respectively are samples from the same parent population. Because only the properties-only and pseudo-properties approaches matched production data, we limit

this test to the final realizations from both approaches only. Popular tests for comparing two histograms include the χ^2-test of homogeneity (Cramer, 1946, pp. 445–450) and the Kolmogorov-Smirnov test. The results from these tests, however, cannot be applied to spatially-correlated variables. Cerioli (2002) and Olea and Pawlowsky-Glahn (2008) have recently presented possible modifications of these standard tests for variables that are spatially correlated. For our purpose however, we formulated a rather simple test for comparing the $\ln k$ (or ϕ) histograms using the proportions of $\ln k$ (or ϕ) values that occur in five selected intervals of the histograms corresponding to 3 peaks and 2 troughs (valleys). Only the test applied to the $\ln k$ histogram is presented here since the underlying process and the final results are the similar for ϕ histograms. Figure 4.11 shows the selected intervals of the $\ln k$ histograms.

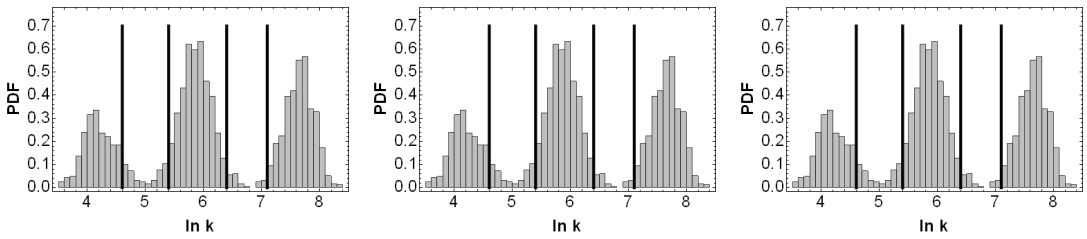

(a) Layer1 (b) Layer2 (c) Layer3

Figure 4.11: Selected intervals from reference $\ln k$ histograms for computing $\ln k$ proportions in each interval. Intervals are numbered 1–5 from left to right and correspond either to a peak or a trough.

The parent distribution of the $\ln k$ proportions in each interval of Fig. 4.11 was approximated from 5000 random realizations of $\ln k$ that were generated using known geostatistical properties (Fig. 4.12). Using a two-tailed t-test with unequal variances, we determined if the interval means of the $\ln k$ proportions from the properties-only and pseudo-properties approaches were statistically different from those of the parent distribution. Although the theory of the t-test is based on normally distributed samples, it is known to work rather well for non-normal distributions (Jensen et al.,

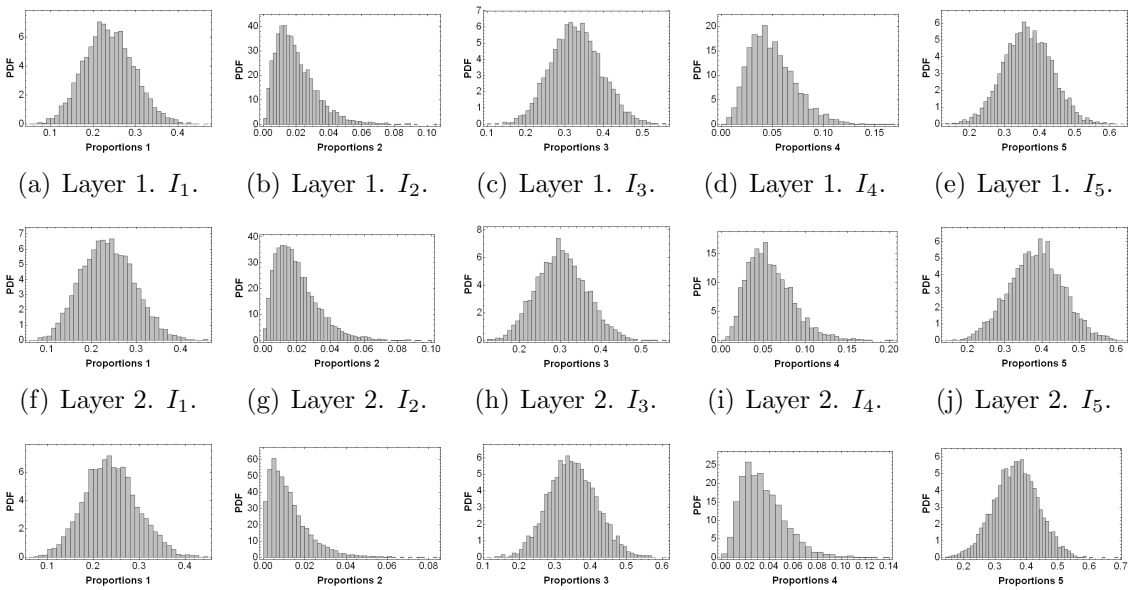

(a) Layer 1. I_1. (b) Layer 1. I_2. (c) Layer 1. I_3. (d) Layer 1. I_4. (e) Layer 1. I_5.

(f) Layer 2. I_1. (g) Layer 2. I_2. (h) Layer 2. I_3. (i) Layer 2. I_4. (j) Layer 2. I_5.

(k) Layer 3. I_1. (l) Layer 3. I_2. (m) Layer 3. I_3. (n) Layer 3. I_4. (o) Layer 3. I_5.

Figure 4.12: Parent histograms of $\ln k$ proportions in the five selected intervals in Fig. 4.11. I_1–I_5 are intervals 1–5 respectively.

2000). The t statistic is given by,

$$t_{I_j} = \left(\frac{\overline{X}_p - \overline{X}_s}{\sqrt{\frac{\hat{\sigma}_p^2}{N_p} + \frac{\hat{\sigma}_s^2}{N_s}}} \right)_{I_j}, \tag{4.22}$$

where the subscripts p and s identify the estimates from the parent and the sample (ensemble of final models) populations respectively. I_j denotes the jth interval; $\overline{X}$ is the mean of the proportions; N is the population size and $\hat{\sigma}^2$ is the estimated variance. Because the variances computed from the parent and sample populations are expected to be unequal, the degree of freedom (DF) for the t-test was computed from the Welch-Satterthwaite equation (Satterthwaite, 1946) as,

$$DF = \frac{\left(\frac{\hat{\sigma}_p^2}{N_p} + \frac{\hat{\sigma}_s^2}{N_s} \right)^2}{\frac{\hat{\sigma}_p^4}{N_p^2(N_p - 1)} + \frac{\hat{\sigma}_s^4}{N_s^2(N_s - 1)}}. \tag{4.23}$$

Based on the foregoing, the null hypothesis (Eq. 4.24) for the t-test is that the means of the proportions of $\ln k$ from all the intervals obtained from the parent distribution

and the final models from the properties-only and the pseudo-properties approaches respectively are not statistically different.

$$H_0 : \bigcap_j \left(\overline{X}_p = \overline{X}_s\right)_{I_j} = \bigcap_j H_0(I_j). \tag{4.24}$$

If the null hypothesis is falsified in any interval, then the alternative hypothesis is accepted. Tables 4.8 and 4.9 show the results of the test applied to the final ensemble of $\ln k$ maps from the pseudo-properties and properties-only approaches using a significance level of 0.05. The test results shows that at 0.05 level of significance, there is

Table 4.8: Results of hypothesis testing for the pseudo-properties approach.

Layer	$H_0(I_1)$	$H_0(I_2)$	$H_0(I_3)$	$H_0(I_4)$	$H_0(I_5)$	H_0
1	Accept	Accept	Accept	Accept	Accept	Accept
2	Accept	Accept	Accept	Accept	Accept	Accept
3	Accept	Accept	Accept	Accept	Accept	Accept

no significant evidence against the conclusion that the final $\ln k$ histograms from the pseudo-properties approach are from the same parent distribution as the reference $\ln k$ histograms. Conversely, at the same level of significance, there is enough evidence to conclude that the final $\ln k$ histograms from the properties-only approach may have come from a different parent distribution than the reference $\ln k$ histograms. These

Table 4.9: Results of hypothesis testing for the properties-only approach.

Layer	$H_0(I_1)$	$H_0(I_2)$	$H_0(I_3)$	$H_0(I_4)$	$H_0(I_5)$	H_0
1	Accept	Reject	Reject	Reject	Accept	Reject
2	Reject	Reject	Accept	Reject	Accept	Reject
3	Reject	Reject	Accept	Reject	Accept	Reject

conclusions agree with earlier qualitative observation where realizations of $\ln k$ maps from the properties-only approach seemed much smoother than one would expect for properties from a facies model. Similar qualitative observation on smoothness of the final $\ln k$ realizations obtained by directly adjusting the multimodal permeability field using EnKF has also been reported elsewhere (Sarma and Chen, 2009).

Clearly, while the properties-only approach matched data fairly well, the final estimates of the petrophysical properties are not geologically plausible. The smoothness in the final $\ln k$ realizations from the properties-only approach results from the EnKF technique seeking and using a Gaussian approximation to the multimodal PDF of $\ln k$ during the update step. Because the facies-only approach suffered from filter divergence, the final $\ln k$ (Fig. 4.10(b)) and ϕ (not shown) fields are geologically implausible and the worst matches to production measurements were obtained for this approach. It is noteworthy that the facies-only approach has been utilized successfully by a number of researchers (Liu and Oliver, 2005b; Agbalaka and Oliver, 2008; Moreno et al., 2008) for the specific case where there is no uncertainty in the petrophysical properties. By using the pseudo-properties approach, it is possible to account for both levels of uncertainty, i.e., uncertainty in the facies boundaries and in the petrophysical properties and adjusting these uncertain variables in a consistent way during history matching resulted in geologically plausible history matched models and reasonable match to data.

Figure 4.13 shows four randomly selected initial and final realizations of the facies model for the pseudo-properties approach. Evidently, some features from the prior models are preserved in the final models and additional features not present in the prior models are observable in the final models reflecting the impact of data conditioning. In additional the realizations of the facies maps in this case appears to be geologically plausible realizations as there is no evidence of history matching artifact in the final realizations.

Estimates of the trend in the facies proportions from the reference, initial and final models (from the pseudo-properties approach) are presented in Fig. 4.14. All the estimates are in general very similar to the analytical trends presented earlier in Fig. 4.3. Notably, the estimated proportions from the initial models are quite close to the reference proportions such that the facies proportions were not significantly

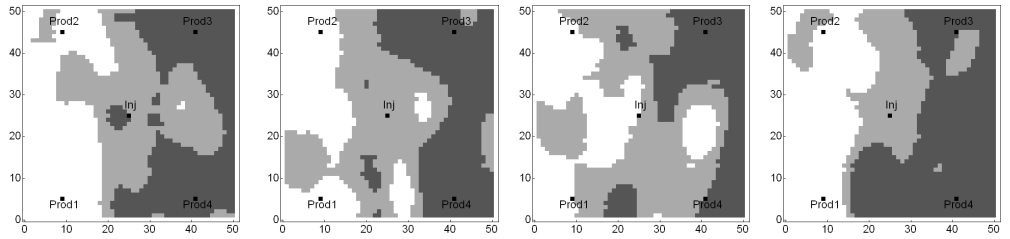

(a) Initial Model #1 (b) Initial Model #2 (c) Initial Model #3 (d) Initial Model #4

(e) Final Model #1 (f) Final Model #2 (g) Final Model #3 (h) Final Model #4

Figure 4.13: Initial (top row) and final (bottom row) Layer 1 facies maps from the pseudo-properties approach in Example 1. Given the features in the initial facies maps, the final facies maps are geologically plausible realizations.

adjusted during history matching for the current example as seen in final estimates of the trend in the facies proportions.

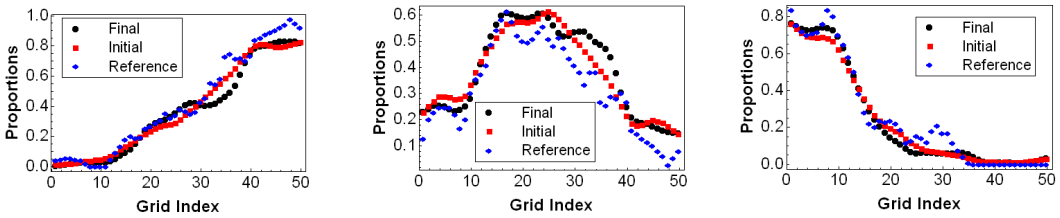

(a) Facies 1 (b) Facies 2 (c) Facies 3

Figure 4.14: Trend in the estimated facies proportions from the reference model, initial and final models (from the pseudo-properties approach) for Example 1. The initial and final estimates of the facies proportions match the reference proportions quite well in this case.

Table 4.10 presents the estimated probability of correct classification of the different facies types at each grid location for the initial and final facies models, i.e., $P(F_{sim} = i|F_{ref} = i)$; where F_{sim} is the simulated or predicted facies, F_{ref} is the reference facies and i denotes the ith facies type. The initial probability of correct facies classification is somewhat high consistent with the observations in Fig 4.14 that the

initial estimates of the nonstationary proportions were fairly close to the reference values. In Example 2, we present a rather extreme case where we start with very poor initial estimates of the facies proportions. For the current example, the probabilities of correct classification of the different facies types after data assimilation were marginally better than the initial probabilities.

Table 4.10: Probability of correct classification of each facies conditional on the facies in the reference model for Example 1. F_{sim} is the simulated facies and F_{ref} is to the reference facies.

$P(F_{sim}=1\|F_{ref}=1)$		$P(F_{sim}=2\|F_{ref}=2)$		$P(F_{sim}=3\|F_{ref}=3)$	
Initial	Final	Initial	Final	Initial	Final
0.72	0.73	0.60	0.61	0.77	0.78

4.6.3 Results for Example 2

In this section we focus on the history matching results from data assimilation using the pseudo-properties approach. Figures 4.15 and 4.16 respectively show the predictions of the q_L and q_w data for producers 1–4 from the ensemble of initial and final models. The impact of starting with an incorrect facies proportion model shows up as significantly higher initial prediction uncertainty (Figs. 4.15(a)–4.15(d) and Figs. 4.16(a)–4.16(d)) compared to the initial prediction uncertainty from Example 1 (Figs. 4.8(e), 4.8(i), 4.8(m) and 4.8(q)) where the nonstationarity in the facies proportions was accounted for. After assimilating data, there is considerable reduction in prediction uncertainty both for history matched period ($\leq$ 220 days) and the "future" prediction period ($>$ 220 days). Even though the initial models in the current example were generated by wrongly assuming stationarity of the facies proportions, the history match to production measurements are quite good.

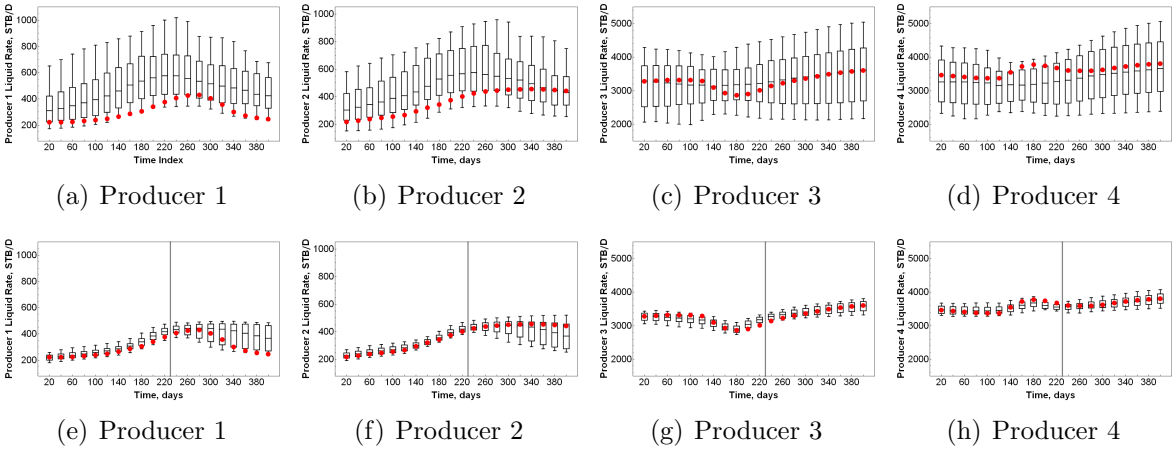

(a) Producer 1 (b) Producer 2 (c) Producer 3 (d) Producer 4

(e) Producer 1 (f) Producer 2 (g) Producer 3 (h) Producer 4

Figure 4.15: Predicted liquid rate data (q_L) from the initial (top row) and final (bottom row) ensembles for Example 2. The vertical line demarcates the end of history matching. The red circles are production measurements and the box-and-whisker plots are ensemble predictions. The match to production data is quite good and data are contained within the future prediction spread of the ensemble.

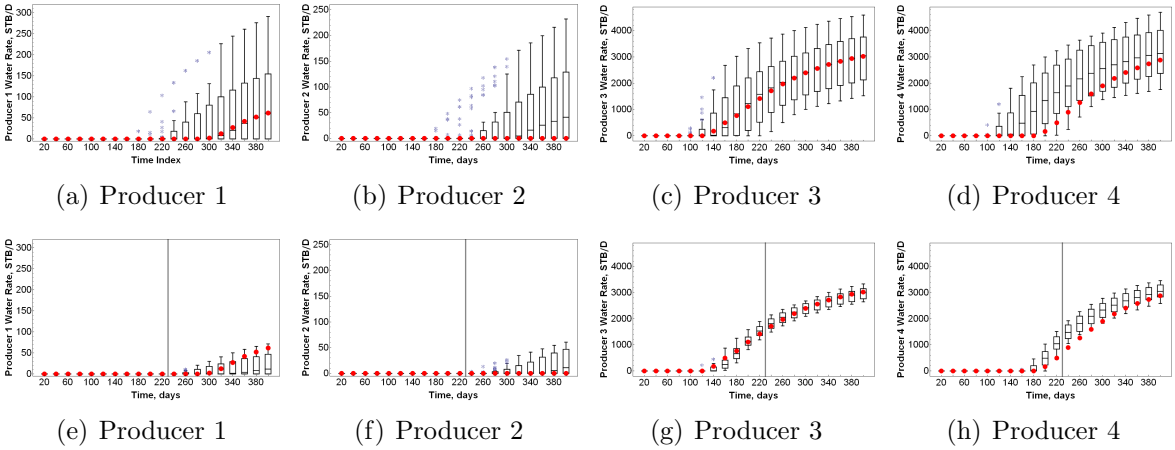

(a) Producer 1 (b) Producer 2 (c) Producer 3 (d) Producer 4

(e) Producer 1 (f) Producer 2 (g) Producer 3 (h) Producer 4

Figure 4.16: Predicted water rate data (q_w) from the initial (top row) and final (bottom row) ensembles for Example 2. The vertical line demarcates the end of history matching. The red circles are the production measurements and the box-and-whisker plots are ensemble predictions. Fairly good match to Prod 1–3 q_w data. Although the match to Prod4 q_w data is somewhat biased, there is a significant improvement over the initial prediction.

4.6.3.1 Updated geological parameters

Figure 4.17 shows four randomly selected realizations of the initial and final estimates of the $\ln k$ maps. The permeability distributions from both the initial and final models are discontinuous, consistent with petrophysical properties distribution from a facies model. However, unlike the reference model where a EW trend in the property field is evident for this layer (Fig. 4.4(c)), there is no clear trend in the four realizations of the initial model (Figs. 4.17(a)–4.17(d)). This reflects the impact of the underlying assumption of stationarity on the distribution of the petrophysical properties in the initial realizations of the facies model.

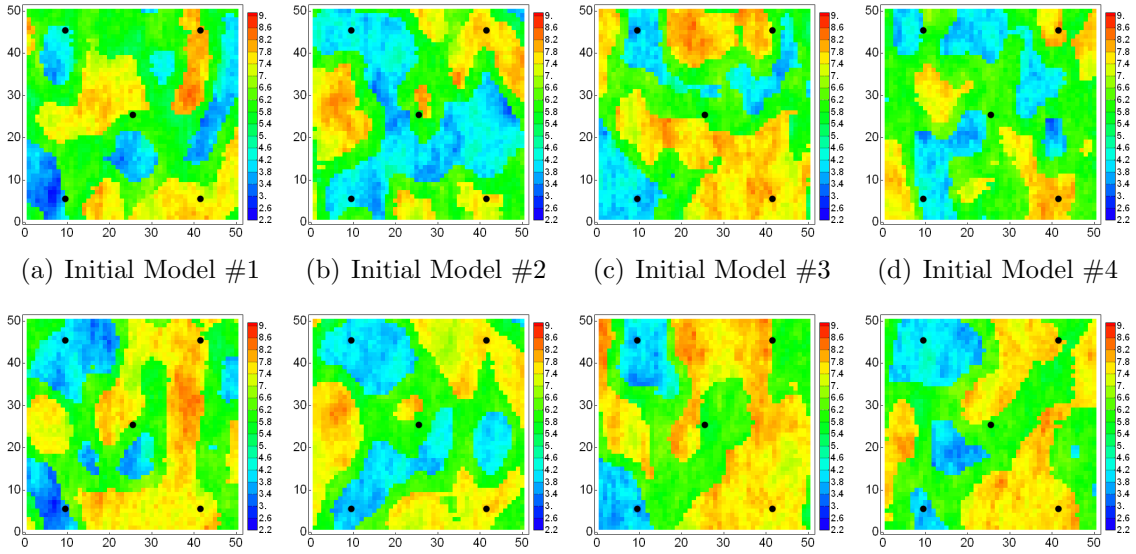

(a) Initial Model #1 (b) Initial Model #2 (c) Initial Model #3 (d) Initial Model #4

(e) Final Model #1 (f) Final Model #2 (g) Final Model #3 (h) Final Model #4

Figure 4.17: Realizations of initial (top row) and final (bottom row) $\ln k$ maps from layer 3 in Example 2. The distribution of the $\ln k$ values in the final model shows both features from data conditioning and from the initial models.

After assimilating data, the final realizations seem to capture the connectivity of the high permeability sand (NE-SE region of the map) between producers 3 and 4 (Figs. 4.17(e)–4.17(h)) observed in the reference model (Fig. 4.4(c)). Producers 1 and 2 did not have water breakthrough data during the period of data assimilation so there is relatively little information on the inter-well connectivity between both

wells and the injector. This may partly account for the reason why the inter-well permeability distribution in the NW–SW region of the maps from the final models appears somewhat similar to the distribution in the initial models.

Estimates of the trend in the expected facies proportions from the reference, initial and final models are presented in Fig. 4.18. Recall that the expected facies proportions in our current example are stationary and equal to $\frac{1}{3}$ for all 3 facies in the model. It appears that even though stationary proportions maps were used to compute the thresholds for generating the initial facies maps, the initial estimate of the facies proportions seem to have inherited some weak trends from using the same long-range correlation as the reference model. However, the initial trends are clearly different from the reference trends and in general, represent a poor approximation to the expected facies proportions. After assimilating data, the expected facies proportions estimated from the final ensemble match the reference proportions quite well.

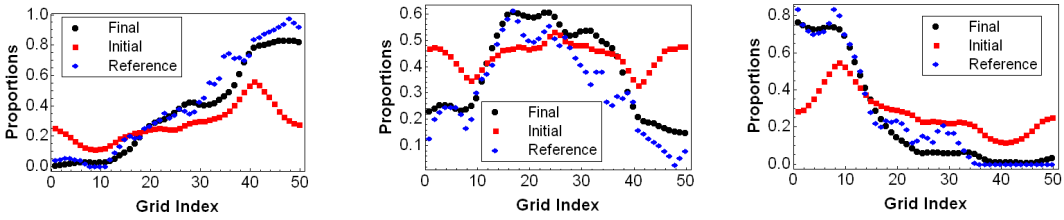

(a) Facies 1 (b) Facies 2 (c) Facies 3

Figure 4.18: Nonstationary facies proportions from the reference model (diamonds), ensemble of initial (squares) and final models (circles) from Example 2. The initial estimates do not match the reference proportions but the final estimates do.

Table 4.11 shows the ensemble estimate of the probability of correct classification of the facies conditional on the facies in the reference model. The estimated probabilities are generally better after data assimilation compared to the initial probabilities.

4.6.4 Results for Example 3

Figures 4.19 and 4.20 show the performance of the initial and final models in predicting the q_L and q_w data respectively for the current example. Using the proposed

Table 4.11: Probability of correct facies classification conditional on the facies present in the reference model for Example 2. F_{sim} represents the simulated facies and F_{ref} refers to the facies in the reference model.

$P(F_{sim}=1\|F_{ref}=1)$		$P(F_{sim}=2\|F_{ref}=2)$		$P(F_{sim}=3\|F_{ref}=3)$	
Initial	Final	Initial	Final	Initial	Final
0.61	0.66	0.53	0.55	0.66	0.73

approach based on updating the more-nearly Gaussian pseudo-properties in each facies, reasonable matches to the water and liquid rate data were obtained for this example. The estimated water breakthrough times predicted by the final models are significantly better than predictions from the initial models. The initial uncertainties in predicted data were reduced considerably after data assimilation and predictions of future production data by the final models match the reference predictions fairly well.

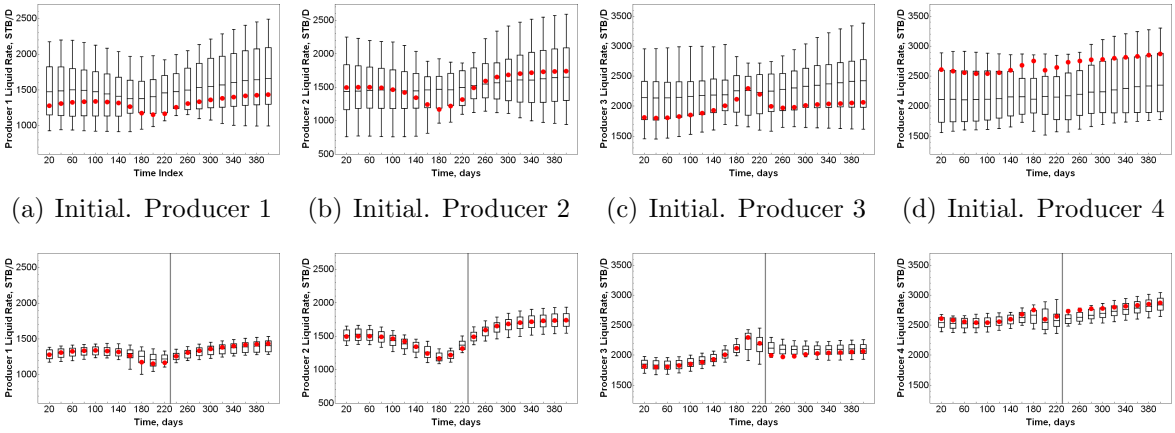

(a) Initial. Producer 1 (b) Initial. Producer 2 (c) Initial. Producer 3 (d) Initial. Producer 4

(e) Final. Producer 1 (f) Final. Producer 2 (g) Final. Producer 3 (h) Final. Producer 4

Figure 4.19: Liquid production rate data predicted by the initial (top row) and final (bottom row) ensemble for Example 3. The vertical line demarcates the end of history matching. The filled circles are production measurements and the box-and-whisker plots are the ensemble predictions. The matches to q_L data is quite good for the history matched and pure prediction periods.

Four randomly selected realizations of the initial and final $\ln k$ maps for layer 2 are presented in Fig. 4.21. For comparison, the reference $\ln k$ map for the same layer

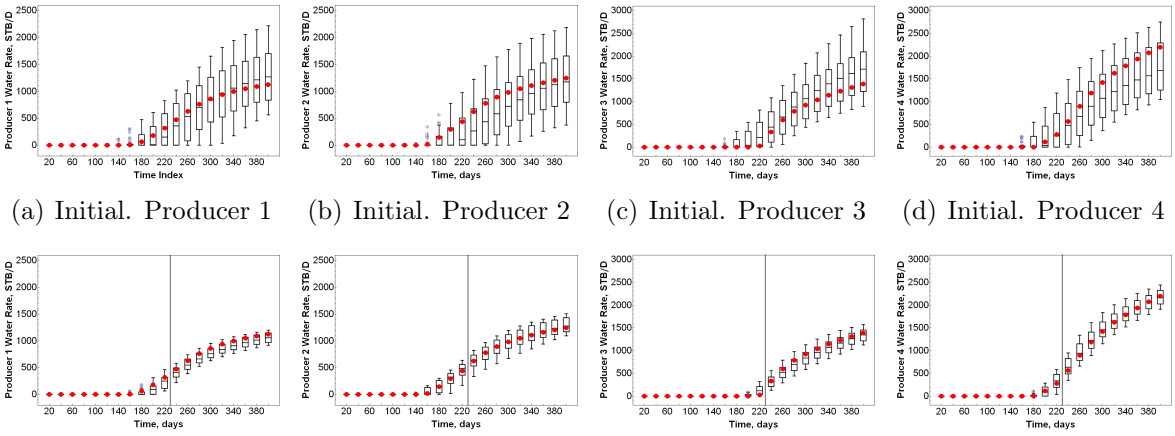

(a) Initial. Producer 1 (b) Initial. Producer 2 (c) Initial. Producer 3 (d) Initial. Producer 4

(e) Final. Producer 1 (f) Final. Producer 2 (g) Final. Producer 3 (h) Final. Producer 4

Figure 4.20: Water production rate data (q_w) predicted by the initial (top row) and final (bottom row) ensemble for Example 3. The vertical line demarcates the end of history matching. The filled circles are production measurements and the box-and-whisker plots are the ensemble predictions. Fairly good matches to data for the history matched and pure prediction periods.

is presented also (Fig. 4.21(a)). Realizations of the final $\ln k$ maps in Fig. 4.21 appear to qualitatively reproduce some of the features present in the reference $\ln k$ map such as the high permeability sand body observed in the left region of the map and the low permeability sand body in the right region of the map.

4.7 Chapter Summary

In this chapter, I have considered the problem of jointly updating the multimodal petrophysical properties and the discrete facies variables from assimilating production and facies data using EnKF. I presented an approach, which updates the more nearly-Gaussian pseudo-properties in each facies class in lieu of the multimodal petrophysical properties. Furthermore a straightforward mapping scheme was introduced for obtaining the updated petrophysical properties from the pseudo-properties. Using the pseudo-properties approach, consistent updates to the multimodal permeability and porosity as well as the GRFs that parameterize the transformed facies variables are obtained at each data assimilation timestep. Comparison of the results from the

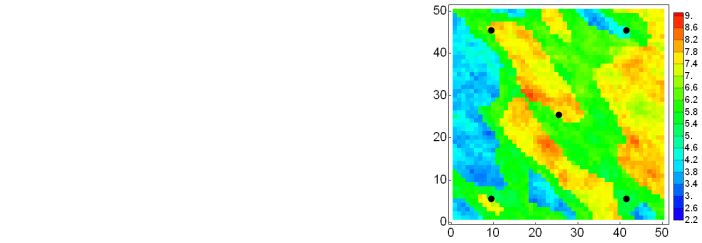

(a) Reference map.

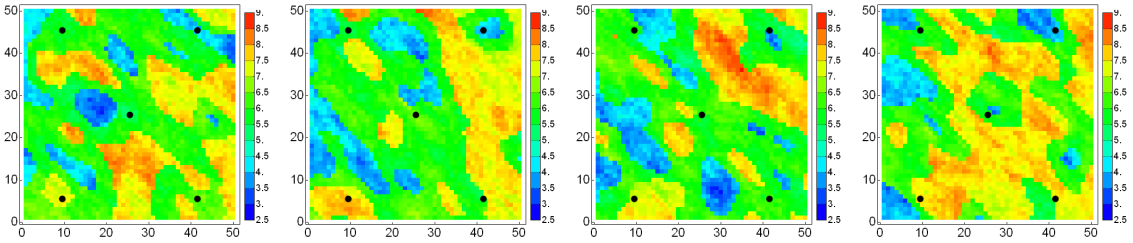

(b) Initial. Ens#1. (c) Initial. Ens#2. (d) Initial. Ens#3. (e) Initial. Ens#4.

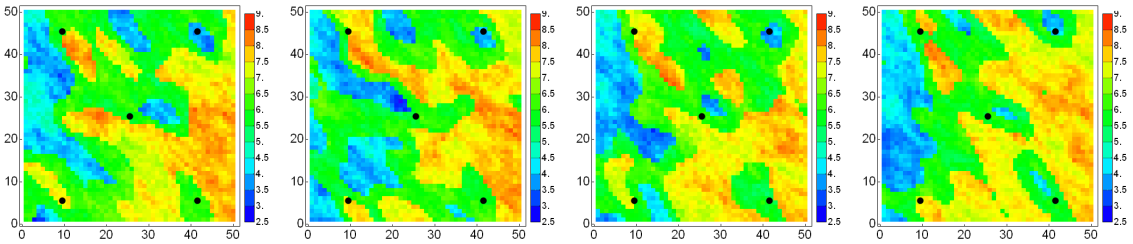

(f) Final. Ens#1. (g) Final. Ens#2. (h) Final. Ens#3. (i) Final. Ens#4.

Figure 4.21: Four randomly selected realizations of layer 2 $\ln k$ maps from the initial and final models for Example 3.

pseudo-properties approach with those from two other approaches based on adjusting only the facies boundaries or directly updating the multimodal petrophysical properties showed the pseudo-properties approach to be better in obtaining both acceptable history matching results and final history matched models that are geologically plausible.

I also addressed, in this chapter, the problem of getting stuck in a local minimum during the iterative enforcement of the constraints on the facies mismatch observations previously discussed in Chapter 3. This situation occurs when the ensemble of predicted facies class at a specific measurement location do not match the facies observation resulting in the absence of variability in the ensemble of facies proxies at the measurement location. It appears that by adding random perturbations to the ensemble of facies proxies, the required variability is re-introduced and the predicted well facies can be constrained to match the facies observations during the iterative enforcement step.

The pseudo-properties approach for estimating multimodal facies properties using EnKF was tested on three sample problems with different assumptions of nonstationarity. For the specific example where the initial models were generated incorrectly using a stationary proportions map, the final estimate of the expected facies proportions reproduced and matched the trend in the reference proportions quite well. This seems to indicate that if the correlation lengths and direction of anisotropy are correctly specified, then the assumption of stationarity or nonstationarity for facies estimation from history matching may be unimportant.

CHAPTER V

PARAMETERIZATION OF VERTICAL TRANSMISSIBILITY BARRIERS FOR HISTORY MATCHING USING ENKF

5.1 Background

Permeability anisotropy results in subsurface flow direction that is generally different from the direction of the pressure gradient. Of importance in reservoir simulation model development is the knowledge of the horizontal anisotropy (alternatively, azimuthal anisotropy) and vertical anisotropy (commonly expressed as a ratio, k_v/k_h; where k_v is the vertical permeability and k_h, the horizontal permeability). Field measurements generally show that horizontal permeability is often several orders of magnitude higher than the vertical permeability (Prats, 1972; Martin and Cooper, 1984; Auzerais et al., 1990; Ehlig-Economides et al., 1990; Ayan et al., 1994). The pronounced vertical anisotropy results from deposition of non-reservoir materials (shales, silts, cemented bands and stylolites) and from crossbedding (Prats, 1972; Lake, 1988; Auzerais et al., 1990; Anderson et al., 1994). In most fields, the k_v/k_h ratio is less than or equal to 1.

Accounting for vertical anisotropy in flow simulation studies is critical as it significantly impacts recovery mechanisms, choice of design for various EOR processes, decision on completions and well control strategies, and selection of optimal well performance parameters (Harpole, 1980; Lord and Collins, 1989; Ehlig-Economides et al., 1990; Tillman and Pittman, 1994; Ayan et al., 1994; Shin and Choe, 2009). Consequently, information (from well logs, cores, outcrops, etc) on the occurrence

and distribution of vertical transmissibility barriers are utilized in building the initial reservoir model. However, as noted by Haldorsen et al. (1987), considerable uncertainties related to the parameters of these flow barriers still exist even after utilizing different sources of information in building the simulation model. These initial uncertainties are reduced by further calibrating the model to production data; a process known as history matching. Figure 5.1 illustrates the impact of vertical flow barrier distribution on recovery efficiency.

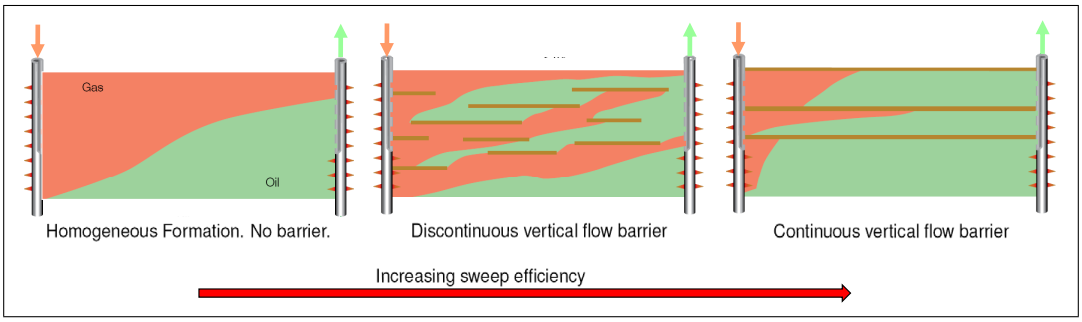

Figure 5.1: Impact of vertical flow barriers on subsurface flow and recovery efficiency. Ayan et al. (1994).

The ensemble Kalman filter will perform poorly in calibrating reservoir models to match production data if only the log-Gaussian vertical and horizontal permeabilities are adjusted during history matching to account for the effect of impermeable barriers on fluid flow. This is due to the limiting behavior typical of log-normal variables where it is difficult to attain the vertical permeability values that are small enough to eliminate communication between zones. Consequently, the presence of transmissibility barriers have to be accounted for explicitly and a suitable Gaussian parameterization of the transformed non-Gaussian (vertical) transmissibility barrier is needed to satisfy the EnKF assumption of Gaussianity at each data assimilation timestep.

In this chapter we consider three alternative parameterizations of the vertical

transmissibility barriers that improves the EnKF performance in estimating the spatial distribution of the vertical flow barriers from assimilating production data. Using a fairly complex synthetic test problem, we show that compared to the case where only the vertical permeabilities are adjusted to account for the effect of vertical flow barriers, these parameterization techniques result in better history matching results and more reasonable estimates of the model parameters. Throughout, the ensemble randomized maximum likelihood filter is used to assimilate data at any timestep where the maximum saturation change by the EnKF is ≥ 0.3.

5.2 Simulation Model Description

The reference model is a two-layer, two-phase, black oil, reservoir model with $50 \times 50 \times 2$ active gridblocks, each of dimension 50 ft $\times$ 50 ft $\times$ 20 ft. The phases present in the reservoir model are oil and water respectively. There are four producers and one injector arranged in a five-spot water injection pattern. Throughout, the injector will be referenced as Inj1 and the four producers respectively as Prod1, Prod2, Prod3 and Prod4. There are two reservoir zones/layers and all the wells are completed (perforated) across both zones. Additionally, each completed interval is operated independently giving a total of 10 producing intervals from which individual production measurements are obtained and different production constraints and/or targets are enforced. A schematic representation of a typical dual zone completion with independent production from each zone is shown in Fig. 5.2.

To distinguish between producing intervals, the top and bottom intervals/zones will be referred to respectively as ZoneA and ZoneB. Additionally, when necessary, the letter for each zone will be appended to the well names to identify the different producing intervals, e.g., Prod4A and Prod4B will refer respectively to the upper and lower producing intervals of Prod4. The grid coordinates of the wells in the simulation model are given in Table 5.1.

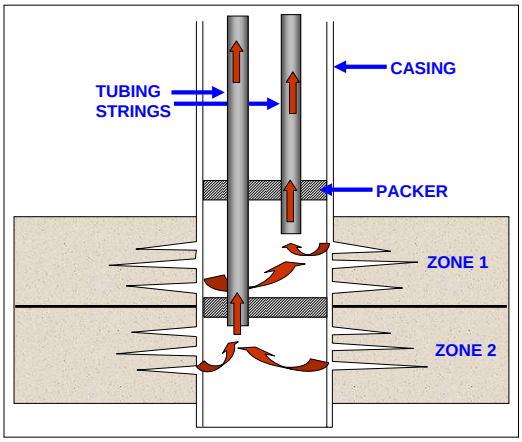

Figure 5.2: Schematic of a dual zone well completion.

Table 5.1: Grid coordinates of the well locations in the simulation model.

Coordinate	Inj1	Prod1	Prod2	Prod3	Prod4
x-coordinate	25	9	9	41	41
y-coordinate	25	9	41	41	9

The porosity (ϕ) and horizontal permeability (k_h) fields in the model are laterally correlated but are vertically uncorrelated. The geostatistical properties for generating both fields are presented in Table 5.2. An exponential covariance model was assumed for both k_h and ϕ.

Table 5.2: Geostatistical properties for generating the petrophysical properties.

Zone	Range	Anis. Ratio	Anis. Angle	Mean k_h	Mean ϕ	Std. Dev. k_h	Std. Dev. ϕ
1	700 ft	1	0°	5.75	0.23	0.75	0.02
2	1000 ft	2	45°	5.75	0.23	0.75	0.02

The reference porosity and permeability fields were generated using the sequential Gaussian simulation technique and the k_h maps for ZoneA and ZoneB are shown in Figs. 5.3(a) and 5.3(b). The reference vertical permeability field, k_v, was obtained by element-wise multiplication of the horizontal permeability field by a correlated random Gaussian field with a mean of 0.18 and a standard deviation of 0.01. The reference distribution of the vertical flow barriers presented in Fig. 5.3(c) shows that the impermeable barrier is discontinuous between Prod2 and the other four wells but

is continuous among these four wells. The gray and white shades are respectively regions with and without impermeable barriers. The black dots are the well locations and the letters "**P**" and "**I**" respectively identify the four producers and the injector.

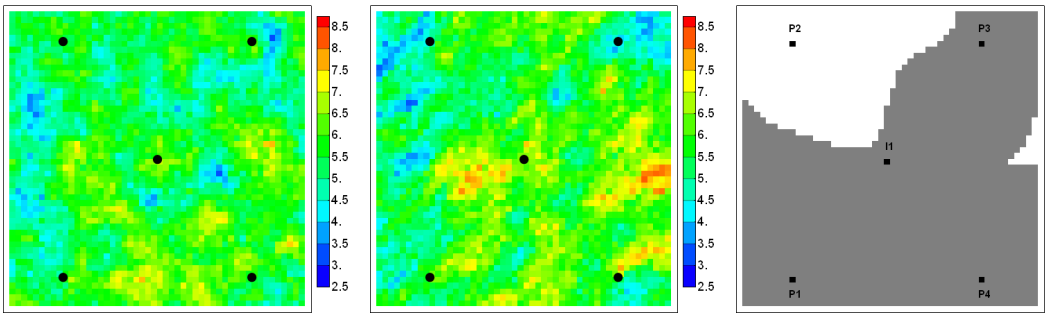

(a) ZoneA – k_h (b) ZoneB – k_h (c) Vertical flow barrier

Figure 5.3: Reference maps of horizontal permeability (k_h) and vertical flow barriers (gray shades are regions with no-flow barriers).

Water injection began on the first day of production and continued throughout the 545 days of production. After 515 days of production, Prod3 and Prod4 were shut in for 15 days and static bottomhole pressure (BHP) measurements, p_{bh}, were obtained from both wells. Following the shut-in period, both wells were returned to production for the remaining period of production. Figure 5.4 shows the BHP responses for Inj1, Prod3 and Prod4 in the reference model for two cases namely: (1) case with impermeable flow barriers (Figs. 5.4(a)–5.4(c)) using the vertical flow barrier configuration of Fig. 5.3(c) , and (2) case without impermeable flow barriers (Figs. 5.4(d)–5.4(f)). Clearly, the flowing and static zonal pressure differences are generally higher for the model with the impermeable barrier. In Prod4, the average static zonal pressure differences over the 15-day shut-in period are respectively 55 psi and 8 psi for the models with and without vertical flow barriers (Figs. 5.4(c) and 5.4(f)). The location of Prod3 is somewhat close to the region with zonal communication leading to a smaller static zonal pressure difference in this well compared to Prod4, which is further away from the region with zonal communication.

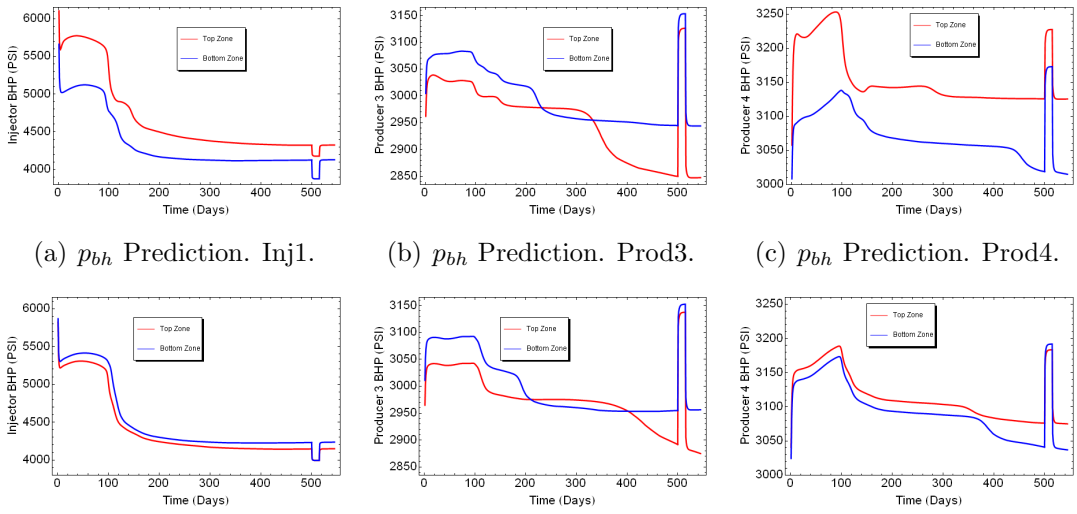

(a) p_{bh} Prediction. Inj1. (b) p_{bh} Prediction. Prod3. (c) p_{bh} Prediction. Prod4.

(d) p_{bh} Prediction. Inj1. (e) p_{bh} Prediction. Prod3. (f) p_{bh} Prediction. Prod4.

Figure 5.4: Effect of vertical flow barriers on zonal bottomhole pressure (p_{bh}) difference. Predictions in top and bottom rows are respectively from same reservoir model with and without zonal flow barriers.

Prod1 and Prod2 were operated at constant bottomhole pressures while Prod3 and Prod4 were operated at a constant liquid rate target, q_L, with a secondary constraint of 500 psi on the minimum bottomhole pressure. Values of the operating targets for the producers are presented in Table 5.3. The injection rate was controlled by the reservoir voidage rates of the surrounding pattern of four producers. Essentially, a quarter of the reservoir voidage from each of the four producers in any zone is replaced by water injected in the same zone. A maximum BHP of 7500 psi was used as the secondary constraint for the injector. Finally, during the shut-in period, the liquid rate targets for Prod3 and Prod4 were set respectively to 10^{-6} STB/D instead of 0 STB/D. This was necessary to obtain values of shut-in bottomhole pressure data from the simulator. Note that after the shut-in phase both producers were returned to their pre-shut-in rate targets presented in Table 5.3.

Table 5.3: Production targets and constraints for Prod1–Prod4. For the shut-in period Prod3 and Prod4 rate targets were reduced to 10^{-6} STB/D.

	$\mathbf{p_{bh}}$ **Constraint (psi)**		$\mathbf{q_L}$ **Target (STB/D)**	
Interval	**Prod1**	**Prod2**	**Prod3**	**Prod4**
ZoneA	1500	1000	150	300
ZoneB	1000	1000	500	500

5.3 Parameterization of Vertical Transmissibility Barriers

In reservoir simulation models, flow between adjacent gridblocks is controlled by the transmissibility values at the gridblock boundaries. The vertical transmissibility, $T_{lz_{k\pm\frac{1}{2}}}$, for any fluid phase, l, between an arbitrary gridblock (i, j, k), and its neighboring gridblock $(i, j, k \pm 1)$, in the z direction is defined by (Ertekin et al., 2001),

$$T_{lz_{k\pm\frac{1}{2}}} = G_{k\pm\frac{1}{2}} \left(\frac{k_{rl}}{\mu_l B_l}\right)_{k\pm\frac{1}{2}}, \tag{5.1}$$

where G is the geometrical factor; k_{rl}, μ_l and B_l are respectively the relative permeability, viscosity and formation volume factor of phase l. Note that depending on the phase, Eq. 5.1 may be expanded to include other saturation and pressure dependent terms like gas solubility, oil gravity etc. Note also that the gridblock subscripts i and j in Eq. 5.1 have been suppressed for notational convenience. For block-centered rectangular grid, the geometrical factor is defined as,

$$\begin{aligned} G_{k\pm\frac{1}{2}} &= \beta \frac{2(A_{z_k} k_{z_k})(A_{z_{k\pm1}} k_{z_{k\pm1}})}{A_{z_k} k_{z_k} \Delta z_{k\pm1} + A_{z_{k\pm1}} k_{z_{k\pm1}} \Delta z_k} T_{Mz_{k\pm\frac{1}{2}}} \\ &= \left(\frac{2A_z\beta}{\Delta z}\right)\left(\frac{k_{z_k} k_{z_{k\pm1}}}{k_{z_k} + k_{z_{k\pm1}}}\right) T_{Mz_{k\pm\frac{1}{2}}}, \end{aligned} \tag{5.2}$$

where β is an appropriate conversion factor, A_z is the cross-sectional area normal to the z direction, Δz is the grid thickness, $k_z = k_v$ is the vertical permeability (alternatively the permeability in the z direction), and T_{Mz} is the vertical transmissibility multiplier. The first equality in Eq. 5.2 is the more general expression for the geometric factor and the second equality is specific to the case where the z-direction

cross-sectional area and the thickness of adjacent gridblocks (with grid indices k and $k \pm 1$ respectively) are equal, such as is the case in the simulation model used for the experiments presented in this chapter.

A commonly used approach by reservoir engineers is to model the effect of partial or complete restriction of flow from one gridblock to the neighbor by using a transmissibility multiplier that takes values between 0 and 1. Flow between adjacent gridblocks may be prevented by setting the transmissibility multiplier at the gridblock interface to zero. Consequently, the vertical transmissibility multiplier, T_{Mz}, was selected as the variable for parameterization during history matching to account for the impact of impermeable barriers on fluid flow. For grid locations with impermeable barriers, T_{Mz} is set to zero thus sealing communication between zones. For any region where there is no vertical barrier to flow, the T_{Mz} values will be set to one and vertical permeability values estimated from the EnKF will be used to determine the vertical transmissibilities in the region. There are two useful conditions that any suitable parameterization of T_{Mz} must satisfy:

1. The variables should be approximately Gaussian so that the use of the covariance for update is appropriate.

2. The variables should have a meaningful geologic interpretation. The problem of parameterizing T_{Mz} may be recast as a dual problem of parameterization a sand-shale sequence where the observation of shale at any location corresponds to $T_{Mz} = 0$ and the observation of sand, to $T_{Mz} = 1$. Hence any parameterization used should satisfy the geostatistical properties of a geologically meaningful sand-shale distribution.

To this end, the transformed vertical transmissibility multipliers are parameterized as correlated, zero mean, Gaussian random variables with unit variance. A Gaussian covariance model was also assumed. The geostatistical properties used for generating

realizations of the Gaussian random field (GRF) are presented in Table 5.4. For our purpose the method of moving averages (Oliver, 1995) was used for generating unconditional realizations of the GRF although other suitable methods for generating correlated multivariate Gaussian fields, such as the sequential Gaussian simulation technique (SGSIM), are equally appropriate. To map the continuous Gaussian field back to the discrete field of transmissibility multipliers two different but related nonlinear functions were considered: the unit step function and a specific form of the sigmoid function.

Table 5.4: Geostatistical properties for generating realizations of the Gaussian random fields, which parameterize the transformed vertical transmissibility multipliers.

Range (ft)	**Angle** (deg.)	**Anis. Ratio**	**Variance**	**Mean**
1200	0.0	1.0	1.0	0.0

The unit step function, $H(\cdot)$, is a nonlinear discontinuous function which takes values of either 0 or 1 (Eq. 5.3). The input value at which the function changes value is the threshold value. Gaussian variables less than the threshold value are mapped to a T_{Mz} value of zero and vice versa. For our purpose, the unit step function is assumed to be "positive from the right", i.e., the function take a value of one at the threshold. The unit step function is defined as,

$$T_{Mz}(i,j) = H(y_{i,j}, \beta_{i,j}) = \begin{cases} 1, & y_{i,j} \geq \beta_{i,j}; \\ 0, & y_{i,j} < \beta_{i,j}, \end{cases} \tag{5.3}$$

where $y_{i,j}$, $\beta_{i,j}$ and $T_{Mz}(i,j)$ are respectively the Gaussian variable, threshold value and the transmissibility multiplier at grid location, (i,j).

The unit step function is non-differentiable at the threshold. Where differentiability of the nonlinear transform function is important, a smooth approximation of the unit step function, a sigmoid function, may be used and the form of the sigmoid function used in this study is given by,

$$T_{Mz}(i,j) = \varphi(y_{i,j}, \beta_{i,j}) = \frac{1}{2}\left[1 + \Phi\left(\frac{y_{i,j} - \beta_{i,j}}{10^{-6}}\right)\right], \tag{5.4}$$

where $\varphi(\cdot)$ is the specific form of sigmoid function used and $\Phi(\cdot)$ is the standard error function. As the denominator of the input to the standard error function approaches zero, the T_{Mz} values from both function are asymptotically equal. Figure 5.5 shows the unit step and sigmoid functions. Note that unlike the unit step function the sigmoid function is continuous for values in the interval, $0 \pm \epsilon$, where ϵ is a small but finite real-valued number.

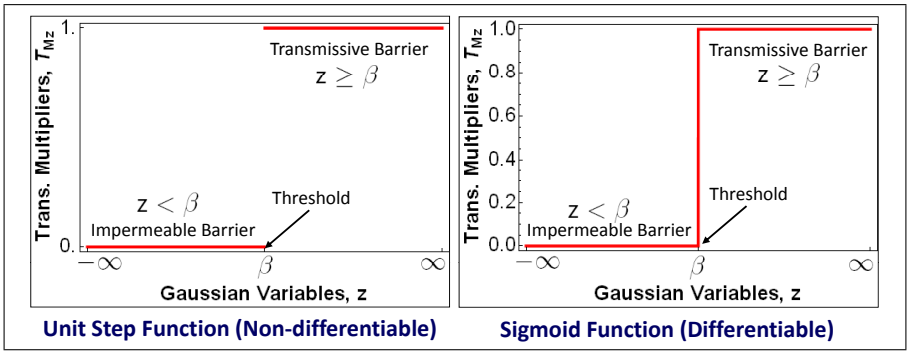

Figure 5.5: Plots of the unit step and sigmoid functions showing the relationship between the Gaussian variables and transmissibility multipliers.

The threshold determines the probability of finding either an impermeable flow barrier ($T_{Mz} = 0$) or transmissive barrier ($T_{Mz} = 1$) at any grid location. From Eqs. 5.3 and 5.4 (see Fig. 5.5 also) it is evident that as the threshold value ($\beta_{i,j}$) increases, the probability that a randomly sampled Gaussian variable is mapped to $T_{Mz} = 0$ also increases and vice versa. Consequently, we consider three possible specifications of the threshold values representing varying degrees of uncertainties in the prior probability of obtaining either an impermeable barrier or a transmissive barrier at each grid location.

1. Constant/uniform threshold: This corresponds to a complete lack of knowledge and the prior probabilities are spatially uniform and constant and equal to a value of one-half at all grid locations; equivalently, the thresholds in all grid locations are assigned a value of zero. Also the thresholds are not adjusted during history matching. Throughout, the results related to realizations of

the reservoir model with vertical transmissibility barriers obtained by using a uniform threshold will be referenced as Barrier1.

2. Nonuniform and uncertain threshold: The prior probabilities are considered uncertain and allowed to vary spatially, i.e., the probability of finding a transmissive or impermeable barrier changes with grid location. This is modeled by allowing the threshold, $\beta_{i,j}$, to vary with grid locations. Because the thresholds are uncertain, they are included as parameters to be estimated during history matching. Initial realizations of the threshold maps are modeled as correlated Gaussian random fields with the same geostatistical properties specified in Table 5.4. Three randomly selected unconditional realizations of the initial threshold maps for this case are shown in Fig. 5.6. Results from simulation models with vertical transmissibility barriers based on thresholds that are nonuniform and uncertain will be referenced as Barrier2.

3. Kriged threshold: In this case, we assume that soft data in the form of probabilities of observing an impermeable barrier at the well locations are available. The values used in our current study is presented in Table 5.5. The soft data are kriged to obtain a smooth probability map (Fig. 5.7(a)), which is then transformed to the corresponding threshold map (Fig. 5.7(b)) using a probit/quantile function defined as,

$$\beta_{i,j} = \Gamma(p_{i,j}) = \sqrt{2}\mathrm{erf}^{-1}(2p_{i,j} - 1), \quad p_{i,j} \in (0,1), \tag{5.5}$$

where $\Gamma(\cdot)$ is the probit function and $p_{i,j}$ is the estimated probability value at gridlock (i,j). Expectedly, the initial probability map obtained from kriging the soft data (Fig. 5.7(a)) captured some of the global features in the reference T_{Mz} map (Fig. 5.3(c)) such as the low probability of an impermeable barrier in the NW region of the model and an increasing probability of an impermeable flow barrier as one moves in the SE direction. The thresholds in the threshold map

in this case are not adjusted during history matching and the same threshold map is used with Eq. 5.3 or Eq. 5.4 to obtain T_{Mz} maps from realizations of the GRFs. Results obtained from using this representation of the threshold will be identified by the nomenclature, Barrier3.

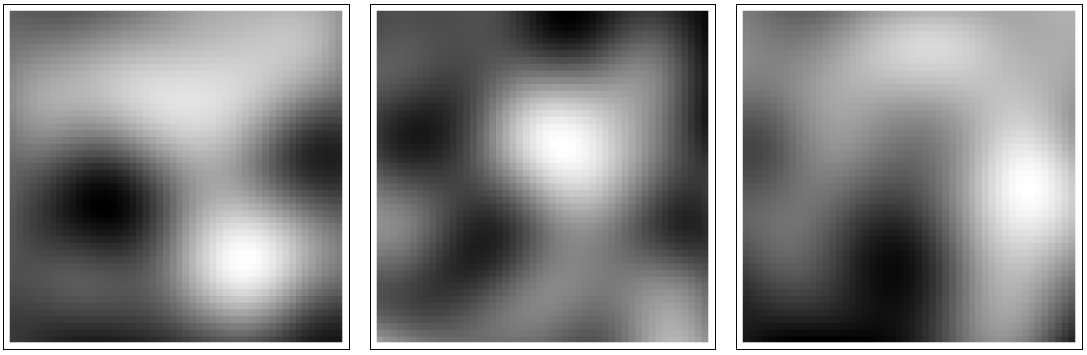

(a) Realization 1. (b) Realization 2. (c) Realization 3.

Figure 5.6: Unconditional realizations of the initial threshold maps. Dark and light shades are respectively low and high probabilities of an impermeable barrier.

Table 5.5: Probability of observing an impermeable barrier at the well locations.

Inj	**Prod1**	**Prod2**	**Prod3**	**Prod4**
0.85	0.85	0.15	0.85	0.85

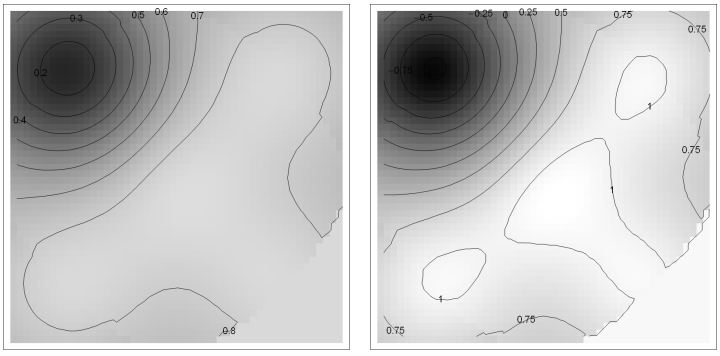

(a) Kriged probability map. (b) Thresholds from probability map.

Figure 5.7: Probability and threshold maps from the Kriged threshold approach. Threshold map (column 2) obtained by inverting the kriged probability map using Eq. 5.5.

Figure 5.8 shows some realizations of the vertical transmissibility multipliers obtained by using the unit step function and the 3 different representations of threshold values. Because these realizations are not conditioned to hard data, the transmissibility multipliers at the wells locations do not necessarily match the values in the reference T_{Mz} map (Fig. 5.3(c)).

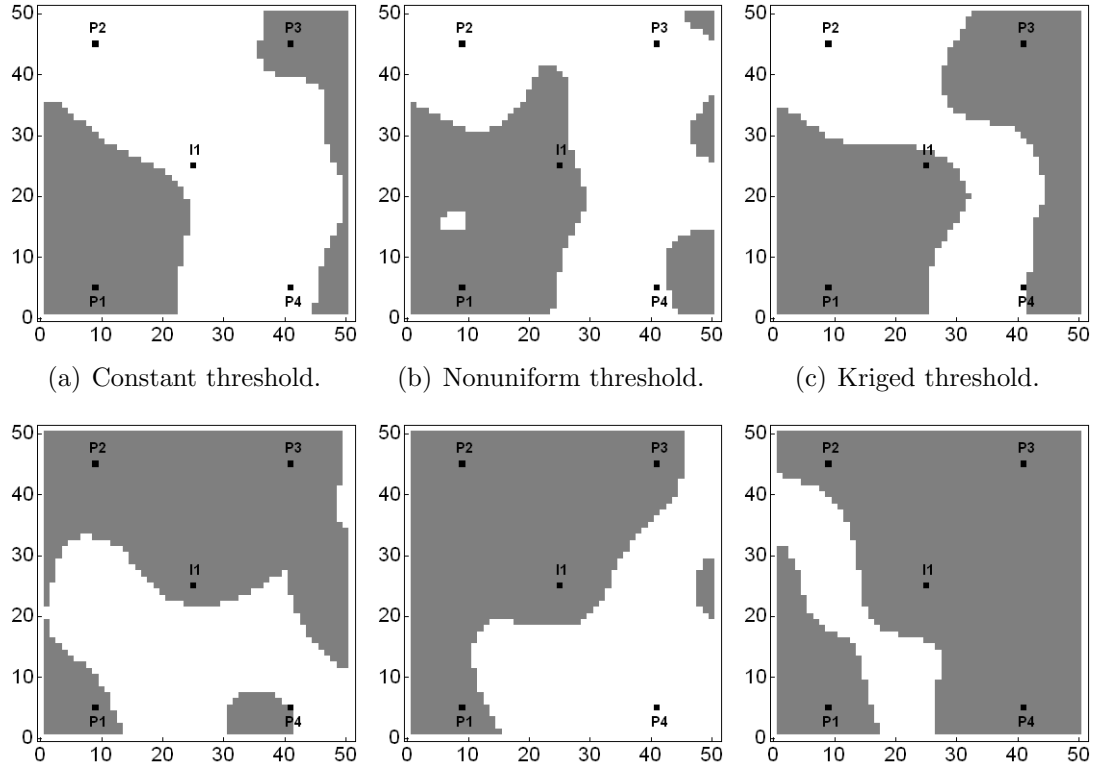

(a) Constant threshold. (b) Nonuniform threshold. (c) Kriged threshold.

(d) Constant threshold. (e) Nonuniform threshold. (f) Kriged threshold.

Figure 5.8: Initial realizations of the vertical transmissibility barrier maps from using a unit step function and different threshold representations to transform the underlying GRFs. The white and gray shades correspond to regions with transmissive and impermeable barriers respectively.

Figure 5.9 shows the maps of the expected initial probabilities of observing a transmissive barrier at each grid location. The maps were obtained by averaging over one hundred realizations of the T_{Mz} maps generated by transforming the corresponding GRFs using a unit step function and the three representations of the thresholds. The

maps of expected initial probability corresponding to Barrier1 (Fig. 5.9(a)) and Barrier2 (Fig. 5.9(b)) show that, on the average, the occurrence of either an impermeable or transmissive barrier is equally probable at any grid location. This is not surprising as the initial realizations of the T_{Mz} maps are not conditioned to any type of data and the expectation of the nonuniform thresholds for Barrier2 should be equal to the uniform threshold for Barrier1. As expected, the ensemble approximation of the expected initial probability map corresponding to the kriged thresholds (Fig. 5.9(c)) is qualitatively similar to kriged probability map (Fig. 5.7(a)) from which the threshold map for Barrier3 was obtained. Although not shown here, using either the unit step

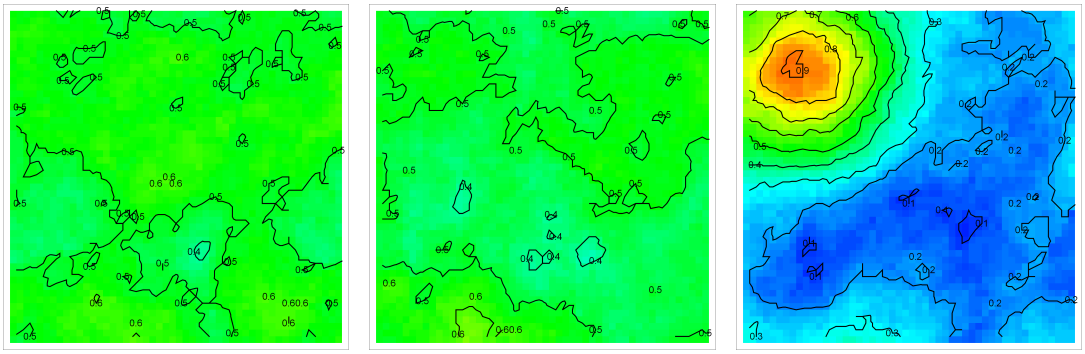

(a) Constant threshold. (b) Nonuniform threshold. (c) Kriged threshold.

Figure 5.9: Initial ensemble approximation of the expected probabilities of observing a transmissive barrier at a grid location. Probabilities from the constant and nonuniform thresholds are noninformative (≈ 0.5) while those from the kriged thresholds approximately honor regions with transmissive vs. impermeable barriers in the reference model fairly well.

or the form of the sigmoid function given in Eq. 5.4 to transform the initial realizations of the GRFs results in qualitatively similar maps of the vertical transmissibility barriers.

5.4 Data Assimilation Parameters

An ensemble size of 100 was utilized for the current data assimilation problem and each state vector, $\mathbf{y}_j$ is given by,

$$\mathbf{y}_j = \begin{bmatrix} \ln \mathbf{k}_h^T & \ln \mathbf{k}_v^T & \boldsymbol{\Upsilon}^T & \mathbf{p}^T & \mathbf{s}^T & \mathbf{d}_{sim}^T \end{bmatrix}^T, \tag{5.6}$$

where $\ln \mathbf{k}_h$ and $\ln \mathbf{k}_v$ are respectively vectors of the log-transformed horizontal and vertical permeabilities; vectors $\mathbf{p}$ and $\mathbf{s}$ are the gridblock pressures and saturations respectively; $\mathbf{d}_{sim}$ is the vector of simulated data comprising the bottomhole pressure data (p_{bh}) from Inj1, Prod3 and Prod4; liquid producing rate data (q_L) from Prod1 and Prod2; and water producing rate data (q_w) from all the producers. $\boldsymbol{\Upsilon}$ is a vector consisting of the GRFs used to parameterize the transformed vertical transmissibility multipliers and where applicable also includes the uncertain threshold values for the nonuniform threshold approach. Note that for EnKF without vertical flow barriers, the vertical transmissibility multiplier is not parameterized and the vector, $\boldsymbol{\Upsilon}$, in Eq. 5.6 is excluded from the state vector.

Production data were assimilated 15 times during the 545 days of production. The first and second sets of data were assimilated respectively at the 10th and 50th day of production. Subsequently, data were assimilated at 50-day intervals until the start of the shut-in period at day 500. During the shut-in phase (days 501–515) data were assimilated more frequently corresponding to seven day intervals of 501, 508 and 515 days. At each data assimilation timestep, a total of 18 production data were assimilated including, 6 bottomhole pressure data, 4 liquid rate data and 8 water producing rate data. The standard error of measurements in the bottomhole pressure and rate (q_L and q_w) data were respectively 10 psi and 10 STB/D. However, before water breakthrough a standard error of measurement of 10^{-3} STB/D was used for the water rate data. The measurement errors were assumed to be independent and identically distributed zero-mean Gaussian errors.

Uncertainty in the estimate of the porosity field is neglected in the investigation presented in this chapter as it has little impact on vertical communication between reservoir zones. As a result, the porosity values for all the models in the initial ensemble were set to the reference porosity values. The horizontal permeability fields are log-normally distributed with a mean of 5.75 and a standard deviation of 0.75. The geostatistical parameters used to generate the reference permeability model were also used to generate the initial realizations of the horizontal permeability (Table 5.2).

The vertical and horizontal permeabilities are assumed to be very weakly correlated. This condition on the weakness of the correlation between k_v and k_h is necessary for history matching problems with vertical transmissibility barriers as it ensures that the final k_h distribution remains geologically plausible. Recall that EnKF without parameterization of the vertical transmissibility adjusts the k_v values to account for the impact of vertical flow barriers on subsurface flow. Some types of data (such as shut-in BHP data) are roughly sensitive to only k_v in the vicinity of the well. If the correlation between k_v and k_h is strong, then adjusting the k_v field to match the shut-in BHP data, for example, will also force an incorrect adjustment to the k_h field. To illustrate, Fig. 5.10 shows the initial (gray) and final (green) histograms of $\ln k_h$ field from history matching a two-layer reservoir model with vertical transmissibility barrier using EnKF without parameterization of the vertical transmissibility. The vertical and horizontal permeability fields are correlated in this example (the correlation coefficient is about 0.2) and we note that the bimodal distribution of the final $\ln k_h$ field is much different from the initial distribution.

Consequently, realizations of the vertical permeability maps were obtained by first generating maps of the k_v/k_h ratio using the SGSIM technique and performing element-wise multiplication of the horizontal permeability fields with the corresponding k_v/k_h ratio maps. The geostatistical parameters (range, angle and anisotropic

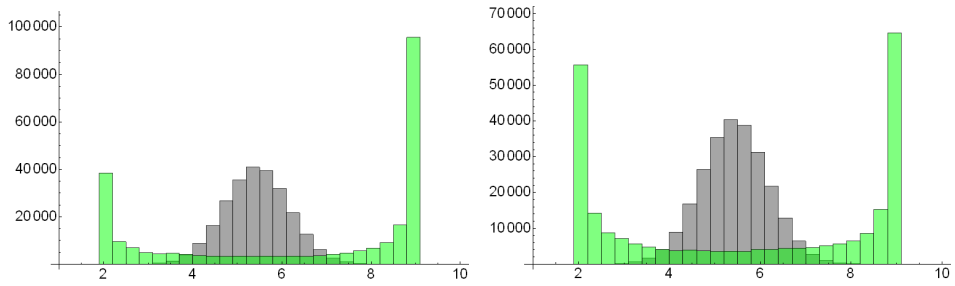

(a) Layer 1. (b) Layer 2.

Figure 5.10: Impact of strong correlation between k_v and k_h on the final (history matched) distribution of the $\ln k_h$ values from EnKF without parameterization. The initial histograms (gray bars) are clearly Gaussian while the final distributions are bimodal (green bars).

ratio) used for the SGSIM are presented in Table 5.2. The k_v/k_h variables are assumed to be log-normally distributed with (natural-log) mean of -5.17 and standard deviation of 1.15. An upper threshold of 1.0 was imposed on the simulated values of the k_v/k_h ratio. Scatterplots of the initial k_v vs. k_h values for the two layers in the reservoir model illustrate the weak correlation between both model variables (Fig. 5.11).

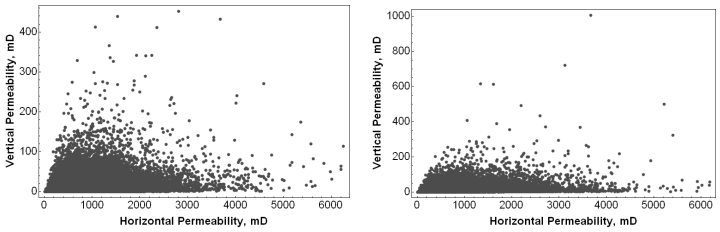

(a) ZoneA. (b) ZoneB.

Figure 5.11: Scatter plots of k_v vs. k_h showing the very weak correlation between k_v and k_h.

5.5 Algorithm for History Matching with Parameterization of the Vertical Transmissibility

In this section we present a brief summary of the steps in implementing EnKF with parameterization of the vertical transmissibility barriers for history matching reservoir

models with vertical flow barriers.

1. Generate an initial ensemble of n_e state vectors. Each state vector contains the vertical and horizontal permeabilities, the Gaussian random field used to parameterize the transformed vertical transmissibility multipliers and the spatially varying thresholds for the case where these are treated as uncertain.

2. Transform the vector of Gaussian variables to the corresponding vector of vertical transmissibility multipliers using either Eq. 5.3 or Eq. 5.4 depending on the choice of the nonlinear function that maps variables from the Gaussian domain to the multiplier (T_{Mz}) domain.

3. Using the k_v, k_h and T_{Mz} fields as inputs to the reservoir simulator, run the simulation for the n_e state vectors until the next data assimilation timestep.

4. Update the ensemble of state vectors (including the Gaussian representation of the T_{Mz} field and the uncertain thresholds where applicable) to match production data.

5. Check if the correction to the state vector by the EnKF (Step 4) is within the range for which linearization is appropriate. If the assumption of linearity is violated, reinforce the consistency between the updated model parameters and the dynamic variables using the EnRML filter.

6. If more data are available for assimilation, return to step 2, else, end history matching.

5.6 Analysis of Results

In this section, we present the history matching performance of the EnKF with four different configurations of the vertical flow barriers namely: (1) No Barrier, (2) Barrier1 (constant/uniform thresholds), (2) Barrier2 (nonuniform and uncertain thresholds), and (3) Barrier3 (kriged thresholds). For convenience, our analysis of the history matching performance will focus primarily on flow results from Prod4 as the impact of the uncertainty in the distribution of the impermeable barriers on history matching is most significant for this well. Additionally, due to similarity of the history matching results using either the unit step (Eq. 5.3) or the sigmoid function (Eq. 5.4) to transform the Gaussian variables to transmissibility multipliers, our discussion in this section will focus primarily on the results from using the unit step function. Note that the same initial realizations of k_v and k_h were used in all the approaches, with and without explicit parameterization of the transmissibility multiplier.

5.6.1 Matching the flowing and static bottomhole pressure data

The predicted bottomhole pressure data at Prod4 by the ensemble of initial (top row) and final (bottom row) models for the cases with and without explicit parameterization of the vertical flow barriers are presented in Figs. 5.12–5.13. The vertical lines in the prediction plots corresponding to the final ensemble (bottom rows of Figs. 5.12 and 5.13) demarcates the period with history matched data and the period of pure prediction. Throughout, the red curves are the ensemble predictions, the blue dots to the left of the green vertical line are the noisy data and the blue dots to the right of the green vertical line are predictions from the reference model. The error bars on the production data are three standard deviations of the standard error of measurements. Predictions were made by rerunning the simulator from time zero using the ensemble of initial or history matched models. The prediction of the initial BHP profile for the different barrier configurations (No Barrier, Barrier1, Barrier2 and Barrier3) are

fairly similar with very high prediction uncertainty. Note that none of the barrier configurations in the initial realizations is conditioned to static well data. After assimilating production data, the prediction uncertainty is reduced considerably and with the exception of a slight bias in the match to early time BHP data for Prod4B by the EnKF without parameterization of the vertical transmissibility (Fig. 5.13(e)), the predicted flowing BHP for the history matched period generally show a reasonable match to data for both producing intervals of Prod4.

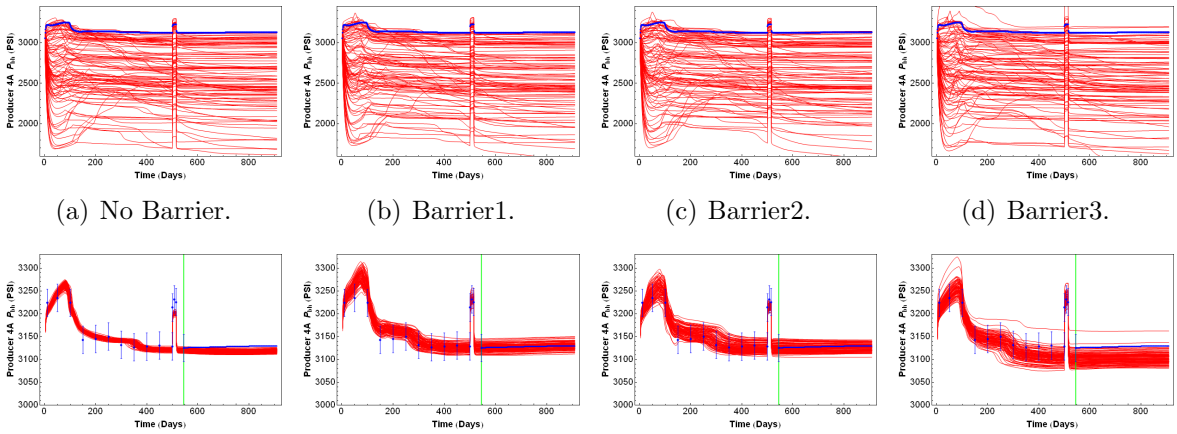

(a) No Barrier. (b) Barrier1. (c) Barrier2. (d) Barrier3.

(e) No Barrier. (f) Barrier1. (g) Barrier2. (h) Barrier3.

Figure 5.12: Predicted BHP data for Prod4A from the ensemble of initial (top row) and final (bottom row) models. The green vertical line demarcates the start of pure prediction period (bottom row). Blue dots are data and error bars are three standard deviations of the measurement error. The prediction of future data for EnKF with barriers generally match the reference prediction better than EnKF without barrier.

A useful measure of the history match quality is the ability of the final models to reasonably predict future data. Prediction of future BHP data for Prod4A (Fig. 5.12) seems quite reasonable for all cases although the results corresponding to the No Barrier and Barrier3 cases appear to be somewhat biased. For Prod4B, the predicted BHP data for the period after history matching from the EnKF without parameterization of the vertical transmissibility failed to match the reference prediction (Fig. 5.13(e)). Future predictions of Prod4B BHP data from EnKF with parameterization of the vertical transmissibility are generally better than EnKF without

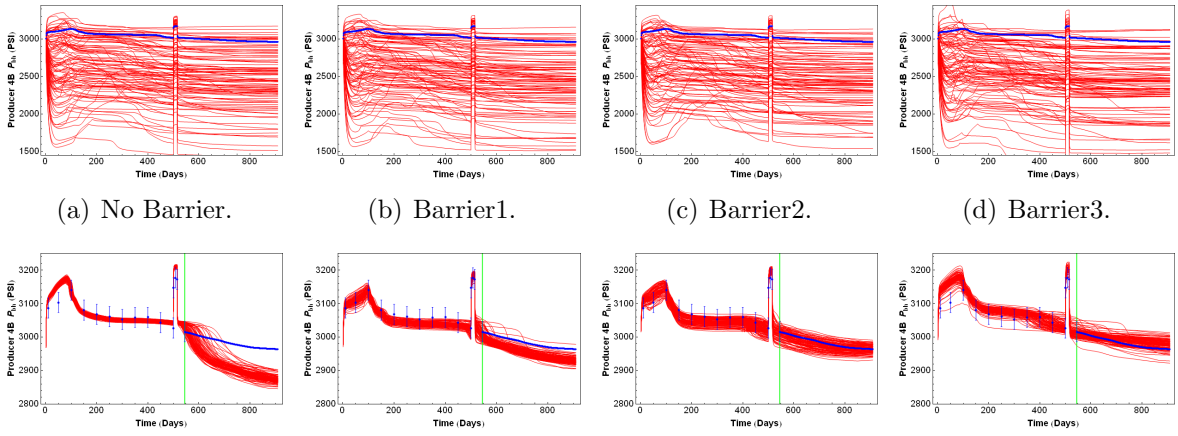

(a) No Barrier. (b) Barrier1. (c) Barrier2. (d) Barrier3.

(e) No Barrier. (f) Barrier1. (g) Barrier2. (h) Barrier3.

Figure 5.13: Predicted BHP data for Prod4B from the initial (top row) and final (bottom row) ensembles. The green vertical line demarcates the start of pure prediction period (bottom row). Blue dots are data and error bars are three standard deviations of the measurement error. Although the match to measurement for the history matching period was fair for EnKF without barriers, the future predictions are generally poor and do not match the reference prediction.

parameterization of the vertical transmissibility and match the reference prediction fairly well (Figs. 5.13(f)–5.13(h)). Although the predictions from Barrier1 in this case appears to be slightly biased (Fig. 5.13(f)), the trend in the ensemble predictions is similar to the reference prediction trend.

The flowing bottomhole pressure (p_{wf}) is generally sensitive to the presence of impermeable flow barriers in a reservoir. History matching, however, is such an ill-posed problem that the p_{wf} data can be generally well matched by adjusting the values of the log-normal k_v and k_h fields without accounting explicitly for the impermeable barriers. We have seen that the flowing bottomhole pressure data for top (Fig. 5.12(e)) and bottom (Fig. 5.13(e)) producing intervals of Prod4 were matched fairly well by the EnKF without parameterization of the vertical transmissibility. By contrast, the static zonal pressure is strongly sensitive to the values of the vertical transmissibility and thus to the presence or absence of impermeable flow barriers. Adjusting only the log-normal k_v and k_h fields is generally insufficient in obtaining a match to static zonal pressure data. We had observed from Fig. 5.4 that the static zonal pressure difference

in a well is higher for regions with impermeable vertical flow barriers compared to regions with zonal communication.

Figure 5.14 shows the predicted shut-in zonal BHP data for EnKF with and without parameterization of the vertical transmissibility barrier. The blue dots in the figure are the assimilated BHP data and the error bars are 3 standard deviations of the measurement error. The top and bottom rows of Fig. 5.14 correspond respectively to the top and bottom producing intervals of Prod4. The first column in Fig. 5.14 is the shut-in BHP data predicted by EnKF without vertical flow barriers and it is evident that the individual static BHP data are poorly matched. The shut-in pressure in ZoneA is underpredicted (Fig. 5.14(a)) and the shut-in BHP in ZoneB is overpredicted (Fig. 5.14(e)). This results from the pressure equilibration between both zones due the inability of EnKF without vertical flow barriers to eliminate zonal communication from adjusting only the log-Gaussian k_h and k_v during history matching. The predicted static BHP data from EnKF with parameterization of the vertical transmissibility (Figs. 5.14(b)–5.14(d) and Figs. 5.14(f)–5.14(h)) match the shut-in BHP data fairly well resulting in qualitatively better history matched solution compared to EnKF without parameterization of the vertical transmissibility.

During the shut-in period, static BHP measurements were assimilated at Prod3 and Prod4 in intervals corresponding to days 501, 508 and 515. To evaluate the performance of the four cases in matching the zonal BHP difference at the shut-in phase, the difference in the static zonal BHP at day 508 was computed for all the realizations and the histograms of the zonal BHP differences for all the cases are presented in Fig. 5.15. The gray and green bars are respectively predictions from the initial and final models. The red vertical line is the zonal BHP difference computed from the zonal BHP measurements assimilated at day 508. Note that the shut-in zonal BHP difference was not assimilated during history matching. The dashed lines delineate three standard deviations of the error propagated from estimating the shut-in zonal

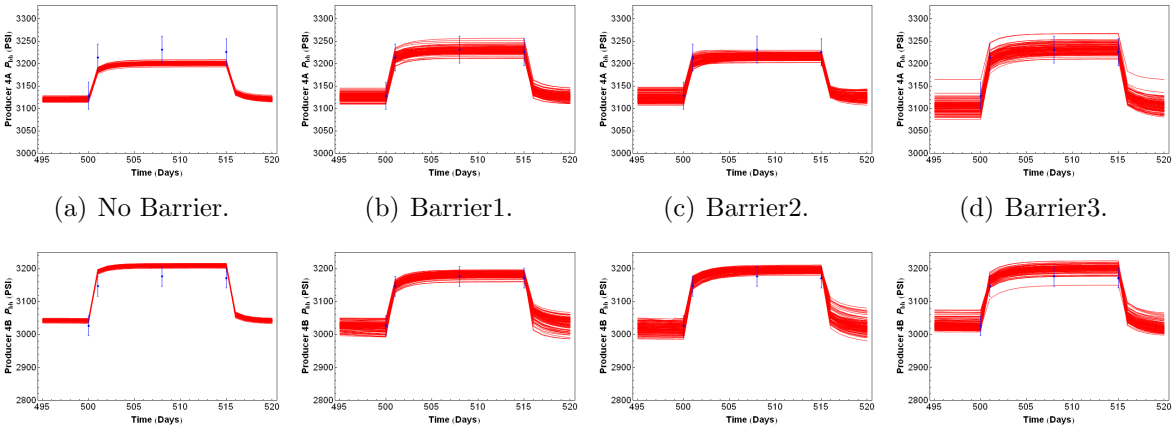

(a) No Barrier. (b) Barrier1. (c) Barrier2. (d) Barrier3.

(e) No Barrier. (f) Barrier1. (g) Barrier2. (h) Barrier3.

Figure 5.14: Prediction of shut-in BHP data from the top (top row) and bottom (bottom row) producing intervals of Prod4. Blue dots are historical data and error bars are three standard deviations of measurement error. The shut-in BHP data are poorly matched by EnKF with no barriers.

BHP difference from noisy measurements. We note that the observation error for the shut-in period is somewhat higher than one would normally use for shut-in BHP data. Figure 5.15(a) shows that Virtually all the initial models from the case with no barriers underpredicted the difference in shut-in BHP between top and bottom zones of Prod4 and are mostly outside three standard deviations of the measurement error. Similarly, some of the initial models for the cases with barriers also underpredicted the shut-in zonal BHP difference although a few of the initial predictions are within the range of uncertainty of the static zonal BHP difference computed from data (Figs. 5.15(b)–5.15(d)). Although it is not obvious from Fig. 5.15(d), the range of uncertainty in the initial prediction of the zonal BHP difference from Barrier3 is considerably higher than the initial predictions from the other barrier configurations with values as high as 400 psi.

For EnKF with no barriers, there is no improvement in the final predictions of the zonal BHP difference at day 508 compared to the initial predictions, although a reduction in the final prediction uncertainty was observed (Fig. 5.15(a)). Also, none of predictions from the final ensemble members matched the static zonal pressure

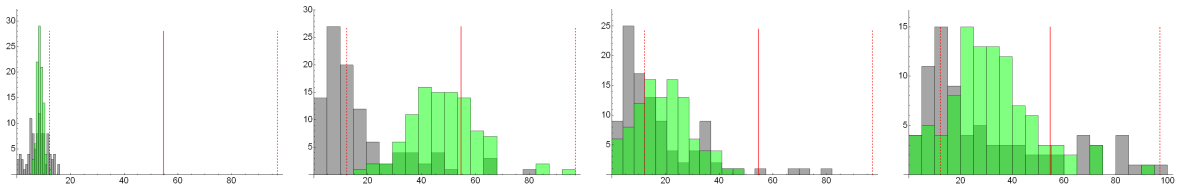

(a) No Barrier. (b) Barrier1. (c) Barrier2. (d) Barrier3.

Figure 5.15: Histogram of Prod4 shut-in zonal BHP difference predicted by the ensemble at day 508. The gray and green bars correspond respectively to the initial and final ensembles. The solid red vertical line is the reference zonal BHP difference the dashed lines are 3 standard deviations of the propagated error. Matches to the reference values are generally better when vertical flow barriers are parameterized than when they are not.

difference computed from data. By contrast, all three representations of the thresholds (Barrier1–Barrier3) from EnKF with barriers generally show an improvement in final predictions of the shut-in zonal BHP difference compared to the initial predictions. Additionally, the final predictions of the shut-in zonal BHP difference from EnKF with barriers match the measured shut-in zonal BHP difference better than EnKF without vertical flow barriers.

The root mean square errors of the shut-in zonal BHP difference at day 508 from Prod4 for all the cases are summarized in Table 5.6. The magnitude of the initial RMSE for all the cases are about the same except Barrier3, whose value is about twice the maximum RMSE of the three remaining cases. This is a result of some T_{Mz} realizations for Barrier3 having impermeable barriers with fairly significant lateral continuity resulting in much higher difference in the values of the individual shut-in pressures between zones. The initial and final RMSE of the static zonal BHP difference predicted by EnKF without vertical flow barriers have equal RMSE reflecting the difficulty in obtaining a good match to the individual shut-in zonal BHP data in this case. The final RMSE for Barrier1 is the lowest and is about the same magnitude as the propagated error from using noisy measurements of the static BHP data to obtain the expression for the static zonal pressure difference. The final

RMSE values of Barrier2 and Barrier3 are somewhat higher than the magnitude of the propagated error. In general the EnKF with barriers match the reference static zonal BHP difference better than EnKF without vertical flow barriers.

Table 5.6: Average RMSE of the shut-in BHP difference for Prod4.

	No Barrier (psi)	**Barrier1** (psi)	**Barrier2** (psi)	**Barrier3** (psi)
Initial Models	47	41	41	87
Final Models	47	14	34	28

5.6.2 Prediction of water producing rate data

Because the vertical transmissibility barrier is not parameterized for EnKF with no barriers, the uncertainty in the distribution of impermeable barriers is ignored during history matching. When the uncertainty in a model parameter is unaccounted for, compensatory updates are made to other model parameters resulting in fairly large (and sometimes unrealistic) corrections to these model parameters and final estimates of the model variables are incorrect. This may show up as a lack of acceptable match to data that are sensitive to the values of the incorrectly adjusted model variables. The water production rate data (alternatively, the water cut data) in a well are generally sensitive to the average value of the model properties (k_v and k_h in this case) between the injector and the producing well and also to the spatial distribution of the vertical flow barriers. If the estimates of these properties are incorrect, then the prediction of the water rate data will also be incorrect.

Figures 5.16 and 5.17 shows the water rate prediction from ensembles corresponding to the cases with and without vertical flow barriers. The water rate data from the top (Fig. 5.16(e)) and bottom (Fig. 5.17(e)) producing intervals of Prod4 predicted by the ensemble of final models from EnKF with no barriers for the period with production measurements (left of the vertical line) failed to give a reasonable match to production data. Also the future water rate predictions from both zones

are clearly biased and the reference model predictions are outside the spread of the ensemble predictions. Water rate predictions (for both periods of history matching and pure prediction) from the final ensemble appear to be generally better when vertical flow barriers are explicitly represented than when they are not. For the history matching period, the predictions from the EnKF with parameterization of the vertical transmissibility seem to match the water rate data reasonably well for Prod4A and Prod4B (Figs. 5.16(f)–5.16(h) and Figs. 5.17(f)–5.17(h)) although Barrier1 appears to be somewhat biased in water rate prediction for Prod4B. The future water rate prediction for the EnKF with barriers seem fairly reasonable and the reference predictions are for the most part contained within the spread of the ensemble.

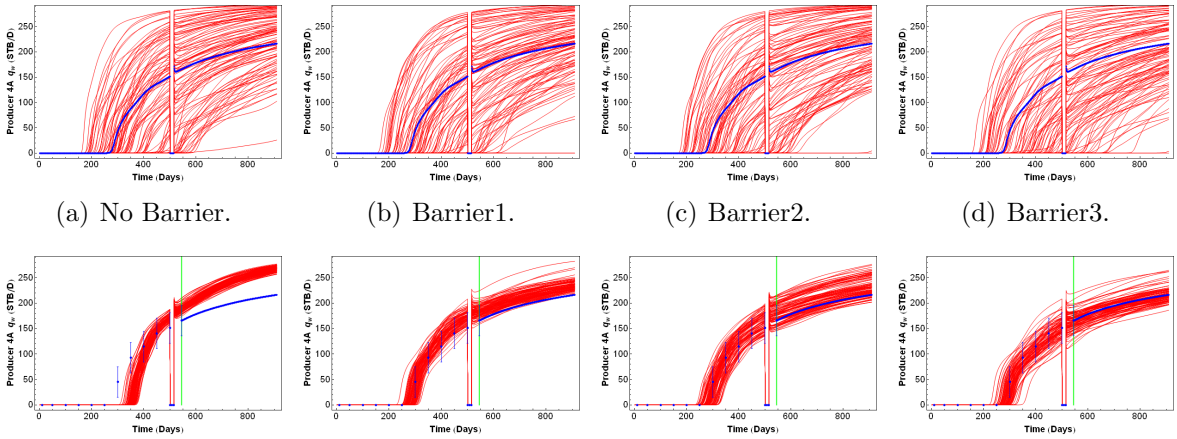

(a) No Barrier. (b) Barrier1. (c) Barrier2. (d) Barrier3.

(e) No Barrier. (f) Barrier1. (g) Barrier2. (h) Barrier3.

Figure 5.16: Predicted q_w data for Prod4A from the initial (top row) and final (bottom row) ensembles. The green vertical line demarcates the pure prediction period. Predictions from EnKF with no barrier are clearly very biased and do not match data very well. Predictions are generally better if the vertical flow barriers are accounted for.

Histograms of the predicted water breakthrough times at Prod4 obtained from the initial (gray bars) and final (green bars) models for all four cases are presented in Fig. 5.18. Recall that the breakthrough time was not assimilated during history matching, so the predicted breakthrough time from the reference model is shown by the red vertical line. The top and bottom rows of Fig. 5.18 correspond respectively to

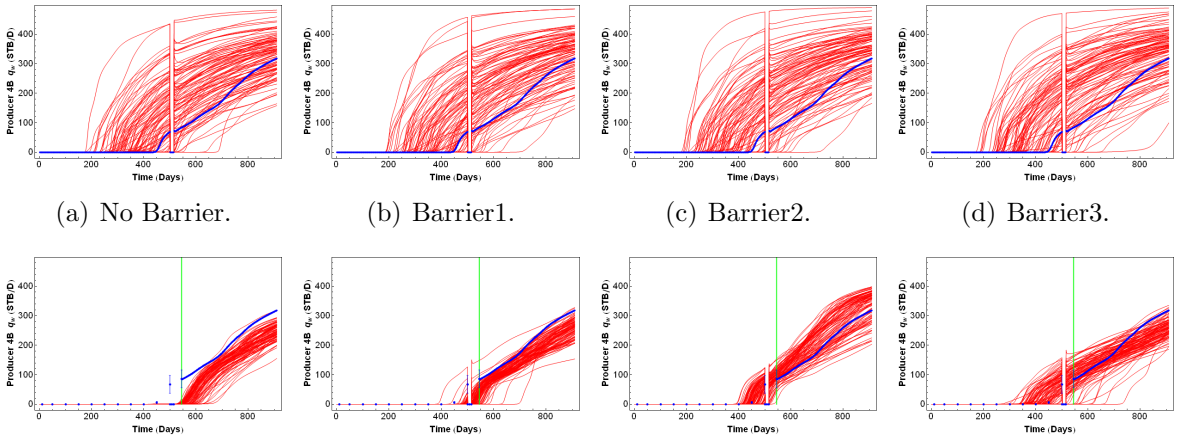

(a) No Barrier. (b) Barrier1. (c) Barrier2. (d) Barrier3.

(e) No Barrier. (f) Barrier1. (g) Barrier2. (h) Barrier3.

Figure 5.17: Predicted q_w data for Prod4B from the initial (top row) and final (bottom row) ensembles. The green vertical line demarcates the pure prediction period. Compared to EnKF with no barriers, prediction of water rate data is generally better for EnKF with barriers.

predicted breakthrough times at Prod4A and Prod4B. In all cases, the breakthrough times predicted by the ensemble of initial models exhibit a high degree of variability due to the significant initial uncertainty. The variability is generally reduced after assimilating production data. For the cases with barriers (Figs. 5.18(b)–5.18(d)), the final predictions of breakthrough times for Prod4A are closely distributed around the reference breakthrough time. For Prod4B, the predicted breakthrough time from the ensemble of final models with barrier parameterization are generally better than the initial predictions and match the reference values fairly well. Barrier2 seems to best match the reference prediction of the water breakthrough times in both zones. For EnKF without vertical flow barriers, the predictions of the water breakthrough times from the final models (Figs. 5.18(a) and 5.18(e)) were unable to match the breakthrough times predicted by the reference model.

To quantitatively assess the EnKF performance, with and without parameterization of the vertical transmissibility, in predicting the water breakthrough time, the RMSE of the breakthrough time predictions from the final ensemble is computed for Prod4A (Table 5.7) and Prod4B (Table5.8). Results for both zones show that

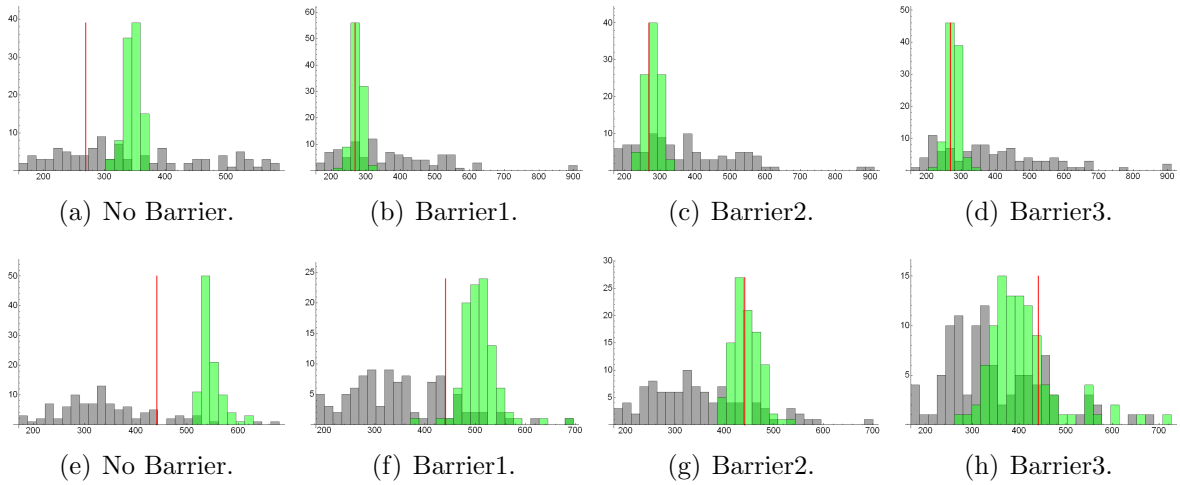

(a) No Barrier. (b) Barrier1. (c) Barrier2. (d) Barrier3.

(e) No Barrier. (f) Barrier1. (g) Barrier2. (h) Barrier3.

Figure 5.18: Histograms of predicted water breakthrough times from the top (first row) and bottom (second row) intervals of Prod4. The gray and green bars are from the initial and final ensembles. The red line is the reference value. Results are generally better if the uncertainty in vertical flow barrier is accounted for.

the final RMSE for the EnKF with barriers is generally lower than the final RMSE for EnKF without vertical flow barriers. Barrier1–Barrier3 have comparable RMSE values for predicted water breakthrough times in Prod4A (Table 5.7). However, for predicted water breakthrough times in Prod4B (Table 5.8), Barrier2 has the smallest RMSE compared to Barrier1 and Barrier3.

Table 5.7: RMSE of predicted water breakthrough time at Prod4A.

	No Barrier (days)	**Barrier1** (days)	**Barrier2** (days)	**Barrier3** (days)
Initial Models	140	171	172	197
Final Models	78	17	23	21

Table 5.8: RMSE of predicted water breakthrough time at Prod4B.

	No Barrier (days)	**Barrier1** (days)	**Barrier2** (days)	**Barrier3** (days)
Initial Models	136	135	140	140
Final Models	108	76	28	83

5.6.3 History match performance in matching other production data

Figure 5.19 shows the performance of the final ensemble from EnKF with no barriers (column 1) and EnKF with barriers (columns 2–3) in obtaining reasonable predictions of the following data for the period with production measurements and the period of pure prediction: (1) BHP data from the Inj1 (Figs. 5.19(a)–5.19(d) and Figs. 5.19(e)–5.19(h)), (2) BHP data from Prod3 (Figs. 5.19(i)–5.19(l) and Figs. 5.19(m)–5.19(p)) and (3) liquid rate data from Prod1 (Figs. 5.19(q)–5.19(t) and Figs. 5.19(u)–5.19(x)). The captions P1–P4 in Fig. 5.19 denotes Prod1–Prod4 and I1 denotes Inj1. The error bars are three standard deviations of the measurement noise. Consistent with observation in the previous sections, Fig. 5.19 shows that the match to data is generally better for the EnKF with barriers compared to EnKF with no barriers.

5.6.4 History matching performance from using a Sigmoid function

So far we have presented and discussed the history matching results based on using the unit step function to transform the Gaussian variables to transmissibility multipliers. For completeness we present some of the results from using a smooth approximation to the unit step function (Eq. 5.4) for transforming the Gaussian variables to transmissibility multipliers. For convenience, only the results from using threshold values that are spatially varying and also uncertain (Barrier2) are presented.

Figures 5.20(a)–5.20(b) show the prediction of the shut-in zonal BHP data and Figs. 5.20(c)–5.20(d) show the predicted water rate data for Prod4A and Prod4B. The history matching results in this case seem to match data reasonably well and the prediction of future data also seems reasonable (Fig. 5.20(c)–5.20(d)). Additionally, compared to similar results based on the unit step function (Figs. 5.14(c), 5.14(g), 5.16(g) and 5.17(g)), both approaches gave qualitatively similar predictive performance.

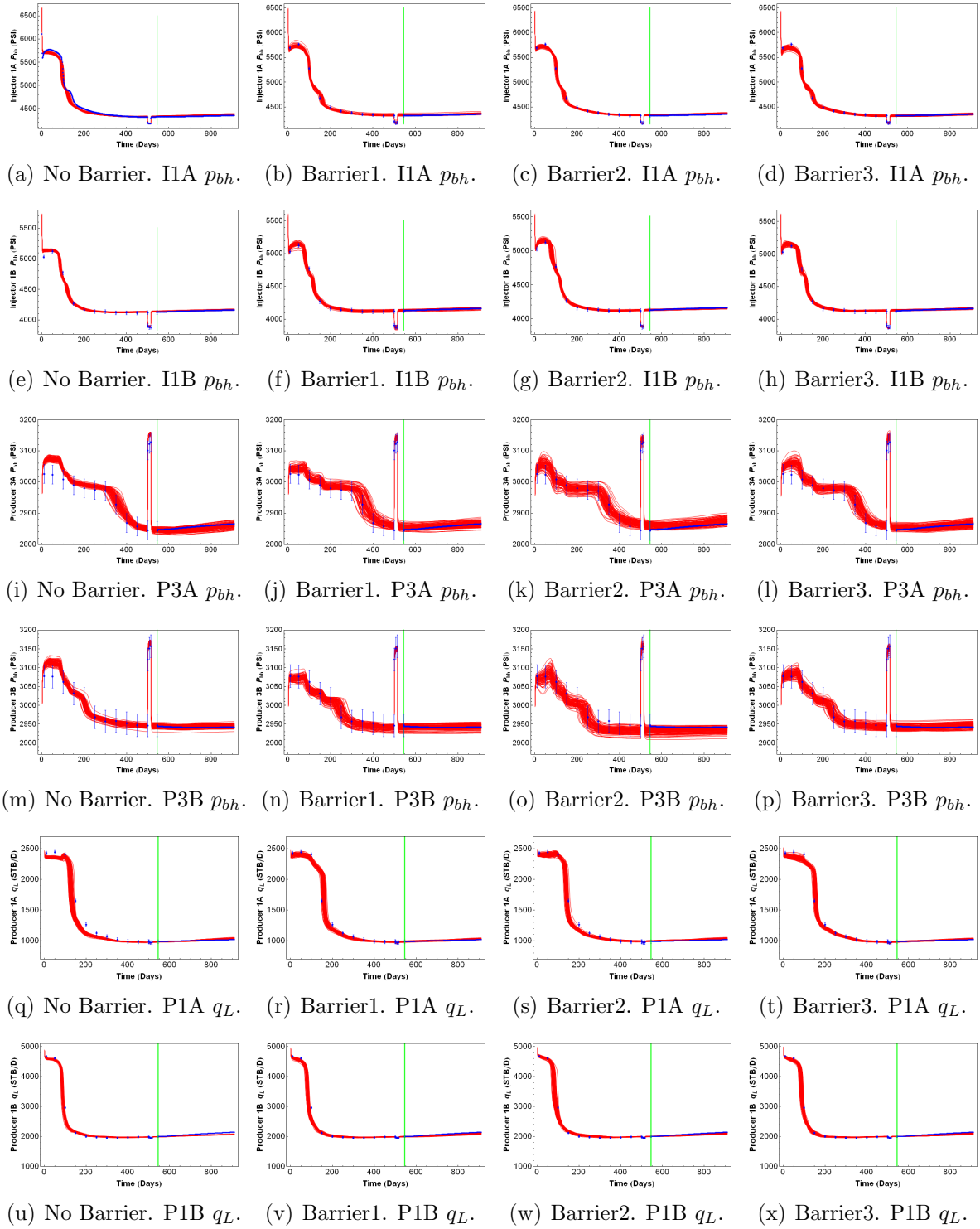

(a) No Barrier. I1A p_{bh}. (b) Barrier1. I1A p_{bh}. (c) Barrier2. I1A p_{bh}. (d) Barrier3. I1A p_{bh}.

(e) No Barrier. I1B p_{bh}. (f) Barrier1. I1B p_{bh}. (g) Barrier2. I1B p_{bh}. (h) Barrier3. I1B p_{bh}.

(i) No Barrier. P3A p_{bh}. (j) Barrier1. P3A p_{bh}. (k) Barrier2. P3A p_{bh}. (l) Barrier3. P3A p_{bh}.

(m) No Barrier. P3B p_{bh}. (n) Barrier1. P3B p_{bh}. (o) Barrier2. P3B p_{bh}. (p) Barrier3. P3B p_{bh}.

(q) No Barrier. P1A q_L. (r) Barrier1. P1A q_L. (s) Barrier2. P1A q_L. (t) Barrier3. P1A q_L.

(u) No Barrier. P1B q_L. (v) Barrier1. P1B q_L. (w) Barrier2. P1B q_L. (x) Barrier3. P1B q_L.

Figure 5.19: Final ensemble predictions of p_{bh} and q_L data for EnKF with and without barriers. "I" denotes the injector and "P" denotes a producer. The green vertical line demarcates the pure prediction period.

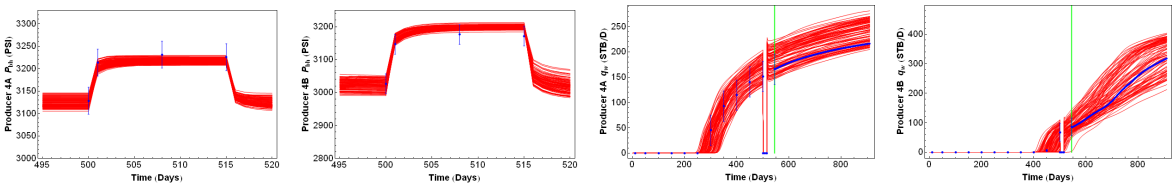

(a) Prod4A p_{bh}. (b) Prod4B p_{bh}. (c) Prod4A q_w. (d) Prod4B q_w.

Figure 5.20: History matching performance from using a sigmoid function and threshold values that vary spatially. The results are qualitatively very similar to those obtained by using the unit step function.

5.6.5 Updated geologic models

Two randomly selected realizations of the final vertical transmissibility multipliers, each from the three different barrier configurations for EnKF with parameterization of the vertical transmissibility, are presented in Fig. 5.21. The well locations are indicated by black dots and the well names are shown next to the dots with "**P**" denoting a producer and "**I**", an injector. The white and gray shades correspond to transmissibility multiplier values of one and zero respectively. The realizations of the final T_{Mz} maps (Fig. 5.21) are markedly different from the corresponding initial realizations (Fig. 5.8), reflecting the impact of data conditioning. Additionally, depending on the threshold representation used, the final estimate of the T_{Mz} map for the same realization is somewhat dissimilar. Nonetheless, compared to the realizations of the initial T_{Mz} maps, all the final maps appear to acceptably reproduce the major features in the reference T_{Mz} map (Fig. 5.3(c)). Some obvious features that are reproduced in all the final realizations include the presence of a transmissive barrier ($T_{Mz} = 1$) in the top left region and an impermeable barrier ($T_{Mz} = 0$) in southern region of the model and between Prod1 and Prod4.

It does seem from the foregoing that the global features in the updated field of vertical transmissibility multipliers (barrier) using EnKF with parameterization of the vertical transmissibility are qualitatively similar to those in the reference model. It is difficult, however, to generalize this conclusion based on inference made from only two

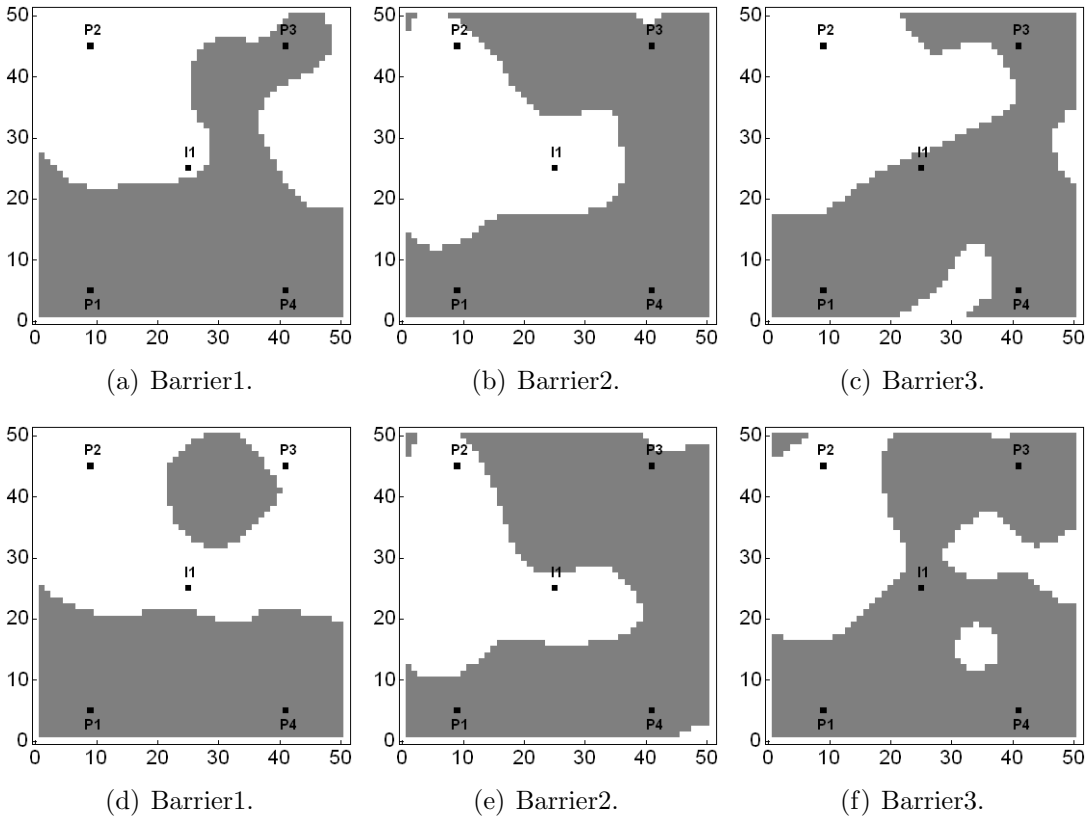

(a) Barrier1. (b) Barrier2. (c) Barrier3.

(d) Barrier1. (e) Barrier2. (f) Barrier3.

Figure 5.21: Conditional realizations of the vertical transmissibility barriers obtained by transforming the GRFs using the unit step function. Global features from the reference map (Fig. 5.3(c)) are reproduced in the T_{Mz} realizations.

randomly selected realizations out of an ensemble of one hundred final realizations. Consequently, the mean T_{Mz} maps obtained from the ensemble of final T_{Mz} maps are presented in Fig. 5.22 for the three cases from EnKF with parameterization of the vertical transmissibility. Each mean T_{Mz} map gives the ensemble approximation of the probability of finding a permeable barrier at each grid location. If the computed mean at any grid location is presented by $\overline{T}_{Mz}$, then values of decreasing $\overline{T}_{Mz}$ will correspond to an increasing probability of finding an impermeable barrier and vice-versa.

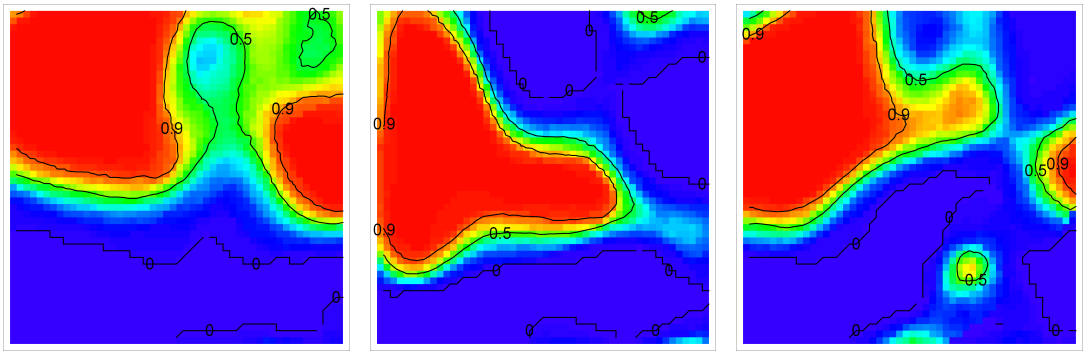

(a) Uniform thresholds. (b) Nonuniform thresholds. (c) Kriged thresholds.

Figure 5.22: Expected probability of observing a transmissive barrier at each grid location approximated from the final ensemble. The blue and red colors correspond respectively to values of 0 and 1. The final maps are very different from the initial probability maps (Fig. 5.9) and regions of high vs. low probabilities generally agree with the reference barrier distributions (Fig. 5.3(c)).

Compared to the initial $\overline{T}_{Mz}$ maps for Barrier1 and Barrier2 (Figs. 5.9(a)–5.9(b)) that were essentially non-informative (the initial $\overline{T}_{Mz}$ values at all the grid locations were ≈ 0.5) the final $\overline{T}_{Mz}$ maps (Figs. 5.22(a)–5.22(b)) are clearly more informative having distinct regions with very high and very low probabilities of permeable or impermeable barriers. The mean map of the final transmissibility multipliers for Barrier3 (Fig. 5.22(c)) is also quite different from the initial informative map (Fig. 5.9(c)) that was conditioned to soft data. Note that the soft data reflects the uncertainty in observing either a transmissive or impermeable barrier at any well location. Unlike

the initial probability maps, the final probability maps of the distribution of vertical flow barriers seem to acceptably represent the probabilistic distribution of the large scale barrier features in the reference T_{Mz} map (Fig. 5.3(c)).

In contrast to the EnKF with barriers, only the log-normal vertical permeability fields were updated by the EnKF without vertical flow barriers to account for the effect of impermeable barriers on fluid flow. To assess the ability of EnKF without vertical flow barriers to estimate the locations with impermeable barriers, we computed the vertical transmissibility at each grid location (Eq. 5.1) using the final estimate of vertical permeability for all the realizations and obtained an average vertical transmissibility map thereafter (Fig. 5.23(a)). For convenience we neglected both the phase-dependent and constant terms in evaluating the gridblock transmissibilities. For better visualization of the gridblock transmissibility values in the map, the natural log values of the average transmissibility were plotted. For comparison, the reference (natural-log) transmissibility map is also presented (Fig. 5.23(b)). Zero transmissibility values in the reference map were set to the minimum average value in the final log-transformed transmissibility map (Fig. 5.23(a)) for EnKF without vertical flow barriers. Clearly, the final estimate of the average transmissibility map for EnKF with no barrier (Fig. 5.23(a)) looks nothing like the reference transmissibility map (Fig. 5.23(b)).

As previously noted, one may expect that the updates to the model variables by EnKF with no barrier could potentially be incorrect since the uncertainty in the distribution of the vertical flow barriers was not accounted for during history matching. Figure 5.24 shows the final estimates of the mean k_h fields from EnKF with and without parameterization of the vertical flow barriers. Compared to the final estimates of the mean k_h field for ZoneA (Figs. 5.24(b)–5.24(d)) and ZoneB (Figs. 5.24(f)–5.24(h)) from EnKF with parameterizations of the vertical transmissibility barrier, the corresponding estimates from EnKF without parameterization (Figs. 5.24(a) and 5.24(e))

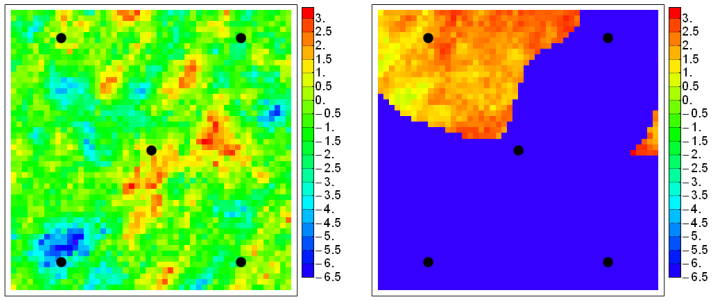

(a) EnKF with no barriers. (b) Reference.

Figure 5.23: Reference transmissibilities and average transmissibilities from without parameterization of vertical flow barriers plotted on a natural-log scale. The estimate of the average transmissibility is clearly very different from the reference values.

show evidence of extreme values of k_h. These extreme values reflect the effect of compensatory updates to the horizontal permeability field during history matching. Note that the top row of Fig. 5.24 show the mean k_h maps for ZoneA and the bottom row show the mean k_h maps for ZoneB. Although not shown here, the initial mean maps of k_h for both zones are essentially featureless with the k_h values approximately equal to the prior mean value of 5.75. The final mean k_h maps from ZoneA (Figs. 5.24(b)–5.24(d)) and ZoneB (Figs. 5.24(f)–5.24(h)) estimated from the EnKF with parameterization of the vertical transmissibility are qualitatively similar to the reference k_h maps (Fig. 5.3(a)–5.3(b)). The spatial distribution of the high vs low horizontal permeability values generally follow the spatial patterns in the reference model.

5.7 Chapter Summary

For reservoirs with impermeable flow barriers, incorporating the uncertainty in the representation of vertical transmissibility barriers is important for reservoir flow simulation and for reliable prediction of reservoir performance. In the standard implementation of the EnKF technique, the log-normal vertical permeability of the gridblocks are usually adjusted to account for the influence of vertical transmissibility barriers

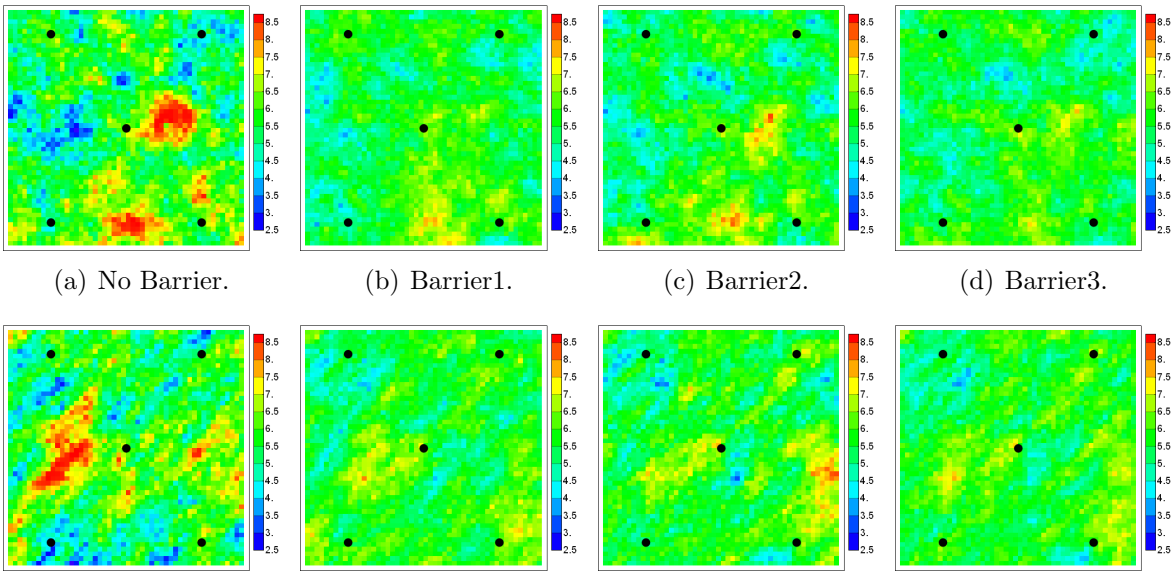

(a) No Barrier. (b) Barrier1. (c) Barrier2. (d) Barrier3.

(e) No Barrier. (f) Barrier1. (g) Barrier2. (h) Barrier3.

Figure 5.24: Estimates of the final mean permeability distribution for ZoneA (top row) and ZoneB (bottom row). EnKF with no barriers shows evidence of extreme k_h values arising from compensatory updates to the k_h field from inadequate parameterization.

on history matching results. In general the history matching results based on adjusting the k_v values will only be correct for reservoirs without sealing barriers. We have shown that in the presence of an impermeable barrier, EnKF without parameterization of the vertical transmissibility barrier fails to match data and also makes incorrect, compensatory changes to the model parameters.

In this chapter, we presented three approaches, which allow for the uncertainty in the distribution of the vertical transmissibility barrier to be incorporated in a consistent way in the ensemble Kalman filter routine. The approaches are based on parameterizing the transformed vertical transmissibility multipliers as correlated Gaussian random variables. Transformation of the Gaussian variables to transmissibility multipliers was achieved using either the unit step function or a form of the sigmoid function. Based on this parameterization, impermeable barriers are obtained by setting the multiplier value to zero and transmissive barriers are obtained by setting the multiplier to a value of one. Vertical flow at grid locations with transmissive

barriers is controlled by vertical permeabilities estimated by EnKF.

Using three different specifications of the prior probability of randomly sampling either an impermeable or permeable barrier at each grid location, different parameterizations of the vertical transmissibility was obtained. The first was a non-informative specification of prior probabilities such that the occurrence of a permeable or impermeable barrier at each grid location is equally probable. The second specification considered the threshold value to be uncertain and also a function of location. The third specification was based on using soft information on the uncertainty of the barrier types at the well location to obtain a kriged map of prior probabilities in all grid locations. The EnKF based on all three cases were generally better at history matching production data and obtaining consistent estimates of the model parameters compared to EnKF without parameterization of the vertical transmissibility.

Based on the results presented here, it is difficult to conclude whether any one of the three approaches to parameterizing the vertical flow barrier is better without further experimentation. However, it does seem that there is no advantage in conditioning the prior probability of impermeable vs. permeable barrier to soft data at the well locations if the geostatistical parameters of the Gaussian random field are correctly specified.

CHAPTER VI

TWO-STAGE ENKF FOR HISTORY MATCHING WITH MULTIPLE MODES

6.1 Background

The Bayesian approach provides a convenient framework for integrating dynamic and static data with the prior model PDF to obtain a formal expression for the conditional model PDF. The randomized maximum likelihood (Oliver et al., 1996) has often been used to generate realizations of the conditional reservoir model, representing an approximate sampling of the posterior PDF. The prior PDF, in this case, is assumed to be Gaussian but the relationship between the model variables and predicted data may be nonlinear. For linear problems with prior Gaussian PDF, the EnKF is equivalent to the randomized maximum likelihood (RML) as the number of ensemble members (realizations of the reservoir models) become very large (Zafari and Reynolds, 2007). Consequently for these types of problems, the EnKF correctly samples the posterior PDF of the conditional models. The method has also been shown to perform quite well on nonlinear reservoir characterization problems with Gaussian priors (Gu and Oliver, 2005; Lorentzen et al., 2005; Gao et al., 2006). Gao et al. (2006) showed that for the well known PUNQ-S3 problem (Floris et al., 2001), the EnKF gave similar characterization of prediction uncertainty as the RML method. Considering that the RML method is computationally more expensive, requiring computation of the gradient or the sensitivity matrix and a large number of iterations to generate a single conditional model, the EnKF performance was indeed encouraging. For history matching problems with multimodal conditional PDF, the history matched models

from the EnKF do not represent a correct sampling of the multimodal PDF (Zafari and Reynolds, 2007) and use of an iterative EnKF with explicit computation of the sensitivity matrix (Li and Reynolds, 2009) is necessary to generate an approximate sampling of the posterior PDF. Because of the need to evaluate sensitivities and the requirement to iterate, the iterative EnKF is computationally more expensive than the standard EnKF.

Usually, model priors that are non-Gaussian have to be transformed to satisfy the EnKF Gaussianity assumption. A number of examples in literature include the following: (1) parameterizing transformed transmissibility multipliers as Gaussian (Evensen et al., 2007; Seiler et al., 2009); (2) representing vertical transmissibility barriers as Gaussian random fields (Agbalaka and Oliver, 2010); (3) parameterization of transformed facies variables as Gaussian variables using the truncated pluriGaussian technique (Liu and Oliver, 2005b; Agbalaka and Oliver, 2008; Zhao et al., 2008) or the level sets method (Moreno et al., 2008; Lorentzen et al., 2009); (4) estimating multimodal inter-facies properties using the "pseudo-model" approach to ensure that the Gaussian assumption is approximately honored at each data assimilation timestep (Agbalaka and Oliver, 2009). Sun et al. (2009a) combined the local ensemble transform filter (Bishop et al., 2001; Ott et al., 2004; Hunt et al., 2007) with a Gaussian mixture model (GMM) clustering technique similar to the cluster EnKF (Smith, 2007) to obtain a consistent update to the multimodal permeability field using the deterministic EnKF (Sakov and Oke, 2008).

In this chapter we consider the problem of using the ensemble Kalman filter for history matching a low-order reservoir model with multiple modes. Because the EnKF uses only the mean and the covariance to update model and state variables, the technique fails to give an acceptable history matching solution to the multimodal history matching problem presented in this paper. By including a second-stage EnKF, in which the history matching process is initialized by sampling around a conditional

mode of the posterior PDF, the history matching results and the conditional estimates of the model variables were generally improved. All the primary model variables in the reservoir model are non-Gaussian so to ensure consistency with the EnKF assumption of Gaussianity, the transformed model variables were parameterized as independent and identically distributed zero-mean Gaussian random variables with unit variance. By utilizing various forms of the shifted sigmoid function in which the domain is the span of the Gaussian values and the range space is a bounded space of the actual model variables, consistent mapping to and from the actual model space is achieved. To ensure that members of the initial ensemble were as diverse as possible, initial sampling was done using low-discrepancy sequence sampling, specifically, the shuffled Halton sequence sampling.

6.2 The Two-Stage Ensemble Kalman Filter, TEnKF

When new data are available for assimilation, the EnKF technique updates the model variables by finding the optimal (weighted) least squares estimate that best approximates the linear relationship between the state vector and the measured data. The EnKF technique is optimal if (1) the probability distribution of the prior state vectors is approximately multivariate Gaussian; and (2) the relationship between the state vector and predicted data is approximately linear (Gaussian likelihood). If any or both of these assumptions fail to hold, the posterior PDF of the models/state vectors will be non-Gaussian and the EnKF reduces to a "best linear-in-the observations" updating technique (Wikle and Berliner, 2007) leading to a suboptimal EnKF performance irrespective of the ensemble size.

A simplified schematic representation of the EnKF update scheme is presented in Figs. 6.1(a)–6.1(c). The model-data relationship ($\mathbf{d} = \mathbf{g}(m)$) in this case is nonlinear (blue curve) and the posterior PDF of the model ($p(\mathbf{m})$) is non-Gaussian and multimodal. The dotted horizontal line, which runs through all the plots is the datum

($\mathbf{d}_{obs}$) predicted by the true model ($\mathbf{m}_{true}$). The true model is generally not observable, only the response from the model may be observed. The axes **D** and **M** may be regarded respectively as the vector spaces of the data and model. During the EnKF update step, the Kalman gain is computed by finding the best-linear fit to the cloud of points formed by the state vector and the corresponding predicted data (Fig. 6.1(a)). Because of the nonlinear model-data relationship the linearized approximation from the ensemble is a very poor representation of relationship. Once determined, the Kalman gain provides the optimum, linear-in-the observations, direction of change to the model variables required to match the observed data, $\mathbf{d}_{obs}$ (Fig. 6.1(b)). Because the true relationship between model variables and predicted data is nonlinear in this case, the update to the models will be incorrect and forecasts from the updated model variables will generally not match the observed data very well (Fig. 6.1(c)). Also note that some of the models that were initially close to $\mathbf{m}_{true}$ are adjusted further away from the truth after the update step and the final ensemble will generally represent a poor sampling of the posterior PDF.

The idea behind the two-stage EnKF is to implement a version of the standard EnKF, which utilizes the best-linear-in-the-observations properties of the standard EnKF to obtain an acceptable history match solution. The technique consists of two-sequential stages namely: (1) a first-stage EnKF, which essentially implements the standard EnKF (Figs. 6.1(a)–6.1(c)), and (2) a second-stage EnKF, which is analogous to a localized randomized maximum likelihood filter. The goal of the second-stage EnKF is to obtain an improvement to the history matching results from the first-stage EnKF by regenerating realizations of the model variables that are sampled close to one of the modes of the conditional PDF. The resampled model variables are the initial ensemble for the second-stage EnKF. The first step (Fig. 6.1(d)) in the second-stage EnKF is to select a best model, $\mathbf{m}_s$, from the first-stage EnKF that

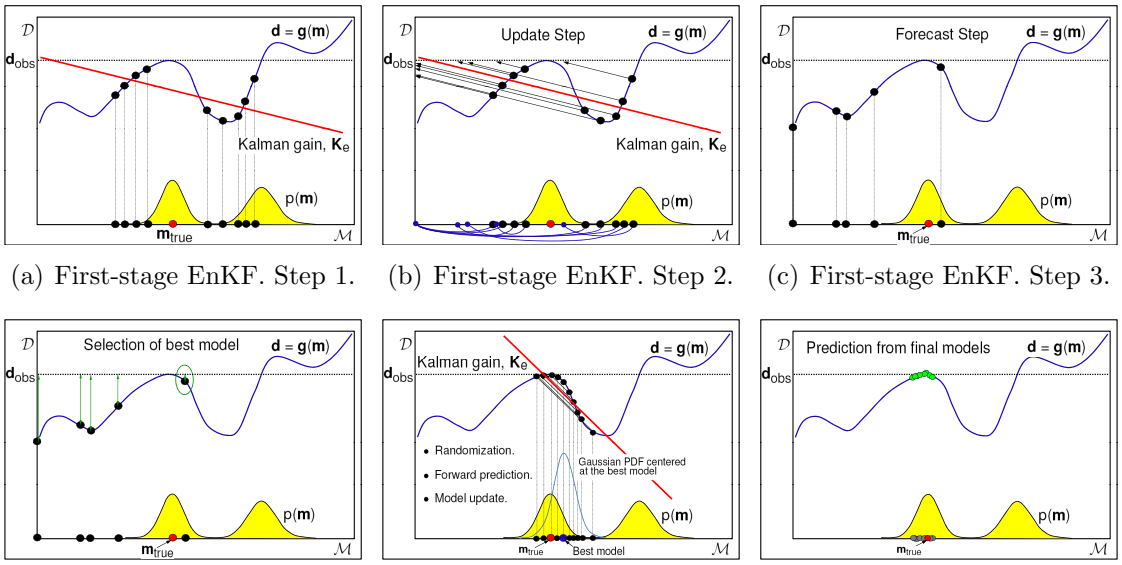

(a) First-stage EnKF. Step 1. (b) First-stage EnKF. Step 2. (c) First-stage EnKF. Step 3.

(d) Second-stage EnKF. Step 1. (e) Second-stage EnKF. Step 2. (f) Second-stage EnKF. Step 3.

Figure 6.1: Simplified schematic representation of the first- (top row) and second-stage (bottom row) EnKF. The blue curve is the nonlinear data model. $\mathbf{d}_{obs}$ is the measured data and $p(\mathbf{m})$ is the multimodal posterior PDF. $\mathbf{m}_{true}$ is the reference/true model, which is usually unknown.

satisfies the following condition,

$$\underset{\mathbf{m}_s}{\operatorname{argmin}} f(\mathbf{m}_s) := \{\mathbf{m}_s \mid \forall \mathbf{m}_i : f(\mathbf{m}_i) \geq f(\mathbf{m}_s); 1 \leq i \leq n_e\}, \tag{6.1}$$

where

$$f(\mathbf{m}) = (\mathbf{g}(\mathbf{m}) - \mathbf{d}_{\text{obs},*})^T \mathbf{C}_D^{-1} (\mathbf{g}(\mathbf{m}) - \mathbf{d}_{\text{obs},*}),$$

evaluates the data mismatch magnitude, $\mathbf{g}(\mathbf{m})$ is the predicted data by the model $\mathbf{m}$ and $\mathbf{d}_{\text{obs},*}$ is the perturbed noisy measurement assimilated by $\mathbf{m}_*$ during history matching. The selected model, $\mathbf{m}_s$, represents the ensemble approximation of the maximum a posteriori probability (MAP) estimate from the first-stage EnKF (Fig. 6.1(d)). The approximate MAP estimate, $\mathbf{m}_s$, is used as the mean of a multivariate Gaussian PDF ($\mathcal{N}(\mathbf{m}_s, \mathbf{C}_{M,s})$) for regenerating the ensemble of model variables for the second-stage EnKF (Fig. 6.1(e)). This process is essentially a randomization about the approximate MAP for generating realizations of the reservoir model. Note that for resampling realizations of the low-order reservoir model used in this paper,

the covariance matrix ($\mathbf{C}_{M,s}$) was specified to ensure that the resampled realizations are in a local region around the ensemble approximation of the MAP. Further details on how the covariance matrix was specified for the current problem are presented in section 6.6. By generating initial realizations for the second-stage EnKF around a MAP estimate approximated from the ensemble, the probability that the linearized model-data relationship will approximately honor the true relationship in the neighborhood of the MAP is increased (Fig. 6.1(e)). Consequently, predictions from the updated models after assimilating data will potentially match data very well and all the ensemble members will be valid samples from the multimodal posterior PDF (Fig. 6.1(f)) even though they may not sample the complete PDF correctly.

We note, based on the foregoing, that predictions from the ensemble of final models from the second-stage EnKF may not quantify the full prediction uncertainty but remark that the goal is primarily to obtain acceptable matches to production measurements, which may be used to quantify some local uncertainty. Later, we present discussions in section 6.10 on the possibility of improving the ability of TEnKF to better approximate the prediction uncertainty by regenerating the initial reservoir models around several modes instead of a single mode. There are three noteworthy implications of generating initial realizations that are fairly close to the ensemble approximation of the MAP (Eq. 6.1) for initializing the second-stage EnKF.

1. The range of adjustments to the model variables at the update steps are further constrained such that linear updates make sense.

2. The relationship between the resampled models and the simulated response from the models can reasonably be approximated as linear in the neighborhood of the ensemble approximation of the MAP estimate.

3. The optimality conditions for the EnKF update step are approximately honored.

6.3 Simulation Model Description

The simulation model is a two-phase (oil and water) black oil model with two layers; Layer1 is the top layer and Layer2, the bottom layer. Two wells, an injector and a producer, are completed in both layers and are located diagonally across each other (Fig. 6.2(a)). Water injection is controlled by a constant surface rate target of 3000 STB/D and production is at a constant bottomhole pressure (BHP) constraint of 500 psi. There are two non-structural faults (Fault1 and Fault2) each about one-third the length of the model and transverse the model in an east-west direction (Fig. 6.2(b)). Fault1 is closest to the injector and Fault2, to the producer. Two different environments of deposition (EODs) are present in model (Fig. 6.2(c)) and include a high permeability channel (EOD2 or channel-axis) embedded in a low permeability background (EOD1 or channel-margin). The channel-axis trends roughly in a north-south direction and consists of two mirror-image structures, which are displaced laterally and vertically to form an **x**-shaped profile (Fig. 6.2(d)). There is a small area of overlap between the channels axes in both layers, located roughly at the center of the model, which provides a continuous fluid conduit for injected water from the injector to the producer. The top and bottom completions of the injector are respectively in the channel-axis and channel-margin while for the producer, the converse holds. Also, both faults in the model cut through parts of the channel-axes in both layers but more so in Layer2 where almost the entire channel-axis width is transverse by the faults. There is no structural uncertainty associated with the spatial configuration and locations of the EODs and the faults in the model.

Production lasted for 9990 days and water injection started from the first day of production. Measurements of bottomhole pressure at the injector, water production rate (q_w) and oil production rate (q_o) at the producer were taken every ninety days and the production history is presented in Fig. 6.3. The production history shows a steady oil production rate $\approx$ 3000 STB/D in the first 2700 days of production. This

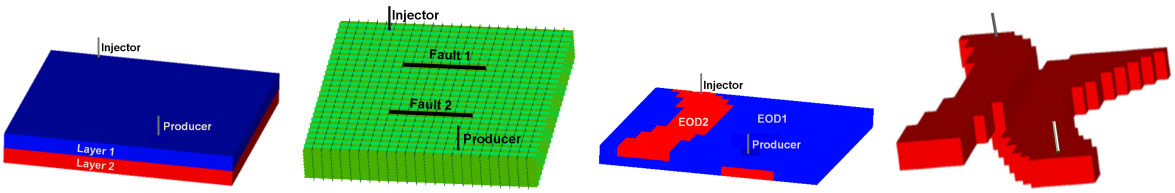

(a) Reservoir units. (b) Faults. (c) EODs. (d) Channel-axis structure.

Figure 6.2: Reservoir simulation model showing the different features that are present.

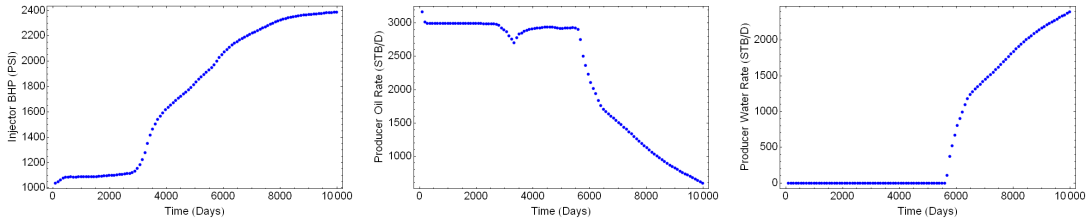

(a) BHP. (b) Oil rate. (c) Water rate.

Figure 6.3: Predictions from the reference model showing the predicted BHP data from the injector and the predicted oil and water rate data from the producer.

was followed by a steady decline over a period of 630 days to a rate $\approx$ 2700 STB/D and then a 540-day increase to a constant oil production rate of 2900 STB/D until the water breakthrough time. Following the water breakthrough time, a consistent and steady decline in oil rate is evident (Fig. 6.3(b)). The start of the short decline in oil production rate coincides with the start of a steady increase in the injector bottom-hole pressure, which continued throughout the 9990 days of production (Fig. 6.3(a)). The increase in the injector BHP is a response to the water front arrival at Fault2 (Fig. 6.2(b)) which constitutes a transmissibility barrier. Since the injector was operated at a constant surface injection rate, an increase in injector BHP was necessary to force some of the injected water through the low permeability fault barrier and the rest to migrate laterally from the channel-axis in Layer2 to the low permeability channel-margin in the same layer. Note that this was also responsible for the decline and subsequent increase in the oil flow rate history.

6.3.1 Specification of the uncertain model parameters

The model parameters that were estimated during history matching include:

1. Vertical transmissibility multipliers at the interfaces of the EODs namely: EOD1–EOD1, EOD1–EOD2 and EOD2–EOD2. Throughout the terms vertical transmissibility and connection transmissibility will be used interchangeably.

2. Fault transmissibility multipliers for Fault1 and Fault2. Only one transmissibility multiplier is used for each fault.

3. Porosity (ϕ) and permeabilities (k_v and k_h) of the two EODs. The petrophysical properties are assumed uniform in each EOD.

In formulating the history matching problem, it was assumed that empirical geologically-based relationships between the petrophysical properties (ϕ, k_v and k_h) and the net-to-gross in the EODs are available (Fig. 6.4). By making this assumption, the history matching problem becomes somewhat more realistic but also a bit more difficult and nonlinear. Throughout the form of the empirical relationships between the petrophysical properties and the NTG values as presented in Fig. 6.4 will be referred to as an NTG-Table. Given any NTG value, the corresponding values of k_h, k_v and ϕ may be determined from the NTG-Table in Fig. 6.4(a).

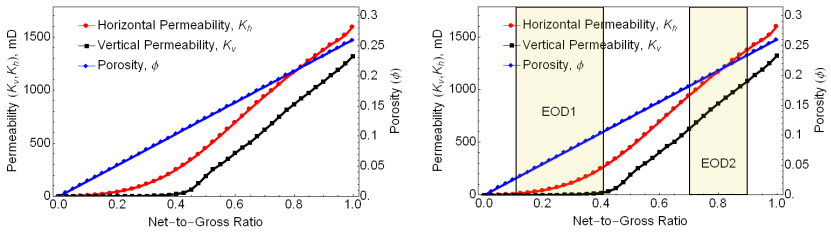

(a) NTG-Table (b) Uncertainty range.

Figure 6.4: Empirical relationship between petrophysical properties and net-to-gross (NTG). Range of uncertainty in EOD NTG is also shown (Fig. 6.4(b)).

The uncertainty in the porosity values of the EODs are assumed implicit in the uncertainty of the NTG values in each EOD. Essentially once the NTG values of the EODs are determined from history matching, the corresponding porosities may be obtained from NTG-Table. By contrast, the uncertainty in the k_h and k_v values of the EODs are implicit not only in the uncertainty of the NTG value but also in the uncertainty of the left ordinate values in the NTG-Table (Fig. 6.4(a)). Essentially, for any fixed estimate of the NTG value, the corresponding k_h and k_v values in the NTG-Table are correct up to an unknown multiplicative constant. The NTG-Tables in Fig. 6.4 correspond to the case with a multiplicative constant equal to 1. Note that applying a constant multiplier to the k_h and k_v values in the NTG-Table does not change the functional relationship between the permeabilities and the NTG values. Throughout the unknown multiplicative constant will be referred to as a permeability multiplier.

The net-to-gross in the channel-axis (EOD2) will be higher than the net-to-gross in the channel-margin (EOD1) and this is reflected in the range of uncertainty of the NTG values in both EODs (yellow boxes in Fig. 6.4(b)). For each EOD, the same permeability multiplier is used to scale the corresponding k_h and k_v values (different permeability multipliers are used for both EODs). We note that while it is a fairly common practice to adjust the uncertain k_h, k_v and ϕ values directly to obtain a match to data, we chose not to do so here as it may violate the empirical relationships in the NTG-Table. The parameters that are adjusted during history matching to obtain estimates of k_h, k_v and ϕ are the NTG values and the multipliers of k_h and k_v in the EODs. Unrealistic changes to the model variables during history matching are avoided by imposing plausible bounds on the range of the uncertain parameter (Table 6.1). Also initial best guess values for all the model variables are assumed to be available. In all, a total of 11 model parameters were estimated during history matching.

Table 6.1: Bounds on the initial model uncertainty.

	Uncertain model parameters	Min.	Best Guess	Max.
1	Fault1 transmissibility multiplier	0.0001	0.1	1.0
2	Fault2 transmissibility multiplier	0.0001	0.1	1.0
3	Connection transmissibility (EOD1–EOD1)	0.0001	0.01	0.1
4	Connection transmissibility (EOD1–EOD2)	0.0001	0.05	0.1
5	Connection transmissibility (EOD2–EOD2)	0.1	0.1	1.0
6	EOD1 net-to-gross ratio. Layer1	0.1	0.2	0.4
7	EOD2 net-to-gross ratio. Layer1	0.7	0.8	0.9
8	EOD1 net-to-gross ratio. Layer2	0.1	0.2	0.4
9	EOD2 Net-to-Gross Ratio. Layer2	0.7	0.8	0.9
10	Permeability multiplier. EOD1	0.5	1.0	2.0
11	Permeability multiplier. EOD2	0.5	1.0	2.0

6.4 Gaussian Parameterization of the Transformed Model Variables

The optimality of the updates to the model variables (state vector) by the EnKF is predicated on an assumption that the prior ensemble of state vectors at each data assimilation timestep are approximately multivariate Gaussian. If this assumption is violated, the history match adjustment at each update step may be incorrect leading to sub-optimal performance of EnKF in estimating reservoir models that match data. Clearly the distribution of the uncertain model parameters that are adjusted at each data assimilation time are non-Gaussian (Table 6.1). Consequently, a suitable transform function is required that will map the non-Gaussian model variables to a Gaussian space during the analysis / update step and map the Gaussian variables back after updating to the actual model space for the prediction run to the next assimilation timestep. It is necessary that this transform function satisfy at least two conditions:

1. The mapping/transform from the model space to the Gaussian space and back must be unique.

2. The unbounded changes made to the Gaussian variables at the update step should preserve the geologic bounds in Table 6.1 when back transformed to the

actual model space.

For this purpose, the shifted-sigmoid function (Eq. 6.2) was formulated as the transform function of choice.

$$\varphi(y) = \xi \left[1 + \text{erf}\left(\frac{y - \beta}{\sqrt{\alpha}} \right) \right] + \eta \tag{6.2}$$

y is a Gaussian random variable; $\varphi(y)$ is the model variable in the actual space corresponding to the variable, y, in the Gaussian space; erf$(\cdot)$ is the standard error function; ξ is a range parameter; β is a location parameter; α is the scale parameter and η is a positive shift parameter. The parameters of the shifted-sigmoid function were chosen such that

1. the lower and upper bounds on the model variables were mapped to Gaussian that were respectively $\leq$ -2.5 and $\geq$ 2.5 standard deviations from the mean of the standard normal PDF;

2. the (transformed) best-Guess model values were set equal to the median/mean of the standard normal PDF.

Consequently, the problem of choosing the parameters of the shifted-sigmoid function that will satisfy the bounds and the best guess values specified in Table 6.1 reduces to an equivalent problem of solving a nonlinear regression problem.

6.5 Low Discrepancy Sequence Sampling

Update to the state vector at each data assimilation time step is based (in part) on the statistics computed from finite number of ensemble members. Since the statistics are obtained from a finite-sized ensemble, they are usually subject to sampling errors. Increasing the ensemble size will mitigate the effect of sampling errors but also increase the computational cost of history matching, thus reducing the overall efficiency

of the process. Another approach for mitigating the sampling error is to generate initial samples that span a significant portion of the model space. Quasi Monte-Carlo methods generally use deterministic sequences known as low discrepancy sequences that are in some sense well distributed over the integration space (Niederreiter, 1992). To this end we utilized a low discrepancy sequence sampling scheme to generate the initial realizations of the model.

Discrepancy is a measure of how uniformly random points are distributed in space. Formally, suppose Q is a k-dimensional sub-rectangle contained in a k-dimensional unit cube, I^k, with sides parallel to the coordinate axes. If $v(Q)$ denotes the volume of Q, then the discrepancy of a sequence of N points, $\{x_1, \ldots, x_j, \ldots, x_n\}$, is given as,

$$D_N = \sup_{Q \in I^k} \left| \frac{\#\text{ of points in } Q}{N} - v(Q) \right|. \tag{6.3}$$

Well known low discrepancy sequences include Halton sequences (Halton, 1960), Hammersley sequences (Hammersley, 1960), Sobol sequences (Sobol, 1967), Faure sequences (Faure, 1982), Niederreiter sequences (Niederreiter, 1992), etc. The basic idea behind generating samples using sequences that are of low discrepancy is to uniformly sample the multidimensional cumulative distribution function of the model variables. The Halton sequence is one of the best known low discrepancy sequences and for our purpose, the vectors of Gaussian random variables used to parameterize the transformed model variables were generated using the Halton sequence sampling

A Halton point in a k-dimensional unit cube is given by the sequence,

$$\begin{aligned} H_k(n) =& (\varphi_{R_1}(n), \varphi_{R_2}(n), \ldots, \varphi_{R_k}(n)) \\ & n = 1, 2, \ldots, N; \end{aligned} \tag{6.4}$$

where $R_1, R_2, \ldots, R_k$ are the first k prime numbers and $\varphi_R(n)$ is the inverse radix number of an arbitrary integer n. To define the form of the inverse radix number, suppose that n and R are two arbitrary integers, then n can be written in radix-R

notation as

$$\begin{aligned} n &\equiv n_m n_{m-1} \ldots n_2 n_1 n_0 \\ &= n_0 + n_1 R + n_2 R^2 + \cdots + n_m R^m, \end{aligned} \tag{6.5}$$

where

$$m = [\log_R n] = \left[\frac{\ln n}{\ln R} \right], \tag{6.6}$$

and the square brackets denote the integral part. The inverse radix number ($\varphi_R(n)$) is a unique fraction between 0 and 1 obtained by reversing the order of the digits in n around the decimal point and given explicitly by,

$$\begin{aligned} \varphi_R(n) &= 0.n_0 n_1 n_2 \ldots n_m \\ &= n_0 R^{-1} + n_1 R^{-2} + n_2 R^{-3} + \ldots + n_m R^{-m-1}. \end{aligned} \tag{6.7}$$

To illustrate, suppose we wish to generate the first five Halton points in a unit square in $\mathbb{R}^2$. The first dimension of the Halton sequence will be based on the first prime number, $R_1 = 2$, and the second dimension on the second prime number, $R_2 = 3$. The specific steps for generating the first four Halton points in 2D is presented in Table 6.2. Note that the sequence of 1D Halton points based on the prime number

Table 6.2: Generating the first four Halton points in two dimensions.

	Dimension 1. R_1=2		**Dimension 2. R_2=3.**	
n	**B2**	**Inverse Radix No.**	**B3**	**Inverse Radix No.**
1	1	$0.100 = \frac{1}{2} + \frac{0}{2^2} + \frac{0}{2^3} = \frac{1}{2}$	1	$0.100 = \frac{1}{3} + \frac{0}{3^2} + \frac{0}{3^3} = \frac{1}{3}$
2	10	$0.010 = \frac{0}{2} + \frac{1}{2^2} + \frac{0}{2^3} = \frac{1}{4}$	2	$0.200 = \frac{2}{3} + \frac{0}{3^2} + \frac{0}{3^3} = \frac{2}{3}$
3	11	$0.110 = \frac{1}{2} + \frac{1}{2^2} + \frac{0}{2^3} = \frac{3}{4}$	10	$0.010 = \frac{0}{3} + \frac{1}{3^2} + \frac{0}{3^3} = \frac{1}{9}$
4	100	$0.001 = \frac{0}{2} + \frac{0}{2^2} + \frac{1}{2^3} = \frac{1}{8}$	11	$0.110 = \frac{1}{3} + \frac{1}{3^2} + \frac{0}{3^3} = \frac{4}{9}$

2 is the well known van der Corput sequence (van der Corput, 1935). If we paired up the four Halton sequence of points from Table 6.2, we obtain a sequence of four points in a unit square given by: $(\frac{1}{2}, \frac{1}{3})$, $(\frac{1}{4}, \frac{2}{3})$, $(\frac{3}{4}, \frac{1}{9})$, $(\frac{1}{8}, \frac{4}{9})$. An arbitrary multidimensional

Halton sequence is generated the same way as presented in Table 6.2. If $n_m = 11$ denotes the number of uncertain model variables and n_e denotes the number of ensemble members, then the standard Halton sequence of length n_e on an n_m-dimensional unit cube, Ψ_{n_m,n_e}, is given by,

$$\Psi_{n_m,n_e} = \begin{bmatrix} H_{n_m}(1) & H_{n_m}(2) & \dots & H_{n_m}(n_e) \end{bmatrix}. \tag{6.8}$$

Each additional multidimensional Halton point may be obtained recursively using the Von Neumann Kakutani transformation, which makes the process of generating additional sample points fairly efficient. Transformation of the multidimensional sample points from the unit cube, of dimension n_m, to the multivariate standard normally distributed points is achieved straightforwardly through the standard integral transform,

$$\mathbf{z}_{n_m,n_e} = \Phi^{-1}(\Psi_{n_m,n_e}), \tag{6.9}$$

where Φ is the standard normal CDF and $\mathbf{z}_{n_m,n_e}$ is the ensemble of Gaussian random vectors used to parameterize the vector of transformed model variables. Figure 6.5 compares the distribution of the first 100 Halton points in 2D with 100 randomly sampled Monte Carlo points. It also shows the corresponding multivariate Gaussian points obtained by transforming the random points in the unit square using Eq. 6.9 for $n_m = 2$. Clearly the Halton points (Fig. 6.5(c)) generally sample the 2D unit cube more uniformly than the pseudo-random points (Fig. 6.5(a)) resulting in better distributed Gaussian points (Fig. 6.5(d)).

6.6 Specification of the History Matching Parameters

An ensemble size of 100 was chosen for the history matching problem presented in this paper. Data were assimilated eleven times over the entire production period corresponding to days 90, 1080, 2160, 2880, 3330, 3780, 5580, 5850, 6300, 8100 and

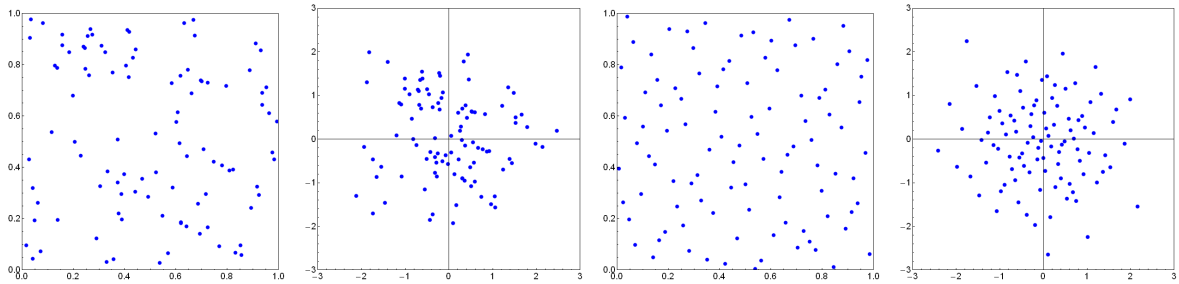

(a) 2D random points. (b) 2D Gaussian points. (c) 2D Halton points. (d) 2D Gaussian points

Figure 6.5: Generation of 100 random points in 2D using random Monte Carlo sampling (first two columns) and Halton sequence sampling (last two columns). Columns 1 and 3 are random points in a 2D unit cube. Columns 2 and 4 are bivariate Gaussian points obtained by transforming random points from the 2D unit cube using Eq. 6.9.

9900. Three types of production measurements (injector BHP, producer water and oil rates) were assimilated at each data assimilation timestep. The standard error of measurement for the different data were 10 psi for the BHP data and 10 STB/D for the rate data. Before water breakthrough occurred in the producer a standard error of measurement of 10^{-3} STB/D was used for the water rate data. This ensured that the water rate data assimilated before the breakthrough time were matched exactly by all the ensemble members.

In our implementation of the EnKF, we chose not to include the dynamic variables in the state vector. Consequently, the state vector of is given by,

$$\mathbf{y}_i = \begin{bmatrix} \mathbf{m}_i^T & \mathbf{g}(\mathbf{m}_i)^T \end{bmatrix}^T, \tag{6.10}$$

where $\mathbf{m}$ is the vector of Gaussian random variables that parameterize the transformed model parameters presented in Table 6.1. Consequently, at the end of each data assimilation timestep, the dynamic variables were re-initialized and the models were reran from time zero using the updated parameters to obtain the ensemble of predicted data at the next data assimilation timestep.

For the first-stage EnKF, the prior model variables were sampled from a zero-mean multivariate Gaussian PDF having a covariance matrix equal to an $n_m \times n_m$ identity matrix. Recall that n_m is the number of uncertain model variables, which is

equal to eleven in this case. For the second-stage EnKF, the values of the diagonal covariance matrix, $C_{M,s}$, of the Gaussian PDF for regenerating the initial ensemble members were chosen to ensure that the resampled models were close to the MAP estimate approximated from the final ensemble of the first-stage EnKF. This was achieved by setting the diagonal elements of the covariance matrix (the variances) to fairly small values. Note that if the variances are set to too small values then the filter may diverge (Maybeck, 1979) during history matching. Filter divergence refers to the situation where available data are progressively ignored due to too small variability in the ensemble. From the results of limited experiments on reasonable choices of model variance necessary to mitigate variance deficiency in the second-stage EnKF, we observed that setting the variances to 0.25 seems to work quite well in obtaining very reasonable match to data.

6.7 History Matching Results from the First-Stage EnKF

The predictions of the injector BHP and the producer oil and water rate data by the initial (Figs. 6.6(a)–6.6(c)) and final (Figs. 6.6(d)–6.6(f)) ensemble of model variables from the first-stage EnKF (standard EnKF) are presented in Fig. 6.6. The predictions were obtained by re-initializing the dynamic model variables and rerunning the simulation from time zero using the initial and final estimated of the models. Predictions from the ensemble of initial models exhibit a high degree of variability reflecting the high uncertainty in the initial estimates of the model variables. Some of the initial models predicted maximum BHP values (Fig. 6.6(a)) as high as 9200 psi and as low as 709 psi even though the maximum BHP predicted by the reference model was about 2400 psi. Interestingly, virtually all the initial models failed to predict the decline in the oil production rate, predicted by the reference model, starting from day 2700 and reaching a minimum value of 2700 STB/D after 630 days from the start of decline

(Fig. 6.6(b)). Only one of the initial models predicted a period of steep decline and increase in oil rate, which occurred before the time predicted by the reference model and the minimum oil rate for the period predicted by this model was much lower than the reference prediction.

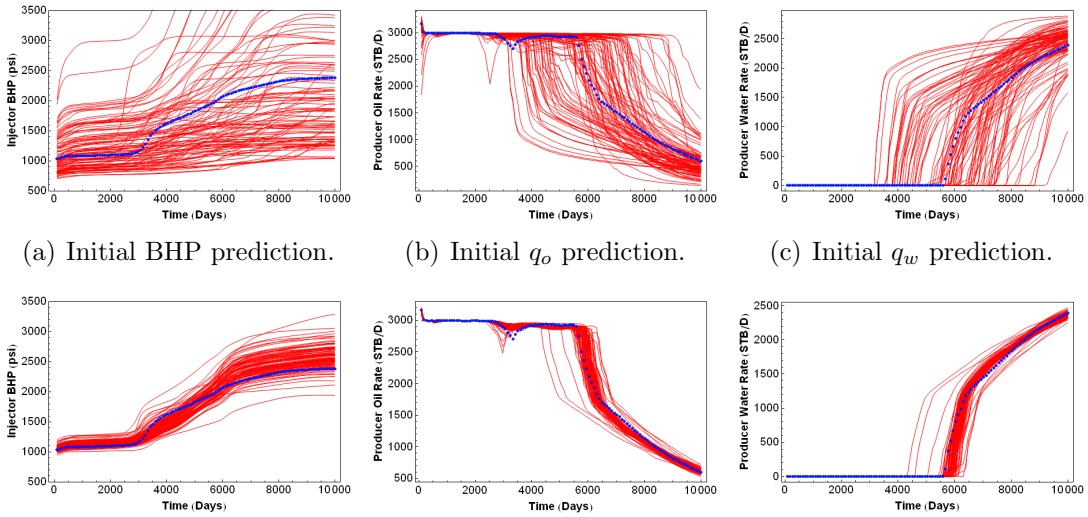

(a) Initial BHP prediction. (b) Initial q_o prediction. (c) Initial q_w prediction.

(d) Final BHP prediction. (e) Final q_o prediction. (f) Final q_w prediction.

Figure 6.6: Predictions from the initial (top row) and final (bottom row) ensembles from the first-stage EnKF. Reference predictions are shown as blue dots. Although initial prediction uncertainty was reduced after data assimilation, the match to data was generally poor.

Compared to the initial ensemble, predictions from the final ensemble generally match the reference predictions better reflecting the impact of assimilating production data on the quality of history matching results (Figs. 6.6(d)–6.6(f)). Because the uncertainty in the estimates of the initial model variables was reduced by assimilating data, the prediction spread from the final models is considerably smaller than the initial prediction spread. However, the variability in the predicted BHP data from the final ensemble is still quite high for the history matching results to be considered acceptable (Fig. 6.6(d)). Additionally, the match to the small dip in oil production data between days 2700–4000 in the reference model (Fig. 6.6(e)) is poor.

6.7.1 Estimation of the model parameters from the first-stage EnKF

At each data assimilation time-step, the Gaussian variables used to parameterize the transformed model variables are updated and the actual model variables are used for the forecast step after back transforming the updated Gaussian variables using Eq. 6.2. Consequently, updates to the transformed model parameters at each data assimilation timestep satisfy the EnKF assumption of Gaussianity. The distribution of the initial (gray histograms) and final (green histograms) estimates of the model variables are shown in Figs. 6.7–6.10. The reference value in each plot is shown by the red vertical line. We note from Table 6.1 that the range of values of the transmissibility multipliers has several orders of magnitude variation. The transmissibility multipliers of Fault1, Fault2 and the EOD connections exhibit up to five orders of magnitude variation ranging from 10^{-4} to 1.0. Consequently, the the natural log transformed values of the transmissibility multipliers are plotted in Figs. 6.7 and 6.10 instead of the actual values for better visualization of the full range of model variables distribution.

Figure 6.7 shows the distribution of the initial (gray bars) and final (green bars) estimates of fault transmissibility multipliers. The final estimate of Fault2 transmissibility multiplier matches the reference value quite well and the initial uncertainty is considerably reduced after data assimilation. By contrast, the initial and final uncertainty in estimates of Fault1 transmissibility multiplier are essentially equal. Recall that of the two faults, Fault1 is closer to the injector and intersects only a small region of the channel-axis in the top layer (Fig. 6.2(b)). The flow of water from the injector to the producer through the channel-axis is not influenced significantly by the presence of Fault1. None of the data (BHP, q_o or q_w) is very sensitive to the values of Fault1 transmissibility.

The first-stage EnKF performed quite well in estimating the permeability multipliers for both EODs and the initial estimates of the multipliers were adjusted towards the reference values after data assimilation (Fig. 6.8). However, the final estimates of

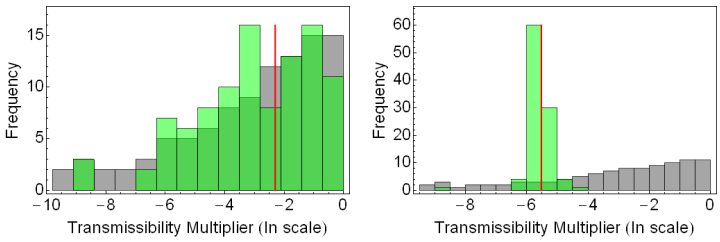

(a) Fault1. (b) Fault2.

Figure 6.7: Initial (gray) and final (green) estimates of the fault transmissibility multipliers on a natural log scale. The red vertical line corresponds to the reference value. Results are from the first-stage EnKF.

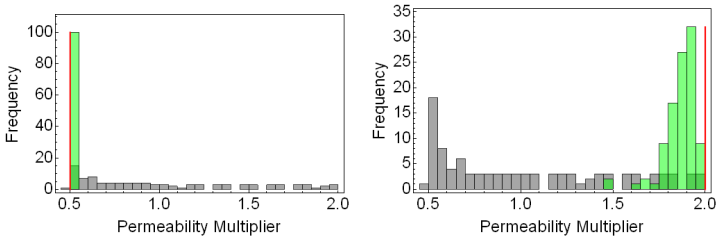

(a) EOD1. (b) EOD2.

Figure 6.8: Initial (gray) and final (green) estimates of the EOD permeability multipliers. The red vertical line is the reference value. Results from first-stage EnKF

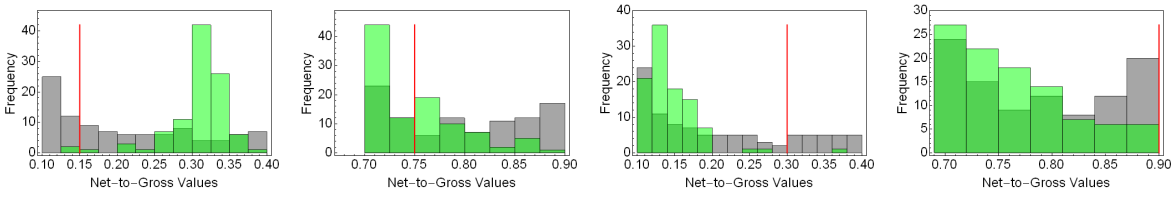

(a) Layer1. EOD1. (b) Layer1. EOD2. (c) Layer2. EOD1. (d) Layer2. EOD2.

Figure 6.9: Initial (gray) and final (green) estimates of EOD net-to-gross values from first-stage EnKF. The red vertical line is the reference net-to-gross.

the NTG values of the EODs appear not to match the reference values (red vertical lines) well (Fig. 6.9). Further discussions on this lack of match to production observation are presented in the next section. Recall that the porosity is determined from the NTG estimate and the permeabilities from the estimates of the NTG values and permeability multipliers. If these estimates are incorrect, then the final estimates of k_h, k_v and ϕ will also be incorrect. The distributions of the final connection transmissibility multipliers for EOD1–EOD1 (Fig. 6.10(a)) and EOD1–EOD2 (Fig. 6.10(b)) show evidence of data conditioning but the range of uncertainty in the final histograms are essentially the same as the initial histograms. However, the final estimates of the connection transmissibility multiplier for EOD2–EOD2 (Fig. 6.10(c)) seem reasonably close to the reference value.

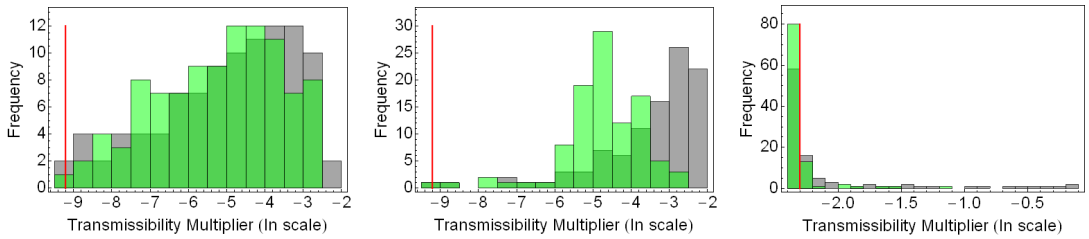

(a) EOD1–EOD1. (b) EOD1–EOD2. (c) EOD2–EOD2.

Figure 6.10: Initial (gray) and final (green) estimates of the connection transmissibility multipliers from first-stage EnKF shown on a natural-log scale. The red vertical line is the reference value.

6.7.2 Estimation of the saturation profile from the first-stage EnKF

The uncertainty in the spatial distribution of the final estimates of the dynamic model variables (gridblock pressures and saturation) are implicit in the uncertainty of the estimates of the static model variables (gridblock porosities and permeabilities). If the final estimates of the static model parameters from the ensemble are far from the reference model, then the distribution of the dynamic variables predicted by the ensemble will be different from the reference distribution. Consequently, the average saturation distribution predicted by the final model variables provides an additional

measure of the history match quality. The reference oil saturation distributions in Layer1 and Layer2 at the end of 9990 days of production are presented in Fig. 6.11. The warm colors correspond to high oil saturation (low water saturation) and the cold colors to low oil saturation (high water saturation). Two modes of flow can be observed from the reference saturation map; predominantly through the channel in Layer1 (Fig. 6.11(a)) and spreading outside the channel in Layer2 (Fig. 6.11(b)). The channel-confined flow in the top layer results from the permeability contrast between the channel-axis and channel-margin permeabilities. Compared to the top layer, the permeability contrast between the channel-axis and channel-margin permeabilities in the bottom layer is smaller resulting in higher transmissibility between the EODs in the bottom layer. This combined with the very low value of Fault2 transmissibility multiplier results in the spreading flow in the bottom layer.

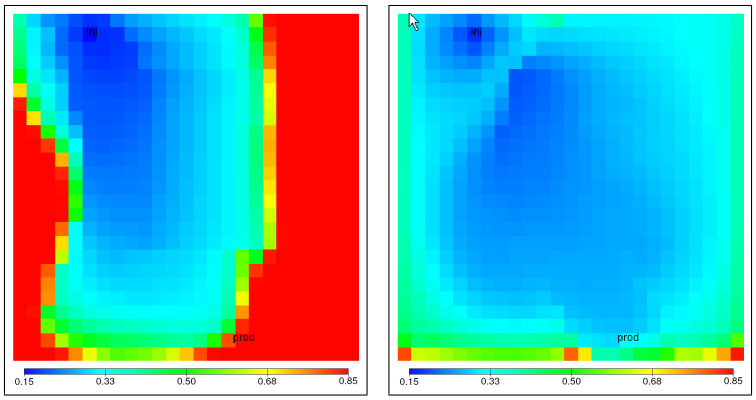

(a) Layer1. (b) Layer2.

Figure 6.11: Reference oil saturation distribution at day 9990.

Sensitivity studies showed that we can get a gross match of rates if one layer has channel flow and the other layer has spreading flow. It seems not to matter which layer is spreading and which is channel flow as long as one of each is obtained in both layers. Note that the channel vs. spreading flow in any of the layers is governed primarily by the horizontal permeability contrasts between the EODs and secondarily by the (vertical) connection transmissibilities of the EODs. For fixed values of the

permeability multipliers and transmissibility multipliers, the channel and spreading flows will correspond respectively to EODs with low and high NTG values. The reference NTG values for EOD1/EOD2 are respectively 0.15/0.75 for Layer1 and 0.30/0.90 for Layer2 resulting respectively in channel flow in Layer1 and spreading flow in Layer2 (Fig. 6.11).

Even though fairly good estimates of the permeability multipliers were obtained from the first-stage EnKF (Fig. 6.8), the non-uniqueness in the estimate of the NTG values in the EODs for both layers (Fig. 6.9) were not well resolved by the first-stage EnKF. The final estimates of the NTG values for EOD1 in Layer1 and EOD1 in Layer2 appears to have converged to one of the local minimum, i.e., high NTG value ≈ 0.3 for EOD1 in Layer1 and low NTG value ≈ 0.15 for EOD2 in Layer2. Note that this is exactly the converse of the case in the reference model. However, the final estimates of the NTG values for EOD2 in both layers did not converge to any value and essentially span the range of initial uncertainty of the models. Examination of the final ensemble-average saturation at the end of the first-stage EnKF (Fig. 6.12) indicates that the models in the ensemble show both flow behaviors (channel flow vs. spreading flow) in both layers.

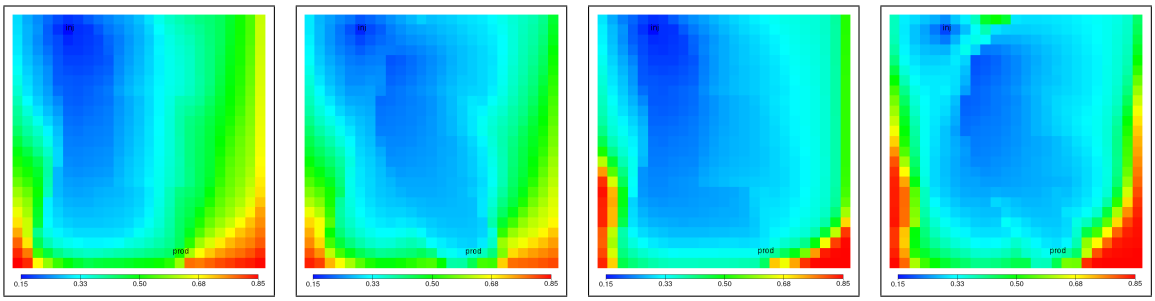

(a) Initial. Layer1. (b) Initial. Layer2. (c) Final. Layer1. (d) Final. Layer2.

Figure 6.12: Distribution of mean oil saturation predicted by the initial and final ensembles from the first-stage EnKF after 9990 days of production.

6.8 History Matching Results from the Second-Stage EnKF

The second stage in the two-stage EnKF is initialized by selecting, from the ensemble of history matched models from the first-stage EnKF, a model with the best match to production data (Eq. 6.1). The ensemble of predicted data from the final models of the first-stage EnKF are shown in Figs. 6.6(d)–6.6(f) and the corresponding predictions from the selected best model are shown in Fig. 6.13. The red and blue dots in Fig. 6.13 are respectively predictions from the reference model and the selected best model. Note that the predictions from some other ensemble members were equally as good as the selected best model and any one of these models could have been selected. The BHP data predicted by the selected model do not match the reference BHP prediction well (Fig. 6.13(a)). Predictions of the oil rate data (Fig. 6.13(b)) and the water rate data (Fig. 6.13(b)) by the selected model match the reference predictions reasonably well. However, the characteristic dip in oil production rate predicted by the reference model between days 2700–4000 was not matched by the predicted oil rate data from the selected model.

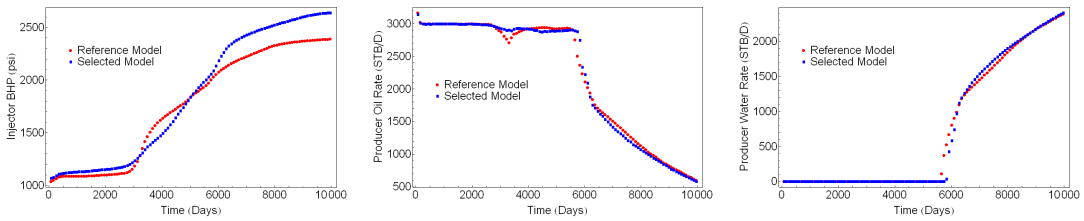

(a) BHP prediction. (b) q_o prediction. (c) q_w prediction.

Figure 6.13: Data predictions by selected best model from first-stage EnKF.

Realizations of the reservoir model for the second-stage EnKF were obtained by randomization around the selected best model. Note that the best model is not included explicitly in the resampled ensemble of state vectors but was used as the mean of the multivariate Gaussian PDF for resampling. Recall that the multivariate Gaussian PDF for resampling has a diagonal covariance matrix with variances of 0.25,

which are much lower than the variances of 1.0 for the first-stage EnKF.

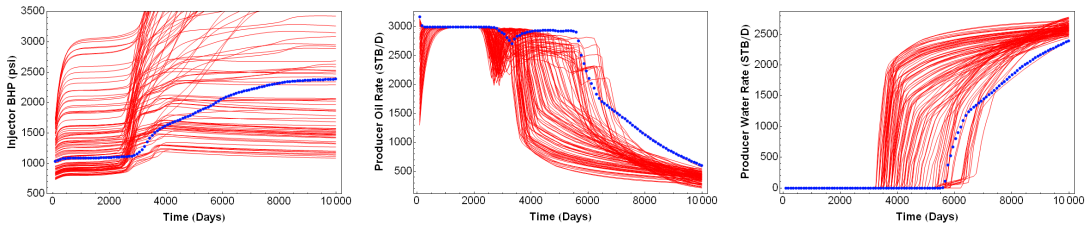

(a) Initial BHP prediction. (b) Initial q_o prediction. (c) Initial q_w prediction.

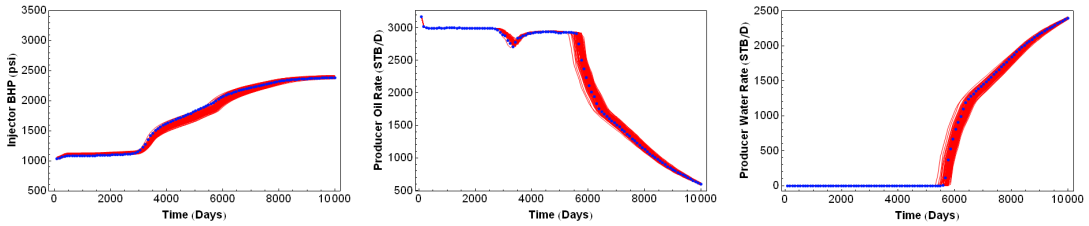

(d) Final BHP prediction. (e) Final q_o prediction. (f) Final q_w prediction.

Figure 6.14: Initial (top row) and final (bottom row) ensemble predictions from the second-stage EnKF. Reference predictions are shown as blue dots.

Predictions of the BHP, oil rate and water rate data from the regenerated initial ensemble for the second-stage EnKF are shown in Figs. 6.14(a)–6.14(c). The nonlinearity of the history matching problem is clearly evident in the predictive performance of the regenerated ensemble of initial models. The predicted oil rate data (Fig. 6.14(b)) and water rate data (Fig. 6.14(c)) from the initial ensemble are evidently very biased even though the initial ensemble members were obtained by perturbing around the best model. Note that the oil and water rate data predicted by the best model did not show such bias and matched the reference predictions of oil and water rate data fairly well (Figs. 6.13(b)–6.13(c)). The predicted BHP data from the initial models show two distinct clusters in prediction profiles. The first cluster failed to predict the consistent increase in BHP data from day 2700 and predicted a constant BHP data after 2700 days of production. The second cluster is marked by a very rapid increase in predicted BHP data from day 2700 to values significantly higher than the maximum reference BHP data.

Compared to the initial model, predictions from the ensemble of history matched

models (Figs. 6.14(d)–6.14(f)) were significantly better and matched the reference data quite well. All the final ensemble members also matched the dip in oil production rate predicted by the reference model quite well (Fig. 6.14(e)). Compared to the first stage EnKF (standard EnKF) the performance of the second-stage EnKF is qualitatively better at matching the reference data.

6.8.1 Estimation of the model parameters from the second-stage EnKF

Histograms of the initial (gray bars) and final (green bars) estimates of the uncertain model variables are presented in Figs. 6.15–6.18. The reference model values are indicated by red vertical lines. Note that for plots of transmissibility multipliers, the natural-log values are plotted in lieu of the actual values for legibility. Histograms of the fault transmissibility multipliers from the initial and final ensemble are presented in Fig. 6.15. As previously noted, because production data are fairly insensitive to values of Fault1 transmissibility multiplier, these appear not to have been adjusted very much during history matching and the distribution of the initial and final estimates are qualitatively very similar (Fig. 6.15(a)). By contrast, estimates of Fault2 transmissibility multiplier improved considerably after conditioning to production data compared to the initial unconditional estimates.

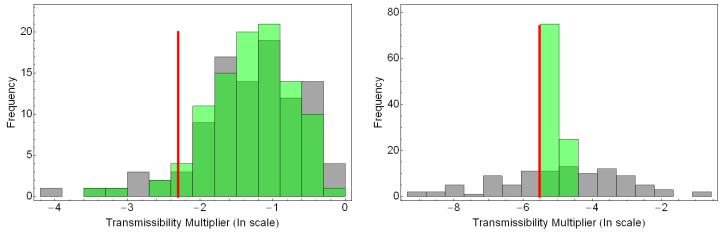

(a) Fault1. (b) Fault2.

Figure 6.15: Initial (gray) and final (green) estimates of fault transmissibility multipliers from second-stage EnKF. The red vertical line is the reference value.

Figures 6.16 and 6.17 respectively show the initial and final estimates of the permeability multipliers and the NTG values in the different EODs. The initial estimates

of the permeability multipliers for EOD1 and EOD2 were fairly good and the distributions of both initial permeability multipliers were generally close to the reference values. However, the conditional estimates of the permeability multiplier for EOD2 underestimate the reference value (Fig. 6.16(b)) after history matching. In our sensitivity studies, we noted that the pressure behavior depends non-uniquely on three factors: NTG values in the EODs, permeability multipliers and Fault2 transmissibility multiplier. For example at a given NTG value, similar pressure behavior was obtained for specific combinations of low values of Fault2 transmissibility multipliers (in the range of 0.0025–0.01) and the permeability multiplier for EOD2. At a fixed fault transmissibility, increasing net-to-gross gives almost the same change in pressure behavior as increasing the permeability multiplier. The inference is that there are many local minima that result from interactions between the effects of net-to-gross, permeability multiplier, and Fault2 transmissibility. We believe that this is why the permeability multiplier for EOD2 and the NTG in Layer1-EOD2 did not converge to the reference values. The history match process has found a local minimum. With the exception of the connection transmissibility multiplier for EOD1–EOD1, the final estimates of the connection transmissibility multipliers are generally close to the reference values. Considering the quality of history match and the absence of appreciable reduction in the spread of the final values of the EOD1–EOD1 connection transmissibility multiplier (Figs. 6.18(a)), it seems that none of the data was very sensitive to values of this model parameter.

6.8.2 Estimation of the saturation profile from the second-stage EnKF

The average oil saturation in Layer1 and Layer2 after 9990 days of production obtained by averaging the predicted oil saturation maps from the initial and final ensemble of reservoir models are presented in Fig. 6.19. The initial maps of the average oil

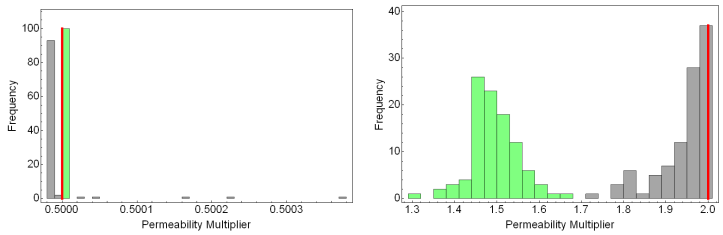

(a) EOD1. (b) EOD2.

Figure 6.16: Initial (gray) and final (green) estimates of permeability multipliers from second-stage EnKF. The red vertical line is the reference value.

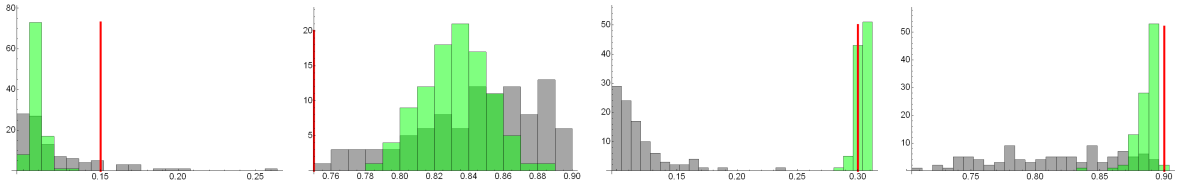

(a) Layer1. EOD1. (b) Layer1 EOD2. (c) Layer2. EOD1. (d) Layer2. EOD2.

Figure 6.17: Initial (gray) and final (green) estimates of EOD net-to-gross from second-stage EnKF. The red vertical line shows the reference value.

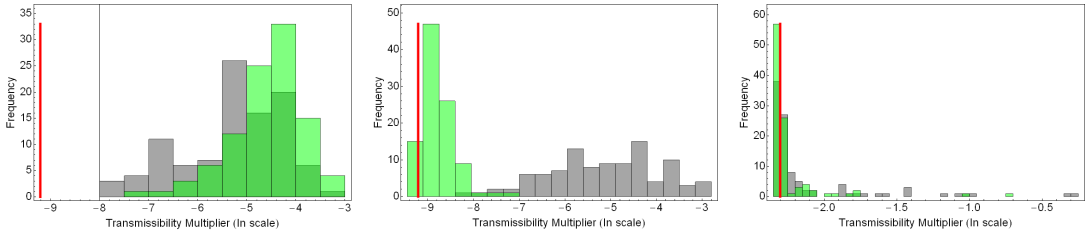

(a) EOD1–EOD1. (b) EOD1–EOD2. (c) EOD2–EOD2.

Figure 6.18: Initial (gray) and final (green) estimates of connection transmissibility multipliers from second-stage EnKF shown on a natural-log scale. The reference value is shown by the red vertical line.

saturation in Layer1 (Fig. 6.19(a)) and Layer2 (Fig. 6.19(b)) reflect the initial uncertainty in the model estimates and are qualitatively very different from the saturation distribution in the reference model (Fig. 6.11). The initial maps exhibit on the average both channel and spreading flows in each layer of the initial models. The average saturation maps (Figs. 6.19(c)–6.19(d)) obtained from the final ensemble have converged to one of the local minimum, i.e., channel flow in Layer1 and spreading flow in layer2. The ensemble average of the final saturation distribution appear qualitatively very similar to the reference saturation maps.

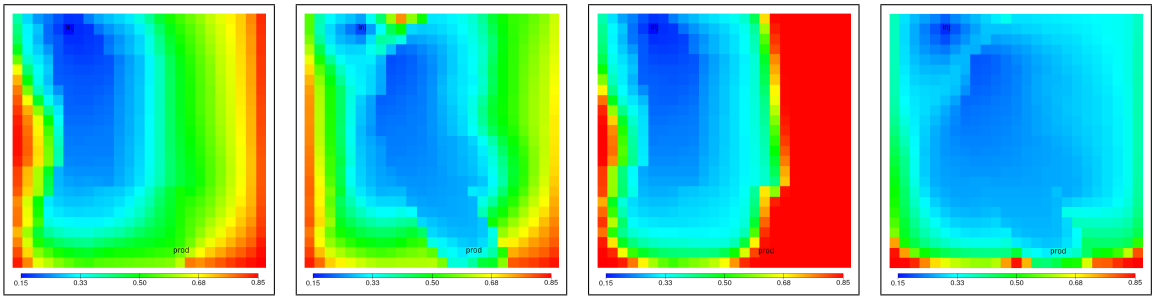

(a) Initial. Layer1. (b) Initial. Layer2. (c) Final. Layer1. (d) Final. Layer2.

Figure 6.19: Mean oil saturation predicted by the initial (regenerated) and final ensemble of model variables from the second-stage EnKF after 9990 days of production.

6.9 Comparison of the History Match Performances of the First-Stage and Second-Stage EnKF

Table 6.3 shows the root mean square error (RMSE) of the predicted data for the history matched period from the initial and final ensembles of the first-stage and second-stage EnKF. The RMSE provides a quantitative measure of the history match quality and the values presented in Table 6.3 were obtained by averaging over predicted data at the data assimilation timesteps. Rows 1 and 2 in Table 6.3 are the RMSE of predicted data from the initial ensembles of the first-stage and second-stage EnKF respectively. Interestingly, predictions from the initial ensemble of the second-stage EnKF have higher RMSE values compared to the first-stage EnKF. This is somewhat

surprising considering that the initial realizations of the second-stage EnKF were generated by adding random perturbations to the ensemble approximation of the MAP estimate from the first-stage EnKF. However, after assimilating production data, the second-stage EnKF gave a significantly better match to data and the RMSE from the second-stage EnKF are about 2–3 times smaller than the RMSE from the first-stage EnKF.

Table 6.3: Average RMSE of predicted data from the first- and second-stage EnKF.

		BHP (psi)	**Oil Rate** (STB/D)	**Water Rate** (STB/D)
1.	First-stage EnKF. Initial ensemble.	745	398	584
2.	Second-stage EnKF. Initial ensemble.	1787	623	831
3.	First-stage EnKF. Final ensemble.	151	120	148
4.	Second-stage EnKF. Final ensemble.	47	55	69

The final ensemble of model variables from the first-stage EnKF gave fairly good estimates of the Fault2 transmissibility multipliers (Fig. 6.7), permeability multipliers (Fig. 6.8) and the EOD2–EOD2 connection transmissibility multiplier (Fig. 6.10(c)). Also the NTG in EOD1 for both layers converged to one of the local minima. However, because the final NTG in EOD2 layers 1–2 and the EOD1–EOD2 connection transmissibility multiplier were not consistent with other parameters, the history match quality from the first-stage EnKF was poor (Table 6.3) and the average saturation maps at the end of the production period were qualitatively very different from the reference saturation maps. After implementing the second-stage EnKF, the final estimates of the NTG in Layer2-EOD2 and the EOD1–EOD2 connection transmissibility multiplier improved considerably and match the reference values better (Figs. 6.18(b) and 6.17(d)). Although, the the permeability multiplier for EOD2 and the NTG in EOD2 of Layer1 converged to a local minimum, the history match quality was considerably better after implementing the second-stage EnKF.

As noted earlier, the distribution of the gridblock pressures and saturation will generally depend on the history matched estimates of the static model variables.

Because the final estimates of the model variables from the second-stage EnKF are better constrained, the ensemble-average of the final saturation maps clearly showed the channel and spreading flow respectively in Layer1 and Layer2 that are also present in the reference saturation field. By contrast the first-stage EnKF failed to converge to either one of the two local minima (with respect to the interchangeability of the layer exhibiting spreading vs. channel flow) and exhibited both types of flow in each layer.

6.10 Discussions

The computational cost of implementing the two-stage EnKF is about twice the cost of the standard EnKF. Compared to the iterative ensemble Kalman filter, however, it is computationally less expensive although some of the iterative EnKF with individual gradient computation using adjoint formulation will perform better at sampling the different modes in the posterior PDF. The overall computational cost of the TEnKF may be reduced by minimizing the number of data assimilation timesteps required in the first-stage history matching. This may be achieved by carefully selecting the data assimilation timesteps with significant information content; for the history matching problem investigated in this paper, this may include timesteps with (1) water breakthrough data, (2) the minimum oil production rate during the dip period, (3) the oil rate datum just before the dip period, etc. Reducing the computational cost by preselecting the data assimilation timesteps in the first-stage EnKF is very important for applications to large scale history matching problems. It is not possible to prescribe a general process for identifying performance features that need to matched at the first- and second-stage EnKF as this will usually depend on a good understanding of the reservoir geology, preprocessing of the data to identify "unusual" data points, informed judgement of the reservoir engineer, etc. We note, however, that the water breakthrough data should be matched whenever available as it contains

valuable information on the average inter-well properties. For the history matching problem presented in this paper, recognizing the oil production dip as an important performance feature to match helped constrain the history matching problem better (particularly for the second-stage EnKF). It is noteworthy that in some cases production data may not be accurate enough to identify some important performance features (the features may be masked by noise in the data) and this may ultimately affect the overall history match quality.

The initial samples of the second-stage EnKF were generated around one of the modes of the posterior conditional PDF using an estimate of the MAP approximated from the final ensemble of the first-stage EnKF. Consequently the quantification of the uncertainty in predicted data for future periods will be underestimated. Conceptually, the future prediction uncertainty may be improved by using multiple ensembles of the initial realizations for the second stage EnKF obtained by sampling around several approximations of the MAP estimate from the final ensemble of the first-stage EnKF, where possible. This may be achieved by using any suitable clustering algorithm (expectation maximization, kernel methods, etc) to group the conditional models from first-stage EnKF and then selecting the best model from each cluster based on the goodness of match to production data. Multiple ensembles may then be obtained by resampling a Gaussian PDF centered at each of the MAP estimates approximated from the ensemble. Data assimilation using each ensemble of state vectors may be done in parallel and predictions from the different ensembles used to better quantify future uncertainty and also to compute various statistics for assessing future performance. For practical implementation, the size of each ensemble may have to be reduced and localization will be required to increase the effective rank of ensemble estimates and also reduce sampling errors. Localization has been used in reservoir engineering to improve history matching results (Agbalaka and Oliver, 2008; Chen and Oliver, 2010; Devegowda et al., 2007). Zhang and Oliver (2010)

discusses a particularly efficient form of localization based on a bootstrap version of the hierarchical filter (Anderson, 2007) that allows fairly small ensemble sizes to be used for data assimilation problems in reservoir engineering with reasonable results.

6.11 Chapter Summary

In this paper I have presented an approach to generating acceptable history matching results for problems with multiple modes using the two-stage ensemble Kalman filter. The first stage is an implementation of the standard EnKF and the updates to the model variables are made about the conditional mean of the Gaussian PDF approximating the multimodal model PDF. The second-stage EnKF regenerates the realizations of the model variables about the conditional mode approximated from the final ensemble of the first-stage EnKF. By generating updates about the conditional mode at each assimilation timestep, the updates to the model variables were generally better constrained resulting in a significantly improved match to production data compared to the standard EnKF from the first stage implementation.

To obtain Gaussian parameterizations of the transformed model variables, I utilized a shifted-sigmoid function. The parameters of the shifted-sigmoid function were chosen to ensure that the geologic bounds were honored when the updated Gaussian variables are back transformed to the actual model variables. Also parameterizing the transformed model variables as Gaussian random variables ensured that the assumption of Gaussianity during the EnKF update step is honored.

Because of the size of the problem, I utilized quasi-Monte Carlo sampling based on low discrepancy sequences to generate the initial ensemble of model variables. The goal is to generate initial models that are sufficiently diverse and also increase the possibility of some of the models converging to one of the modes of the posterior PDF from the first stage EnKF.

CHAPTER VII

CONCLUSIONS

The focus of this dissertation is on the application of the ensemble Kalman filter to history matching problems with complex, non-Gaussian model parameters. Such problems require a modified formulation of the EnKF update step and/or some form of Gaussian parameterization of the non-Gaussian model variables to honor the Gaussian assumption at each update step.

For the problem of EnKF applied to facies, I identified and addressed several difficulties in the implementations related to: (1) assimilating the static facies data and dynamic production data in a consistent way and (2) mitigating excessive loss in ensemble variability, which usually requires very large ensemble size. I also analyzed the problem of the best starting point for future prediction after data assimilation. I showed that by decoupling the assimilation of production and facies data and assimilating firstly the production data and secondly the facies data, it is possible to prevent large changes to the pressure and saturation fields. Based on this "decoupling" approach, updated dynamic variables that are consistent with the estimates of the model parameters are obtained and the problem of destroying previously matched facies observation while iterating to reenforce the constraint on facies observation is also avoided. I also showed that by localizing the updates to the facies variables when facies data are assimilated, excessive loss in ensemble variability is significantly mitigated. Furthermore, results from localization showed that an ensemble size on the order of 100 seemed sufficient for the history matching problem investigated.

The difficulty of jointly updating the discrete facies variables and the multimodal permeabilities and porosities was also addressed in this dissertation. I introduced an

approach based on the use of pseudo-model variables that allowed the multimodal permeabilities and porosities to be updated in a consistent way within the EnKF framework. By using pseudo-model variables, a Gaussian approximation to the multimodal model variables are updated in lieu of the actual model variables. A nonlinear mapping is then used to obtain realizations of the multimodal model variables from the ensemble of pseudo-model variables for the prediction run. In contrast to the results from using EnKF to directly update the multimodal permeability and porosity, where the final estimates of the petrophysical properties were too smooth for properties from a facies model, the final ensemble of petrophysical properties from the pseudo-properties approach remained geologically plausible at the end of data assimilation. Also, the history matching results from the pseudo-properties approach were good.

I also investigated the EnKF performance in estimating the distribution of vertical flow barriers in a reservoir model with flow barriers where zonal communication exists in some areas of the reservoir but not in others. I showed that the EnKF performed poorly in matching production data and in the prediction of future production when only the log-Gaussian horizontal and vertical permeabilities are updated to account for the effect of vertical transmissibility barrier on fluid flow. Also the history matched model variables were poorly estimated as incorrect and compensatory changes were made to correct for the fact that the uncertainty in vertical flow barriers were not accounted for. I described a representation of the vertical flow barriers using vertical transmissibility multipliers, which were parameterized as spatially correlated Gaussian random variables after transformation. Three alternative parameterizations of the vertical transmissibility multipliers were used to obtain different vertical flow barrier configurations and significant improvement in history matching results and the estimates of the model parameters was observed.

A two-stage EnKF was introduced for application to history matching problems

with multiple modes and non-Gaussian model parameters. The method is based on implementing two sequential stages of the standard EnKF. Following the first stage, the initial ensemble of reservoir models was regenerated by resampling about the maximum a posteriori model obtained from the final ensemble from the first-stage EnKF. For both stages of the ensemble Kalman filter, a slightly modified form of the EnKF was used—the dynamic model variables were not updated at each data assimilation timestep but were obtained by rerunning the simulator from time zero using the updated model parameters. Results of the two-stage EnKF showed a better-converged history match solution compared to results from the standard EnKF.

REFERENCES

Aanonsen, S. I., Using model error with the ensemble Kalman filter for more accurate model updates and predictions (SPE 119096-MS), in *Proceeding of the 2009 SPE Reservoir Simulation Symposium*, The Woodlands, Texas, USA, 2009.

Agbalaka, C. C. and D. S. Oliver, Application of the EnKF and localization to automatic history matching of facies distribution and production data, *Mathematical Geosciences*, **40**(4), 353–374, 2008.

Agbalaka, C. C. and D. S. Oliver, Automatic history matching of production and facies data with non-stationary proportions using EnKF, SPE 118916, in *Proceedings of the 2009 SPE Reservoir Simulation Symposium, The Woodlands, Texas*, 2009.

Agbalaka, C. C. and D. S. Oliver, Parameterization of vertical transmissibility barriers for history matching using EnKF, *Mathematical Geosciences*, **(Submitted.)**, 2010.

Anderson, B., I. Bryant, M. Lüling, B. Spies, and K. Helbig, Oilfield anisotropy: Its origins and electrical characteristics, *Oilfield Review*, **6**(4), 48–56, 1994.

Anderson, J. L., Exploring the need for localization in ensemble data assimilation using a hierarchical ensemble filter, *Physica D: Nonlinear Phenomena*, **230**(1–2), 99–111, 2007.

Anderson, J. L. and S. L. Anderson, A Monte Carlo implementation of the nonlinear filtering problem to produce ensemble assimilations and forecasts, *Monthly Weather Review*, **127**(12), 2741–2758, 1999.

Anderson, J. L., B. Wyman, S. Zhang, and T. Hoar, Assimilation of surface pressure observations using an ensemble filter in an idealized global atmospheric prediction system, *Journal of the Atmospheric Sciences*, **62**(8), 2925–2938, 2005.

Armstrong, M., A. G. Galli, G. L. Loc'h, F. Geffroy, and R. Eschard, *Plurigaussian Simulations in Geosciences*, Springer, New York, 2003.

Arulampalam, S. M., S. Maskell, N. Gordon, and T. Clapp, A tutorial on particle filters for online nonlinear/non-Gaussian Bayesian tracking, *IEEE Transactions on Signal Processing*, **50**(2), 174–188, 2002.

Auzerais, F. M., D. V. Ellis, S. M. Luthi, V. Dussan, and B. J. Pinoteau, Laboratory characterization of anisotropic rocks (SPE-20602), in *65th SPE Annual Technical Conference and Exhibition*, 1990.

Ayan, C., N. Colley, G. Cowan, E. Ezekwe, M. Wannell, P. Goode, F. Halford, J. Joseph, A. Mongini, G. Obondoko, and J. Pop, Measuring permeability anisotropy: The latest approach, *The Oilfield Review*, **6**(4), 48–56, 1994.

Bishop, C. H., B. J. Etherton, and S. J. Majumdar, Adaptive sampling with the ensemble transform Kalman filter. part I: Theoretical aspects, *Mon. Wea. Rev.*, **129**(3), 420–436, 2001.

Brown, M. and A. Forsythe, Robust tests for the equality of variances, *Journal of the American Statistical Association*, **69**(346), 364–367, 1974.

Burgers, G., P. van Leeuwen, and G. Evensen, Analysis scheme in the ensemble Kalman filter, *Monthly Weather Review*, **126**(6), 1719–1724, 1998.

Cerioli, A., Tests of homogeneity for spatial populations, *Statistics & Probability Letters*, **58**(2), 123–130, 2002.

Chen, Y. and D. S. Oliver, Ensemble-based closed-loop optimization applied to Brugge Field (SPE 118926), *SPE Reservoir Evaluation & Engineering*, **13**(1), 56–71, 2010.

Chen, Y., D. S. Oliver, and D. Zhang, Data assimilation for nonlinear problems by ensemble Kalman filter with reparameterization, *Journal of Petroleum Science and Engineering*, **66**, 1–14, 2009.

Chen, Y. and D. Zhang, Data assimilation for transient flow in geologic formations via ensemble Kalman filter, *Advances in Water Resources*, **29**(8), 1107–1122, 2006.

Corser, G. P., J. E. Harmse, B. A. Corser, M. W. Weiss, and G. L. Whitflow, Field test results for a real-time intelligent drilling monitor, SPE-59227, in *Proceedings of the 2000 IADC/SPE Drilling Conference*, 2000.

Cramer, H., *Mathematical methods of statistics*, Princeton University Press, 1946.

Deutsch, C. V. and A. G. Journel, *GSLIB: Geostatistical Software Library and User's Guide*, second edn., Oxford University Press, New York, 1998.

Devegowda, D., E. Arroyo-Negrete, A. Datta-Gupta, and S. G. Douma, Efficient and robust reservoir model updating using ensemble Kalman filter with sensitivity-based covariance localization (SPE-106144), in *SPE Reservoir Simulation Symposium*, 2007.

Dowd, P. A., C. Xu, K. V. Mardia, and R. J. Fowell, A comparison of methods for the stochastic simulation of rock fractures., *Mathematical Geology*, **39**(7), 697–714, 2007.

Ehlig-Economides, C., D. Ebbs, M. Fetkovich, and D. N. Meehan, Factoring anisotropy into well design, *Oilfield Review*, **2**(4), 24–33, 1990.

Eisenmann, P., M.-T. Gounot, B. Juchereau, and S. J. Whittaker, Improved Rxo measurements through semi-active focusing, SPE-28437, in *Proceedings of the SPE 69th Annual Technical Conference and Exhibition*, 1994.

Ertekin, T., J. H. Abou-Kassem, and G. R. King, *Basic Applied Reservoir Simulation*, vol. 7 of *SPE Textbook Series*, Society of Petroleum Engineers, Richardson, TX, 2001, 406 pp.

Evensen, G., Sequential data assimilation with a nonlinear quasi-geostrophic model using Monte Carlo methods to forecast error statistics, *Journal of Geophysical Research*, **99**(C5), 10,143–10,162, 1994.

Evensen, G., The ensemble Kalman filter: Theoretical formulation and practical implementation, *Ocean Dynamics*, **53**, 343–367, 2003.

Evensen, G., J. Hove, H. C. Meisingset, E. Reiso, K. S. Seim, and Ø. Espelid, Using the EnKF for assisted history matching of a North Sea reservoir model (SPE 106184), in *Proceedings of the 2007 SPE Reservoir Simulation Symposium,*, 2007.

Faure, H., Discrépance de suites associées à un système de numération (en dimension s), *Acta Arithmetica*, **41**, 337–351, 1982.

Floris, F. J. T., M. D. Bush, M. Cuypers, F. Roggero, and A.-R. Syversveen, Methods for quantifying the uncertainty of production forecasts: A comparative study, *Petroleum Geoscience*, **7**, 87–96, 2001.

Franssen, H. J. H. and W. Kinzelbach, Ensemble Kalman filtering versus sequential self-calibration for inverse modelling of dynamic groundwater flow systems, *Journal of Hydrology*, **365**(3–4), 261–274, 2009.

Furrer, R. and T. Bengtsson, Estimation of high-dimensional prior and posterior covariance matrices in Kalman filter variants, *J. Multivar. Anal.*, **98**(2), 227–255, 2007.

Galli, A., H. Beucher, G. Le Loc'h, B. Doligez, and H. Group, The pros and cons of the truncated Gaussian method, in *Geostatistical Simulations*, pp. 217–233, Kluwer Academic, Dordrecht, 1994.

Gao, G., M. Zafari, and A. C. Reynolds, Quantifying uncertainty for the PUNQ-S3 problem in a Bayesian setting with RML and EnKF, *SPE Journal*, **11**(4), 506–515, 2006.

Gaspari, G. and S. E. Cohn, Construction of correlation functions in two and three dimensions, *Quarterly Journal of the Royal Meteorological Society*, **125**(554), 723–757, 1999.

Gu, Y. and D. S. Oliver, History matching of the PUNQ-S3 reservoir model using the ensemble Kalman filter, *SPE Journal*, **10**(2), 51–65, 2005.

Gu, Y. and D. S. Oliver, The ensemble Kalman filter for continuous updating of reservoir simulation models, *Journal of Energy Resources Technology*, **128**(1), 79–87, 2006.

Gu, Y. and D. S. Oliver, An iterative ensemble Kalman filter for multiphase fluid flow data assimilation, *SPE Journal*, **12**(4), 438–446, 2007.

Haldorsen, H. H., D. M.Chang, and S. H.Begg, Discontinuous vertical permeability barriers: a challenge to engineers and geologists, in *North sea oil and gas reservoirs*, (edited by J. Kleppe), pp. 127–151, Norwegian Institute of Technology, Graham and Trotman, Trondheim, Norway, 1987.

Halton, J. H., On the efficiency of certain quasi-random sequences of points in evaluating multi-dimensional integrals, *Numerische Mathematik*, **2**, 84–90, 1960.

Hamill, T. M. and C. Snyder, Using improved background-error covariances from an ensemble Kalman filter for adaptive observations, *Monthly Weather Review*, **130**(6), 1552–1572, 2002.

Hamill, T. M., C. Snyder, D. P. Baumhefner, Z. Toth, and S. L. Mullen, Ensemble forecasting in the short to medium range: Report from a workshop, *Bull. Amer. Meteor. Soc.*, **81**, 2653–2664, 2000.

Hamill, T. M., J. S. Whitaker, and C. Snyder, Distance-dependent filtering of background error covariance estimates in an ensemble Kalman filter, *Monthly Weather Review*, **129**(11), 2776–2790, 2001.

Hammersley, J. M., Monte Carlo methods for solving multivariable problems, *Annals of the New York Academy of Sciences*, **86**, 844–874, 1960, numerical Properties of Functions of More Than One Independent Variable.

Harpole, K. J., Improved reservoir characterization: A key to future reservoir management for the West Seminole San Andres Unit, *Journal of Petroleum Technology*, **32**(11), 2009–2019, 1980.

Hoffman, T. B. and J. Caers, History matching by jointly perturbing local facies proportions and their spatial distribution: Application to a North Sea reservoir, *JPSE*, **57**, 257–272, 2007.

Houtekamer, P. L. and H. L. Mitchell, Data assimilation using an ensemble Kalman filter technique, *Monthly Weather Review*, **126**(3), 796–811, 1998.

Houtekamer, P. L. and H. L. Mitchell, A sequential ensemble Kalman filter for atmospheric data assimilation, *Monthly Weather Review*, **129**(1), 123–137, 2001.

Hu, L. Y., M. L. Ravalec, and G. Blanc, Gradual deformation and iterative calibration of truncated Gaussian simulations, *Petroleum Geoscience*, **7**, 25–30, 2001.

Hunt, B. R., E. J. Kostelich, and I. Szunyogh, Efficient data assimilation for spatiotemporal chaos: A local ensemble transform Kalman filter, *Physica D: Nonlinear Phenomena*, **230**(1–2), 112–126, 2007.

Jazwinski, A. H., *Stochastic Processes and Filtering Theory*, Academic Press, New York, 1970.

Jensen, J. L., P. W. Corbett, L. W. Lake, and D. J. Goggin, *Statistics for Petroleum Engineers and Geoscientists*, Handbook of Petroleum Exploration ans Production 2, second edn., Elsevier Science Ltd, 2000.

Journel, A. G. and E. H. Isaaks, Conditional indicator simulation: Application to a Saskatchewan uranium deposit, *Journal of Petroleum Science and Engineering*, **16**(7), 685–718, 1984.

Julier, S. J. and J. K. Uhlmann, A new extension of the Kalman filter to nonlinear systems, **3**, 26, 1997.

Kalman, R. E., A new approach to linear filtering and prediction problems, *Transactions of the ASME, Journal of Basic Engineering*, **82**, 35–45, 1960.

Kalman, R. E. and R. Bucy, New results in linear prediction and filtering theory, *Trans. AMSE J. Basic Eng*, pp. 95–108, 1961.

Lake, L. W., The origins of anisotropy, *Journal of Petroleum Technology*, **40**(4), 395–396, 1988.

Le Loc'h, G., H. Beucher, A. Galli, B. Doligez, and H. Group, Improvement in the truncated Gaussian method: Combining several Gaussian Functions, in *Proceedings of ECMOR IV, Fourth European Conference on the Mathematics of Oil Recovery*, 1994.

Le Loc'h, G. and A. Galli, Truncated plurigaussian method: Theoretical and practical points of view, in *Geostatistics Wollongong '96*, (edited by E. Y. Baafi and N. A. Schofield), vol. 1, pp. 211–222, Kluwer Academic, 1997.

Levene, H., Robust tests for equality of variances, *In Contributions to Probability and Statistics: Essays in Honor of Harold Hotelling*, pp. 278–292, 1960.

Lewis, J. M., S. Lakshmivarahan, and S. Dhall, *Dynamic Data Assimilation: A Least Squares Approach*, vol. 104 of *Encyclopedia of Mathematics and Application*, Cambridge University Press, 2006.

Li, G. and A. C. Reynolds, Iterative ensemble Kalman filters for data assimilation, *SPE Journal*, **14**(3), 496–505, 2009.

Liu, F., J. M. Mendel, and A. M. Nejad, Forecasting injector/producer relationships from production and injection rates using an extended Kalman filter (SPE 110520-pa), *SPE Journal*, **14**(4), 653–664, 2009.

Liu, N. and D. S. Oliver, Automatic history matching of geologic facies, *SPE Journal*, **9**(4), 188–195, 2004.

Liu, N. and D. S. Oliver, Critical evaluation of the ensemble Kalman filter on history matching of geologic facies, *SPE Reservoir Evaluation & Engineering*, **8**(6), 470–477, 2005a.

Liu, N. and D. S. Oliver, Ensemble Kalman filter for automatic history matching of geologic facies, *Journal of Petroleum Science and Engineering*, **47**(3–4), 147–161, 2005b.

Lord, M. E. and R. E. Collins, Effects of crossbedding on well performance (SPE 19587), in *Proceedings of the 64th SPE Annual Technical Conference and Exhibition*, San Antonio, TX, 1989.

Lorentzen, R. J., K. M. Flornes, and G. Nævdal, History matching channelized reservoirs using the ensemble Kalman filter, in *International Petroleum Technology Conference*, Doha, 2009.

Lorentzen, R. J., G. Nævdal, B. Vàlles, A. M. Berg, and A.-A. Grimstad, Analysis of the ensemble Kalman filter for estimation of permeability and porosity in reservoir models, SPE–96375, in *SPE Annual Technical Conference and Exhibition*, 2005.

Mansure, A. J., G. L. Whitlow, G. P. Corser, J. Harmse, and R. D. Wallace, A probabilistic reasoning tool for circulation monitoring based on flow measurements, (SPE 56634), in *Proceedings of the SPE 69th Annual Technical Conference and Exhibition*, 1999.

Martin, J. H. and J. A. Cooper, An integrated approach to modeling permeability barrier distribution in a sedimentologically complex reservoir (SPE 13051), in *Proceedings of the 59th SPE Annual Technical Conference and Exhibition*, Houston, TX, 1984.

Matheron, G., H. Beucher, C. de Fouquet, A. Galli, D. Guerillot, and C. Ravenne, Conditional simulation of the geometry of fluvio-deltaic reservoirs, SPE 16753, in *Proc. of 62nd Ann. Tech. Conf. of the SPE*, pp. 123–131, 1987.

Maybeck, P. S., *Stochastic models, estimation, and control*, vol. 141-1 of *Mathematics in Science and Engineering*, 1979.

Mitchell, H. L., P. L. Houtekamer, and G. Pellerin, Ensemble size, balance, and model-error representation in an ensemble Kalman filter, *Monthly Weather Review*, **130**(11), 2791–2808, 2002.

Moreno, D., S. Aanonsen, G. Evensen, and J.-A. Skjervheim, Channel facies estimation based on Gaussian perturbations in the EnKF, in *11th European Conference on the Mathematics of Oil Recovery (ECMOR)*, 2008.

Nævdal, G., T. Mannseth, and E. H. Vefring, Near-well reservoir monitoring through ensemble Kalman filter: SPE 75235, in *Proceedings of SPE/DOE Improved Oil Recovery Symposium*, 2002.

Niederreiter, H., *Random number generation and quasi-Monte Carlo methods*, Society for Industrial Mathematics, 1992.

Olea, R. A. and V. Pawlowsky-Glahn, Kolmogorov-Smirnov test for spatially correlated data, *Stochastic Environmental Research and Risk Assessment*, **23**(6), 749–757, 2008.

Oliver, D. S., Moving averages for Gaussian simulation in two and three dimensions, *Mathematical Geology*, **27**(8), 939–960, 1995.

Oliver, D. S., N. He, and A. C. Reynolds, Conditioning permeability fields to pressure data, in *European Conference for the Mathematics of Oil Recovery, V*, pp. 1–11, 1996.

Ott, E., B. R. Hunt, I. Szunyogh, A. V. Zimin, E. J. Kostelich, M. Corazza, E. Kalnay, D. J. Patil, and J. A. Yorke, A local ensemble Kalman filter for atmospheric data assimilation, *Tellus A*, **56**(5), 415–428, 2004.

Phale, H. A. and D. S. Oliver, Data assimilation using the constrained ensemble Kalman filter (SPE 125101), in *SPE Annual Technical Conference, 4–7 October 2009, New Orleans, Louisiana, U.S.A.*, 2009.

Prats, M., The influence of oriented arrays of thin impermeable shale lenses or of highly conductive natural fractures on apparent permeability anisotropy (SPE-4163), *Journal of Petroleum Technology*, **24**(10), 1219–1221, 1972.

Ravalec-Dupin, M. L., F. Roggero, and R. Froidevaux, Conditioning truncated Gaussian realizations to static and dynamic data, *SPE Journal*, **9**(4), 475–480, 2004.

Reichle, R. H., D. B. McLaughlin, and D. Entekhabi, Hydrologic data assimilation with the ensemble Kalman filter, *Monthly Weather Review*, **130**(1), 103–114, 2002.

Sakov, P., G. Evensen, and L. Bertino, Asynchronous data assimilation with the EnKF, *Tellus Series A-Dynamic Meteorology and Oceanography*, **62**(1), 24–29, 2010.

Sakov, P. and P. R. Oke, Implications of the form of the ensemble transformation in the ensemble square root filters, *Monthly Weather Review*, **136**(3), 1042–1053, 2008.

Sarma, P. and W. H. Chen, Generalization of the ensemble Kalman filter using kernels for nonGaussian random fields (SPE 119177), in *Proceedings of the 2009 SPE Reservoir Simulation Symposium*, 2009.

Satterthwaite, F., An approximate distribution of estimates of variance components, *Biometrics Bulletin*, **2**(6), 110–114, 1946.

Seiler, A., G. Evensen, J.-A. Skjervheim, J. Hove, and J. G. Vabø, Advanced reservoir management workflow using an EnKF based assisted history matching method (SPE 118906), in *Proceedings of the 2009 SPE Reservoir Simulation Symposium*, 2009.

Shin, H. and J. Choe, Shale barrier effects on the SAGD performance (SPE 27966), in *Proceedings of the SPE/EAGE Reservoir Characterization and Simulation Conference*, Abu Dhabi, UAE, 2009.

Smith, K. W., Cluster ensemble Kalman filter, *Tellus Series A*, **59**(5), 749–757, 2007.

Sobol, I., On the distribution of points in a cube and the approximate evaluation of integrals, *USSR Computational Mathematics and Mathematical Physics*, **7**(4), 86–112, 1967.

Sun, A., A. Morris, and S. Mohanty, Sequential updating of multimodal hydrogeologic parameter fields using localization and clustering techniques, *Water Resources Research*, **45**(7), W07,424, 2009a.

Sun, A. Y., A. P. Morris, and S. Mohanty, Comparison of deterministic ensemble Kalman filters for assimilating hydrogeological data, *Advances in Water Resources*, **32**(2), 280–292, 2009b.

Thomas, S. J., J. P. Hacker, and J. L. Anderson, A robust formulation of the ensemble Kalman filter, *Quarterly Journal of the Royal Meterological Society*, **135**(Part B), 507–521, 2009.

Tillman, R. W. and E. D. Pittman, Barriers to flow in tidal sandstone reservoirs, Sun Ranch Field, Wyoming (SPE 27966), in *Proceedings of the University of Tulsa Centennial Petroleum Engineering Symposium*, Tulsa, OK, 1994.

van der Corput, J. G., Verteilungsfunktionen, *Akademie van Wetenschappen*, **38**, 813–821, 1935.

Wan, E. A. and R. Van Der Merwe, The unscented Kalman filter for nonlinear estimation, in *Proceedings of IEEE Symposium*, pp. 153–158, 2000.

Wang, D., Y. Chen, and X. Cai, State and parameter estimation of hydrologic models using the constrained ensemble Kalman filter, *Water Resources Research*, **45**(W11416), 2009.

Wen, X.-H. and W. H. Chen, Some practical issues on real-time reservoir model updating using ensemble Kalman filter, *SPE Journal*, **12**(2), 156–166, 2007.

Wikle, C. K. and L. M. Berliner, A Bayesian tutorial for data assimilation, *Physica D: Nonlinear Phenomena*, **230**(1–2), 1–16, 2007, data Assimilation.

Wu, Z., A. C. Reynolds, and D. S. Oliver, Conditioning geostatistical models to two-phase production data, *SPE Journal*, **4**(2), 142–155, 1999.

Xu, C., P. A. Dowd, K. V. Mardiac, and R. J. Fowella, A flexible true plurigaussian code for spatial facies simulations, *Computational Geosciences*, **32**, 1629–1645, 2006.

Zafari, M. and A. C. Reynolds, Assessing the uncertainty in reservoir description and performance predictions with the ensemble Kalman filter, *SPE Journal*, **12**(3), 382–391, 2007.

Zang, X. and P. Malanotte-Rizzoli, A comparison of assimilation results from the ensemble Kalman filter and a reduced-rank extended Kalman filter, *Nonlinear Processes In Geophysics*, **10**(6), 477–491, 2003.

Zhang, F. and A. C. Reynolds, Optimization algorithms for automatic history matching of production data, in *Proceedings of 8th European Conference on the Mathematics of Oil Recovery*, 2002.

Zhang, Y. and D. S. Oliver, History matching using a hierarchical stochastic model with the ensemble Kalman filter: A field case study, SPE-118879, in *Proceedings of the 2009 SPE Reservoir Simulation Symposium, The Woodlands, February 2–4*, 2009.

Zhang, Y. and D. S. Oliver, Improving the ensemble estimate of the Kalman gain by bootstrap sampling, *Mathematical Geosciences*, **42**(3), 327–345, 2010.

Zhao, Y., A. C. Reynolds, and G. Li, Generating facies maps by assimilating production data and seismic data with the ensemble Kalman filter, SPE-113990, in *Proceedings of the 2008 SPE Improved Oil Recovery Symposium, Tulsa, Oklahoma, April 21–23*, 2008.

Zupanski, M., Maximum likelihood ensemble filter: Theoretical aspects, *Monthly Weather Review*, **133**(6), 1710–1726, 2005.